FLAME PROPERTIES AND FIRE SPREAD ON CYLINDRICAL FUEL BEDS

Danijela Ivkovic
BSc (Hons)

A thesis submitted in fulfilment
of the requirements for the degree of
Doctor of Philosophy

University of Tasmania

April 2010

DECLARATION OF ORIGINALITY

I hereby declare that this submission is my own work and to the best of my knowledge contains no materials previously published or written by other persons, nor material that has been previously accepted for the award of any other degree or diploma, except where due acknowledgement is made in the thesis.

Date: 30/04/2010

STATEMENT OF AUTHORITY OF ACCESS

This thesis may be made available for loan and limited copying in accordance with the *Copyright Act 1968*

Date: 30/04/2010

ACKNOWLEDGEMENTS

I wish to express my gratitude to my supervisors for all the help they have provided me through different stages of completion. The assistance I received from Professor Larry Forbes with the numerical model and my writing style, combined with his general encouragement, were crucial to my competing this thesis. I am grateful to Associate Professor Manuel Nunez and Dr Wendy Catchpole for suggesting fire research and all their help, suggestions and feedback in the initial stages of my candidature. I am also thankful to Dr Simon Wotherspoon for his feedback on the statistical modelling.

I also wish to thank: Dr Bret Butler from USDA for providing me with the information on the black body design, Nikola Ivković and Graham Evans from Evans Engineering for its manufacture, and also for allowing me unlimited access to their workshop, and Gavin Freemen and the officers and staff of the Hobart Fire Brigade who lent me their radiometer for experimental work and never complained when I set off fire alarms. I am thankful to Dr Mick Russell for generously donating his time to teach me to program and use data-loggers and to Darren Turner who was of great help by giving me prompt access to network and software licences on my several computers, the lifespans of which were shorter than my candidature.

I am grateful to Dr Jon Osborne whose encouragement helped me cross the finish line. I wish to acknowledge the general staff of the Geography and Maths and Physics departments at the University of Tasmania whose prompt assistance in a friendly and supportive manner have made working here very enjoyable.

I am very glad to have had the friendship of Lily Sekuljica during this time.

I am thankful to the University of Tasmania for awarding me a Tasmanian University Strategic Scholarship.

Finally, I am deeply grateful to my family. My mum, dad and brother have always been my great support and encouragement in any endeavour.

ABSTRACT

This thesis investigates the properties of flame and the propagation of fire on cylindrical fuel beds composed of several types of wood. The majority of experiments were conducted on Tasmanian Oak, although several other fuel types were considered as well. Empirical and physical models of flame propagation are presented.

The shape of a flame envelope around a fully ignited horizontal wooden brand was studied experimentally. The change in the flame shape during the period of burning, the time over which burning occurred and the burn efficiency were modelled empirically. Correlations relating these quantities to the geometry of the fuel bed and the rate of the fuel mass loss were performed. These are compared with results previously reported in the literature.

A further set of experiments was then performed on flame propagation along the cylindrical brand, for several wood types. The speed of the flame front, the flame height and width, the rate of fuel consumption and the efficiency were all measured, and their behaviour was correlated to the angle of the fuel bed to the horizontal, and to the diameter of the fuel cylinder and the initial moisture content. Some additional experiments were also performed on parallel horizontal cylindrical fuel brands, and the separation between them was found to have a significant effect on flame height. Some mechanisms for this effect are proposed.

The emissivity of small flames was measured for different fuel types, and for different geometrical arrangements of the fuel load. Experiments were performed using Tasmanian oak, nogal, ramin, white berch, pine, balsa, sapelli and pine needles as fuels.

A mathematical model is presented for describing flame propagation along a horizontal fuel bed. This results in a system of two non-linear coupled partial differential equations involving temperature and available fuel, as functions of time and the distance along the fuel bed. A detailed comparison with the experimental observations is undertaken. Some of the experimentally derived rules are used in the model, and some model parameters have been determined from the experimental observations. The model is capable of predicting the observed behaviour.

Contents

List of Figures

List of Tables

Chapter 1

Introduction

The ability of matter to burn has been of benefit and hindrance to human kind since prehistoric times. Understanding the processes that govern fire ignition, combustion and spread are of importance in fire safety studies of urban dwellings, fighting and controlling wildfires, managing natural landscapes, as well as designing internal-combustion engines such as turbines or automobiles.

Fire is a rapid and persistent exothermal chemical change that releases heat and light. Volatile gases released from the burning fuel and fine suspended matter envelope the burning fuel, forming a flame. For a process of burning, combustion, to occur, three elements termed 'fire triangle' are necessary: fuel, oxygen and energy. Energy transfers heat to fuel causing vaporisation of volatiles into gaseous fuel, as well as maintaining the fuel temperature ensuring fire persistence. Oxygen is essential in the chemical process of the combustion and insufficient access to oxygen will cause fire to cease. Fuel can be solid, liquid or gas. Solid fuel can be divided into non-charring and charring fuel. Non-charring fuel burns completely leaving no residue, whereas combustion of charring fuel, such as wood, produces a significant amount of residue.

The primary focus of this thesis is to study wood ignition and flame progression on small fuel. The initial chapters contain experimental results and empirical fits for the flame and combustion properties of wooden fuel. In the final chapter, a numerical model is developed to predict flame spread using heat transfer equations with a one-step chemical reaction rate, which is then compared to the experimental observations. In each of the chapters, an overview of the rel-

evant literature is presented. In this chapter a general overview of the current state of the science in general combustion and ignition is discussed.

1.1 Ignition

Every fire is started with an ignition, a process of marked transition of a system from a non-reactive equilibrium state to a self-sustaining reactive state (Atreya 1998). There are two types of ignition: spontaneous and piloted ignition. Spontaneous or auto-ignition is initiation of combustion without a spark or flame (NFPA 2001). Simms (1962) defines spontaneous ignition of wood by radiation as ignition where the rate of heating is high enough for the volatiles to be emitted from the surface, to mix with the air and for flame to appear and to flash down to the surface. Piloted (forced or induced) ignition is ignition of combustible gasses or vapours by a secondary source of energy, such as flame, spark, electrical arc or glowing wire (ISO 2000). The mixture of fuel vapours and air needs to be in proximity of the fuel and within the flammability limits of the composition, however external source of heat is needed to initiate the combustion (Kanury 1972). Piloted ignition is more important from the fire research perspective because it requires lower ignition threshold and it is the mechanism responsible for fire spread (Atreya 1998). In pilot ignition studies the element is usually preheated by a source with a constant heat (e.g. radiant panels) and ignited using pilots such as electrical spark or small flame.

For the ignition of fuel to occur, energy is needed to vaporise moisture and volatiles (Anderson 1969). This is the endothermic part of the reaction. If the density of volatiles evaporated is sufficient for the flammability to occur and there is oxygen present, the exothermic part of the reaction will begin.

The temperature at which fuel begins to burn is defined as the ignition temperature (Williams 1982). A variety of ignition temperatures are reported in the literature: $603°K$ Simms & Law (1967) , $593°K$ Anderson (1969), Kanury (1972), Baines (1990) and Rothermel (1972), $600°K$ Albini & Reinhardt (1995), $623°K$ Drysdale (2002), $643 - 650°K$ Williams (1976) Williams (1976, 1982), $598 - 648°K$ Atreya (1998).

Ignition is marked with onset of flaming (Chandler et al. 1991).

1.2 Chemical decomposition of wood

The decomposition of wood is a complicated process which occurs in several stages. There are many species of wood, and their physical structure and chemical composition vary with species as well as age of the tree. Wood is an inhomogeneous and non-isotropic material. It is composed predominantly from cellulose, hemicellulose and lignin as well as a wide range of extractives and mineral constituents (Chandler et al. 1991). The proportions of these components in wood vary between species. Generally, hardwoods contain $40-44\%$ cellulose, $23-40\%$ hemicellulose and $18-25\%$ lignin, whereas the composition of softwoods is $40-44\%$ cellulose, $20-32\%$ hemicellulose and $25-35\%$ lignin (Spearpoint 1999). Cellulose is a long chain polymer with repeated units of sugar D-glucose - $(C_6H_{10}O_5)_n$. Cellulose molecules are aligned into microfibril which form the structurally strong framework in the cell walls. The thermal decomposition of cellulose occurs at temperatures of $240-350°C$. Hemicellulose is a carbohydrate resembling cellulose but more soluble. Unlike cellulose, it has a random, amorphous structure with little strength. Its thermal degradation occurs at temperatures of $200-260°C$. The microfibrils are bound together with lignin, which is a high molecular weight polymer. Degradation of lignin occurs at temperatures of $280-500°C$ (Drysdale 2002).

The grain structure of wood affects some of its properties. The thermal conductivity of the wood is greater along the grain than in the perpendicular direction, as is also the gas permeability. The volatiles generated underneath the surface of the wood escape easier along the grain, which is evident from jets formed on the sides of burning brands.

Water molecules are usually present in wood through different physical mechanisms. In a live tree, 'free' or 'capillary' water is present in a liquid form and is held by weak capillary forces (Moghtaderi 2006). Water molecules in cell walls bound to hydroxyl groups such as cellulose, hemicellulose and lignin are referred to as 'bound' or 'hygroscopic' water (Moghtaderi 2006). Moisture content in trees can range from 30% be more than 200% of the weight of the wood substance (*Wood Handbook - Wood as an Engineering Material* 1999). After the tree is cut, free water is gradually become replaced with air (*Wood Handbook - Wood as an Engineering Material* 1999). When the cell walls are completely saturated but no 'free' water is present, wood has reached a fiber

saturation point. Average fiber saturation point for wood is about 30% but does vary between the species (*Wood Handbook - Wood as an Engineering Material* 1999). When only bound water is present, an equilibrium is formed between the moisture content of the wood and the relative humidity and the temperature of the surrounding air (Spearpoint 1999).

When exposed to external heating, the temperature of wood gradually increases from the surface inwards. When a temperature of $100°C$ is reached, free moisture evaporates. Some of the moisture evaporates into the unburned zone and re-condenses where temperatures are below $100°C$ (Janssens 2004). For wood temperatures below $200°C$ all of the chemical reactions are endothermic. Between $200°C$ and $280°C$ cellulose begins a chemical dehydration process. Exothermic reactions predominate when the temperature rises above $280°C$ (Chandler et al. 1991). Between $280°C$ and $350°C$ cellulose breaks down and decomposition products, volatiles and moisture flow out of the hot wood surface and the wood begins to char. As the charred layer deepens, cracks perpendicular to the direction of grain appear and widen, allowing volatiles easier escape to the surface. Combustible volatiles mix with the surrounding air and when the flammability limit for the fuel-air mixture is reached, it can be ignited with a pilot. Glowing reaction starts at the temperatures of $500°C - 600°C$.

1.3 Pyrolysis

Once fuel is ignited the process of pyrolysis occurs. Pyrolysis is the chemical degradation of a substance by action of heat (Babrauskas 2004). The pyrolysis of fuel plays an important role in the ignition and growth of fire. The heat released in the pyrolysis can allow for the self-sustained combustion to occur. The treatment of pyrolysis in modeling divides fire spread models into two broad categories thermal and comprehensive (Moghtaderi 2006). In thermal models the rate of pyrolysis is obtained from the energy balance, based on some critical pyrolysis criterion for the conversion of virgin fuel into its products. Temperature of ignition, mass loss rate or heat release rate are commonly used as criterion for ignition. Comprehensive models use a combination of chemical kinetic schemes with equation of energy and/or mass transfer. These models

$$\text{Virgin Fuel Components (i)} \xrightarrow{R_i} \text{Volatiles + Char}$$

can be further categorized as analytical, numerical or integral models.

Comprehensive models consider kinetic schemes of fuel degradation, where fuel is converted into the by-products of combustion, volatiles, char and gas. The fuel can be treated as a lumped product (one-step) or some of it's constitutes can be treated with different reaction rates (multi-step).

The rate of reaction, k, is described with Arrhenius reaction rate

$$k = Ae^{-\frac{E_a}{RT}},$$

where E_a is the activation energy, R is the universal gas constant, T is the temperature and A is the pre-exponential constant. This relation describes the dependence of the rate constant k of the chemical reaction on the absolute temperature T. The activation energy E_a is the energy that must be overcome in order for a chemical reaction to occur. The pre-exponential factor A, has the same units as the rate constant, which depends on the order of the reaction. In the first order reaction, these are s^{-1}, which is why A is sometimes referred to as a frequency factor. Most simply, if k is the number of collisions per second which result in a reaction, then the pre-exponential A is the total number of collisions and $e^{-\frac{E_a}{RT}}$ is the probability that any given collision will result in a reaction.

1.4 Heat Transfer

Physical or semi-physical models of fire initiation or spread are based on heat transfer from flame and glowing fuel bed to the unignited fuel. It is then important to define the methods of heat transfer and energy balance. Work presented in this section is available in any text book on heat transfer (e.g. (Rohsenow et al. 1985), (Incropera & DeWitt 1981)).

Heat is a form of energy associated with the motion of atoms or molecules. It can be defined as a form of energy transferred by virtue of a temperature difference (Rohsenow et al. 1985). There are three mechanisms of heat transfer: conduction, radiation and convection.

1.4.1 Conduction

Conduction is the transfer of heat from higher temperature part of an object to the lower temperature parts. It is a transfer that is associated with both temperature difference and the physical contact for a transfer to occur. Conduction occurs on molecular level, where higher temperature is associated with more energetic particles. In particle collisions, energy is transferred to less energetic particles. Therefore if there is a temperature difference within an object, energy transfer towards lower temperatures. The rate energy transferred is proportional to the temperature gradient and in one dimension it can be expressed as

$$q''_{cond} = -k\frac{\partial T}{\partial x}, \tag{1.1}$$

where k is thermal conductivity, T is temperature, x is the direction of the heat transfer and $\dot{q}''_{cond}$ (Wm^{-2}) is the heat flow in $x-$direction per unit area perpendicular to the transfer direction. This is known as Fourier's law of heat conduction. Thermal conductivity is characteristic of the material.

The net heat transferred than through a slab of cross-section area A and length Δx between two ends of temperatures T_1 and T_2 is then

$$q = \frac{\Delta T}{\frac{\Delta x}{kA}}, \tag{1.2}$$

where $\frac{\Delta x}{kA}$ is thermal resistance.

1.4.2 Radiation

Radiative transfer is energy emitted by all objects with temperature above absolute zero. The energy is attributed to changes in electron configurations

of the atoms and molecules in the matter, and is emitted at the expense of the internal energy of the matter. Radiation is transmitted by electromagnetic waves and hence it does not require for object to be in contact for the transfer to occur.

If an object is a perfect radiator it emits black body radiation, where the rate of energy radiated is described by Plank's law:

$$q''_{\lambda,T} = \frac{2\pi c^2 h \lambda^{-5}}{e^{\left(\frac{hc}{\lambda k_b T}\right)} - 1}, \tag{1.3}$$

where $q''_{\lambda,T}$ is radiative flux (Wm^{-2}) of an object at temperature T at wavelength λ, c is the speed of light ($3 \times 10^8 ms^{-1}$), h is Planck's constant ($6.63 \times 10^{-34} Js$), k_b is Boltzmann's constant ($1.38 \times 10^{-23} JK^{-1}$) and T is the temperature of the object. Total energy emitted by a black body of temperature T is then given by Stefan-Boltzman law:

$$q'' = \sigma T^4, \tag{1.4}$$

where σ is the Stefan-Boltzman constant ($5.67 \times 10^{-8} Wm^{-2} K^{-1}$).

Most objects are not perfect emitters. Emissivity of an object ε,is a ratio of the energy emitted by an object to the energy emitted by a perfect radiator. Emissivity can be wavelength dependent. Detailed description of monochromatic emissivity and emissivity of flames is presented in Chapter 3. In practise it is convenient to describe emissivity independent of wavelength. Such object is said to be a 'gray body', where the rate of energy release is described by Plank's law with emissivity factor ε:

$$q'' = \varepsilon \sigma T^4. \tag{1.5}$$

This is the rate at which energy is emitted by a surface of an object per unit area. Radiative heat transfer between objects of temperatures T_1 and T_2 is given by

$$q''_{rad} = A_2 F_v \varepsilon_1 \varepsilon_2 \sigma \left(T_1^4 - T_2^4\right), \tag{1.6}$$

where F_v is view factor between the two surfaces, and $\varepsilon_1$and ε_2 are surface emissivities.

View factor (sometimes called shape factor) is the fraction of energy leaving the object that is 'seen' by the second object. View factor between two surfaces

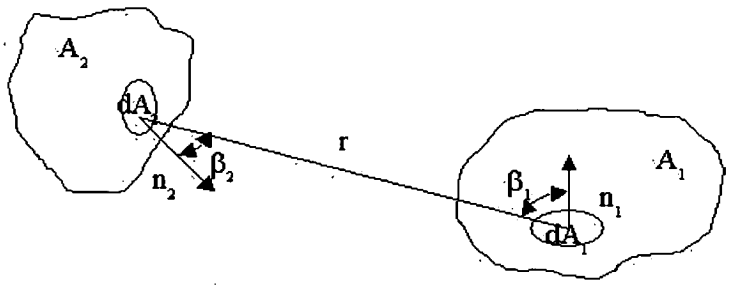

Figure 1.1: View Factor coordinates

A_1 and A_2 is defined by:

$$F_{v\,A_1\text{-}A_2} = \frac{1}{A_1}\int_{A_1}\int_{A_2}\frac{\cos\beta_1\cos\beta_2}{\pi r^2}dA_1dA_2, \tag{1.7}$$

where r is the distance between two infinitesimal areas dA_1 and dA_2 and the line of connection forms polar angles β_1 and β_2 with surface normals n_1 and n_2, Figure 1.1. Numerous view factor calculations for common shapes are available in the literature (e.g. (Sparrow & Cess 1978)).

1.4.3 Convection

Convective is a transport of energy by bulk motion of fluid. A parcel of air at higher temperature then its surrounding becomes lighter than surrounding air and thus rises transferring heat to higher altitudes. This process is termed "free" convection. When fluid motion is influenced by mechanical means, such as wind, fan, pump, the convection is termed "forced".

This form of transfer is significant for the fire spread over a sloped surface, or in presence of wind, where the flame is at an angle to the surface, creating turbulence in hot gasses transferring an amount of heat to the surface. The concept of heat transfer due to convection is described as if a thin film were developed between the fluid and a surface and heat is presumed to be transferred by conduction through the film:

$$q''_{conv} = h_c\left(T_f - T_s\right), \tag{1.8}$$

where T_f and T_s are the temperatures of the fluid and the surface and h_c is

the heat transfer coefficient ($Wm^{-2}K^{-1}$). This expression is called Newton's law of cooling.

Heat transfer coefficient depends on the surface geometry, nature of convection, and thermodynamic and transport properties. It can be found from dimensional analysis with numerical constants derived from experimental data. For forced convection the heat transfer coefficient is generally found from Nusselt (Nu) and Reynolds (Re) numbers correlation, where $Nu = \frac{h_c l}{k}$ and $Re = \frac{Ul}{n}$, l is characteristic particle dimension, k is thermal conductivity of the fluid, U is velocity of fluid flow past the particle, and n is fluid viscosity. For free convection, the heat transfer coefficient is a function of Nusselt and Grashof, Gr numbers, where $Gr = \frac{\beta g \Delta T l^3 \rho^2}{\nu^2}$, β is the coefficient of thermal expansion, g is acceleration due to gravity, ΔT is temperature difference.

1.4.4 Energy Balance

Exchange of heat between an object and its surroundings is summarized by the energy balance equation

$$\dot{E}_{in} + \dot{E}_g - \dot{E}_{out} = \dot{E}_s \tag{1.9}$$

where $\dot{E}_{in}$ and $\dot{E}_{out}$ are the rates of heat loss and gain by the object, $\dot{E}_s$ is the the rate of energy storage by the system and $\dot{E}_g$ is the rate of energy generated by the system. The heat stored in the object effects its temperature by

$$E_s = \rho V c_p \Delta T, \tag{1.10}$$

where c_p is the specific heat of the object, ρ is the density and V is the volume, so then

$$\dot{E}_{st} = \rho V c_p \frac{dT}{dt}$$

If an object of surface area A is immersed in a fluid of higher temperature T_∞, its temperature will increase for time t until it eventually reaches T_∞. For a thermally thin object the temperature gradients within the object are negligible and the temperature change can be estimated using lumped capacitance method. Then the energy balance equation is

$$\dot{E}_{in} = \dot{E}_{st} \tag{1.11}$$

where $\dot{E}_{in}$ is convective energy gained. So then

$$hA_s\left(T - T_\infty\right) = \rho V c_p \frac{dT}{dt} \tag{1.12}$$

where A_s is the the surface area of the object.

Assumption of thermally thin object or a lumped capacitance method is convenient and simple to use. However to asses the validity of the assumption of thermal thinness, one needs to consider the steady state heat transfer at the surface of the object. If an object is exposed to temperature T_∞ and the temperature at the centre of the object is T_0 then the temperature of the surface will be at an intermediate value T_s, where $T_0 < T_s < T_\infty$.

For an object that is thermally thick transient heat transfer needs to be considered.

1.5 Fire Spread Models

The first known publication of scientific model of fire ignition and spread was published by Bamford et al. (1945) who offered a closed form solution to the heat conduction equation, postulating a critical lower-limit mass loss rate criterion for sustained ignition. Kanury (1972) offers a review of the early models of ignition of solids. Other models which ignore features of the gas phase and focus on solving heat transfer problem include Anderson (1969), Albini & Reinhardt (1995),

Many approximate analytical solution based on heat transfer considerations are reported in literature. Objective of most of these studies is to relate time to ignite the wood to the level of irradiance. The first such study was by Lawson & Simms (1952) who used inert heating equation as a starting point for developing a method to treat the experimental data. Other approximate analytical solutions have been obtained Atreya (1983) who used one step kinetic scheme for one dimensional heat conduction, allowing for variable thermo-physical properties and moisture desorption, Panagiotou & Delichatsios (1989) for charring fuel using an integral model approximation, Moghtaderi et al. (1997) for charring and non-charring materials, or Spearpoint & Quintiere (2000) to name a few.

Model which include the chemical reaction, termed comprehensive models, can have one-step (Atreya (1983) , Moghtaderi et al. (1997), Weber et al. (1997), Higuera (2002), Mandel et al. (2008)) or multi-step kinetic reaction treatment (Forbes & Gray (1998), Hastaoglu & Berruti (1989), Blasi (1993),Blasi (1994))

.

1.6 THESIS STRUCTURE

The aim of this thesis is to investigate flame dimensions, progression and fuel properties over wooden fuel on a micro-scale. Experiments were performed on a range of fuel configurations and empirical models to describe the flame behaviors were developed in the first three chapters. A numerical model with parameters drawn from the experimental observations is developed and the rate of spread simulated is compared to that predicted in the final chapter.

The main fuel used in the experiments and modelling was Tasmanian oak which is a generic name for Tasmanian eucalypt species: *Eucalyptus delegatensis, Eucalyptus obliqua and Eucalyptus regnans.* Experiments on flame and combustion properties were also conducted on: sapelli (*Entandrophragma Cylindricum*) a semi-hard wood from central Africa with high sap content, ramin (*Gonystylus macrophyllum*), a tropical hardwood species from South Asia, nogal, a chocolate brown South American walnut from the *Juglandaceae* family and white birchwood species of the *Betulaceae* family.

In experiments where emissivity of flame over different fuel was measured (Chapter 4), other than the above mentioned fuel, balsa *(Ochroma pyramidale)* pine and pine needles from *Pinus radiatà* were also used.

Chapter 2: Focus of this chapter is in examining flame properties of horizontal cylindrical elements ignited along their length. Changes in flame height and mass loss rate, duration of the flaming and changes in the flame length are examined over the flaming time. The flaming time, and start and the end of the flaming are related to the fuel parameters used to describe mass loss rate and flame height. The width of the flame envelope is also empirically related to the fuel dimensions.

Chapter 3: In this chapter, flame spread along an elements is investigated for various configurations. Flame height and width, rate of spread and residence time are parametrized in terms of fuel moisture content, orientation and its diameter. An effect of separation between two elements whilst the flame is merged above them is also studied.

Chapter 4: Flame emissivity of small flames is measured in this chapter. Experiments were performed to estimate mean effective emissivity of flames for different configurations. Emissivity of flames above horizontal elements with varied diameters was measured to provide emissivity factor in later chapters, in order to quantify the radiative effect on the flame spread. Emissivity of flames above more elements with separation varied between them was also examined. Emissivity is commonly parametrized in terms of pathlength. This relationship was studied on small flames as well as flames of up to a metre depth. Theoretical overview of emissivity predictions is also given in this chapter.

Chapter 5: In this chapter a numerical model based on the heat transfer and one-step heat of chemical reactions is developed to describe flame spread along a horizontal cylindrical wood element. The parameters used in the model are derived from the experimental observations in the previous chapters, and the rate of flame spread simulated was compared to those observed for different element diameters and fuel moisture content.

Chapter 6: The main findings of the thesis are summarized in this chapter.

Appendix A: Measurements of heat of combustion were conducted on all of the fuel used in the thesis. These are presented in this appendix.

Appendix B: Coefficients from empirical fits in Chapter 2 are given in this appendix

Chapter 2

Flame Height and Mass Loss Rate Experiments

2.1 INTRODUCTION

As an aid in understanding fire behaviour, this study concentrates on the processes of fire ignition on a micro scale. As part of this study it is necessary to understand the flame geometry of a single element on a fine scale.

Wood is an inhomogeneous and non-isotropic material. When exposed to temperatures above $200°C$, wood constituents begin to break down and wood begins to char. As the charred layer deepens, cracks perpendicular to the direction of grain appear and widen, allowing volatiles easier escape to the surface. When thin pieces of wood are ignited, the heat loss to the unignited material is sufficiently low for a self sustained burn to occur, and a flame envelope develops around the element. As wood burns and cracks in the wood surface appear, the jets of volatiles 'escaping' to the surface create 'alligatoring' flame pattern. Degradation of the top surface of the wood allows for more volatiles to escape, creating the flame envelope around the burning wood.

Sets of experiments were conducted to investigate changes in flame envelope over time. Horizontal cylindrical brands of Tasmanian oak (Tasmanian *Eucalyptus* species) were suspended in air and ignited along their length. The changes in the flame shape and in the mass loss of the burning element are

studied in the experiments given in this chapter. The effect of the element's diameter is related to: the efficiency of the combustion, flame height, effective flame length, the rate of mass loss and the residence time or the active flaming time of the element. Results of experiments for Tasmanian oak are then compared to the experiments using nogal (from the *Juglandaceae* family), for which brands of smaller diameter were available. The results for both are then compared to the existing models for flame heights and mass loss relationship. Finally the flame-standoff, or the width of the flame envelope, is also studied with respect to the element's diameter.

2.2 LITERATURE REVIEW

A vast amount of work on flame height and mass loss rate measurements and theoretical predictions exists in the literature. Experiments have been performed on different types of fuel (solid, liquid or gaseous, natural or processed materials), various fuel geometries (cylinders, sheets, solids, fine fuel, etc...) and orientations (vertical, horizontal, at an angle), combustion governed by external heat source or by the flame, and so on. It would be impossible to review all of the work that has been of importance to this field of study; hence the sources cited here are only those directly relevant to this study for comparison purposes.

Flame height is most commonly correlated to the rate of mass loss of fuel. Thomas et al. (1961) were the first to parametrise the flame height of fires in wooden fuel using dimensional analysis where buoyancy was the driving force. They related flame height over a characteristic dimension to a Froude number, $\frac{\dot{m}^2}{\rho^2 g D^5 \beta \Delta T}$, where $\dot{m}$ is a mass flow rate, ρ is the density of the burning gas and D is the characteristic diameter of the fuel bed. The parameter group $g\beta\Delta T$ represents the influence of buoyancy, where g is acceleration due to gravity, β is the expansion coefficient of air and ΔT is the difference in flame temperature to that of the surrounding air. They tested the relationship experimentally on horizontal cribs of wooden sticks (Spruce) where the average of the maximum flame height reached was used, and different mass loss rates were obtained by changing the fuel loading, to obtain the following relationship $\frac{H}{D} \propto \left(\frac{\dot{m}^2}{D^5}\right)^{0.3}$. On a non-dimensional scale this was re-written as $\frac{H}{D} \propto \left(\frac{\dot{m}''}{\rho_0 (gD)^{0.5}}\right)^{0.61}$ (Thomas

1963), where $\dot{m}''$ is the rate of mass loss per unit area, ρ_0 is the air density, g is acceleration due to gravity and D is the base length of the fuel bed.

Fons et al. (1963) used a modified Froude number for flame height correlations in experiments where flame propagated across a long crib bed. They found that for $\frac{D}{w} < 1.0$, where D is the flaming zone and w is the width of crib, $\frac{H}{D} \propto \left(\frac{C^2G^2}{\rho^2 gD}\right)^{0.43}$ where C is the weight of gas produced per unit weight of solid fuel, and G is the rate of burning per unit area of the crib. For $\frac{D}{w} < 0.5$ the relationship obtained was $H \propto \dot{m}^{\frac{2}{3}}$. Kodson et al. (1969) correlated flame height to the rate of mass loss of the fuel for vertical cylinders of $\alpha-$cellulose and birchwood using $\frac{H}{D} \propto \left(\frac{\dot{m}^2}{D^5}\right)^{0.24}$.

Numerous experiments have been performed on gaseous fuel with flame in buoyancy controlled range to obtain a range of coefficient values for different values of the Froude number. Putnam & Speich (1963) obtained a coefficient of 0.2, as did Blake & McDonald (1993) when correlating flame height to the density weighted Froude number for a range of gases.

Other non-dimensional groups were used to relate flame height to the rate of mass loss of the fuel. Heskestad (1983, 1991, 1999) related flame height to a non-dimensional group N, where $\frac{H}{D} = f(N)$ and $N = \left[\frac{c_p T_0 r^3}{g\rho^2 h_c}\right] \frac{\dot{m}^2}{D^5}$. In this equation c_p is specific heat of air, T_0 is the air temperature, h_c is the heat of combustion and r is the stoichiometric mass ratio of air to volatiles.

Another dimensionless group used by Zukoski (1986) is $\dot{Q}^*$, the 'dimensionless heat release rate', defined as $\frac{\dot{Q}_c}{C_p \rho_0 T_0 \sqrt{gD} D^2}$, where $\dot{Q}_c$ is the heat release rate, calculated from $\eta h_c \dot{m}$ in which h_c is the heat capacity and η the efficiency of the combustion. A range of experimental values reported can be found related to $\dot{Q}^*$ (Drysdale 2002). Zukoski (1986) postulated that the power coefficient varies for different ranges of $\dot{Q}^*$. For example, for values of $0.5 < \dot{Q}^* < 7$ Zukoski (1986) suggest a coefficient of $\frac{2}{3}$, which is in agreement with the results obtained by Thomas (1963). However for the values of $0.2 < \dot{Q}^* < 0.5$ a linear relationship seems more appropriate, whereas for $\dot{Q}^* < 0.2$ a power law appears more fitting. High values of $\dot{Q}^*$ indicate momentum driven, fully turbulent jet fires.

The closest to this study for comparison purposes is work by Muraszew (1974) who conducted experiments on horizontal cylindrical firebrands, obtaining the

relationship $H = 163\dot{m}'^{0.662}$ for flame height and rate of mass loss per unit length of the firebrand ($\dot{m}'$).

2.3 METHODS

In this set of experiments Tasmanian oak horizontal cylindrical elements were ignited along the entire length, to investigate the change in the flame height and mass loss rate over time for different diameters of elements. Tasmanian oak is a generic name given to tree types of Tasmanian eucalypt species: *Eucalyptus delegatensis, Eucalyptus obliqua* and *Eucalyptus regnans.*

The experiment was conducted with Tasmanian oak cylinders of diameters 4, 5, 6, 8 and 9.5 mm. The length of elements used were predominantly about 10 cm, although some lengths between 6 and 12 cm were used as well. For each diameter approximately 20 repetitions were performed. All elements used were dried overnight in an oven at $110°C$ and prior to the burn kept in a desiccator at room temperature. Elements were ignited with an external source along their length, which was removed when self-sustained flame was developed along the entire length of the element. Since diameters smaller than 4 mm were not available for Tasmanian oak, a set of experiments was performed on nogal, a South American walnut from the *Juglandaceae* family, for diameters: 2, 3, 4, 5, 6, 8 and 10 mm to evaluate the behaviour of elements of smaller diameters and compare to the results obtained for Tasmanian oak.

Set up

Elements were held above ground by a stand which was placed on a balance, and mass was recorded every second. A VCR camera was placed in front of the element, and a video capturing device was connected between the camera and a laptop computer to recorded images of the burning process once a second. The stand was marked with a 5 cm vertical line to relate the shape and movement of the flame to a distance scale. Both balance and capturing device were operated through a laptop computer and data logging was synchronized throughout the experiment.

Figure 2.1: The experimental set up for flame detection

Image Analysis

Images from each burn were analyzed using IDL program code, in which each image is converted into an array of colour values for each pixel of the image. Flame is the brightest area on the image and hence is determined as the pixels with the highest values on all channels. For example, consider the colour index of the image in Figure 2.2: the date stamp in red has colour index of around $[230, 15, 15]$ on the $0 - 255$ red, green and blue channels; the pixels of the background have values of between 100 and 200 in all three channels; the pixels of the vertical scale line on the stand have values lower than 100 on all three channels, whereas the pixels of the flame have values greater than 230 on all three channels.

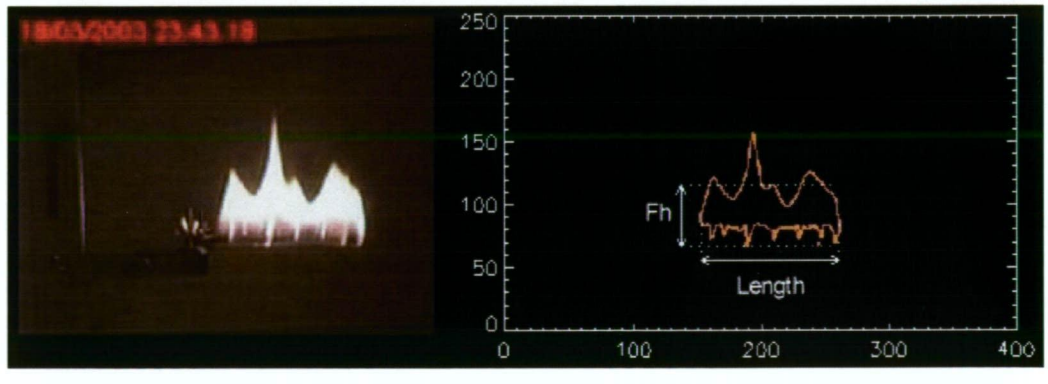

Figure 2.2: Image of a horizontal element burning along its length and the contour of the flame detected. Flame height and width measured are marked on the image to the right.

Scale

The 5 *cm* vertical line on the stand was detected by searching for the pixels with values lower than 100 on all three channels, with the condition of minimum number of pixels in the $y-$ direction. This condition was employed in order to avoid random single dark points on the rest of the image. A visual conformation that the line was properly detected was employed in a similar way to the flame detection method discussed below. The number of pixels detected vertically in the line was used to determine the scale of that image S *cm/pixel* and thus relate the flame height from pixels detected to centimetres.

Flame Detection

In order to ensure all of the flame was detected, the colour limit for the flame was set to 200 minimum on all channels with the sum of all three greater than 550. Testing this constraint on numerous images had shown it to be a liberal one, allowing detection of all bright spots related to the flame. However, this allowed for the flame reflection on the butterfly nut, used to clamp the element, to be detected as well. In order to avoid this, the end of the element where it was clamped to the stand was selected manually for each burn, and the program applied to the image area excluding the stand. This was done so that no constraints needed to be set as glowing and breaks in the flame were required to be measured to analyze the change of the flame in time. An image of the flame detected was stored with the original image for a further visual confirmation of correctly detected flame. The coordinates of the pixels for the detected flame were stored in a set, from which values for the flame height, width, the beginning and the end of the flame were extracted.

Mass Loss and Flame Data Coordination

The balance, on which the stand and the element were placed, logged the mass of the system on a computer once a second using the computer time. The time marks, of the computer times, were stamped on all the images of burn process captured by the video capturing device. This time, at which the image was

taken, was then used to synchronise the mass recordings to the flame related data extracted from the image.

Flame Data Extraction

The flame was detected using the method described in previous paragraphs. Images in Figure 2.2 show an example of a flame and the image detected.

From the set of detected flame points, flame height and width were recorded. It can be seen in the image in Figure 2.2 that due to the thickness of the element and the transmissivity of the flame, as the flame starts to break, the section of the flame below the element can be transparent and the bottom of the flame was often not detected for each $x-$ coordinate. To ensure that the flame is measured from a fixed reference point below the element, the y value of the bottom of the flame was manually detected for each burn and was measured in pixel heights on the image. That $y-$ coordinate, Y_0, was considered to be the bottom of the flame for the images from that burn. For each $x-$ coordinate in the flame set, the maximum $y-$ coordinate Y_x was found, and the flame height at coordinate x was calculated as

$$h_x = (Y_x - Y_0 + 1) \times S, \tag{2.1}$$

where S is the scale factor. The average flame height over the element was then calculated. This method was at times invalid if in the later stages of the burn the element bent upwards or downwards. The flame height values in these cases were disregarded.

The flame length was defined using the maximum count of flame pixels in the horizontal direction. The length of the element initially ignited, however, was used for the mass loss per unit length calculations.

After the average flame height values were calculated for all of the images, the data was merged with the measured mass loss. The beginning of the burn was defined to be from the first image where the ignition source was removed until the end of flaming combustion.

2.4 RESULTS

2.4.1 Efficiency

The efficiency of burn was calculated to account for the effect of the diameter on the completeness of combustion. Efficiency, η, is the ratio of the mass of wood burned to the total mass available.

For an element placed in a stand, a part of its length is clipped in the stand and does not burn in the experiment. At the end of each burn, the charred part of the element was removed, and the remaining part measured. This value was subtracted from the recorded values, to obtain the true weight of the burning element.

The fraction of the weight lost during combustion thus found was correlated with the diameter D of the elements. The average values of the data measured, shown in the figure 2.3, indicate exponential decay in the efficiency of combustion with diameter. Data fitting gave the equation

$$\eta = 0.976e^{-17.0D} \tag{2.2}$$

with a correlation R^2 obtained from the χ^2 goodness of fit test equal to $R^2 = 0.979$. The diameter D in the equation (2.2) is measured in metres.

2.4.2 Mass Loss Rate

Changes in the mass of an element during combustion were recorded once a second. The mass loss rate recorded here for the single element burning individually was plotted against time, with starting time $t = 0$ taken to be the time when 50% of weight loss was achieved. The results for sample burns of four different diameters are shown in Figure 2.4.

The rate of mass loss obtained in the experiments was parameterized through the following Gaussian function,

$$\dot{m}' = m'_{\max} e^{-\frac{t^2}{2\sigma_m^2}}, \tag{2.3}$$

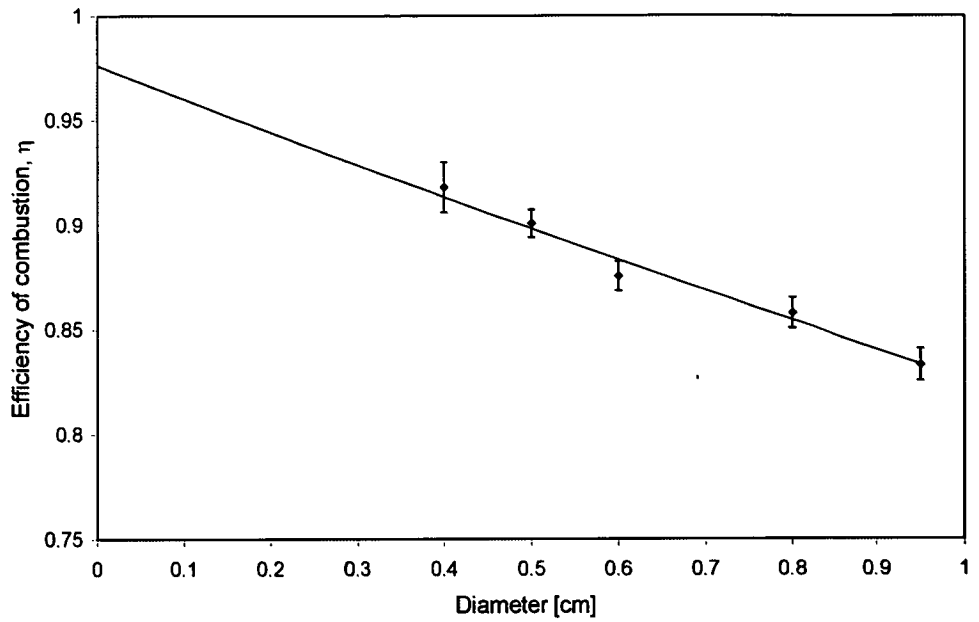

Figure 2.3: Efficiency of the complete single element combustion versus diameter. Error bars represent the standard error in the measured sample.

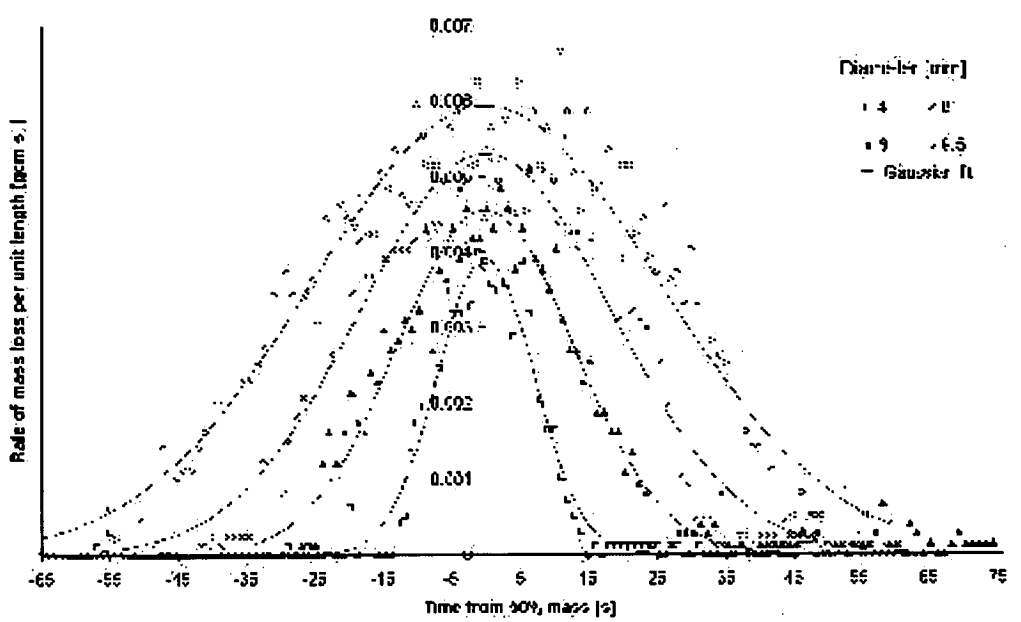

Figure 2.4: This figure shows the rate of mass loss recorded and the Gaussian fit in combustion of four elements of 4, 5, 6 and 9.5 mm diameters.

where $\dot{m}'$ is the rate of mass loss per unit length $[kgs^{-1}m^{-1}]$, t is the time (where $t = 0\ s$ represents time when 50% of mass is consumed) and σ_m is the measure of the spread of the Gaussian.

Values measured for the rate of mass loss were fitted to the Gaussian function $\dot{m} = \dot{m}_{\max} e^{-\frac{\left(t'-t'_{50\%}\right)^2}{2\sigma_m^2}}$, where $t'_{50\%}$ is the time when 50% of mass is consumed. Note that t' is the experimental measurement time, and $t = t' - t'_{50\%}$, where 50% of the mass loss occurs at $t = 0s$. From the results obtained here for $t'_{50\%}$, the time scale was adjusted to $t = 0$ at 50% weight loss. All measurements in this section are given with respect to the time scale t.

The model was fitted using the *Curvefit* function in *IDL* programing language based on code from Bevington (1969, p237-239). The error in the data points was assumed to be no more than 10% of the maximum value for mass loss rate measured and all data points were given equal weight. The parameters obtained, the estimated standard error in the parameters, the R^2 correlation between the observed and predicted data, and the reduced χ^2 values are given in the Table B.1 in Appendix B. The model tends to overestimate at the tail ends of the distribution, but provides an acceptable model for the central section of the data. Figure 2.5 shows the values for the rate of mass loss observed versus the predicted values. Note that there is a bias (under-prediction on average). The Gaussian model obtained was considered acceptable for the diameter values used in these experiments.

Consider now the parameters of the Gaussian function. For a combustion of efficiency η, the total mass loss M_T during combustion is ηM_a, where M_a is the initial mass of the element or the mass available. The total mass loss M_T for an element during combustion is the area under the Gaussian curve,

$$M_T = m_{\max}\sqrt{2\pi}\sigma_m.$$

The mass loss rate per unit length can then be written

$$\dot{m}' = \frac{M'_T}{\sqrt{2\pi}\sigma_m} e^{-\frac{t^2}{2\sigma_m^2}}, \tag{2.4}$$

where M'_T is the total mass consumed per element length,

$$M'_T = \frac{\eta M_a}{l} = \frac{\eta D^2 \rho \pi}{4}. \tag{2.5}$$

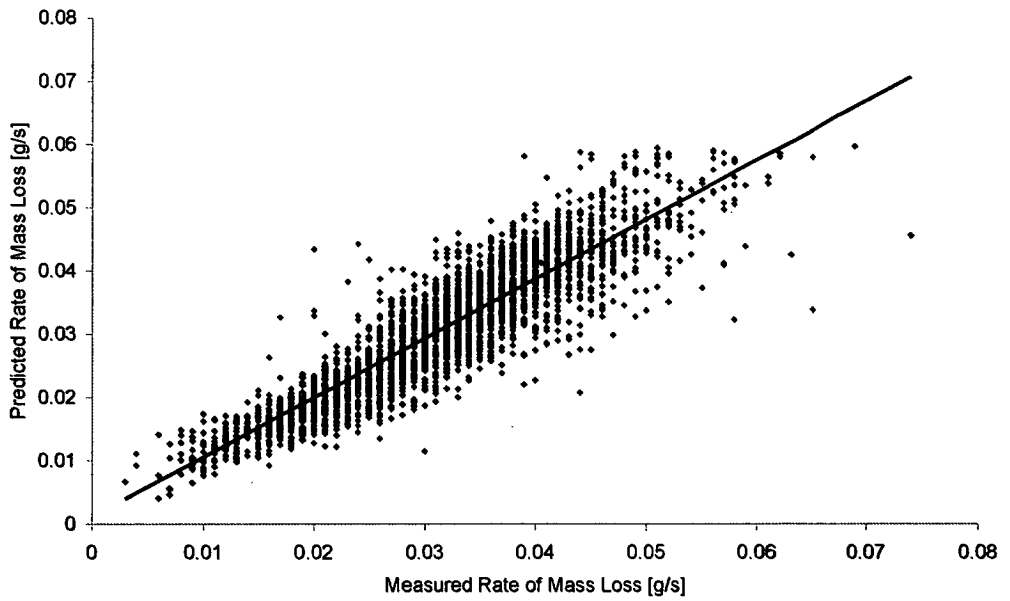

Figure 2.5: Observed versus predicted rate of mass loss. *Predicted* = 0.9413 × *Observed* with $R^2 = 0.8087$.

The spread of the fitted Gaussian, σ_m, is directly related to the flaming time or the residence time of the element. In later sections it is compared to the flaming time measured from flame height data. Weighted linear regression, using the estimated standard errors in fitted σ_m, was used to calculate the weighted average σ_m for each diameter, and these are shown in Figure 2.6. The values obtained yield the following equation

$$\sigma_m = 3.27 \times 10^4 \times D^{1.54} \tag{2.6}$$

in SI units, with $R^2 = 0.985$.

Due to the variations in density within each tree species, the density of the samples used was subject to some variation. The mass and length of each dry element were measured prior to each burn, hence σ_m could be compared to M'_T, the total mass of fuel consumed per unit length. The result is plotted in Figure 2.7, and the following power law relation was fitted

$$\sigma_m = 418 \times M_T'^{0.833} \tag{2.7}$$

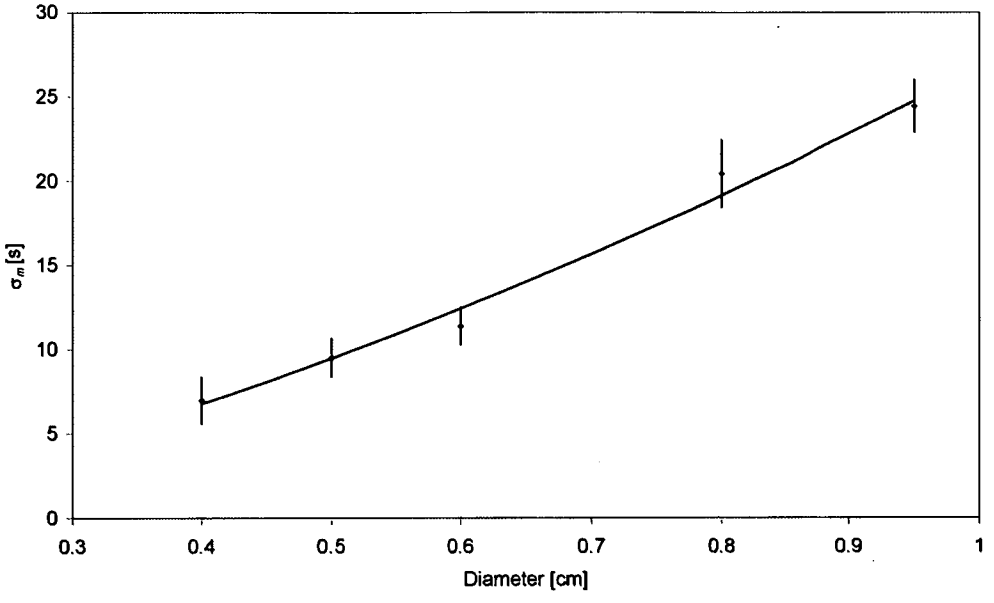

Figure 2.6: σ_m versus diameter of the element. Error bars represent one standard deviation.

in SI units, with $R^2 = 0.9723$.

We can then compare the peak rate of mass loss to the total mass consumed. Inserting equation (2.7) into equation (2.4) we obtain

$$\dot{m}' = 9.54 \times 10^{-4} M_T'^{0.167} e^{-\frac{t^2}{2\sigma_m^2}}. \tag{2.8}$$

Using equations (2.5) and (2.2), the dependency of the peak rate of mass loss per unit length on the diameter can be expressed as

$$\dot{m}'_{\max} = 2.68 \times 10^{-3} e^{-2.77D} D^{0.334}, \tag{2.9}$$

for horizontal cylinders of Tasmanian oak, assuming a density of 640 kgm^{-3}.

2.4.3 Flame Height

In most of the experiments reviewed by the author, flame height was studied during a quasi steady state, where an average reading was compared to the average rate of mass loss. In the sets of experiments described here, fuel used

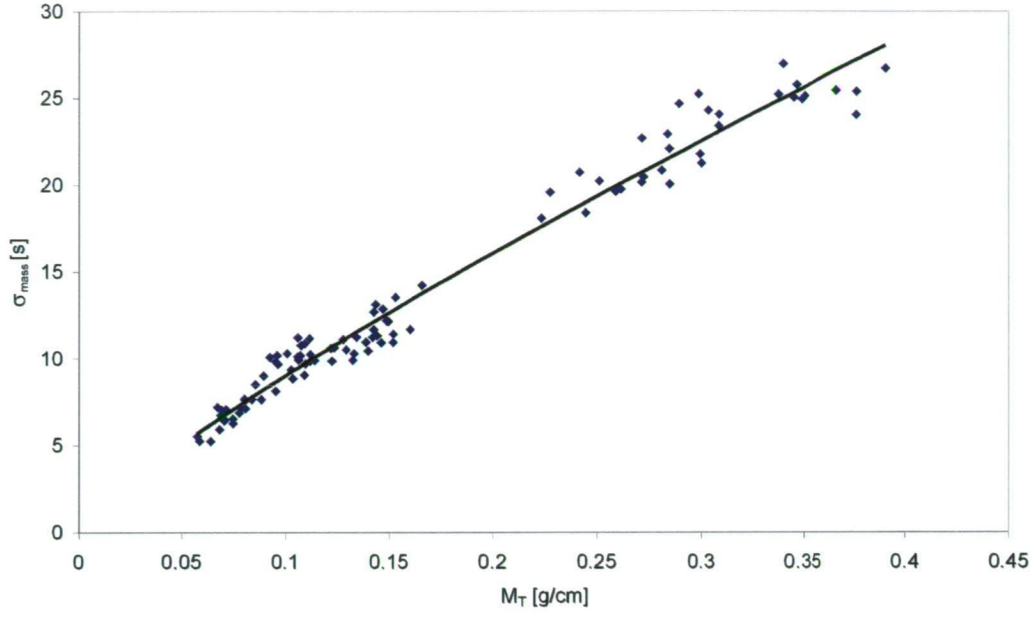

Figure 2.7: σ_m for Tasmanian oak versus total mass of element consumed in combustion per unit length, for 97 samples.

is of a smaller diameter and a quasi-steady phase was never reached. Indeed, after self-sustained reaction was obtained, the size of the full flame reached the peak height, after which it started to break into smaller jets, consequently reducing in average height. An example of the burning stages of two cylinders of 4 mm and 8 mm diameter is shown in Figures 2.8 and 2.9 respectively.

Analyzing the flame height over time it was found that average flame height may be adequately described with the Gaussian distribution shape as well. The average height data was fitted to

$$H = H_{\max} e^{-\frac{1}{2}\left(\frac{t-t^*}{\sigma_f}\right)^2}, \tag{2.10}$$

where time t was measured from 50% weight consumed. The time variable t^* denotes the time difference between the maximum in mass loss rate and the maximum in the flame height. The limits on the time are placed by defining the start of the ignition and the end of the flaming, which is dealt with in the next section.

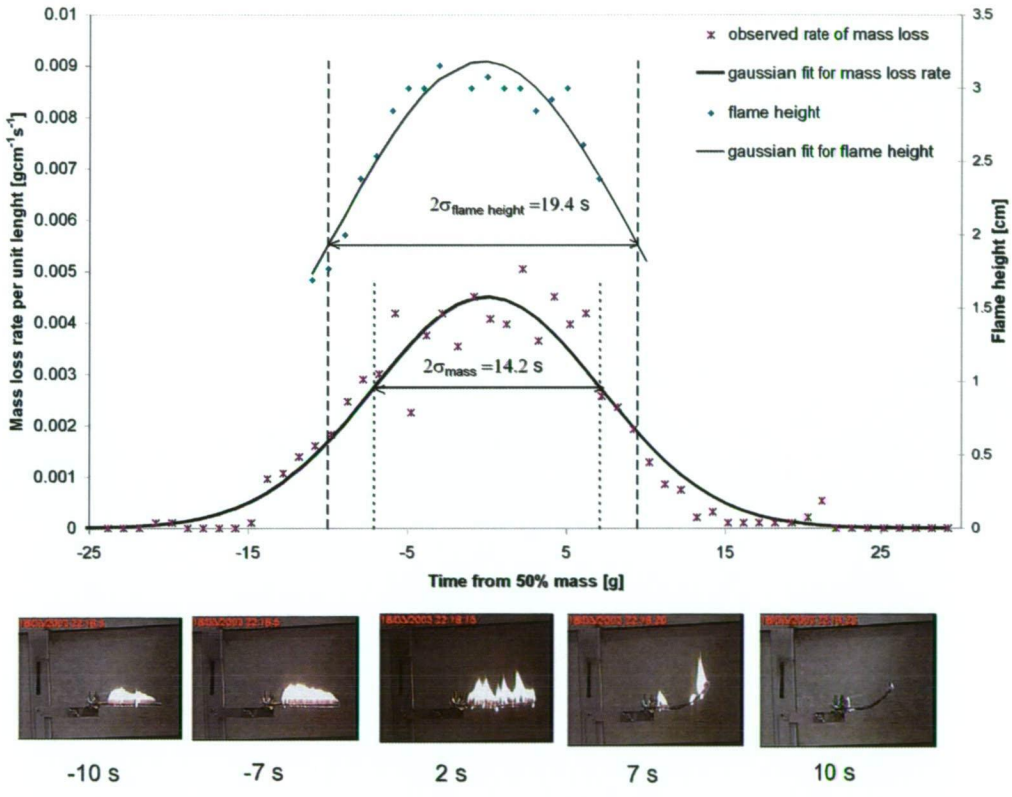

Figure 2.8: Mass loss rate and the flame height images for 4 mm oak. The Gaussian fit for mass loss rate and flame height are plotted with the observed values. Note the difference between σ_m and σ_f

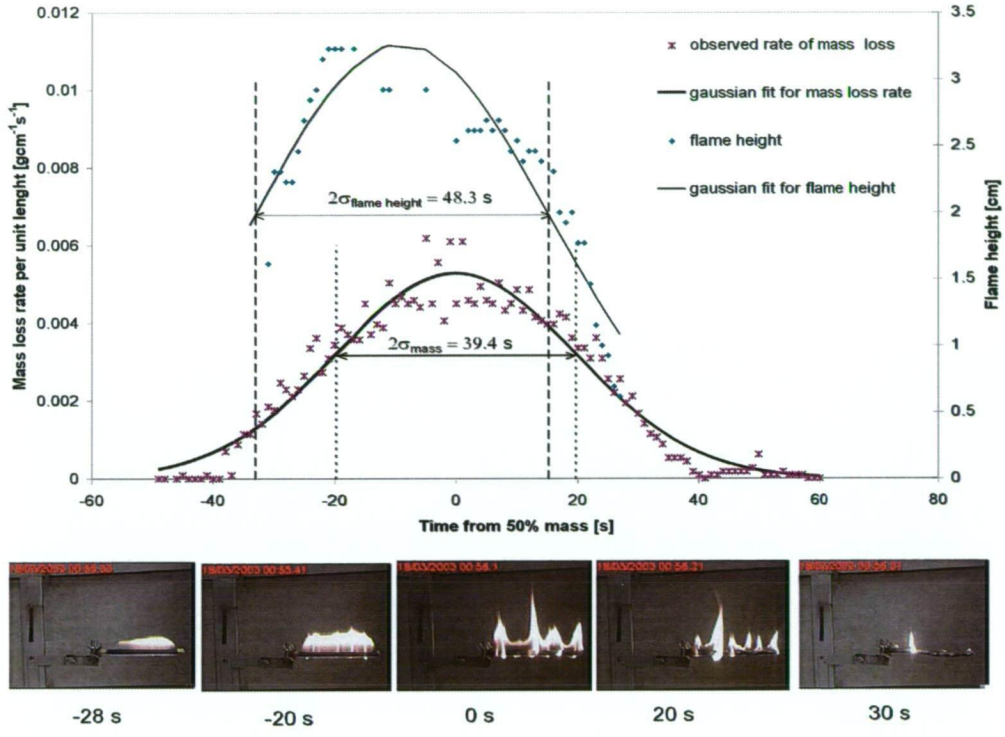

Figure 2.9: Mass loss rate and the flame height images for 8 mm oak. The Gaussian fit for mass loss rate and flame height are plotted with the observed values. Note the difference between σ_m and σ_f as well as the difference in the positions of the peak values.

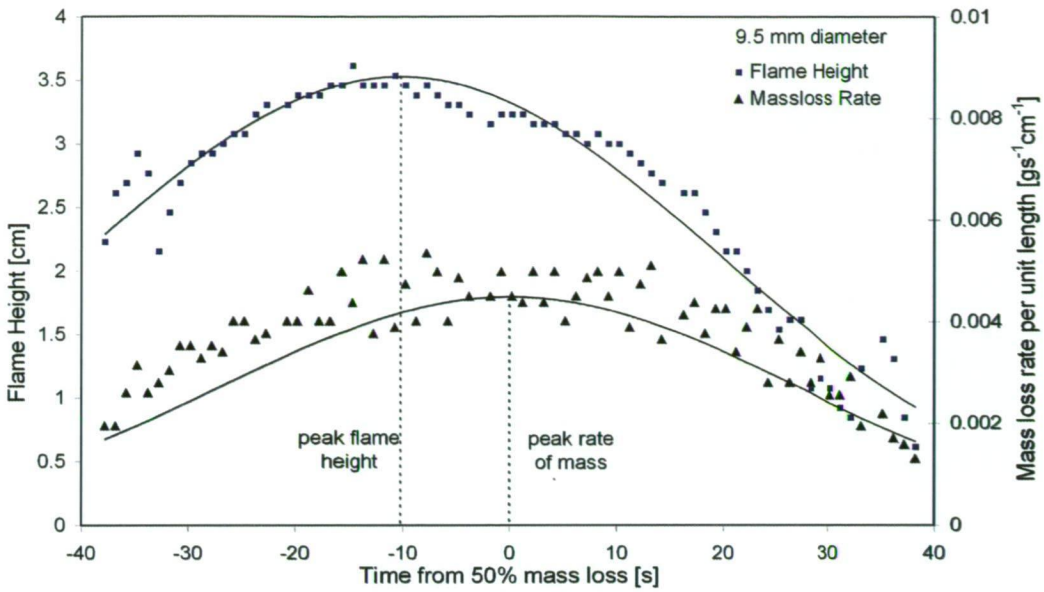

Figure 2.10: Flame height and mass loss rate measurements with Gaussian fits for 9.5 diameter Tasmanian oak. Note that the average flame height peaks approximately 10 seconds before the mass loss rate does.

The analysis of the data is similar to that for the rate of mass loss and the results are recorded in Appendix B. It is interesting to note that there was significant difference between the spread of the Gaussian distribution between the flame height and mass loss rate, and that the peak flame height was reached before the peak rate of mass loss (Figure 2.10). The difference between the peak in the flame height and the peak rate of mass loss increases with the increase in the diameter (Figure 2.13). This effect most likely can be attributed to the heated volatiles underneath the burning surface escaping along the grain to the ends of the element, or through the developing cracks in the wood creating 'side-jets' of flame. This break in the laminar envelope is shown in Figures 2.8 and 2.9. Most of the jets are expunged at low speeds and flame upwards marginally increasing the width of the flame envelope, but still contribute to the average flame height detected. However, occasionally a strong velocity jet occurs sideways flaming for several seconds and is not detectable by the camera, thus the resultant increase in the rate of mass loss is not reflected in the flame height observation.

Figures 2.11, 2.12 and 2.13 show means of the parameters obtained from the

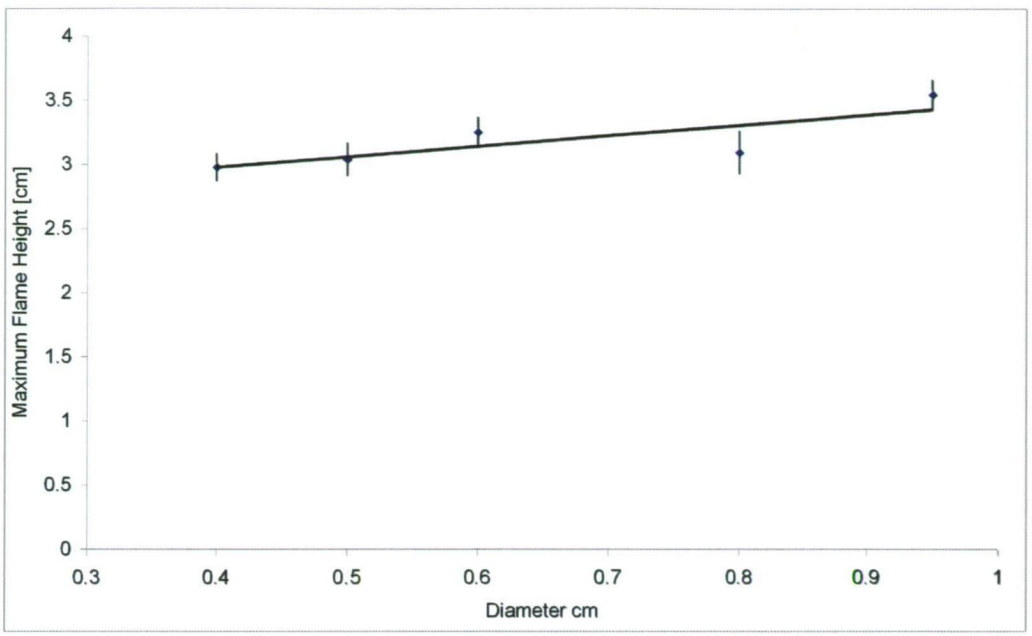

Figure 2.11: Maximum flame height over completely ignited element versus diameter. Error bars represent two standard errors.

Gaussian fit, which were modelled relative to the diameter of the element, producing the following relations:

$$H_{\max} = 0.0848 D^{0.192}, \tag{2.11}$$

$$\sigma_f = 7.31 \times 10^4 D^{1.67}, \tag{2.12}$$

$$t^* = -6.61 \times 10^4 D^{1.83}, \tag{2.13}$$

in SI units. The weakest of these relationships is for the peak flame height in equation (2.11) and R^2 obtained is 0.828. The relationships for σ_f and time offset t^* resulted with R^2 of 0.972 and 0.944 respectively. The relationship for maximum flame height appears to be well described with a linear model; however, comparing the Tasmanian oak data to the results obtained for nogal (section 2.4.6), it is evident that the power form of the relation is a better description of the data.

The relationship of the spread of the Gaussian function for flame height to that from the mass loss rate is shown in Figure 2.14. This gave the linear fit

$$\sigma_f = 1.23 \sigma_m \tag{2.14}$$

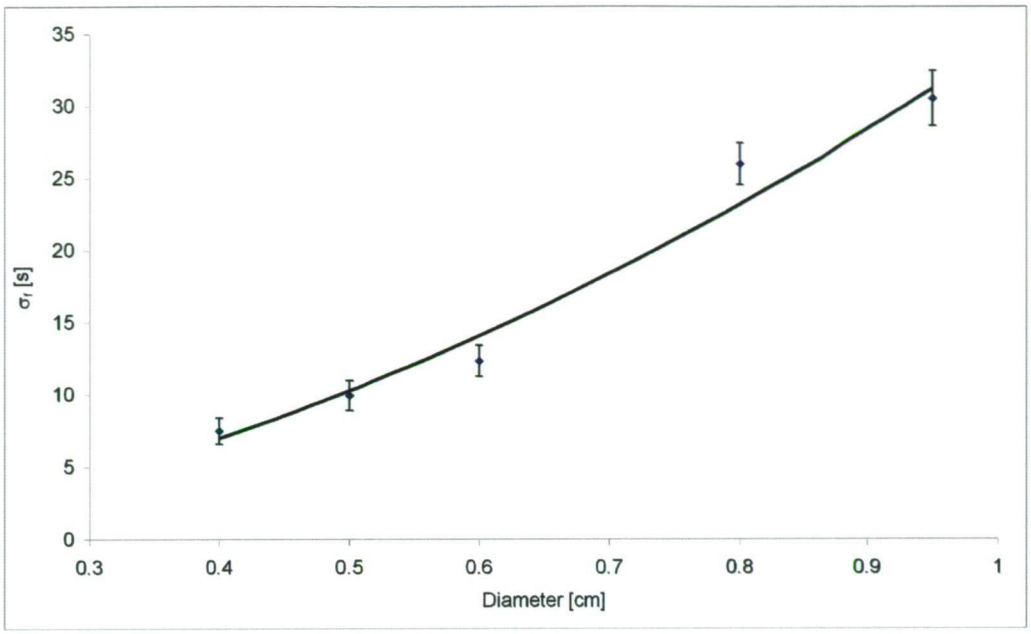

Figure 2.12: σ_f versus diameter for completely ignited elements. Weighted average values are used, error bars represent two standard errors

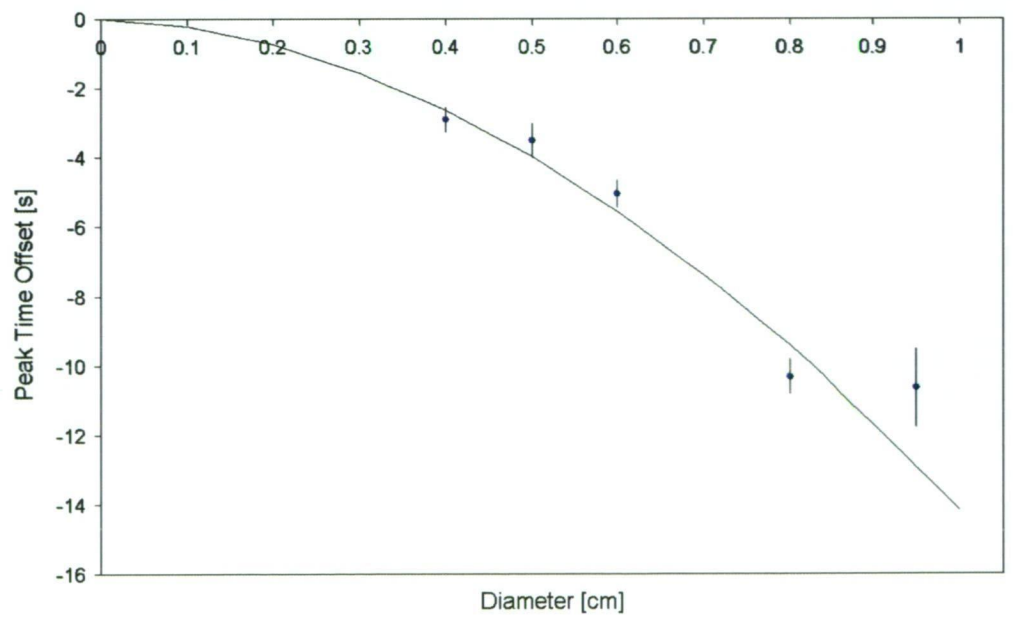

Figure 2.13: Time offset between the peak in mass loss rate and maximum flame height. Weighted averages are used in the calculation, error bars represent one standard error.

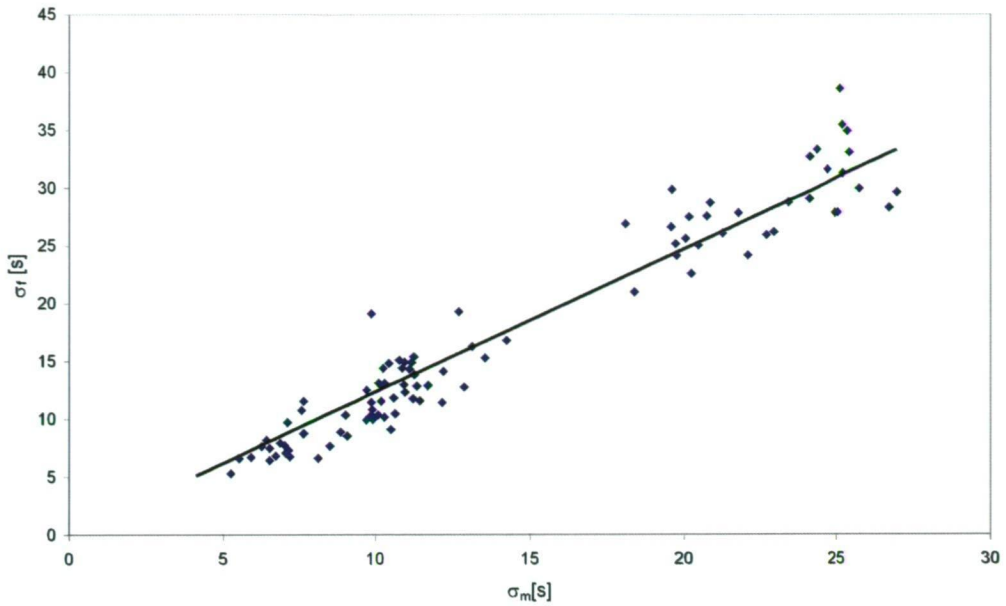

Figure 2.14: Relationship between σ_m and σ_f.

with $R^2 = 0.93$.

2.4.4 Residence Time

Visual observation of the residence time or flaming time from the removal of the ignition source until the flame extinguished was compared to the weight loss of the element during the combustion. On average, the flame was ignited after $6.75 \pm 0.74\%$ of the total mass was consumed and extinguished after $91.59 \pm 3.54\%$. The visually observed flaming time was compared to the spread of the Gaussian functions fitted to mass loss rate and flame height, σ_m and σ_f. Figure 2.15 shows the relation of the flaming time observed to the σ_m and σ_f values fitted to the data.

The Gaussian functions for mass loss rate and flame height are related to the time scale in which $t = 0$ at 50% mass loss. Thus the beginning and the end of each burn were calculated using this time scale. It was noted that the element was ignited at time

$$t_0 = (-1.35 \pm 0.02)\,\sigma_m \tag{2.15}$$

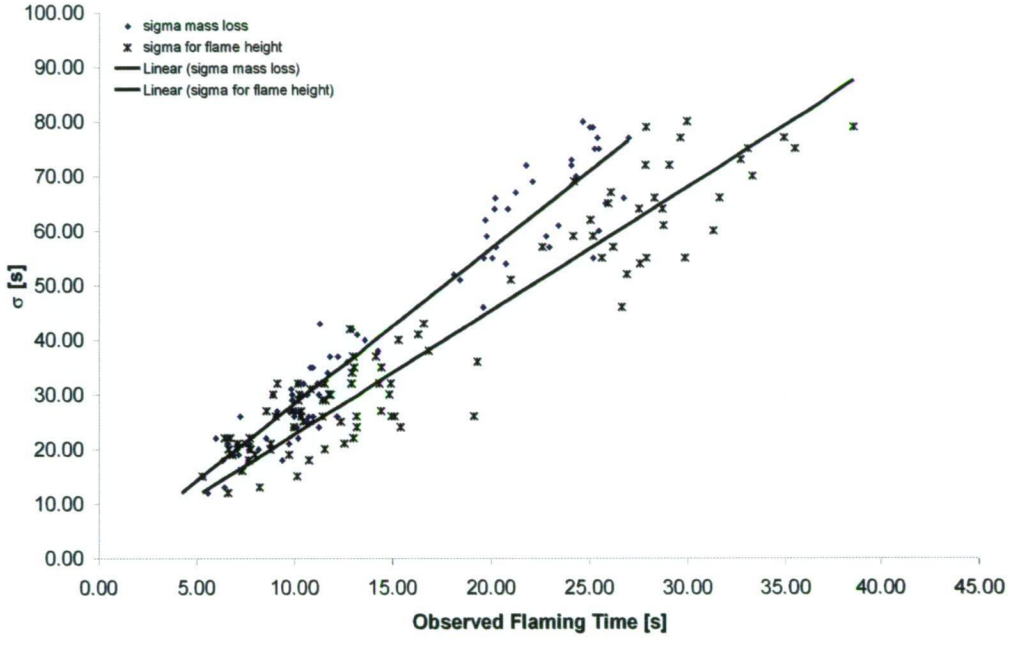

Figure 2.15: Flaming time versus σ_m and σ_f. The linear relationship obtained for σ_m was $t_r = 2.84\sigma_m$, with $R^2 = 0.934$, and $t_r = 2.27\sigma_f$ with $R^2 = 0.887$ for the σ_f.

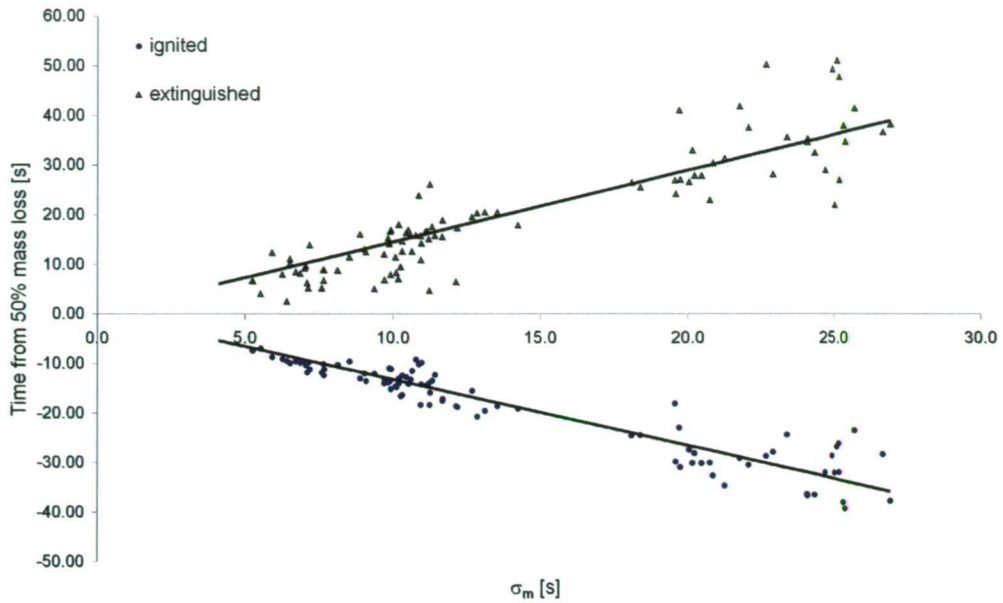

Figure 2.16: Visually estimated begining and the end of flaming of the element were plotted relative to σ_m.

and ceased to flame at

$$t_{end} = (1.43 \pm 0.04)\,\sigma_m. \tag{2.16}$$

with R^2 of 0.92 and 0.82 respectively. These relationships are plotted in Figure 2.16.

In the previous sections the difference in the peak between the rate of mass loss and the flame height was discussed. Observed ignition and extinction of the element were compared to the time scale where $t^{\Diamond} = 0$ when the peak flame height is reached $\left(t^{\Diamond} = t - t^{*}\right)$. Then

$$\begin{aligned} t_0^{\Diamond} &= (-0.565 \pm 0.003)\,\sigma_f \\ t_{end}^{\Diamond} &= (1.38 \pm 0.003)\,\sigma_f. \end{aligned} \tag{2.17}$$

This indicates that the flame reaches its peak relatively fast, after which it slowly decays. However, the ignition time of the element is not incorporated here and from equation (2.10) the flame height is $H = 0.85 H_{\max}$ at ignition.

The average of the residence times observed for each diameter is plotted in Figure 2.17, and the following relationship was obtained:

$$t_r = 9.87 \times 10^4 D^{1.55} \tag{2.18}$$

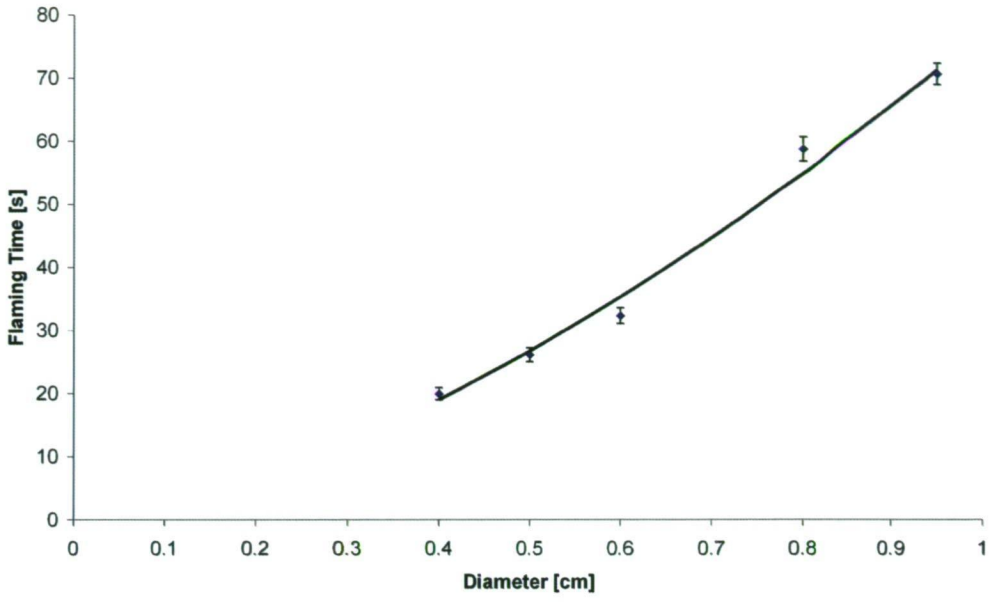

Figure 2.17: Flaming time observed versus diameter of the element. Error bars represent standard error.

with $R^2 = 0.987$, in SI units. This relationship is in agreement with the results reported by Muraszew (1974), Steward & Tennankore (1981) and Thomas (1974). It is however considerably lower than the values obtained by Anderson (1969), who obtained a linear relation of $t_r = 189D$ in cgs units.

Many authors such as Thomas (1974) have pointed out the fact that the power law relation of approximately $\frac{3}{2}$of the residence time and the diameter or the thickness of the element, stems from the thermal diffusion considerations. Considering an element immersed in flame, with a fixed surface temperature constraint, the propagation of pyrolysis would be described by the diffusion square law; however, allowing for the more realistic conditions of surface cooling, the adjustment to the $\frac{3}{2}$ power law in equation (2.18) appears to be a reasonable approximation.

2.4.5 Flame Length

The definition of the flame length that is sometimes found in the literature is to the flame height. This is particularly case for leaning flames, where the

length is defined as the distance from the flame base to the tip. In this case, however, the flame length is related to the distance along the element ignited, whilst flame width is measured across the element's diameter (Figure 2.2).

Care was taken to ensure that the entire element length was ignited simultaneously. This was hard to achieve in practice and the ignition source was removed when a flame envelope developed along most of the element's length. The decision on when this is the case is rather subjective, and the errors caused by the initial ignition length are further discussed in this section.

After the removal of the ignition source, a laminar flame envelope develops along the entire element length. As the temperature of the element increases, the wood begins to char, cracks develop and widen, and this permits volatiles to escape to the surface, creating jets of flame. The initial laminar shape of the flame envelope thus converts into sets of jets, gradually reducing the effective flame length.

The change in flame length during the combustion was compared to two functions: Gaussian shape and trapezoidal form. The Gaussian shape was modelled similarly to the flame height and mass loss rate, and took the form

$$l = L_{\max} e^{-\frac{1}{2}\left(\frac{t-t_l^*}{\sigma_l}\right)^2},$$

where $L_{\max}$ is the peak value of the function, σ_L the spread of the function and t_l^* the time difference in reaching the maximum relative the peak rate of mass loss (with time scale such that $t = 0$ at the peak mass loss rate).

The following trapezoidal function was also used to model the flame length:

$$l = \begin{cases} M_1 t - (M_1 t_1 - l_{av}) & t_{ig} < t < t_1 \\ l_{av} & t_1 < t < t_2 \\ M_2 t - (M_2 t_2 - l_{av}) & t_2 < t < t_{end} \end{cases}.$$

Here, three sections of burning are indicated. The initial stage, $t < t_1$ where t_1 marks the time when 80% of the element's length has been ignited, was modelled as linear increase in the flame length. The middle section of the function represents the time while the length of the flame is greater than 80% of the element length and is described as the average length measured during that time. After time t_2 the flame has broken into jets, and the total length detected has reduced below 80% of the element length.

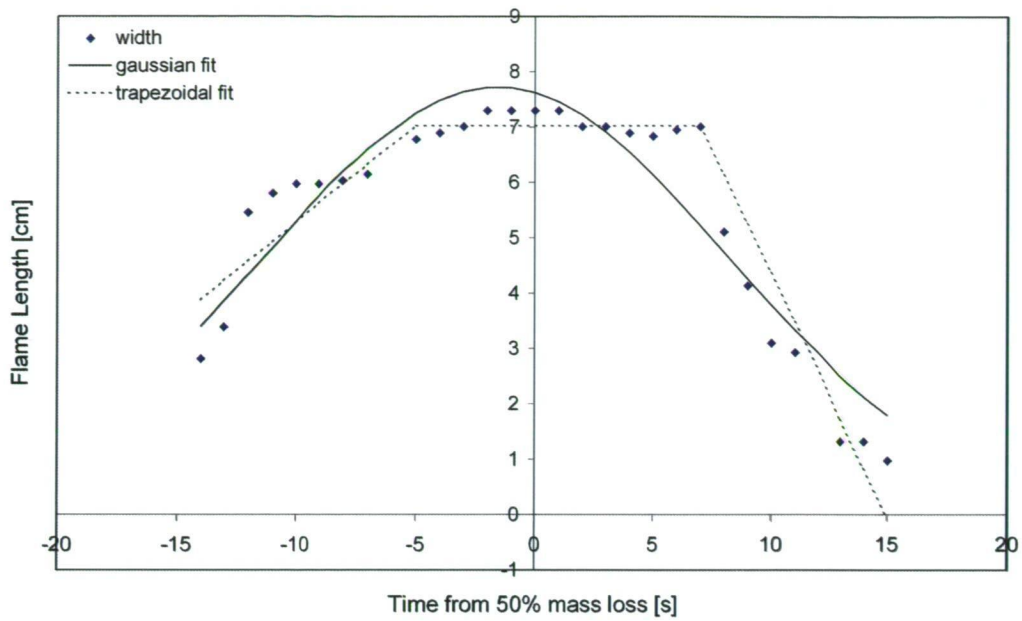

Figure 2.18: Flame length fit and measurements for a 5 mm diameter oak. Note that the sharp drop in the length at t=10s is due to a side jet.

A Gaussian function commonly provided a reasonable fit for the middle and final stages of the combustion, if a large percentage of the length is initially ignited. However, if the initial percentage of the length above which flame developed was low then the full length was reached relatively fast since the entire length of the element was preheated and a transparent flame around the circumference of the element had developed prior to removing the ignition source. The Gaussian model then attempts to fit the initial and final stages of the burning, misrepresenting the non-symmetrical rates in the increase and the decrease of the flame lengths (Figure 2.18). The advantages to using the Gaussian fit are in the reduced number of parameters.

Gaussian parameters obtained were modelled in the following fashion. The peak length was compared to the length of element to obtain

$$L_{\max} = 0.934 \times l,$$

with R^2 of 0.523. Results are shown in Figure 2.19.

The spread of the Gaussian for the length was compared to the spread of the

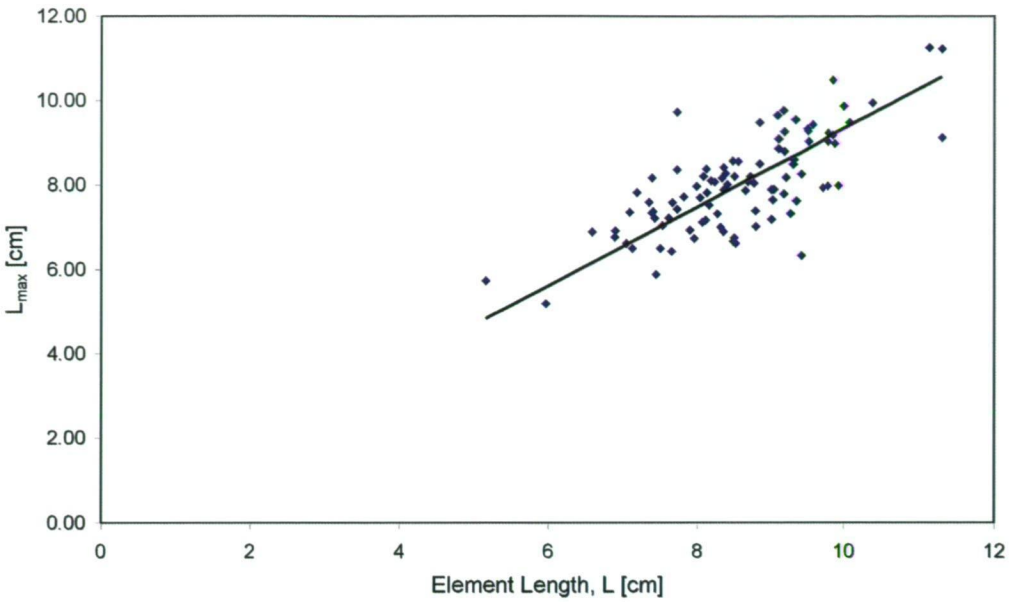

Figure 2.19: $L_{\max}$ versus element length

Gaussian fit to the mass loss rate, σ_m. This gave the linear relationship

$$\sigma_L = 1.054 \times \sigma_m,$$

with R^2 of 0.8767. Average values for the spread of the Gaussian function weighted using standard deviations in the averages for flame length parametrized with respect to the element diameter yield

$$\sigma_L = 0.0372 D^{1.44},$$

with R^2 of 0.982. Data from these two models are presented in Figures 2.20 and 2.21 respectively.

The time t^* when the peak flame length is reached is parameterized against diameter as

$$t_2^* = 0.0294 D^{1.17},$$

with R^2 of 0.913. Experimental values and this fitted curve are given in Figure 2.22. This occurs prior to the peak rate mass loss, but after the peak in the average flame height. This variable is one of the faults in using the Gaussian

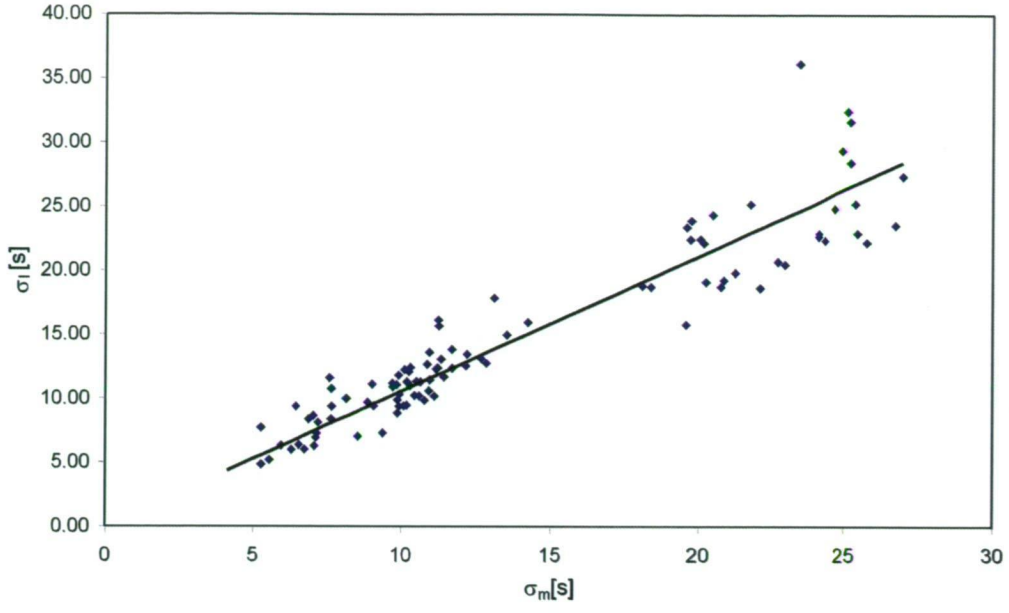

Figure 2.20: Comparison of σ_l to σ_m

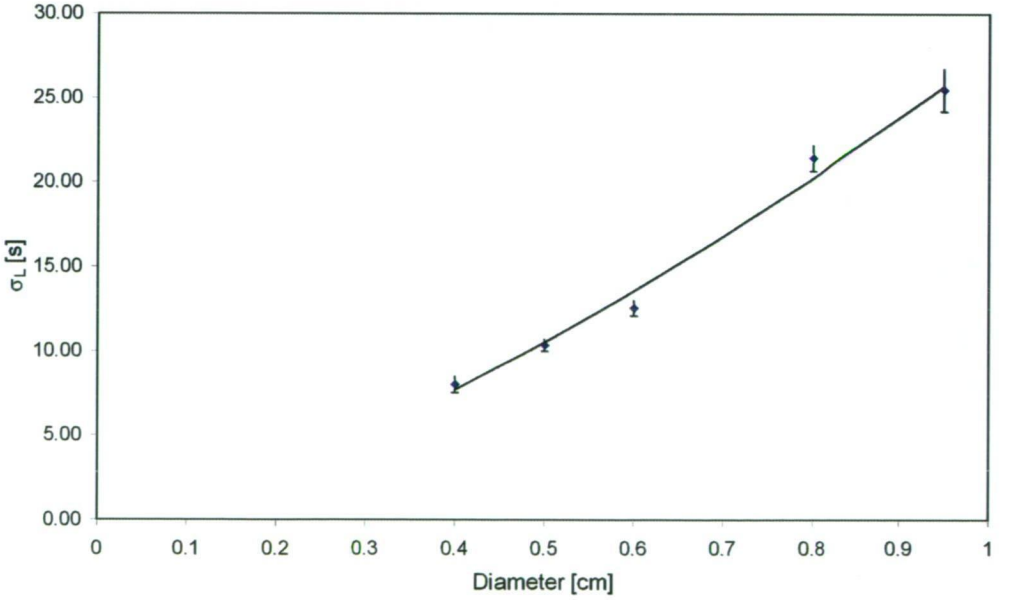

Figure 2.21: σ_L versus diameter

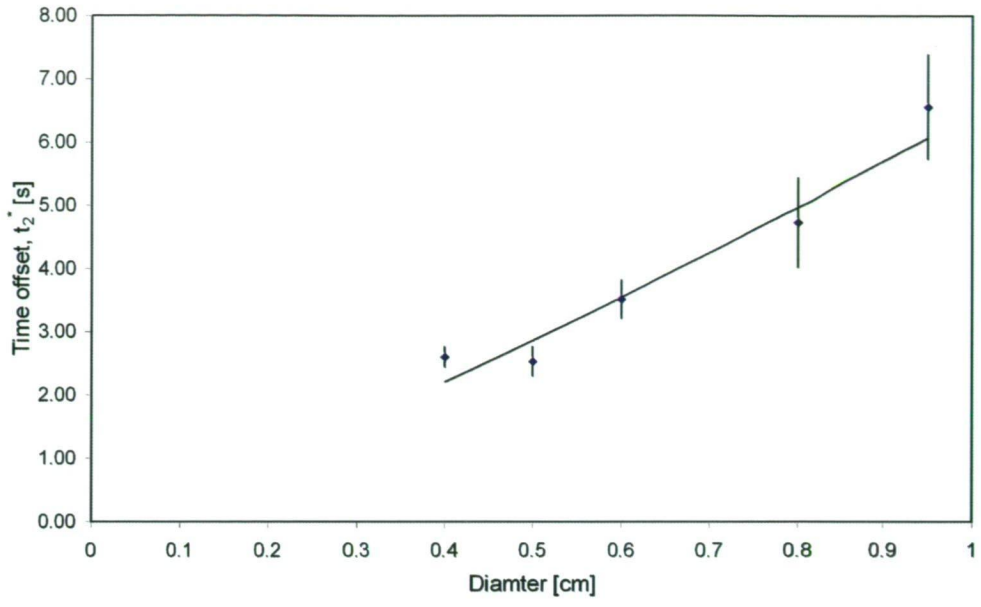

Figure 2.22: Time offset versus diameter for length Gaussian fit

function to represent the flame length. When the full element is burning, it continues to burn at full length until the flame breaks into jets forming an 'alligatoring' shape. Hence there is no physical peak, but a flat top to the function. This is why an attempt to fit a trapezoidal shape function was employed.

The data modelled for 80% cut-off is shown in the Figures 2.23, 2.24 and 2.25. In figure 2.25, the top diagram was plotted against the ignition time and the end of flaming time. The left hand side shows the relationship between t_1 and t_{ig} and the right-hand side gives the relationship between t_2 and t_{end}. The bottom diagram shows the relationship between t_1 and t_2 and $\sigma_{m,}$ the spread of the Gaussian function for the rate of mass loss.

The following results were obtained for the parameters of the trapezoidal model:

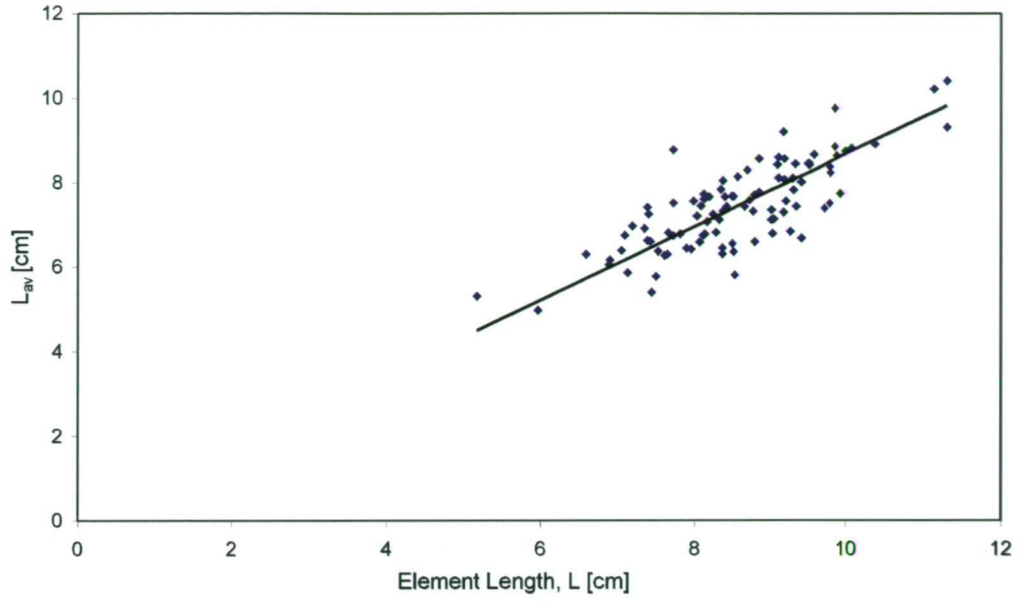

Figure 2.23: L_{av} from trapezoidal fit versus element length

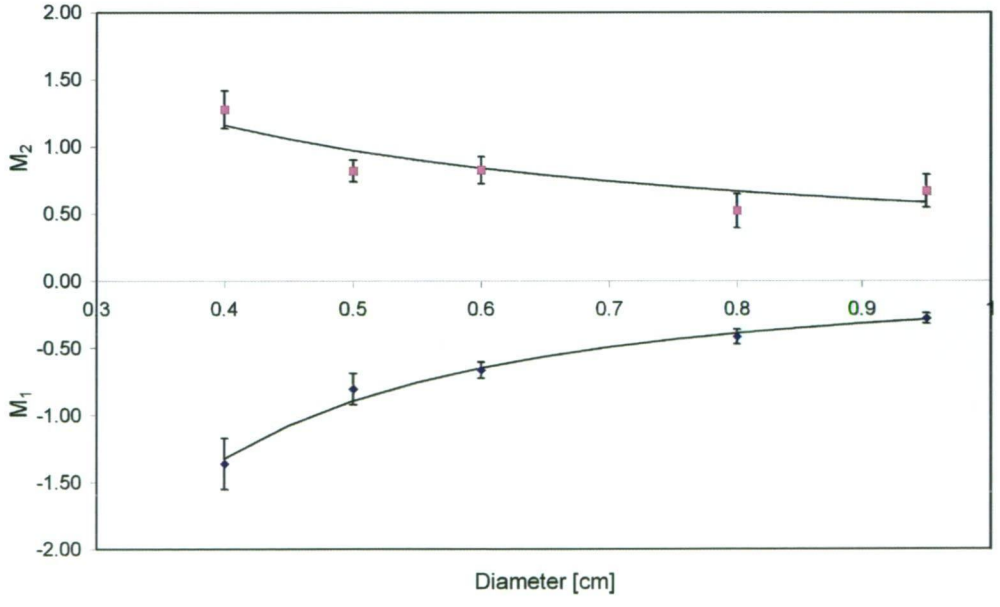

Figure 2.24: Coefficients m_1 and m_2 for the trapezoidal fit averaged against diameter. Error bars indicate standard errors.

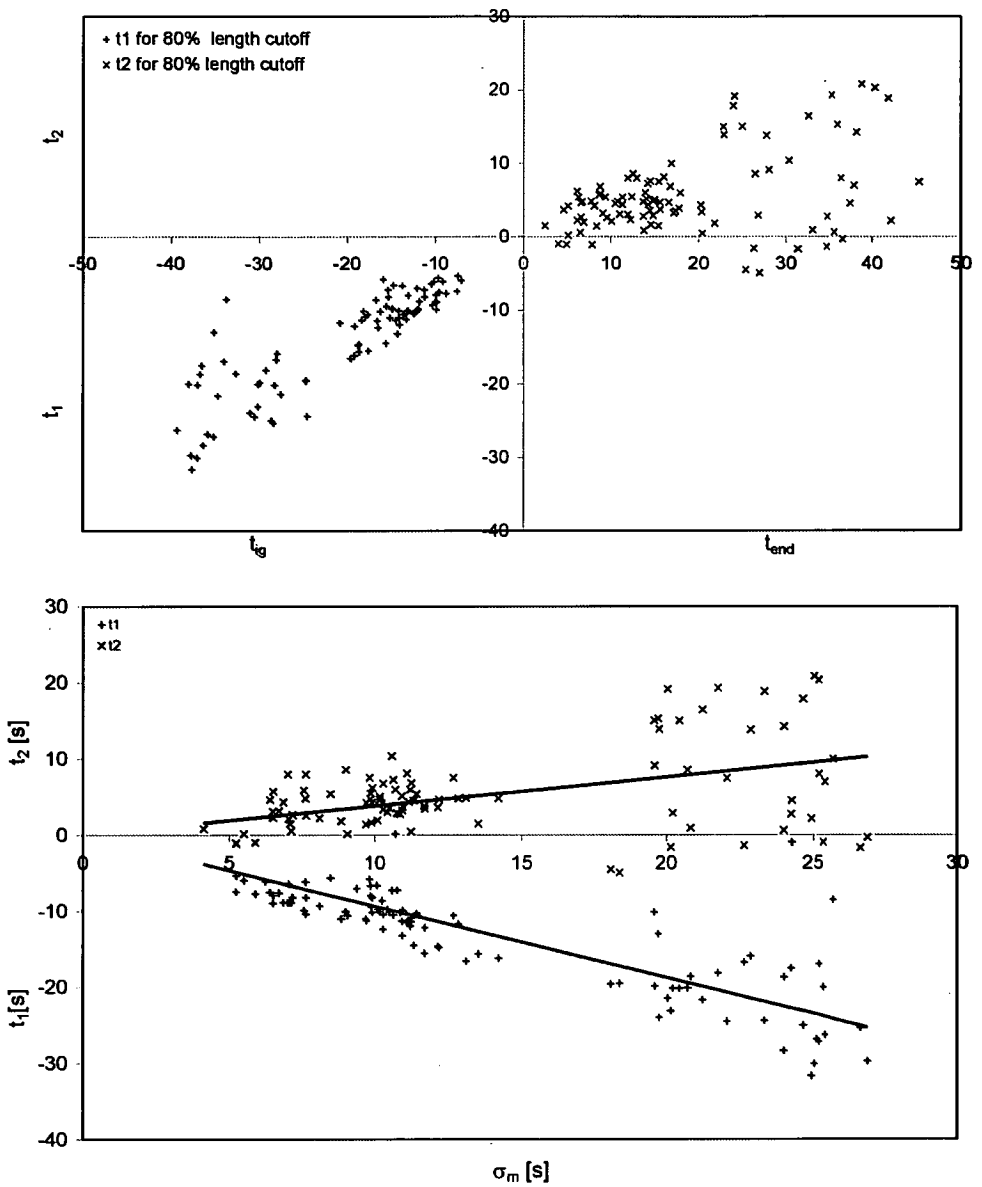

Figure 2.25: Time breaks t_1 and t_2 during combustion for trapezoidal fit.

$$L_{av} = L_{element} \times 0.869, \quad R^2 = 0.618 \tag{2.19}$$

$$M_1 = 21.9D^{-0.796}, \quad R^2 = 0.706 \tag{2.20}$$

$$M_2 = -874D^{-1.76}, \quad R^2 = 0.988 \tag{2.21}$$

$$t_1 = -0.937 \times \sigma_m, \quad R^2 = 0.64 \tag{2.22}$$

$$t_2 = 0.38 \times \sigma_m, \quad R^2 = 0.15 \tag{2.23}$$

For using the trapezoidal function, two cut-off lengths were tried: 80% and 90%. Using 90% of the maximum width provided a better fit for each individual burn than using 80%; however, the parameters obtained were more sporadic than the parameters obtained for 80% cut-off. This was in particular case for t_1 and t_2. The trapezoidal fit with 80% cutoff provides better parametrization of the flame length than the Gaussian fit. The average root-mean-squared for the trapezoidal fit is 0.53 of the average root-mean-squared of the Gaussian fit. However, estimating cut-off time t_2 is the weakest part of fitting the model. The sporadic nature of t_2 can be attributed to the jets flaming along the grain out of the end of the element.

2.4.6 Parametrization of the Nogal Combustion

In order to estimate the flame properties for elements with diameter less than 4 mm, a set of experiments was conducted using nogal, a chocolate brown heartwood of South American walnut from *Juglandaceae* family. The following diameters were used: 2, 3, 4, 5, 6, 8 and 10 mm. The results are compared to those obtained for Tasmanian oak.

The mass loss rate for nogal was modelled using the Gaussian function $\dot{m}' = \frac{M'_T}{\sqrt{2\pi}\sigma_m} e^{-\frac{t^2}{2\sigma_m^2}}$ similarly to the Tasmanian oak described in the previous section. The time scale was adjusted to $t_{50\%}$ scale, where $t = 0$ when 50% of the mass has been depleted. The quantity M'_T is the total mass consumed per unit length and the difference in this value to those derived for Tasmanian oak are due to the differences in the efficiency of combustion and density of the samples. The average efficiency of combustion is 12% higher for Tasmanian oak (Figure 2.26).

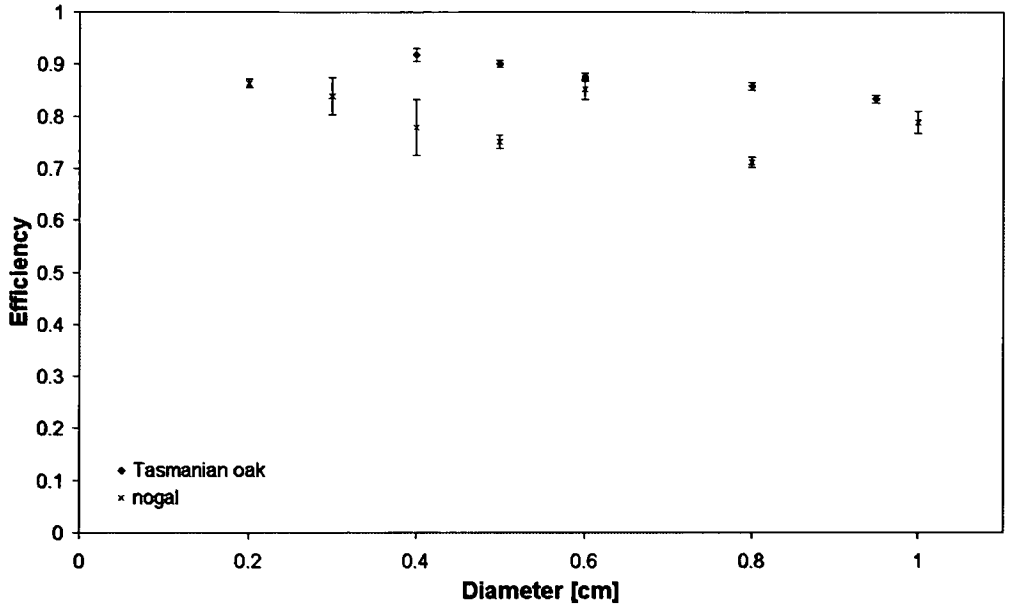

Figure 2.26: Efficiency versus diameter for Tasmanian oak and nogal.

Flame heights for nogal were modelled, similarly to Tasmanian oak described in the previous section, using the Gaussian function $H = H_{max}e^{-\frac{1}{2}\left(\frac{t-t^*}{\sigma_t}\right)^2}$.

A comparison of maximum flame height for nogal and Tasmanian oak is presented in Figure 2.27. It can be seen that the maximum flame heights fitted to a Gaussian function are comparable for the two species. Applying a general linear model to a logarithm transformation of the equation

$$H_{\max} = \alpha D^{\beta},$$

shows that there is no evidence that the α and β coefficients differ between the two wood types ($p = 0.196$ for α and $p = 0.177$ for β). Consequently the maximum flame height can be described by

$$H_{\max} = 0.0867 D^{0.199} \tag{2.24}$$

for both species. The decrease in the peak flame height for smaller diameters in nogal indicate that using a power law fit for modelling peak flame height for Tasmanian oak in equation (2.11) is justified.

The spread of the Gaussian function for flame height is of the same order for nogal and Tasmanian oak (Figure 2.28); however, a general linear model of the

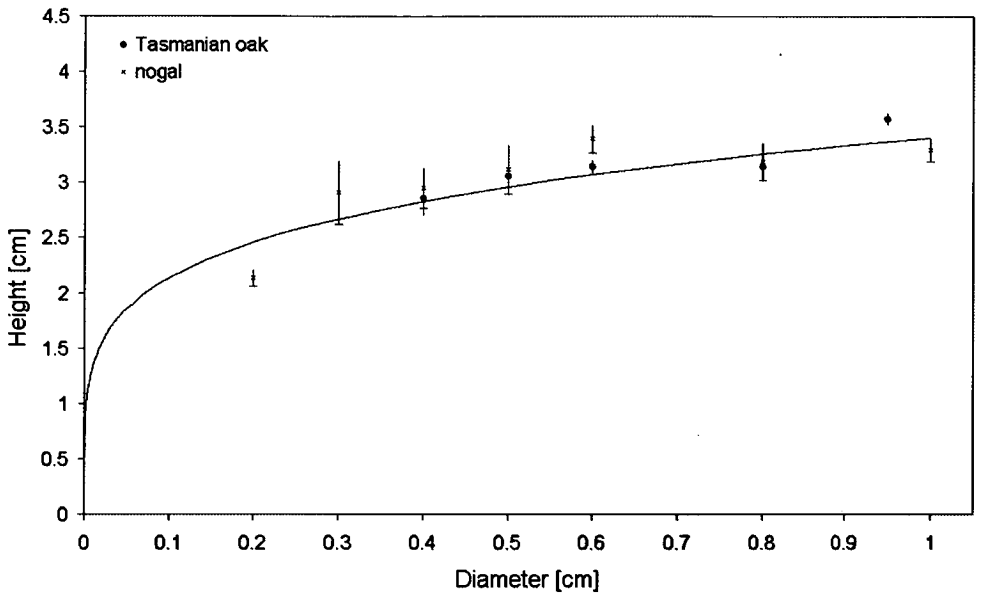

Figure 2.27: Maximum flame height for Tasmanian oak and nogal versus diameter

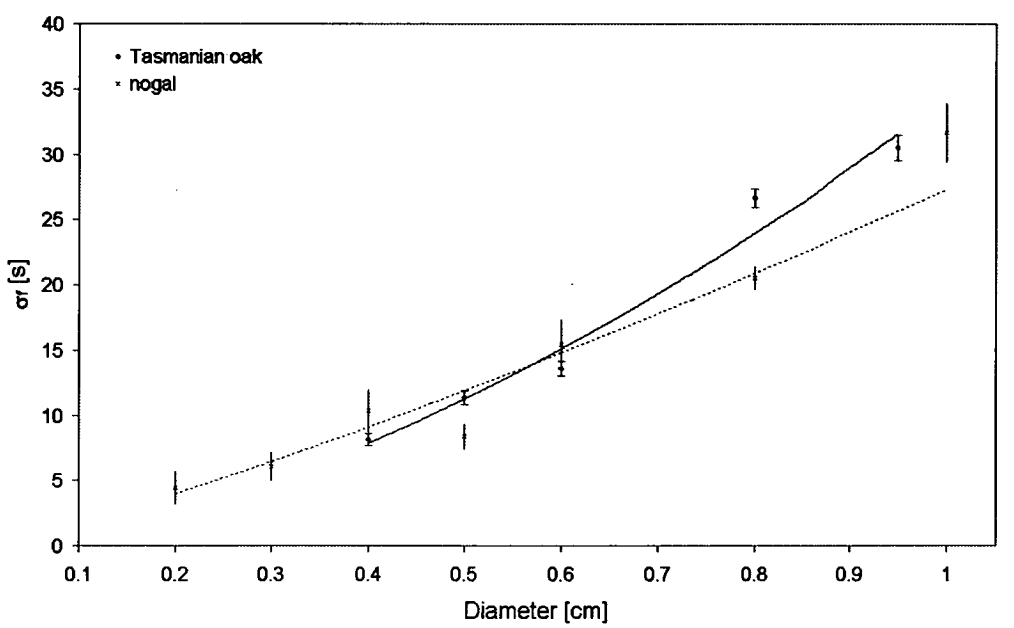

Figure 2.28: Spread of the Gaussian fit for flame height for Tasmaian oak and nogal

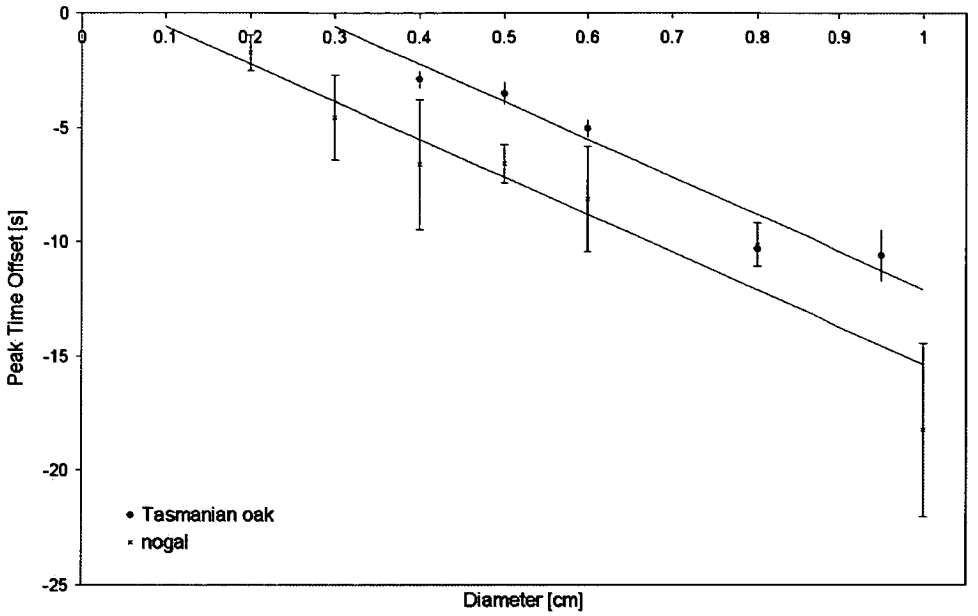

Figure 2.29: Time offset between peak rate of mass loss and flame height for Tasmanian oak and nogal. Error bars represent standard error.

logarithmically transformed equation

$$\sigma_f = \alpha D^{\beta}$$

showed that there is no evidence of the coefficients α or β being the same for the two wood types ($p = 0.003$ for α and $p = 0.002$ for β). The spread of the Gaussian for flame height is hence described as

$$\sigma_{f\,oak} = 7.31 \times 10^4 D^{1.67} \quad (2.25)$$

$$\sigma_{f\,nogal} = 0.91 \times 10^4 D^{1.26}. \quad (2.26)$$

The main difference between the two species was detected in the time offset between the peak rate of mass loss and the peak flame height. Considering a general linear model of the data for the time off-set, it is seen that there is strong evidence for the same slope and different offset between the wood types ($p = 0.000$), and no evidence of different slopes ($p = 0.669$). The peak off-set could thus be described using

$$t^*_{oak} = 1.06 - 1650D \quad (2.27)$$

$$t^*_{nogal} = 4.35 - 1650D, \quad (2.28)$$

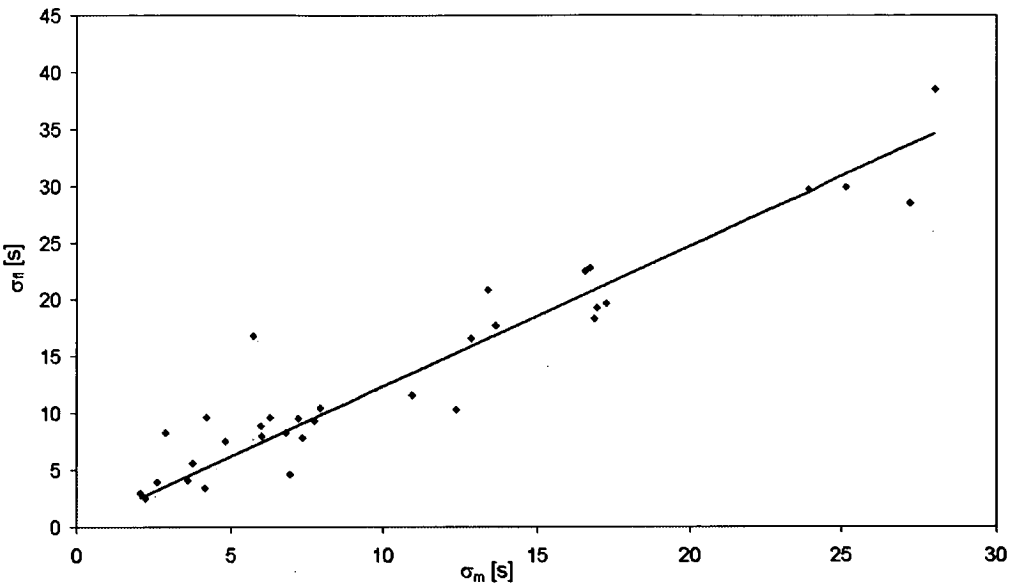

Figure 2.30: Relation between spread of the Gausian function for flame height and mass loss rate for nogal

from where it is seen that nogal reaches peak flame height sooner than oak for the same diameter, on the $t_{50\%}$ time scale.

The relationship between σ_m and σ_f for nogal is

$$\sigma_f = 1.23\sigma_m \tag{2.29}$$

with R^2 of 0.894, which is identical to the relationship obtained for Tasmanian oak in equation (2.14). This is shown in Figure 2.30.

Figure 2.31 shows the residence time for nogal and Tasmanian oak. General linear model of the logarithmically transformed equation

$$t = \alpha D^{\beta},$$

shows that there is no evidence that α and β are different for the two wood types ($p = 0.551$ for α and $p = 0.443$ for β). Thus there is no significant difference in the flaming time for the nogal and Tasmanian oak, and it can be described with the equation

$$t_r = 1.33 \times 10^5 D^{1.61}, \tag{2.30}$$

with R^2 of 91.8%.

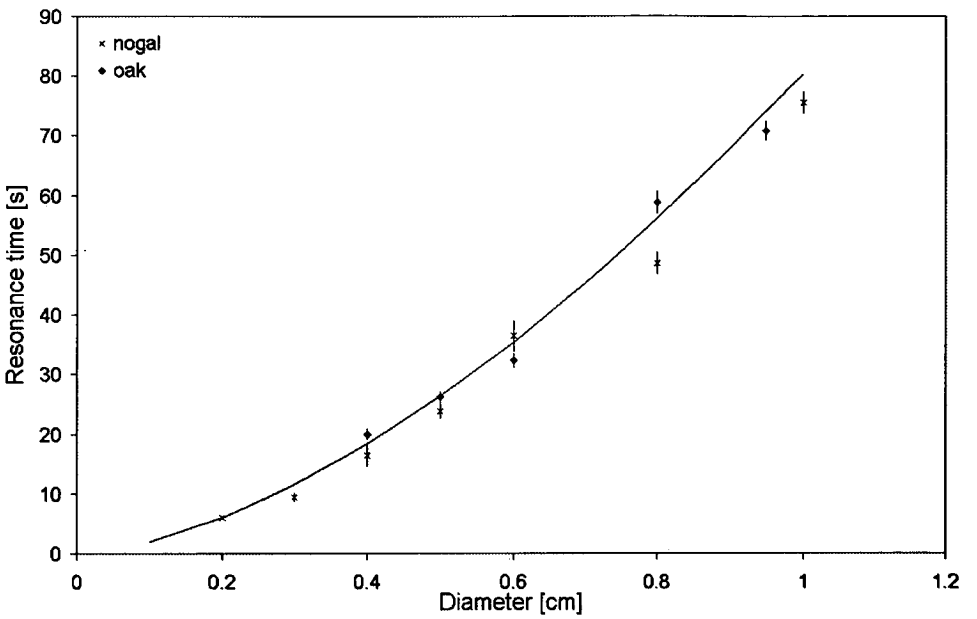

Figure 2.31: Residence time versus diameter for nogal and Tasmanian oak

2.4.7 Comparison with Flame Height Versus Mass Loss Rate Models in the Literature

It has been noted in the literature review (section 2.2) that most of the flame height models encountered in the literature compare flame height to the rate of mass loss, either through a Froude number, relative heat release rate or a similar dimensionless group. Most of these relationships were experimentally tested on a steady state of burning by using large fuel loads or with the continuous steady flame of gas burners. Considering the configuration used in these set of experiments, a steady state of burning was never reached. In order to compare the flame height to the mass loss rate over the flaming time using the Gaussian fits obtained above, consider the following. From the Gaussian fit to the flame height, equation (2.10), we have

$$H = H_{\max} e^{-\frac{1}{2}\left(\frac{t-t*}{\sigma_f}\right)^2} = H_{\max} e^{-\frac{1}{2}\left(\frac{t}{\sigma_f}\right)^2} \times F(D,t), \qquad (2.31)$$

where $F(D,t)$ is the factor $e^{-\frac{1}{2}t^*\left(\frac{t^*-2t}{\sigma_f^2}\right)}$.

Using equations (2.12) and (2.13) for spread of the Gaussian fit σ_f and the

time delay t^*, the exponent of the factor $F(D,t)$ becomes

$$\begin{aligned} -\frac{1}{2}t^*\left(\frac{t^*-2t}{\sigma_f^2}\right) &= -\frac{1}{2}\left(\frac{\left(-6.61\times10^4 D^{1.83}\right)^2}{\left(7.31\times10^4\right)^2 D^{3.34}} - 2t\frac{-6.61\times10^4 D^{1.83}}{\left(7.31\times10^4\right)^2 D^{3.34}}\right) \\ &= -0.818D^{0.32} - 1.824\times10^{-5}tD^{-1.51}, \end{aligned}$$

therefore

$$F(D,t) = e^{\left(-0.818D^{0.32}-1.824\times10^{-5}tD^{-1.51}\right)} \tag{2.32}$$

To estimate the variation in factor F during the burn, consider F at the start and the end of the ignition. Element is ignited at $t = t_0$, which from equations (2.15) and (2.6) is

$$t_0 = -4.41\times10^4\times D^{1.54}. \tag{2.33}$$

Then

$$F(D,t_0) = e^{-0.818D^{0.32}+0.804\times D^{0.03}} = \begin{cases} 1.67 & \text{for } D = 9.5\times10^{-3}\ m \\ 1.72 & \text{for } D = 4\times10^{-3} m \end{cases}. \tag{2.34}$$

At the peak mass loss rate $t = 0s$,

$$F(D,0) = e^{-0.818D^{0.32}} = \begin{cases} 0.83 & \text{for } D = 9.5\times10^{-3}\ m \\ 0.87 & \text{for } D = 4\times10^{-3}\ m \end{cases}. \tag{2.35}$$

At the end of flaming, $t = t_{end}$, it follows from equations (2.16) and (2.12) that

$$t_{end} = 4.68\times10^4\times D^{1.54}, \tag{2.36}$$

thus

$$F(D,t_{end}) = e^{-0.818D^{0.32}-0.854D^{0.03}} = \begin{cases} 0.40 & \text{for } D = 9.5\times10^{-3}\ m \\ 0.42 & \text{for } D = 4\times10^{-3}\ m \end{cases}. \tag{2.37}$$

We can see from 2.34, 2.37 and 2.35 that variations in factor F over the range of diameters used are less than 5% for any given time, however there is significant decrease in value of F during the burn.

Now using relations 2.31 and 2.14, the flame height H becomes

$$H = H_{\max}F(D,t)\left[e^{-\frac{1}{2}\left(\frac{t}{\sigma m}\right)^2}\right]^{\frac{1}{1.23^2}}. \tag{2.38}$$

Rearranging equation (2.4) and substituting it in the above gives

$$H = F(D,t)\frac{H_{\max}}{(\dot{m}'_{\max})^{0.66}}\dot{m}'^{0.66}. \tag{2.39}$$

From equations (2.11) and (2.9),

$$\begin{aligned} H &= F(D,t)\frac{0.0848D^{0.192}}{(2.68\times10^{-3}e^{-2.77D}D^{0.334})^{0.66}}\dot{m}'^{0.66} \\ &= 4.225\frac{e^{1.83D}}{D^{0.0284}}F(D,t)\,\dot{m}'^{0.66}, \end{aligned} \tag{2.40}$$

where $F(D,t) = e^{-0.93\sqrt{D}+1.87\times10^{-5}tD^{-1.42}}$. Using equations (2.34), (2.37) and (2.35), the flame height equation becomes

$$H = \begin{cases} 8.20\dot{m}'^{0.66} & \text{for } 9.5\times10^{-3}\ m \\ 8.56\dot{m}'^{0.66} & \text{for } 4\times10^{-3}\ m \end{cases} \text{at } t = t_0$$
$$H = \begin{cases} 4.07\dot{m}'^{0.66} & \text{for } 9.5\times10^{-3}\ m \\ 4.33\dot{m}'^{0.66} & \text{for } 4\times10^{-3}\ m \end{cases} \text{at } t = 0 \tag{2.41}$$
$$H = \begin{cases} 1.96\dot{m}'^{0.66} & \text{for } 9.5\times10^{-3}\ m \\ 2.09\dot{m}'^{0.66} & \text{for } 4\times10^{-3}\ m \end{cases} \text{at } t = t_{end}$$

in SI units. Data observed for flame height is plotted in Figure 2.32. The exponent in this relation is in agreement with Muraszew (1974) who compared flame height to the rate of mass loss per unit length for horizontal cylinders to obtain an exponent 0.663 for the peak flame height. The exponent of 0.66 was obtained from the relation between σ_m and σ_f for oak (equation (2.14)). The same relation was obtained for nogal (equation (2.29)) indicating the same power law applies; however, different coefficients are obtained due to the differences in the efficiency of combustion, time offset and wood density.

To compare the results obtained here to the models where flame height was related to dimensional numbers such as the Froude number (Thomas et al. 1965) or the relative heat release rate (Zukoski 1986), we need to relate flame height over a characteristic diameter to the rate of mass loss. In most of the cases cited in the literature review (section 2.2) the fuel was either square or circular; hence the characteristic dimension was either the diameter or the side length of the fuel bed. In this case the fuel base is rectangular with $l >> D$, so if we consider equation (2.39) relative to mass loss $\dot{m}$, rather than rate of mass loss per unit length, $\dot{m}'$, the equation (2.40) becomes

$$H = F(D,t)\frac{98e^{0.0185D}}{D^{0.061}\rho^{0.11}l^{0.66}}\dot{m}^{0.66}, \tag{2.42}$$

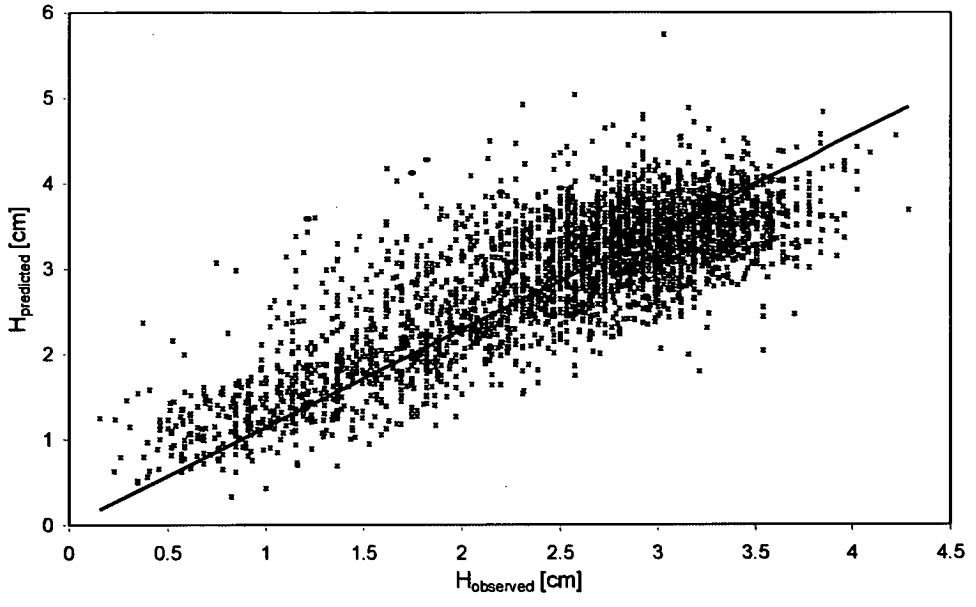

Figure 2.32: Flame height observed versus flame height predicted from the mass loss rate model

indicating much stronger dependence on the length than the diameter. Then

$$\frac{H}{l} \cong \frac{98e^{0.0185D}}{D^{0.061}\rho^{0.11}} \left(\frac{\dot{m}^2}{l^5}\right)^{0.33}, \tag{2.43}$$

which is in agreement with Thomas's (1963) results. However, to compare with the results of (Zukoski 1986), we need to compare the exponent to the values proposed for the appropriate dimensionless heat release rate $\dot{Q}^*$. (Zukoski 1986) postulates that the power relation varies with the dimensionless heat release rate value, $\dot{Q}^* = \frac{\eta H_c \dot{m}}{C_p \rho_0 T_0 \sqrt{g D^* D^{*2}}}$, where D^* is the characteristic diameter. Using $D^* = \sqrt{Dl}$, a range of values $3 < \dot{Q}^* < 17$ is obtained, indicating that the exponent of 0.66 is comparable with Zukoski's (1986) results.

2.4.8 Width of the Flame Envelope

A set of experiments was conducted observing an element along its axis (Figure 2.33) in order to measure the width of the flame envelope relative to the diameter of the element. The initial phase of the combustion produced a laminar flame around the element. In the second stage of the combustion, particularly

for diameters of 8 and 9.5 mm, the elements begin to break and irregular jets of flame burst out sideways, thus increasing the measured width of the flame envelope. This however represents the local width at the jet origin, not the average width along the element. Parametrizing this phenomenon is beyond the scope of this study; hence, widths recorded during the laminar stage were used for flame envelope measurement.

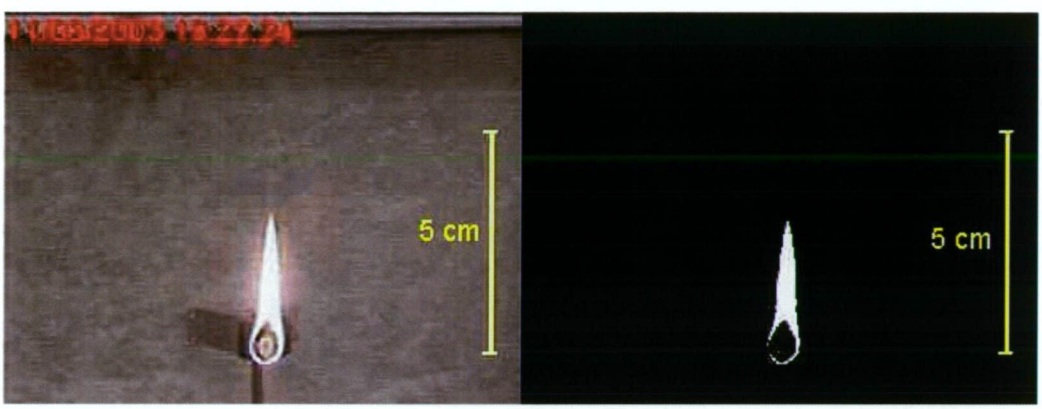

Figure 2.33: Measurement of the width of the flame envelope.

The average width measured was correlated against the diameter of the element to obtain

$$W = 0.932D + 4.015 \tag{2.44}$$

with R^2 of 0.972, where W and D are the total flame width and element diameter in millimetres. Muraszew (1974) reported the flame width to be approximately $1.2D$ which underestimates the values observed in this study (Figure 2.34).

2.5 CONCLUSION

In this chapter, flaming combustion of horizontal oak and nogal wood dowels of diameters ranging form 2 to 9.5cm was investigated. Flame dimensions and mass loss rate were plotted in time, and were found to follow Gaussian

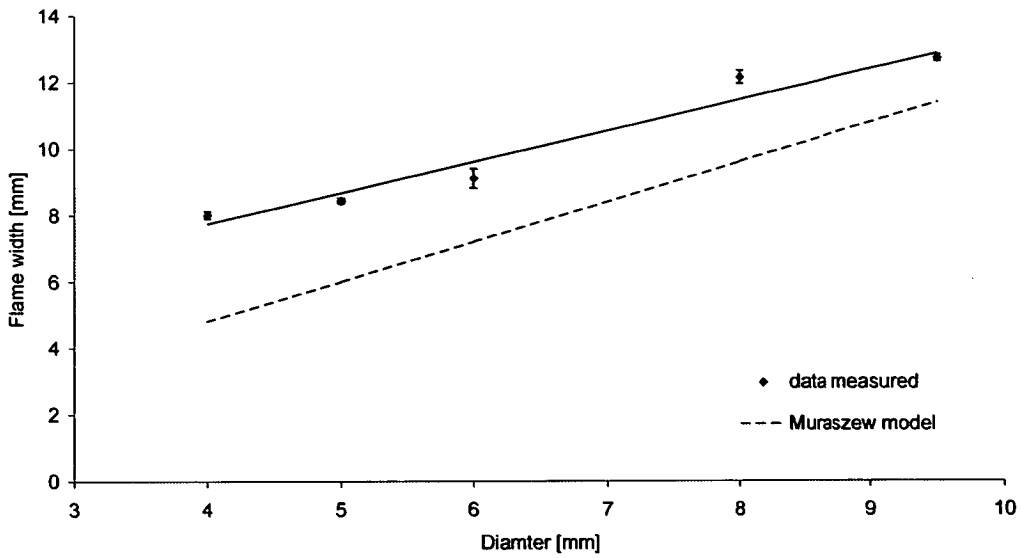

Figure 2.34: The width of the flame envelope versus diameter. The error bars represent the standard deviation

function, with peak flaming and mass loss occurring at the half point of the residence time. To total flaming time was correlated to the element diameter, and flame height to the mass loss rate of the element, with results in agreement to those published in literature.

Chapter 3

Flame Progression Along An Element

3.1 INTRODUCTION

In the sets of experiments described in this chapter, some of the factors which affect the shape of a flame as it progresses along an element are studied. Many factors play a role in the flame geometry. Flame height depends on the rate of volatile release from the fuel and buoyancy of the flame gases. Fuel moisture content, fuel orientation and thickness affect the rate of the flame spread. The diameter of the element also influences its burning time. Thus the width of the flame spreading over an element will depend on all these factors. When two elements burning separately are brought closer, the resulting flame is larger than the two independent flames, but smaller than if the two elements have no separation between them. Cutting wood along the grain or perpendicular to it, affects the thermal conductance of the wood, as well as the transportation of the volatiles below the ignition surface. In this set of experiments however, only wood cut along the grain is considered. There are also many intrinsic properties of different woods that are essential to the accurate parametrization of the flame properties. That is a complex parameterization, and most of the experiments were conducted on one type of wood, Tasmanian oak (from the Tasmanian *Eucalyptus* family). However, four different woods of the same geometry, orientation and moisture were used in order emphasize the effect that

intrinsic wood properties have on the fire spread. In these experiments, the flame geometry was studied by varying: fuel moisture content, fuel orientation, diameter, wood type and separation between two elements while measuring the flame height, width, rate of flame spread and mass loss of the elements. The effect of these factors on the rate of spread and residence time is investigated and consequently, their effect on the flame width, height and the rate of the mass loss.

3.2 LITERATURE REVIEW

The thickness of an element greatly effects the rate of flame spread. If an element can be treated as 'thermally thin' (has no temperature gradient across the thickness) then through lumped thermal capacity model, it can be shown that the rate of flame spread is inversely proportional to the thickness of the element. This was demonstrated by Magee & McAlevy (1971) for downward spread on vertical cellulosic fuels, which thickness was less then 1.5mm. Suzuki et al. (1994) showed that for fuel samples prepared from filter paper, as the thickness of fuel increases the rate of spread becomes less dependent as the fuel thickness increases, becoming constant in the 5-7mm range, and that the rate became erratic for samples thicker than 8.4mm. As thickness of fuel increases, there is a change in the dominant mode of heat transfer from gas phase for thin fuels to heat conduction through the sold for thick fuels (Drysdale 2002). Similar results are shown for the downward spread on PMMA sheets (Fernandez-Pello & Williams (1974), Pizzo et al. (2008)).

Flame progressing across this elements was studied by Weber (1990), Weber & De Mestre (1990) and Lyons & Weber (1993), who investigated the effects of fuel moisture content and angle on the rate of flame spread in pine needles. Lyons & Weber (1993, 1991) also studied the effect of the orientation on eucalyptus leaves, sheet fuels and boxboard strips, and the dependence of rate of flame spread on the dimensions of the strips of fuel and Ito et al. (2005) on thick PMMA slabs for orientations 0 to -180 degrees (ceiling fire spread). Upward flame spread and flame height correlations were developed by Tsai & Drysdale (2002) for wall fires, Delichatsios (2000) for vertical cylinders. Magee & McAlevy (1971) studied spread rates for upward spread on strips of filter

where as Hirano et al. (1974) found that for thin fuel the downward rate of spread was nearly constant for angles $-90°$ to $-30°$, then increasing nearly three times for the horizontal fuel, and up to fifty fold increase from vertically downwards to vertically upwards spread where as Sibulkin & Lee (1974) found that for PMMA rods of up to 1.25cm diameter the rate of spread increased by factors 5 to 8, as the angle increased from -90 to $+40$ degrees.

Effects of the separation between elements on a combined flame have been studied by Thomas et al. (1965), Putnam & Speich (1963), Kurosaki et al. (1971) and Lyons & Weber (1993, 1991). Putnam & Speich (1963) compared flame height over multiple jets close together to the height of a single jet. Thomas et al. (1965) studied critical merging of two flames, that is the maximum separation and the resultant flame height of the combined flame above two separate fuel beds. Kurosaki et al. (1971) investigated effects of separation between two sheet fuels on the downward rate of spread, whilst Lyons & Weber (1993, 1991) compared the rate of flame progression over single element to those of a fuel bed. Fonda (2001) studied fine fuel comparing flame height, rate of mass loss and burning and flaming time for range of pine needles.

3.3 METHODS

The sets of experiments described here involve spread of a flame from one end of the element to the other. The effect of the diameter, angle and fuel moisture content on flame height, rate of spread and mass loss and the reaction time was analysed.

3.3.1 Set Up and Flame Detection

Flame properties were recorded (Diagram 2.1) and extracted from the images in the manner described in the previous chapter. Flame detection was similar to that of the previous chapter as well. The colour limit for the flame was set to 200 minimum on all channels with the sum of all three greater than 550.

In the case of a whole element ignited, described in the previous chapter, the flame reflection on the butterfly clip illuminated a significant number of pixels

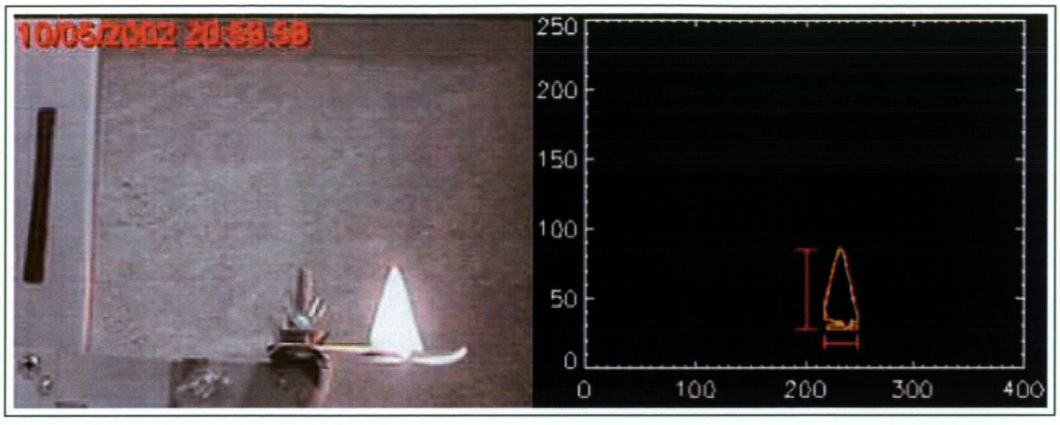

Figure 3.1: Image of a flame above an element of 2 mm diameter with the contour of the detected flame on the right. The red lines on the right image represent the flame height and width measured from the contour.

to warrant it being manually excluded from the analysed region for each burn. In case of the flame progressing along the element, that was not the case. The reflection on the stand in this set of experiments was minor and those pixels were discarded from the flame image by placing a restraint on a minimum number of bright pixels in the y direction or presence of a minimum number of bright pixels in its neighbourhood in the x direction.

Another constraint needed to be used to avoid detection of the wood glowing after the flame had passed (3.1). The constraint on a minimum number of bright pixels in the y direction was used for all except the experiments where angle was varied. Under this constraint, for all x coordinates where the number of pixels detected in the y direction is greater than the set limit, the pixels are stored as the flame, for all other pixels, the x direction constraint is applied. Thus the tip of the flame will be detected despite the lack of pixels in the x direction, and likewise the constraint in x direction ensures the edges of the flame are detected.

In the experiments where angle was varied such constraints would result in losing the ends of the flame. However in this case, a weak y constraint requiring detection number of pixels larger than the element diameter was used to avoid detecting the glow of the element, and the bright pixels of the reflection of the stand were avoided by manually selecting only the area of the image that contains the element. This included finding the pixel values of the front of the

element for each burn and applying the program only to that area.

Similarly to the processes described in the previous chapter, an image of the flame detected was stored with the original image for a further visual conformation of correctly detected flame. The data of the flame detected was stored and merged with the mass loss information recorded.

The beginning of the burn was defined as the time end of the element has stopped flaming and the end when the flame reached the stand. These were determined visually for each burn.

3.3.2 Flame Data

Flame height

For all the experiments described here, excluding the variation in the angle of the element, the height of the flame was defined from the maximum and minimum pixels in the $y-$direction. From the entire set of the pixels were the flame was detected, pixels with maximum and minimum values in $y-$direction were sought. The flame height was then defined as

$$H = (Y_{\max} - Y_{\min} + 1) \times S, \tag{3.1}$$

where S is the scaling factor detected.

Flame width

The beginning and the end of the flame were found from the widest section of the flame. The row with the largest number of flame pixels is considered to be the widest section of the flame (on the Figure 3.2 that is at the position Y_k).

The constraints set on flame detection described above were weak enough to allow for the flaming tip of the element to still be detected. For the elements with thicker diameters, the tip of the element would often continue burning after the main flame had passed. This was taken into consideration when defining the width of flame.

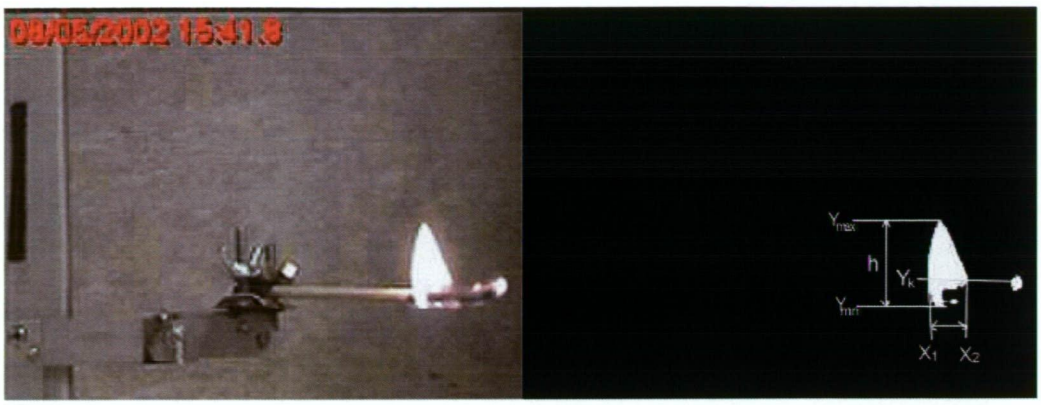

Figure 3.2: Image of a flame detected for a flame spread across a 4 mm horizontal Tasmanian oak cylinder. Definitions of the flame dimensions are shown on the second image.

The beginning of the flame is defined as the minimum value of the $x-$ coordinate in the Y_k row, i.e. pixel $X_{\min,k}$. The row is then searched for breaks in the flame. This is done to ensure that the true end of the flame is detected. On the image 3.2 it can be seen that the maximum value at Y_k row is a pixel that marks the end of the element, not the end of the flame. If there is a break in flame larger than 10 pixels, than the last pixel prior to the break is considered to be the end of flame $X_{2,k}$. The width of the flame is thus

$$W = (X_{2,k} - X_{\min,k} + 1) \times S. \tag{3.2}$$

Rate of spread

The rate of spread for each burn was found to be constant and the rate of flame spread was calculated from the rate of progress of the flame front (X_1) multiplied by the scaling factor S :

$$R = S \times \frac{dX_1}{dt}. \tag{3.3}$$

For each burn correlation R^2 was recorded, which was found to be greater than 0.95 for all horizontal samples, indicating that the rate spread was constant and that the beginning and the end of the burn appropriately determined.

Flame dimension for non-horizontal measurements

For the experiments where the element was at an angle, the above definitions could not be used.

The angle of inclination was the angle of the element to the horizontal, where upward moving flame had positive and downward moving flame negative angle.

Three coordinates were measured for the flame dimensions calculations, flame tip (X_{top}, Y_{top}), flame front (X_{start}, Y_{start}) and the flame end (X_{end}, Y_{end}) (Figure 3.3).

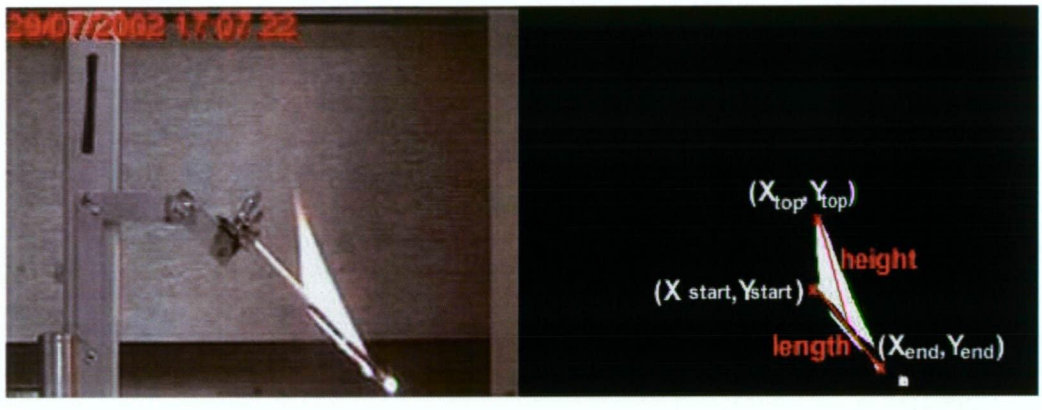

Figure 3.3: Image of a burn recorded at 45^0 and image of the flame contour detected by the program

The flame tip was defined at the position were the maximum y pixel, Y_{top}, was detected. That position (Y_{top}, X_{top}) is the top of the flame. The minimum pixel detected in the $x-$ direction X_{start}, marks the beginning of the flame. Minimum y pixel at the position X_{start} detected, Y_{start}, is the second coordinate of the flame front. The program then searches for a break in the flame. As above, a break larger than 10 pixels is considered to mark the end of the flame. The $x-$ coordinate where the end of the flame is detected is X_{end}, and the minimum y pixel at that position is Y_{end}.

Often there is only one y pixel detected at the positions X_{start} and X_{end}. This would accurately define the beginning of the flame if the flame tip does not precede the flame front. Flame tip could precede the flame front at times, usually by only a few pixels and for flames that are progressing up steeper angles

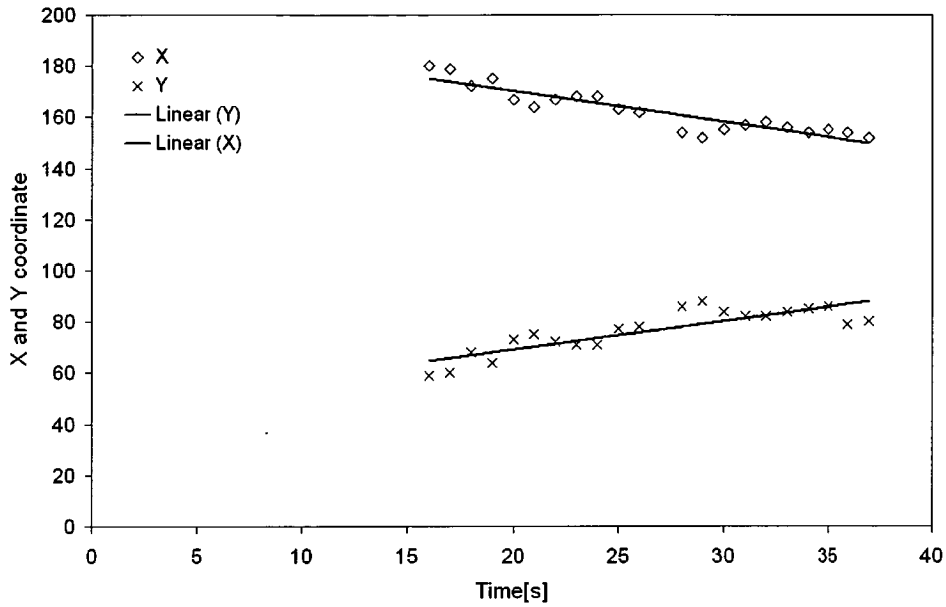

Figure 3.4: Front of the flame coordinates versus time. Rate of change of the $X-$coordinate is $1.09mm/s$ with $R^2 = 0.71$, whereas for $Y-$coordinate it is $1.22mm/s$ with $R^2 = 0.84$. Note that the origin is in the bottom right hand corner and that the orientation of the element was such that the flame progresses as $X-$coordinate decreases and $Y-$coordinate increases (Figure 3.3)

then 45° to the horizontal. When this was the case, the coordinates recorded for the beginning and the end of the flame would show marked difference in angle from the remaining data. To ensure that the $y-$coordinate detected for the beginning and the end of the flame were as close to the element as possible, the angle between (X_{start}, Y_{start}) and (X_{end}, Y_{end}) was noted and compared to the angle of the element.

Most commonly, the flame front does not lead ahead of the combustion of the element, in which case the flame front and end are detected just above or just below the element. It was impossible to set a list of conditions were the front and the end of the flame were detected either below or at the top of the element. This resulted in small error for the flame height and the calculation for length of element ignited. Since the diameter 4 mm is used, the maximum error occurring is ± 2 mm in height, and less than a millimetre for the length. However measurements of rate of change of all of the X_{start}

and Y_{start} coordinate with time yield R^2 values predominantly in the range of $0.8 - 1.0$, with values only occasionally lower than values due to the detection of the flame below the element (3.4), but never below 0.6.

Flame width: The length of the element in flame is calculated from the flame start and the end coordinates as

$$L = S \times \sqrt{(X_{end} - X_{start})^2 + (Y_{end} - Y_{start})^2}. \tag{3.4}$$

This was not the case for angles of $\pm 90°$. For flame burning down a vertical element ($-90°$), the flame length was

$$W = S \times (Y_{end} - Y_{start}) \tag{3.5}$$

In experiments where the element was ignited at the bottom and the flame was burning up a vertical element ($+90°$), it was impossible to recognize where the element covered in flame was ignited. Thus the data for this orientation was not included in the results.

Flame height: For this configuration, flame height was defined as the distance between the flame top (X_{top}, Y_{top}) and the mid-point between the flame front and end

$$(X_{middle}, Y_{middle}) = \left(\frac{X_{start} + X_{end}}{2}, \frac{Y_{start} + Y_{end}}{2} \right), \tag{3.6}$$

which is calculated using

$$H = S \times \sqrt{(X_{top} - X_{middle})^2 + (Y_{top} - Y_{middle})^2}. \tag{3.7}$$

The beginning of the burn was defined as the time when the flame progressed past the ignited end of the element. The end of the burn was defined as the time when the flame front is approximately 10 pixels away from the stand. The flame information between these values was used to calculate the rate of mass loss, average flame height and width, and the position of the front of the flame versus time was used to calculate the rate of flame spread. Note that for the vertical elements it was difficult to detect the middle point of the combusting

element. For the angle of $-90°$ the flame height was half of the total flame detected

$$H(-90°) = S \times (Y_{top} - Y_{bottom})/2$$

As the flame progresses down an element we can assume that at the top of the flame the element is still burning, whereas for angle of $+90°$ the flame height was simply

$$H(90°) = S \times (Y_{top} - Y_{bottom}) \tag{3.8}$$

as it was difficult to accurately determine the mid-point of combusting element due to the flame enveloping the element. This point was thus not included in models but was shown on the graphs.

Rate of Spread: The rate of flame spread for elements at an angle was calculated from

$$R = \sqrt{R_x^2 + R_y^2} \tag{3.9}$$

where R_x and R_y are the rates of change of X_{start} and Y_{Start} multiplied by the scaling factor S

$$R_x = S \times \frac{dX_{start}}{dt} \text{ and } R_y = S \times \frac{dY_{start}}{dt} \tag{3.10}$$

Rate of spread of the flame up a vertical element ($+90°$) was not included in the results, as flame front was impossible to detect. Only flame tip and the flame bottom could be detected.

Efficiency

The efficiency of combustion is a ratio of mass lost in combustion to the mass available,

$$\eta = \frac{m_f - m_i}{l\left(\frac{D^2}{4}\right)\pi\rho}. \tag{3.11}$$

However, to avoid depending on the accuracy of the readings at only two points, the beginning and the end of a burn, another way of calculating efficiency can be employed, using instantaneous mass loss rate and the rate of spread, which were constant during the burns.

Consider a flame progressing along an element of diameter D at a rate of spread R. If at time $t = t_{end}$ flame front is at $X = l$ (Figure 3.5), then

$$R = \frac{l}{t_{end}}. \tag{3.12}$$

The rate of mass loss is

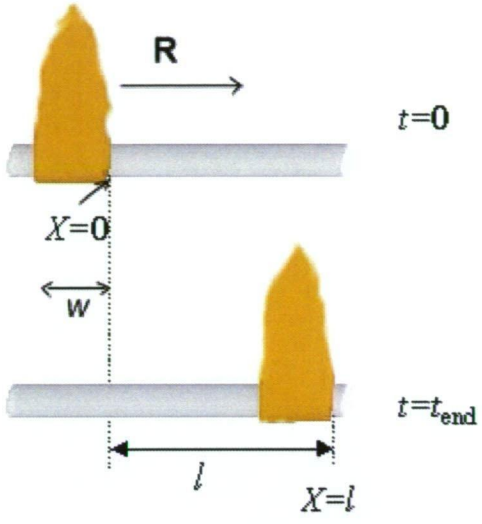

Figure 3.5: Flame progression at two positions: $t = 0$ until $t = t_{end}$

$$\dot{m} = \frac{\Delta m}{\Delta t} = \frac{\eta l \left(\frac{D}{2}\right)^2 \pi \rho}{t_{end}} = \frac{1}{4}\eta D^2 \pi \rho R,$$

and the efficiency then can be calculated using

$$\eta = \frac{4\dot{m}}{D^2 \pi \rho R}. \tag{3.13}$$

Residence Time

Residence time is the time of active flaming of a section of the element, or the time necessary for a flame to progress past a point. It is calculated from the flame width and the rate of spread.

Consider Figure 3.5: at time $t = 0$, point $X = 0$ begins to burn. It will cease to flame in the time t_r; front of the flame will be at a position $X = W$, and

the back of the flame will be at $X = 0$. Since the flame progresses at the rate of spread R, it follows that

$$t_r = \frac{W}{R}. \tag{3.14}$$

3.3.3 Data extraction

The beginning and the end of each burn were decided upon visually and hence were subjective. However, confirmation that the steady rate of spread was reached and recorded was obtained from the measure of linearity of the flame spread readings. An example of data obtained from a burn is given in Figure 3.6 for 2 *mm* white birchwood element.

Readings obtained for flame height, weight, position of the flame front and the mass of an element were recorded every second. Note that the initial 10 seconds marks the ignition of the element, and the high values of flame height are the measurements of the ignition source. The last 20 seconds mark the flame extinguishing and the glow of the element. The trend line estimates the average mass loss rate as the established flame spreads across the element. The slope of the line $-0.00224 \pm 0.00003\ gs^{-1}$ is the rate of mass loss of the element. Likewise the change in the position of the flame front represents the rate of flame spread, $0.0776 \pm 0.0010\ cms^{-1}$, where the line describing the progression of the flame front in time has R^2 of 0.996. Values of R^2 close to 1 for the flame spread rate were used to confirm that the proper end and the beginning of the burn were defined visually.

Ten repetitions were performed for a specific configuration and the averaged values obtained for the flame height, width, rate of spread and mass loss rate were used for correlation testing.

This setup was used for experiments with the flame progressing from one end of an element to the other in which the diameter, fuel moisture content and angle of an element were varied; flame progressing along two elements where the separation between the elements was varied, and for four different types of wood of the same diameter. For the experiments where the diameter was varied two types of wood were used, Tasmanian oak and nogal. Tasmanian oak is a generic name given to tree types of Tasmanian eucalypt species: *Eucalyptus delegatensis, Eucalyptus obliqua and Eucalyptus regnans.* For Tasmanian oak,

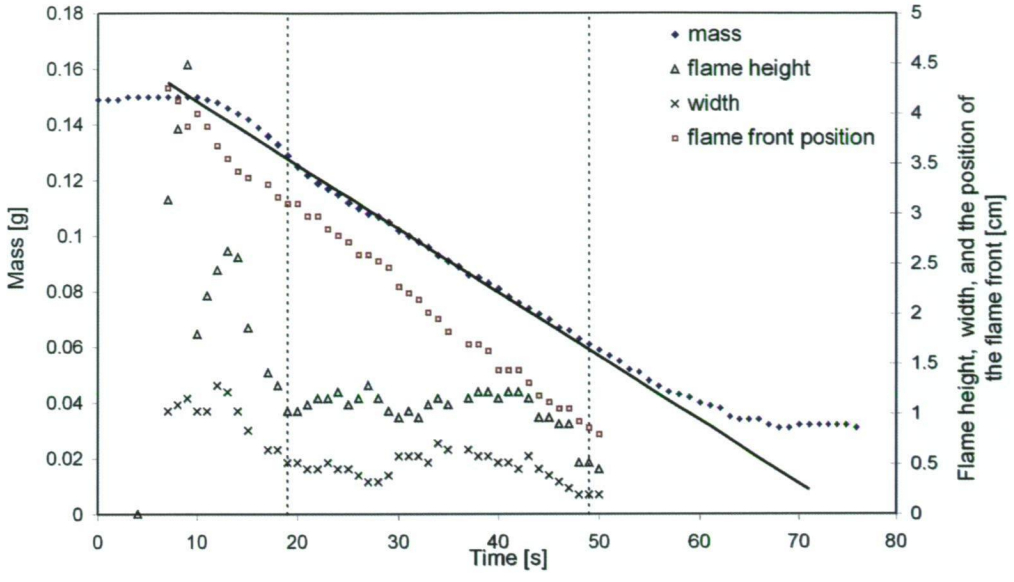

Figure 3.6: Flame properties and mass of an element recorded (white birch toothpick, 2 mm diameter) as flame progresses from one end of the element to the other.

cylinders of 4, 5, 6, 8 and 9.5 *mm* diameter were used. Nogal is a generic name for South American walnut; with this species, the following diameters were used: 2, 3, 4, 5, 6, 8 and 10 *mm*. For the experiments on fuel moisture content and separation between two elements, white birch toothpicks of 2 *mm* diameter were used. Effects of the angle on flame shape and progression were performed using white birch toothpicks (2 *mm* diameter) and Tasmanian oak cylinders (4 *mm* diameter). Spread of flame along an element was also performed on four species of the same diameter and orientation. The species used were 4 *mm* cylinders of: Tasmanian oak, nogal, sapelli and ramin. Summary of the experiments completed specifying fuel type, size, moisture content and orientation of the elements used are given in Table 3.1.

Table 3.1: Flame height experiments

Type	fuel	variable	D $[mm]$	M_f	θ
	TO	D	4, 5, 6, 8, 9.5	oven dry	horizontal
	N	D	2,3,4,5,6,8,10	oven dry	horizontal
flame	O	θ	4	oven dry	$-90°$ to $90°$
spead	TO, N, S, R	fuel type	4	oven dry	horizontal
	WB	M_f	2	$0-10$	horizontal
	WB	separation	2	oven dry	horizontal
TO-Tasmanian Oak, N-Nogal, WB-white birchwood, S-sapelli, R-ramin					

3.4 RESULTS

3.4.1 Effects of Diameter

This experiment was conducted to investigate effects of diameter of horizontal wood cylinders on flame properties. Fuel was oven dried at $110°C$, and placed in a desiccator to ensure that all fuel was at the room temperature and remained dry. The elements were horizontally oriented and ignited at one end. Two species were used: Tasmanian oak (*Eucalyptus* species) and nogal (South American walnut from the *Juglandaceae* family). The following diameters were used: $4, 5, 6$ and 8 mm for oak and $2, 3, 4, 5, 6$ and 8 mm for nogal. After igniting one end of the element a flame would progress along the element, while the tip of the element from where the flame originated would continue to burn for a period of time that increased with the increase in the element's diameter. This occurred due to the volatiles beneath the surface of the unaffected wood escaping along the grain, towards the end of the element.

For the diameters used in this study, the elements used were sufficiently long to consider the readings after the end has ceased to burn. For diameters larger than 8 mm it was noticed that the second flame would often originate from the flaming end (Figure 3.7). This occurs because the flame that spreads along the top layer of the dry element does not provide sufficient energy in the flaming time of the top layer to sustain the complete ignition of the element. However as the top layer has burned off, the flame still burning at the tip of the element spreads along the now thinner element. Therefore 8 mm is the largest diameter used in this study.

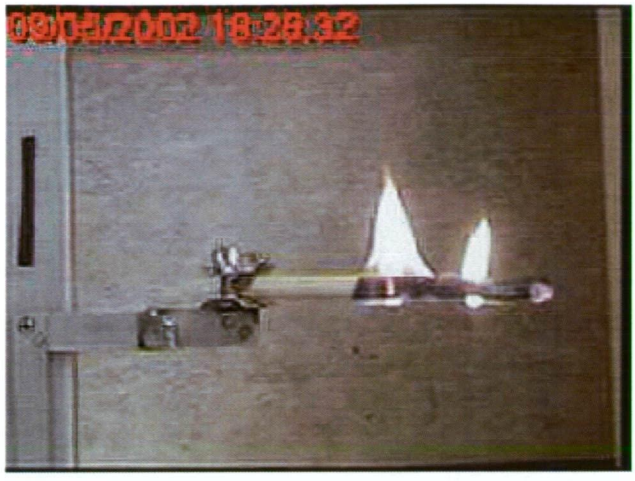

Figure 3.7: Image of the flame progression across 9.5 mm diameter Tasmanian oak. The image shows second flame passing along the element after the first flame had passed.

Rate of Spread

Measurements of the rate of flame progression for each burn provided best fit when modelled as exponential decrease with the increase of diameter:

$$R_{oak} = 1.19 \times 10^{-3} e^{-92.4D} \quad (3.15)$$

$$R_{nogal} = 2.61 \times 10^{-3} e^{-180D} \quad (3.16)$$

in SI units, where data for nogal provided a fit with R^2 of 0.5367, whereas the model for oak yielded R^2 of 0.7845. Data averaged for each diameter value used are shown in Figure 3.8.

Model for power dependence on diameter were fitted as

$$R_{oak} = 4.54 \times 10^{-5} D^{-0.531} \quad (3.17)$$

$$R_{nogal} = 1.84 \times 10^{-5} D^{-0.747} \quad (3.18)$$

with R^2 of 0.483 and 0.564 respectively. Applying the logarithmic transformation to the data and using general linear model showed that instead of the

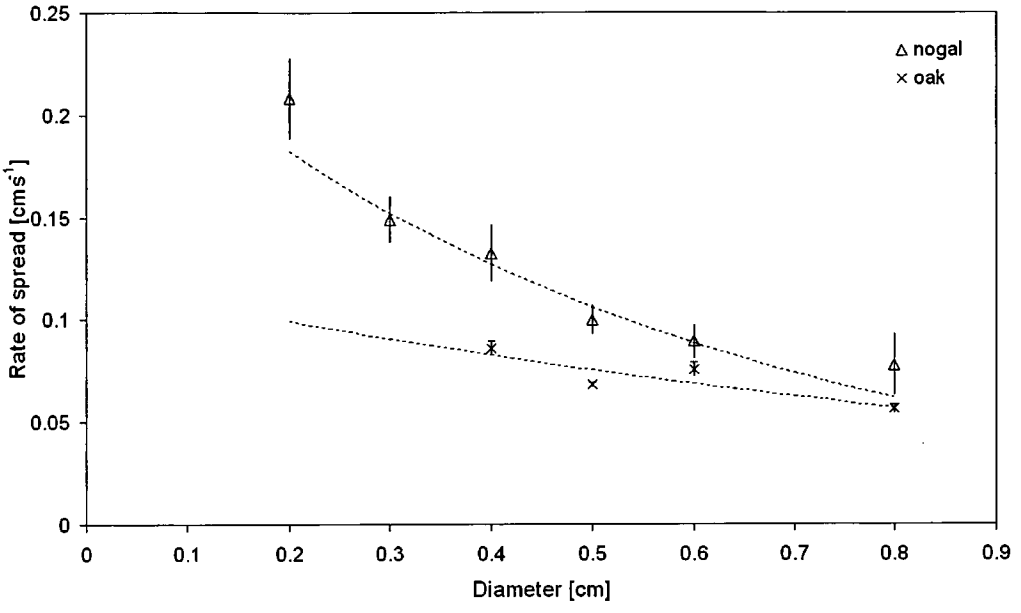

Figure 3.8: Rate of spread versus diameter for oak and nogal. Error bars represent the sandard errors in the measured samples.

power relations 3.17 and 3.18, the rate of flame spread versus the diameter can be represented with the same equation for both wood types

$$R = 2.95 \times 10^{-5} D^{-0.639}, \tag{3.19}$$

with p value of 0.2170 indicating the same power and 0.362 the same constant, with R^2 of 0.716.

Flame Height

Average values obtained for the flame height above different diameters are shown in Figure 3.9. The data was best parameterized with a parabolic fit:

$$H_{oak}(D) = -1202D^2 + 15.5D - 0.02 \tag{3.20}$$

$$H_{nogal}(D) = -828D^2 + 9.05D + 0.0063, \tag{3.21}$$

with R^2 of 0.96 and 0.98 for Tasmanian oak and nogal respectively in SI units.

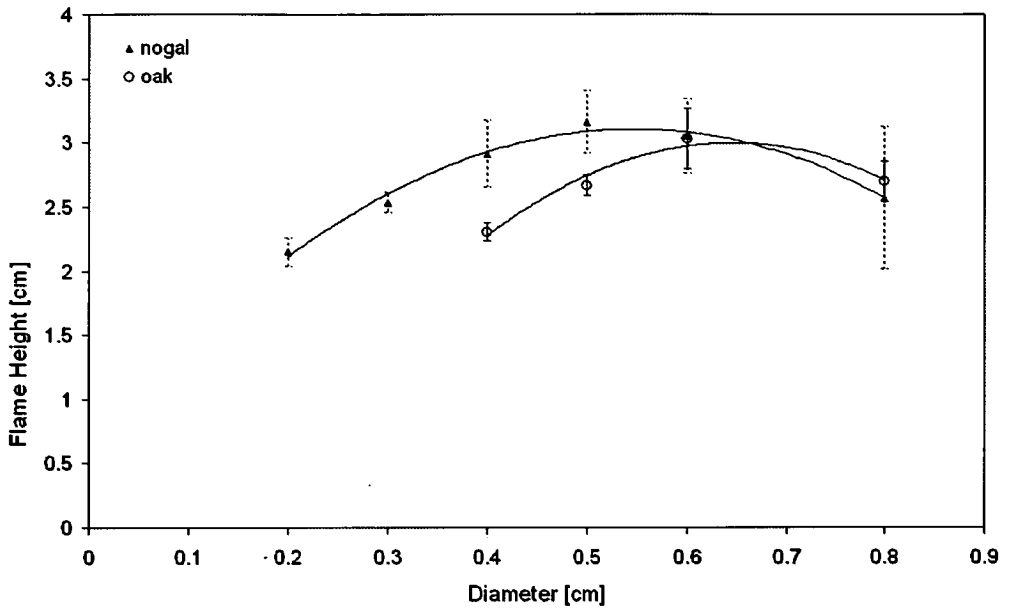

Figure 3.9: Flame height versus diameter for oak and nogal. Error bars represent standard errors.

Rate of Mass Loss

Rate of mass loss for oak and nogal was modelled as linearly dependent on the diameter,

$$\dot{m}_{oak}(D) = 1.59 \times 10^{-3} D \quad (3.22)$$

$$\dot{m}_{nogal}(D) = 2.05 \times 10^{-3} D \quad (3.23)$$

in SI units with standard error in coefficients of 3×10^{-5} and 8×10^{-5} for oak and nogal respectively and $p < 0.001$ with fit forced though zero. The results obtained are plotted in the Figure 3.10.

Average density for oak and nogal were measured to be 637 kgm^{-3} and 578 kgm^{-3} respectively. Incorporating these in the equations (3.22) and (3.23) we obtain

$$\dot{m}_{oak}(D) = 2.50 \times 10^{-6} \rho D \quad (3.24)$$

$$\dot{m}_{oak}(D) = 3.54 \times 10^{-6} \rho D, \quad (3.25)$$

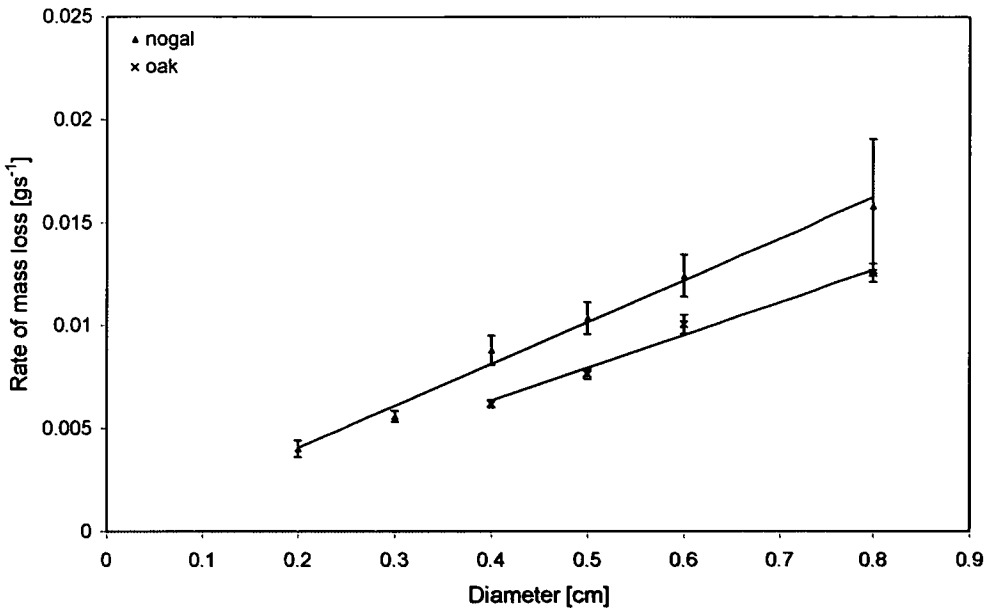

Figure 3.10: Mass loss rate versus diameter for oak and nogal. Error bars represent standard error.

with standard errors in coefficients 6×10^{-8} and 13×10^{-8} respectively. It appears that the difference in the density between two woods does not describe the difference in the rate of mass loss between two wood types.

However, incorporating the width of the flame and the diameter of the element, we can investigate the effect of the diameter on the rate of mass loss per unit volume of fuel consumed (3.11). It is common in the fire literature to label the rate of change in a parameter per unit length with one dash ($\dot{m}'$) and the rate of change per unit area with two dashes ($\dot{m}''$), so the label used here for the rate of mass loss per unit volume is with three dashes, $\dot{m}'''$.

Rate of mass loss per unit volume for oak and nogal was modelled using power dependence on the diameter as

$$\dot{m}'''_{oak}(D) = 4.86 \times 10^{-3} D^{-1.67} \quad (3.26)$$

$$\dot{m}'''_{nogal}(D) = 5.55 \times 10^{-3} D^{-1.56}, \quad (3.27)$$

in SI units, with R^2 of 94.5% and 93.2% for Tasmanian oak and nogal respectively.

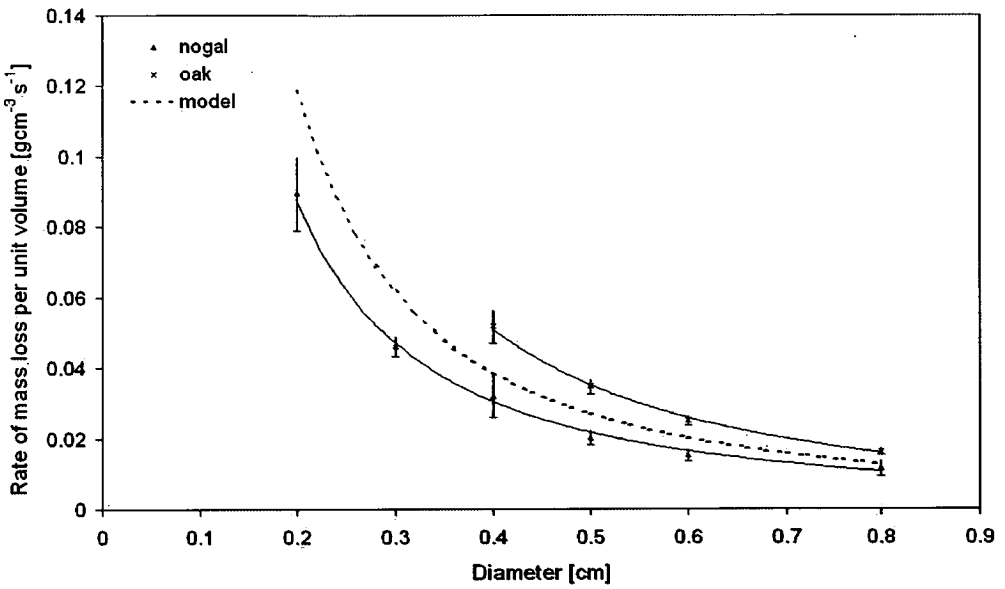

Figure 3.11: Mass loss rate per unit volume versus diameter for oak and nogal. Error bars represent two standard errors. The dashed line is the model given by the equation 3.28, where as the two full lines represent models ?? and 3.27.

After applying logarithmic transformation to the data, general linear model was used to test whether the data could be described using the same parameters. The model showed that there was strong evidence of the same power ($p = 0.282$) and the same constant ($p = 0.822$) so that the following model can then be used:

$$\dot{m}'''(D) = 5.19 \times 10^{-3} D^{-1.615}. \tag{3.28}$$

Efficiency

Efficiency was calculated using equation (3.13). Average values for both oak and nogal. are plotted in Figure 3.12. As expected, the efficiency of combustion significantly decreases as the thickness of the wood increases. It was modelled as exponential decay. There is no evidence of significant difference between the two wood types in either exponential ($p = 0.135$) or pre-exponential constant ($p = 0.085$), and the efficiency for both wood types may be described using

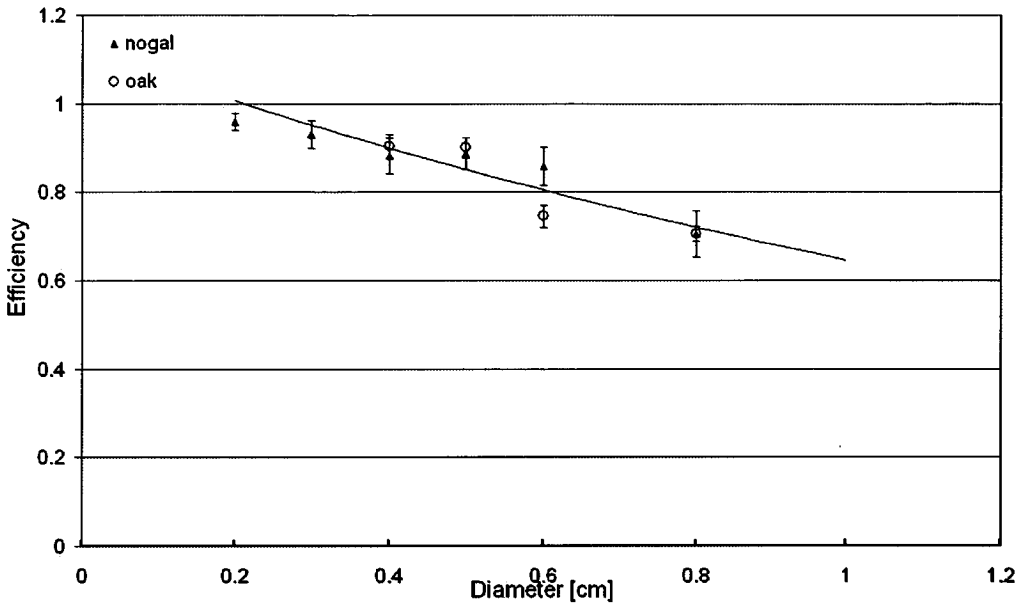

Figure 3.12: Efficiency versus diameter for oak and nogal where flame progresses along an element. Error bars represents one standard error in the measured sample

$$\eta = 1.123e^{-55.5D}, \tag{3.29}$$

with R^2 of 0.86.

Width

Flame width values observed are shown in Figure 3.13. They were parametrized similarly to flame height, using a parabolic fit,

$$W_{oak}(D) = -332D^2 + 5.52D - 0.0073 \tag{3.30}$$

$$W_{nogal}(D) = -732D^2 + 9.75D - 0.0036, \tag{3.31}$$

in SI units where R^2 for oak is 0.969 and 0.967 for nogal.

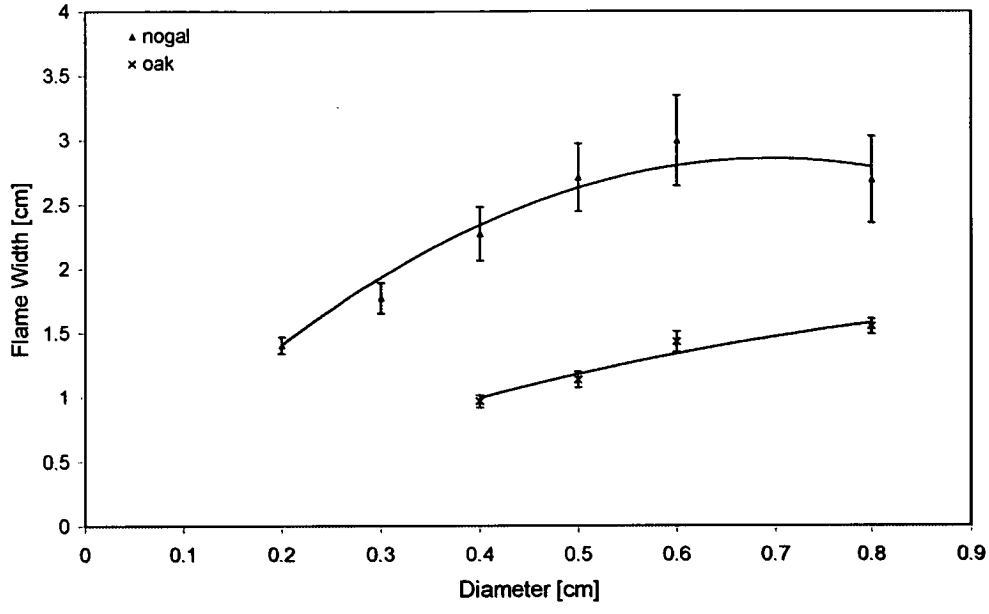

Figure 3.13: Flame width versus diameter for oak and nogal

Residence Time

Using equation (3.14) residence times for each burn were calculated with the mean flame width and the rate of spread for that burn. Values obtained for residence times averaged over diameter are plotted in Figure 3.14.

Predicting residence time from models derived for flame width (equation 3.30) and rate of spread (equation 3.15) we have

$$t_{r\,oak}(D) = \frac{W}{R} = \left(-2.79 \times 10^5 D^2 + 4640D - 6.13\right) e^{92.4D} \tag{3.32}$$

for Tasmanian oak, and from 3.31 and 3.16, residence time for nogal is

$$t_{r\,nogal}(D) = \frac{W}{R} = \left(-2.8 \times 10^5 D^2 + 3740D - 1.38\right) e^{180D} \tag{3.33}$$

In can be seen in Figure 3.14 that the model derived for nogal does not manage to adequately predict the residence time for nogal the diameter of 8 mm due to the large standard error in this reading. Comparing observed data to the values predicted by models (3.32) and (3.33), coefficients of correlation $R^2 = 0.909$ and $R^2 = 0.814$ are obtained respectively.

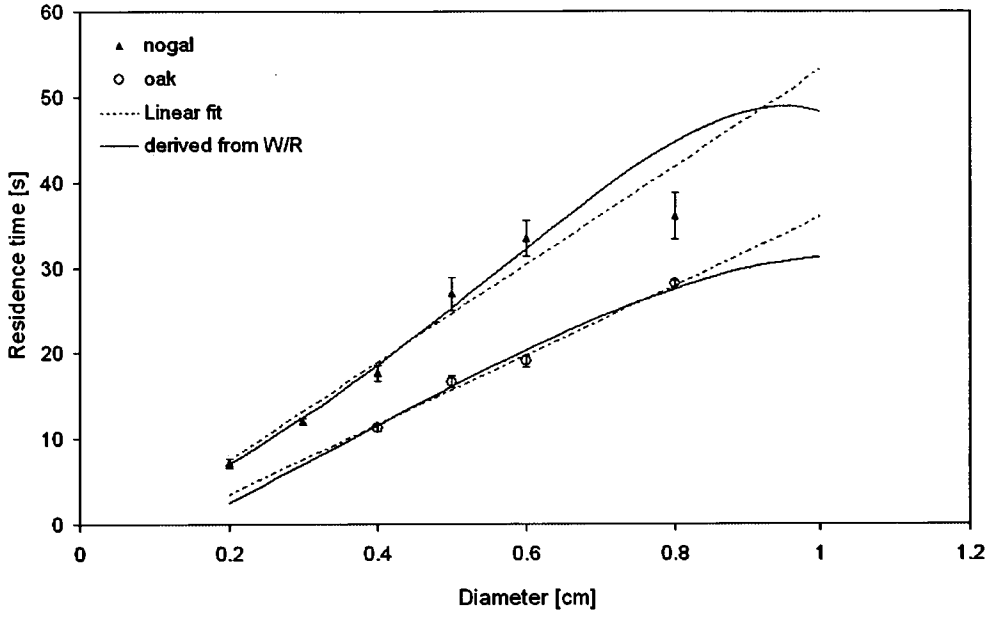

Figure 3.14: Residence time versus diameter for oak and nogal. Error bars represent standard errors

For the range of diameters used however, a simple linear model appear to adequately represent the observed residence time (Figure3.14), which is described using equations:

$$t_{r\,oak}(D) = 4056D - 4.59 \tag{3.34}$$

$$t_{r\,nogal}(D) = 5723D - 3.94 \tag{3.35}$$

with R^2 of 0.91 and 0.81 respectively.

3.4.2 Effects of Fuel Moisture Content

Fuel moisture content (M_f) is a measure of the amount of moisture present in a fuel, expressed as a fraction or percentage of the over-dry weight of the fuel (*Wood Handbook - Wood as an Engineering Material* 1999). In these experiments moisture content M_f is expressed as percentage.

The experiments were performed by burning 2 mm diameter white birchwood (of the *Betulaceae* family) toothpicks. All of the elements used in the experiments were kept in the laboratory under the same conditions prior to the start of the experiment.

Elements were then divided into several groups which were dried in the oven for different periods of time, to achieve different fuel moisture content. There was approximately 20 minutes time difference in drying the samples. It is impossible to estimate the fuel moisture content of the burnt fuel prior to combustion. Thus ten elements from each sample were used for the experiments and the rest was weighted and returned to the oven for fuel moisture determinations. The remaining elements were dried in an oven over a period of 24 hours at the temperature of $95°C$. Elements which were removed from the oven and used for the flame property measurements were placed in a plastic ziplock bag to ensure its moisture content remained the same until they reached the room temperature.

Ten elements were burned for each fuel moisture measurement, and the average values of the readings are shown in Figures 4.23, 4.25 and 3.17.

Empirical Fit

Figures 4.23, 4.25 and 3.17 show that the rate of spread decreases as fuel moisture increases, the flame width decreases, as do flame height and mass loss rate. The weighted averages showed the best empirical fit to exponential models, where the dependence of mass loss rate on fuel moisture content (M_f) is given by

$$\dot{m}\left(M_f\right) = 3.37 \times 10^{-6} e^{-0.0423 M_f}, \tag{3.36}$$

with R^2 of 0.66. Average values of flame height H, width W and rate of spread R were also modelled exponentially to obtain with the following equations:

$$R\left(M_f\right) = 1.66 \times 10^{-3} e^{-0.0625 M_f} \tag{3.37}$$

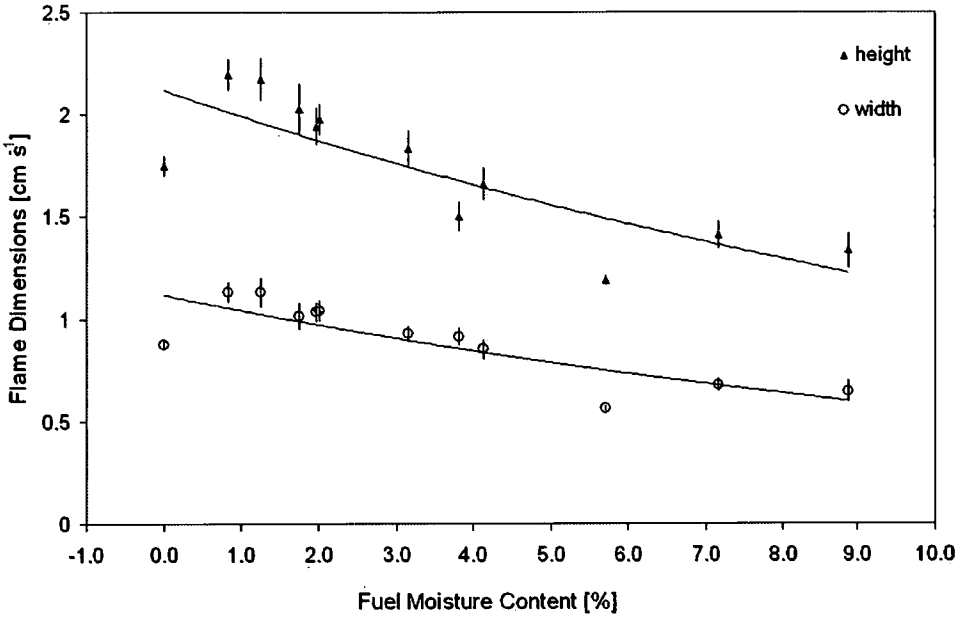

Figure 3.15: Flame height and widthversus fuel moisture contents for 2 *mm* birchwood elements. Error bars represent standard error in averaging samples.

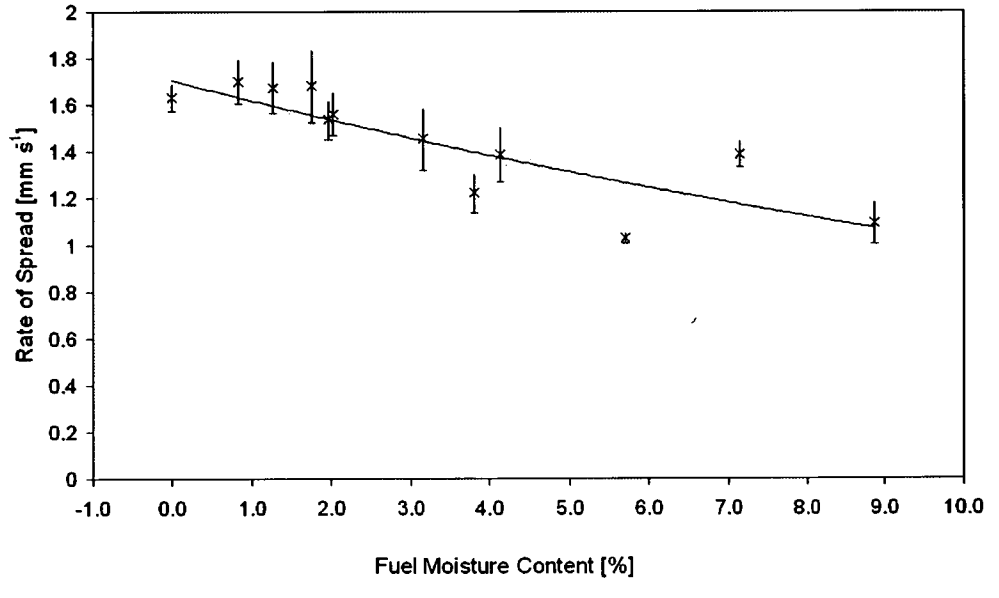

Figure 3.16: Rate of flame spread versus fuel moisture contents for 2 *mm* diameter birchwood elements. Error bars represent standard errors.

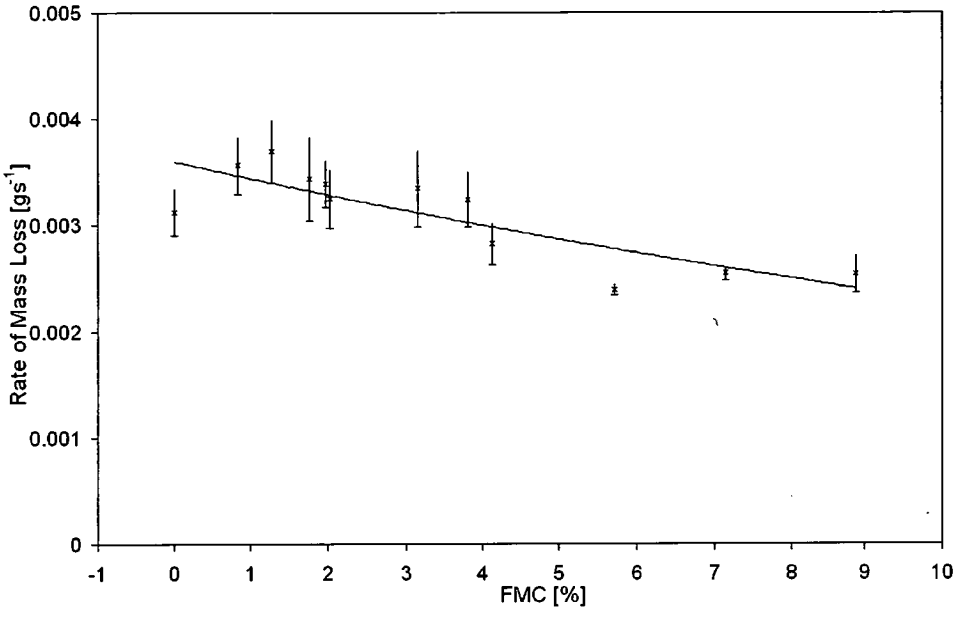

Figure 3.17: Rate of mass loss versus fuel moisture content for 2 mm diameter elements. Error bars represent one standard error.

$$H\left(M_f\right) = 2.07 \times 10^{-2} e^{-0.068 M_f} \tag{3.38}$$

$$W\left(M_f\right) = 1.05 \times 10^{-2} e^{-0.0668 M_f} \tag{3.39}$$

with adjusted R^2 of 0.66, 0.57 and 0.63 respectively. All the variables are in SI units and the moisture content is a percentage of water to the dry mass of the fuel.

After applying logarithmic transformation to the data, general linear model was used to test whether the data could be better described using the same exponential constant for all of the variables. The model showed that there was strong evidence of different pre-exponential constants for all of the data ($p < 0.001$), but that the same exponential component can be used (p values of: 0.431 for the flame height, 0.024 for the flame width, 0.447 for the rate of spread and 0.022 for the rate of mass loss). The data can then be described using:

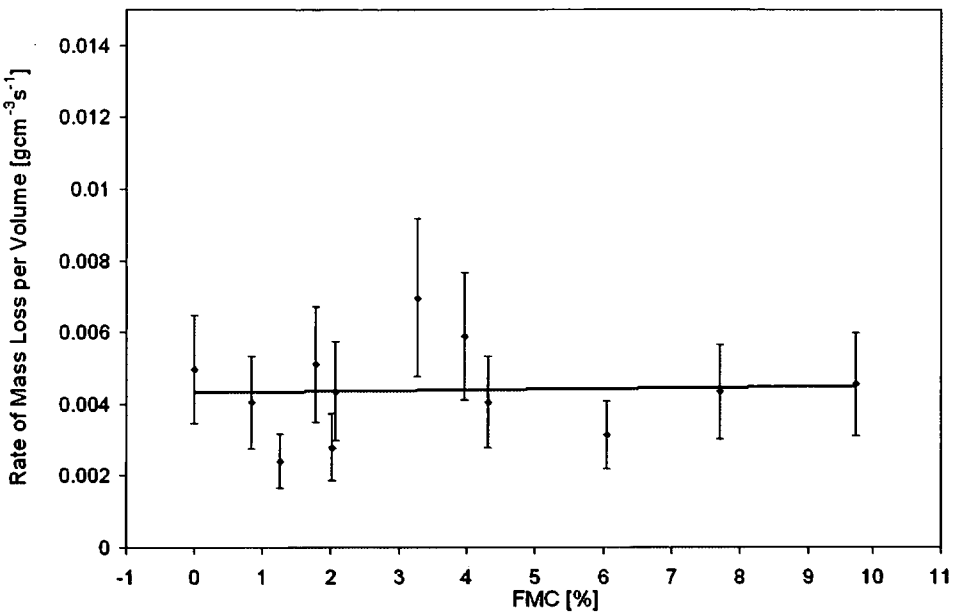

Figure 3.18: Rate of mass loss per unit volume versus fuel moisture content for $2mm$ diameter elements. Error bars represent one standard error.

$$\dot{m}\left(M_f\right) = 3.45 \times 10^{-6} e^{-0.0519 M_f}, \tag{3.40}$$

$$H\left(M_f\right) = 2.07 \times 10^{-2} e^{-0.0519 M_f}, \tag{3.41}$$

$$W\left(M_f\right) = 1.09 \times 10^{-2} e^{-0.0519 M_f}, \tag{3.42}$$

and

$$R\left(M_f\right) = 1.65 \times 10^{-3} e^{-0.0519 M_f}. \tag{3.43}$$

Similarly to the previous experiment (3.4.1), the rate of mass loss per unit volume was calculated dividing the rate of mass loss by the length of the element in flame and its the cross-sectional area. Average values obtained are plotted versus the fuel moisture content in the figure 3.18. The rate of mass loss per unit volume was modelled linearly against the fuel moisture content to obtain

$$\dot{m}\left(M_f\right) = 101 + 3.01 M_f, \tag{3.44}$$

in SI units, with R^2 of 59.8%.

Rate of Spread Relative To The Dry Fuel Rate

Weber & De Mestre (1990) estimated rate of flame spread for fine fuel (ponderosa pine needles) based on thermodynamic considerations, comparing the rate of spread to that of the dry fuel. We follow their method here to compare with the results obtained for this fuel.

The heat required to ignite fuel of moisture content M_f is calculated using

$$Q_{ig}(M_f) = Q_f + M_f Q_m = Q_f \left[1 + M_f \frac{Q_m}{Q_f}\right], \tag{3.45}$$

where Q_f is the ignition heat of dry fuel and Q_m is the heat required to raise water from ambient temperature to $100°C$ and then to evaporate it. The ratio of the two is then given by

$$\frac{Q_m}{Q_f} = \frac{c_w(373 - T_0) + L}{c_p(T_{ig} - T_0)} \tag{3.46}$$

where c_p is specific heat of dry fuel, c_w is specific and L latent heat of water vaporisation and T_0 and T_{ig} are the ambient and the ignition temperatures.

Then using Rothermel's (1972) model for rate of spread

$$R = \frac{\dot{q}}{\rho Q_{ig}}, \tag{3.47}$$

where $\dot{q}$ is the heat transfer rate across the interface $[W/m^2]$, it follows that

$$R(M_f) = \frac{\dot{q}}{\rho Q_f \left[1 + M_f \frac{Q_m}{Q_f}\right]} \tag{3.48}$$

Using the values defined in Table 3.2, from equation (3.46) then $\frac{Q_m}{Q_f} = 3.58$. Since M_f is expressed as percentage, we would expect rate of spread to vary with moisture content according to

$$R(M_f) = \frac{R(0)}{[1 + 0.0358 M_f]}. \tag{3.49}$$

Fitting the experimental data to this model, the best coefficient obtained was

Table 3.2: Table of constants for average specific heat calculations

c_p	2385	$Jkg^{-1}K^{-1}$	Incropera & DeWitt (1981)
c_w	4190	$Jkg^{-1}K^{-1}$	*CRC Handbook of Chemistry and Physics, 80th Edition* (1999)
L	2257	$kJkg^{-1}$	*CRC Handbook of Chemistry and Physics, 80th Edition* (1999)
T_{ig}	600	K	Albini & Reinhardt (1995)
T_0	300	K	measured

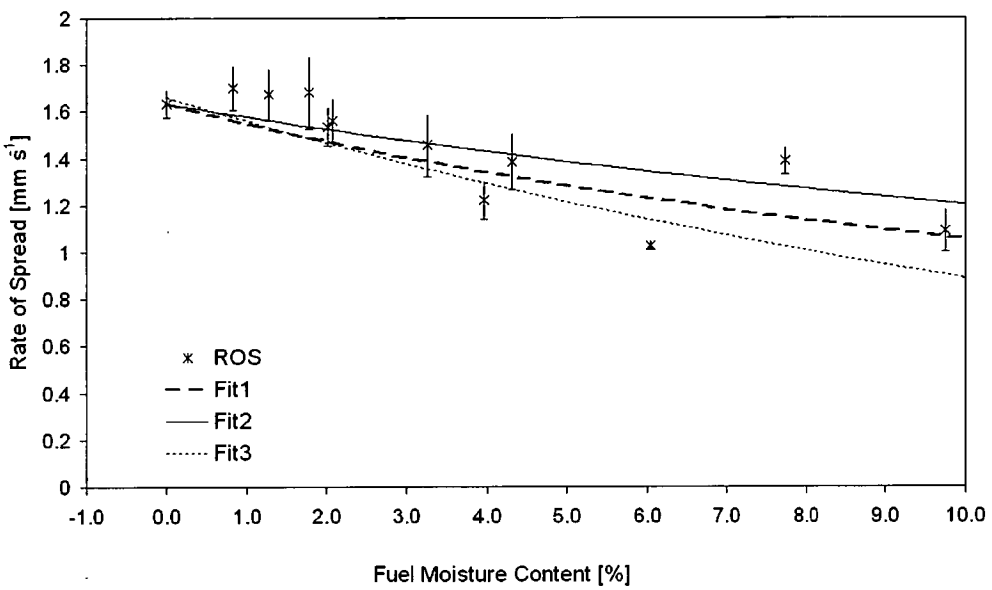

Figure 3.19: Rate of spread versus moisture content. Fit1 represents model represented by equation 3.49, Fit2 by equation 3.50, and Fit3 is the best empirical fit given by equation 3.37

$$R(M_f) = \frac{R(0)}{[1 + 0.0544 M_f]}, \tag{3.50}$$

with reduced χ^2 of 0.99. This indicates that the moisture content of 18.4% would halve the rate of spread. The models 3.49 and 3.50 as well as the empirical fit 3.37 are plotted in Figure 3.19.

Residence Time

The residence time, or time required for a flame to progress pass a point, is then given by ratio of flame with to rate of spread (equation 3.14)

$$t_r = \frac{W}{R} = 6.62 \pm 0.26, \tag{3.51}$$

where equation (3.42) and (3.43) are used for flame width and rate of spread. Standard errors in the coefficients in equations (3.42) and (3.43) where used to calculate the standard error of 0.26 for residence time.

Residence time was also calculated using the mean values of flame width and the rate of spread for each burn. Comparing average residence times obtained and correlating them with the fuel moisture content directly results in R^2 of 0.079 indicating no correlation. Overall average value for the residence times measured from all the experiments for 2mm birchwood is:

$$t_r = 6.3 \pm 0.1s. \tag{3.52}$$

The average residence time calculated for each fuel moisture level are plotted in Figure 3.20.

Efficiency

The dependence of efficiency on moisture content could not be determined in this set of experiments. For this element, after the flame passed a point, glowing continued until only fine ash remained. Efficiency was thus very high for all elements, but the exact value was undeterminable.

3.4.3 Effects of Angle

In this experiment one element was burned at different angles in order to measure different flame height, and rate of spread depending on the element orientation. Fuel used was $4mm$ diameter oven dried oak

however the flame spread for the angles of -90 and $-75°$ was at times not achievable as the flame extinguished before reaching the end of the fuel.

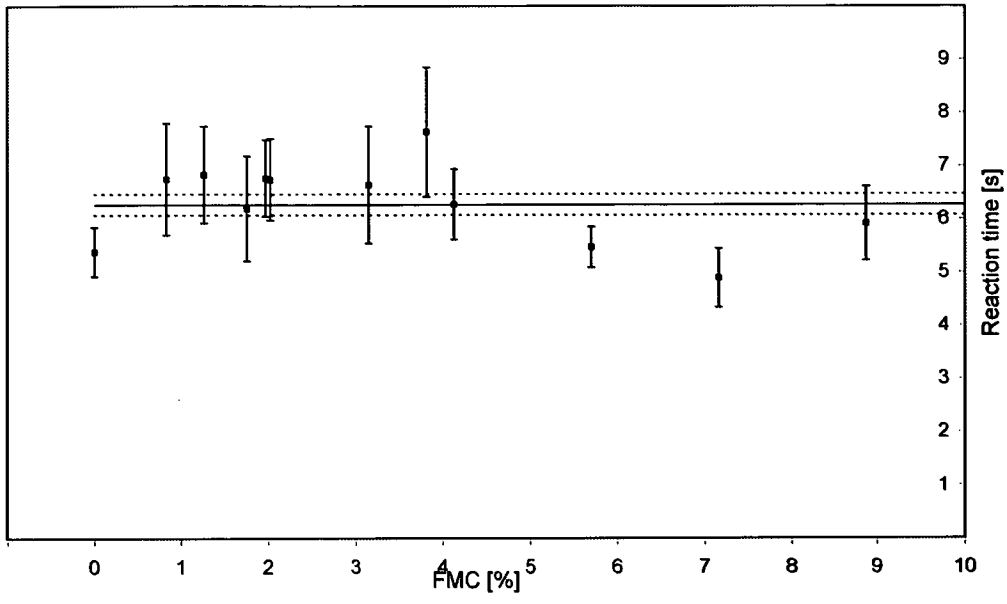

Figure 3.20: Residence time versus fuel moisture content. Error bars represent standard deviation.

Rate of Spread

Following Weber & De Mestre's (1990) model where the dependence on angle is related to the rate of spread of the horizontal element, the following model was obtained

$$R(\theta) = \frac{R(0)}{1 - 0.809 \sin\theta} \tag{3.53}$$

with reduced chi-squared 16.1. This is in close agreement with the results published by Weber & De Mestre (1990) who had obtained 0.8 coefficient.

This model is placing significant weight at the accuracy of the measurement of the horizontal element. Modelling to a function $R(\theta) = \frac{a}{1+b\sin\theta}$, we obtain

$$R(\theta) = \frac{0.657 \times 10^{-3}}{1 - 0.868 \sin\theta} \tag{3.54}$$

in SI units, with reduced chi-squared, $\chi_r = 0.298$. Both models are plotted against the data in Figure 3.21.

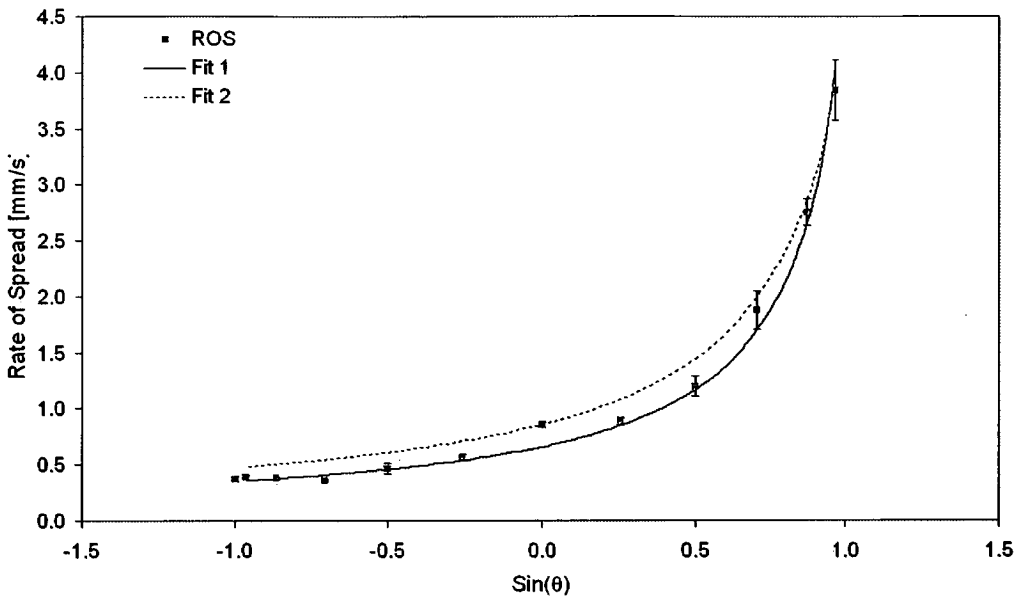

Figure 3.21: Rate of flame spread versus angle of fuel inclination. Fit 1 is modelled according to 3.54 and fit 2 follows 3.53.

Flame Height

Modelling flame height in the similar fashion we obtain

$$H(\theta) = \frac{H(0)}{1 - 0.939 \sin\theta} \tag{3.55}$$

with reduced χ^2 of 4.09 or but freeing $H(0)$, we have

$$H(\theta) = \frac{2.29 \times 10^{-2}}{1 - 0.843 \sin\theta}, \tag{3.56}$$

in SI units, with reduced χ^2 of 5.44. As shown in Figure 3.22 both fail to capture entire data range (in particular +75 and +90 angles), with model 3.56 being somewhat better.

Flame Width

Flame width in data is, for steep angles, similar to flame height due to their definitions (Equations 3.7 and 3.4). The flame width was thus modelled in

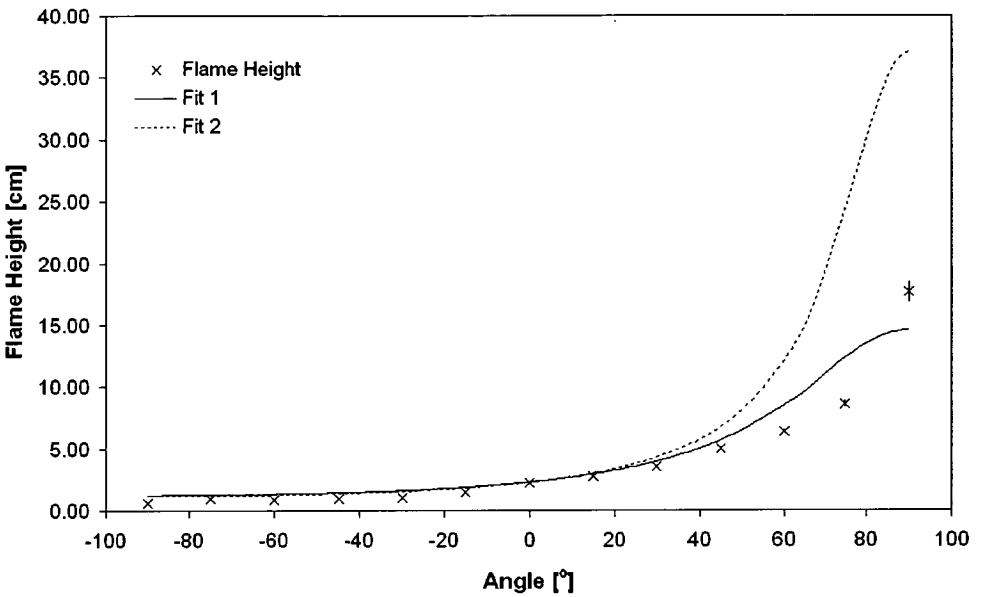

Figure 3.22: Flame height versus angle of inclination of the fuel. Fit 1 represents model 3.56 and Fit 2 model 3.55

similar fashion to obtain

$$W(\theta) = \frac{W(0)}{1 - 0.887 \sin\theta} \tag{3.57}$$

and

$$W(\theta) = \frac{1.415}{1 - -0.845 \sin\theta} \tag{3.58}$$

with reduced χ^2 of 6.96 and 10.3 Both models are shown in Figure 3.23, with average values obtained experimentally. The both provide better fit than obtained for flame height, though Equation (3.57) has better χ^2. It is worth noting that we do not have a reading for $+90°$ for flame width.

Mass Loss Rate

Residence Time

Residence time is found by dividing the width of the flame by the rate of spread (Equation 3.14). Average values for each reading are shown in Figure 3.26. It

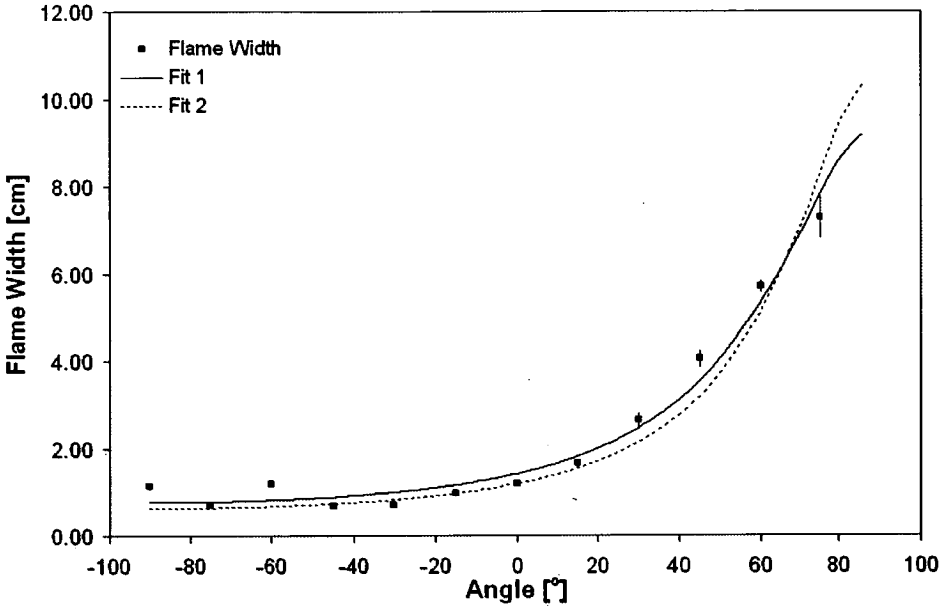

Figure 3.23: Flame width versus angle of fuel. Error bars represent the standard errors. Fit one is calculated from the equation 3.58 and Fit 2 from 3.57

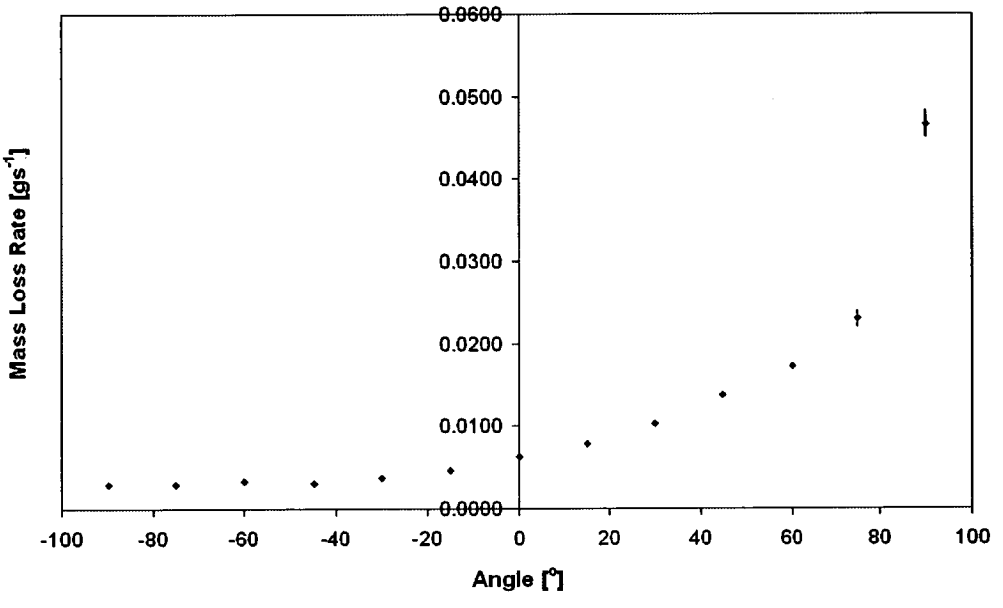

Figure 3.24: Rate of mass loss versus angle of element inclination. Error bars represent standard error

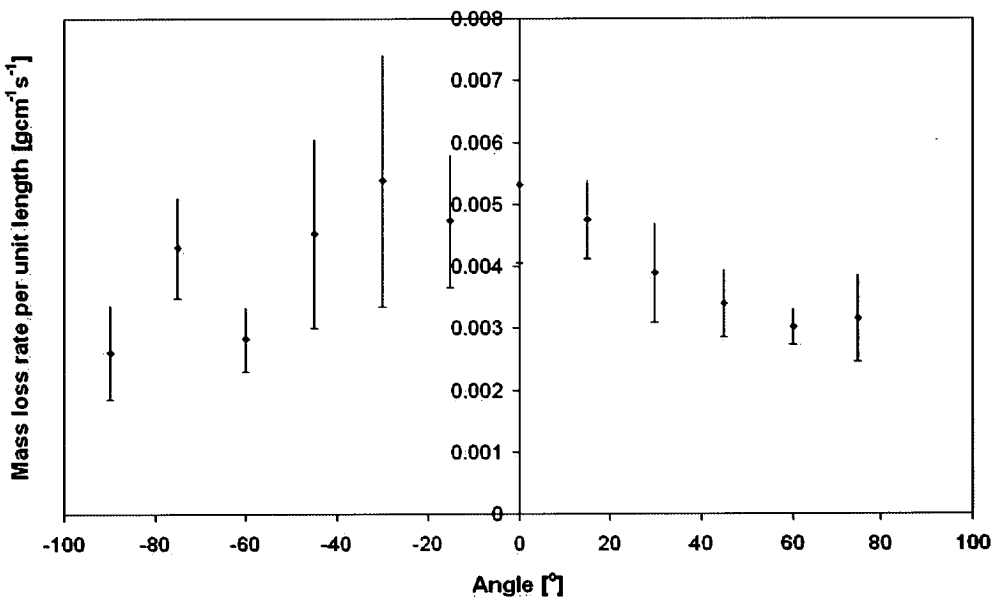

Figure 3.25: Rate of mass loss per unit width versus angle. Error bars represent combination of standard errors in mass loss and flame width readings. Note that the large the large error bars are due to the large variance in length measurements.

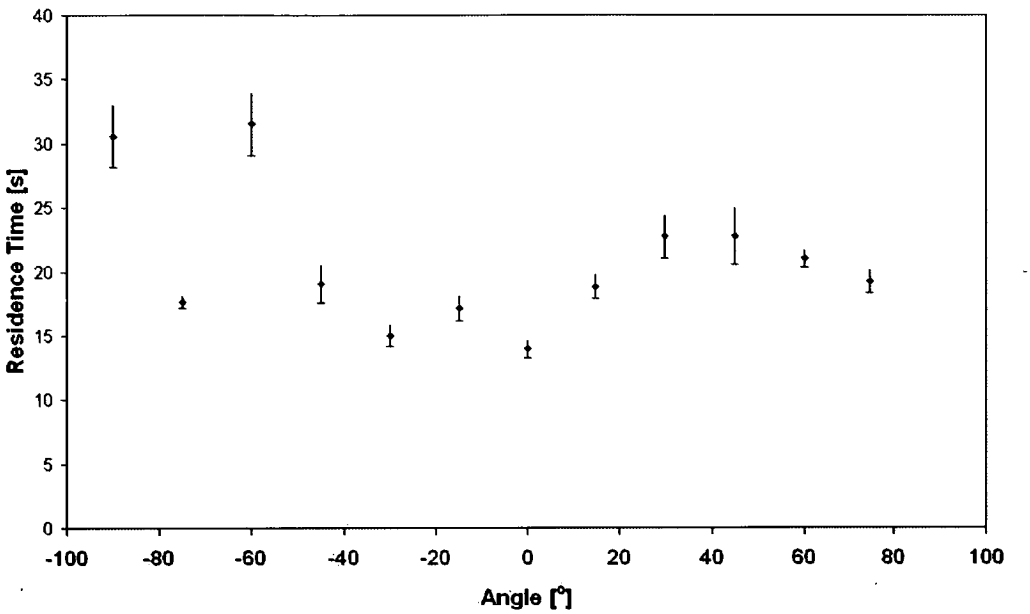

Figure 3.26: Residence time versus element orientation. Error bars represent standard errors.

is hard to quantify the results as the errors in width and rate of spread will combine in determining the residence time. whilst it appears that the residence time is significantly higher for steep downwards spread, it is also worth noting that some elements had not been able to achieve the sustained spread for these angles and extinguished before reaching the end of the element. Only the elements that achieved a sustain rate were included in results.

As these elements had the same diameter and moisture content, it seems that only efficiency of the combustion should affect the residence time, which has also given inconclusive results.

Efficiency

Efficiency of combustion appears unaffected for the angles $-90°$ to $+45°$, and then decreases for steep angles (Figure 3.27). As efficiency is calculated from rate of mass loss and rate of spread, it is hard to conclude that this is not due to the larger uncertainty in the measurements of rate of spread for steep angles. The results for the rate of mass loss per flame width (Figure 3.25),

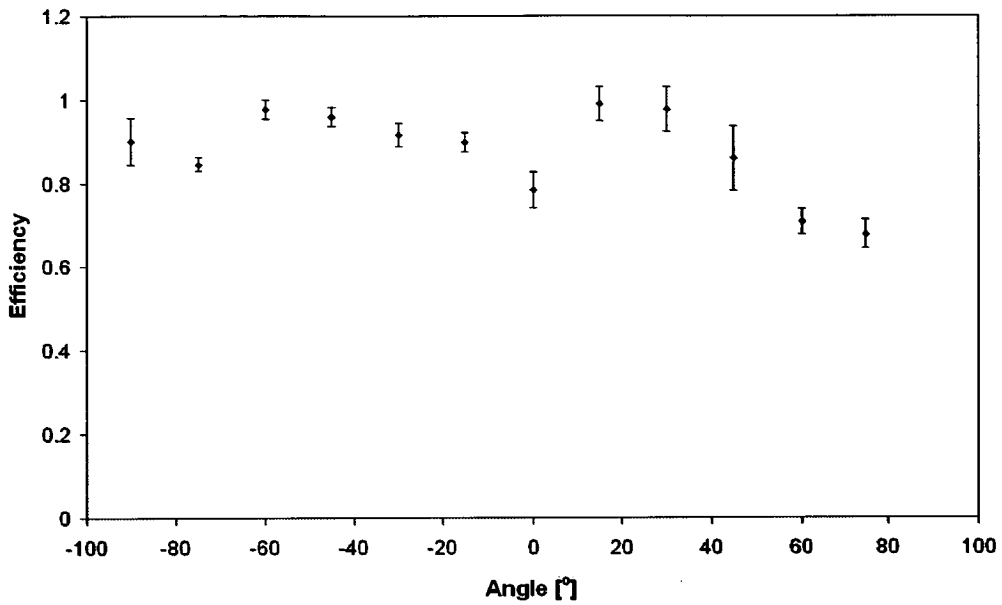

Figure 3.27: Efficiency of combustion versus angle. Error bars represent standard error of the mean.

would indicate that the efficiency reduces for steeper angles.

3.4.4 Effects of Separation Between Fuel Elements

When two elevated elements are separated, buoyancy of the gasses and hence the flame height are affected. Thomas et al. (1965) theorized that flame merging depended on the pressure drop between two flames and the air entertainment from the other side resulted in the flames leaning towards each other. Conditions for a just merged flame were described as:

$$\frac{H}{D} = 9\sqrt{\frac{S^3}{DW^2}} \tag{3.59}$$

where H is the flame height for the just merged flames, D is the depth of the flame, S is the separation between the elements, and W is the width of the flame.

In these experiments two elements were burned and the separation between them was varied, in order to parametrise flame shape relative to the separation

and affect it may have on the rate of spread. Elements used were 2 mm birchwood cylinders, dried in an oven at $110°C$. Prior to a burn, elements were placed in a desiccator prior to burning to achieve room temperature.

The results obtained are plotted in Figures 3.28, 3.30, 3.32, 3.29 and 3.31. Note that on the graphs, $8mm$ separation resulted in two separate flames. Other data points represent merged flame.

From the average values for each separation measured, it is seen that the most significant effect occurred for the flame height Figures 3.28. Flame height was modelled using parabolic fit, to obtain

$$H = -0.0805S^2 + 0.603S + 2.81, \tag{3.60}$$

with R^2 of 0.986, where separation S is given in millimetres and flame height H in centimetres. Thus the maximum flame height occurs at $S = 3.74\ mm$ where $H_{\max}$=3.94 cm, or $1.4H_0$, and H_0 is the height of the two elements with no separation.

The increased flame height and thus radiative heat flux appears to have not affected the rate of flame spread (Figure 3.29) which remained constant at $1.31 \pm 0.03 mms^{-1}$.

The residence time was also unaffected (Figure 3.31) and thus the width of the flame (Figure 3.30) and mass loss rate (Figure 3.32) which were on average $8.09 \pm 0.24s$, $1.64 \pm 0.02 mms^{-1}$ and $0.00548 \pm 0.00023 gs^{-1}cm^{-1}$ respectively and are shown as lines on the graphs.

Similarly to the fuel moisture experiments the efficiency of each burn for the $2mm$ birch wood was 100%.

The flames were separated at 8mm separation. This is in agreement with Equation (3.59). Table 3.3 shows the equation parameters calculated for at different separations. Note that the flame depth is calculated to be 20% larger than the element diameter as suggested by Muraszew (1974). We can see that the measurements are in agreement with Thomas et al.'s (1965) findings and that the critical separation for the flame merging for these elements is between 7 and 8 mm.

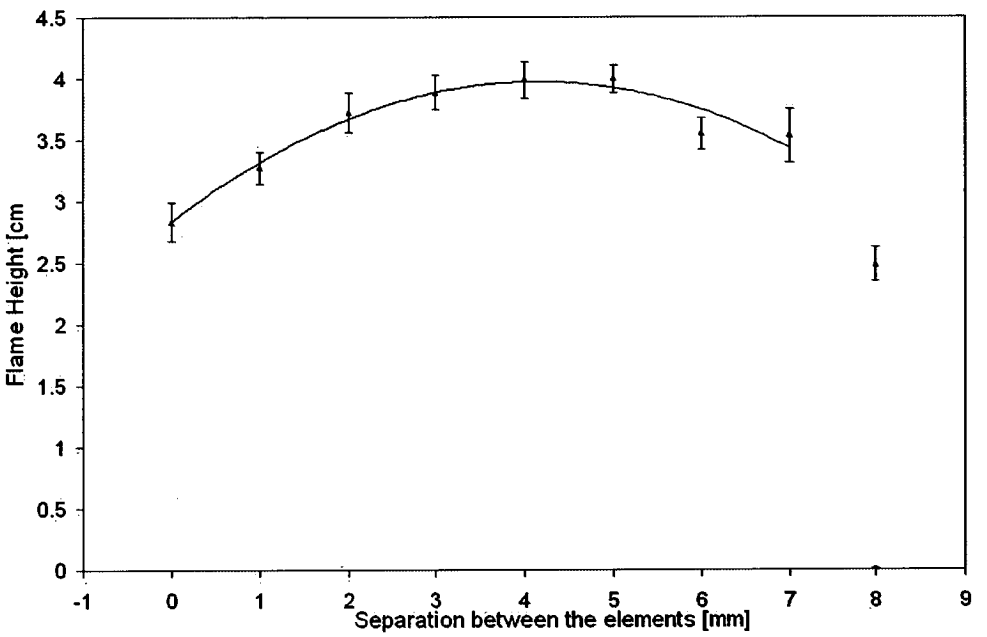

Figure 3.28: Flame height versus separation between elements for spread of flame along two cylinders (2mm diameter, white birchwood). Note that for 8mm separation, the flames were separated. Error bars represent standard errors.

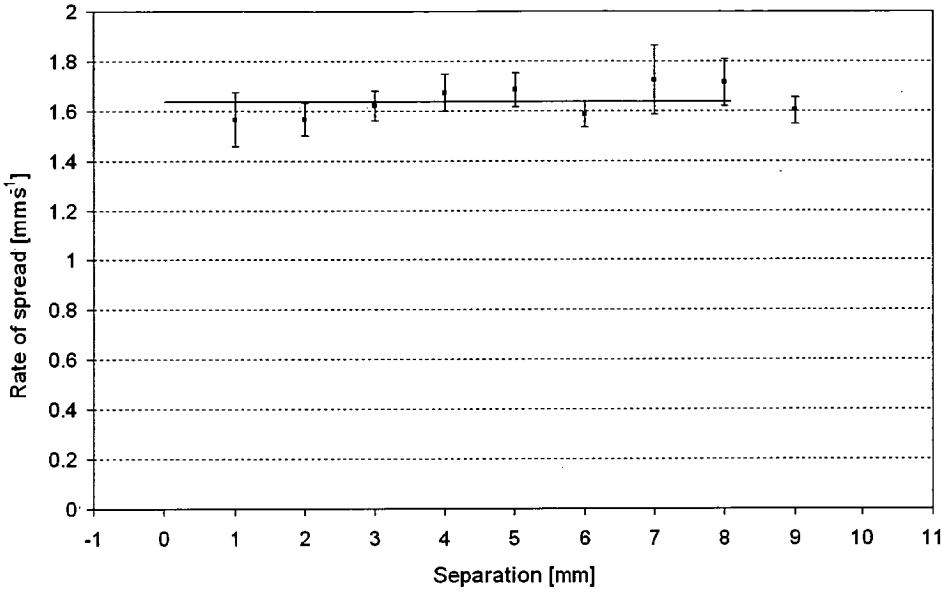

Figure 3.29: Rate of flame spread across two element versus separation between them. Note that the flame was not merged at 8mm separation. Error bars represent standard errors.

3.4.5 Effects of Wood Type

In the previous sections we studied the effects of moisture, fuel orientation and dimensions and the separation between elements on the flame rate of spread and characteristics. A further set of experiments were conducted to illustrate the enormous effects intrinsic characteristics of different types of wood have on the flame shape and burning rate. The elements used were horizontally oriented, oven-dried, 4 mm diameter cylindrical sticks of: Tasmanian oak, sapelli, ramin and nogal. This experiment was conducted to investigate whether difference in flame properties and rate of spread for elements of the same dimensions, orientations and fuel moisture content can be related to some differences in the wood characteristics.

Sapelli, *Entandrophragma Cylindricum,* is a semi-hard wood from central Africa of 600 to 750 kg/m^3 density and a high sap content. Ramin, *Gonystylus macrophyllum,* is the least dense of the four fuels used. Ramin provided least resistance to cutting, whereas sapelli is the hardest of the samples used. Nogal is a chocolate brown heartwood, South American walnut from *Juglandaceae*

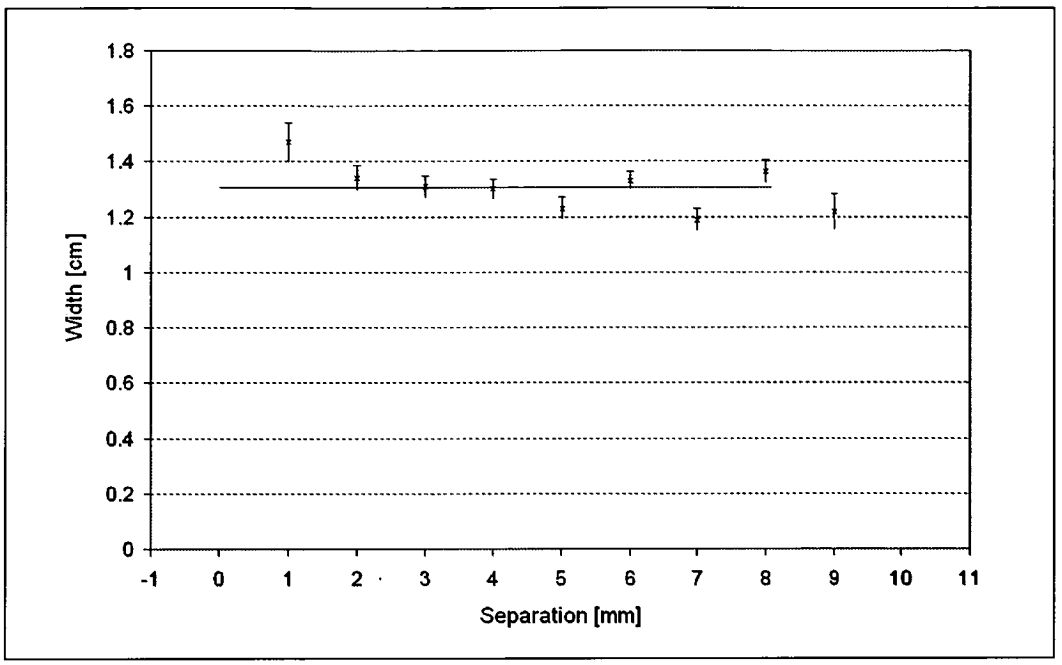

Figure 3.30: Flame width for flame spread across two elements with different separation. Note that the flame was not merged at 8mm separation. Error bars represent standard errors.

family. Tasmanian oak is a generic name given to tree types of Tasmanian *Eucalyptus* species: *Eucalyptus delegatensis, Eucalyptus obliqua and Eucalyptus regnans.*

The measured rate of spread was lowest for sapelli, as the pockets of liquid sap were pushed to the surface of the element ahead of the flame, slowing the flame spread or even extinguishing it. Liquid pockets of sap appearing in front of the flame were only visible on sapelli out of the elements used. The calorific value of the fuel used was measured (Appendix A), and the values obtained for Tasmanian oak were significantly different to sapelli, nogal and ramin, which showed no significant difference between each other. The sapelli calorific value had the highest standard error, most likely due to the uneven sap distribution within the samples used.

Values obtained for flame properties and mass loss rate are shown in Figure 4.22. All properties were tested using analysis of means in Min (2000), and the significant differences recorded are given in Table 3.4. Table 3.5 shows emissivity and temperate values for the fuel.

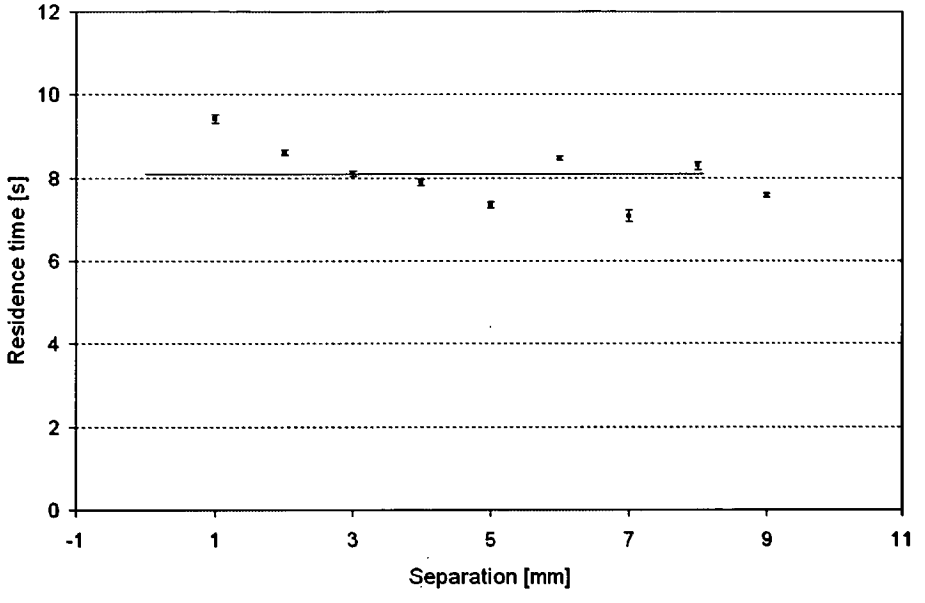

Figure 3.31: Residence time for flame spread across two elements versus separation between them. Note that the flame was not merged at 8mm separation. Error bars represent standard errors.

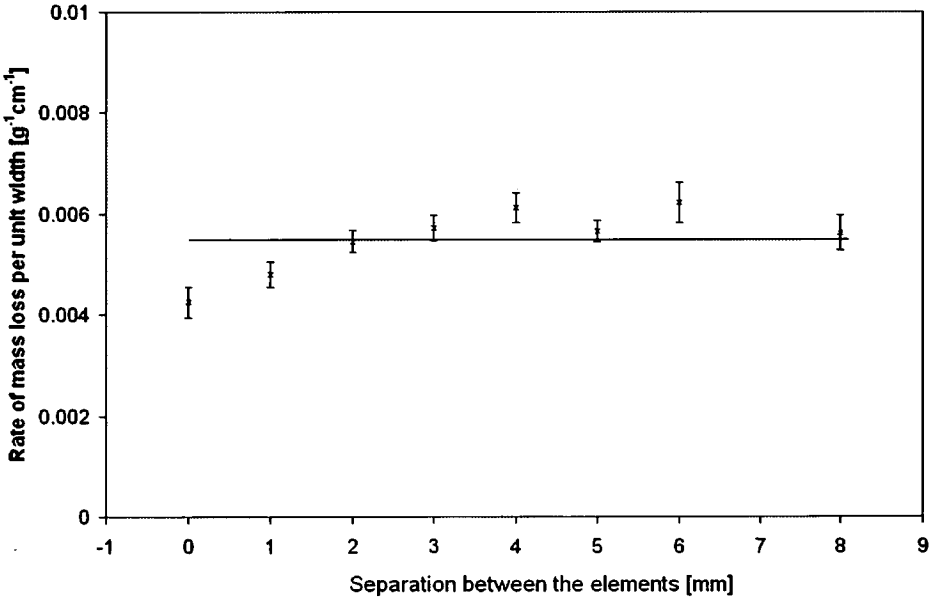

Figure 3.32: Rate of mass loss per flame width over two element versus separation between elements. Error bars represent combinatiion of standard errors for measurements of mass loss and width.

Table 3.3: Applying flame merging conditions to the data shows that indeed the critical separation between the element separation and flames remaining merged where $\frac{H}{D} = 9\sqrt{\frac{S^3}{DW^2}}$ is between 7 and 8 mm.

Separation [mm]	H/D	$9\sqrt{\frac{S^3}{DW^2}}$	$\frac{H/D}{9\sqrt{\frac{S^3}{DW^2}}}$
0	11.8	0.0	–
1	13.6	0.4	31.5
2	15.5	1.3	12.4
3	16.2	2.3	6.98
4	16.6	3.8	4.40
5	16.7	4.9	3.41
6	14.8	7.2	2.06
7	14.7	7.9	1.87
8	10.4	10.8	0.96

Table 3.4: Significant difference in measured flame properties between four different wood types was tested using one-way ANOVA. Pairs were significant difference was detected for a given properties are marked with an appropriate symbol.

	Oak	Sapelli	Ramin	Nogal
Oak	×	h, h_c	$\dot{m}, R, h_c$	$\dot{m}, w, R, h_c$
Sapelli	×	×	h, t_r, R	h, w, R, η
Ramin	×	×	×	w, t_r, η
Nogal	×	×	×	×

$\dot{m}$– rate of mass loss, h – flame height, t_r– reaction time, w – width, R – rate of spread, η– efficiency, h_c– heat of combustion

3.5 CONCLUSION

The thickness of the fuel affected the rate of spread significantly. It is expected from the lumped capacitance model that the rate of spread for thermally thin fuels ($\lesssim 1.5\ mm$) be inversely proportional to the fuel thickness, but it becomes less dependent on thickness becoming approximately constant for until the continuous spread is no longer possible. On Tasmanian oak and nogal fuel, it was shown that with the fuel thickness in the range of $2\ mm - 8\ mm$, the rate of spread is proportional to $D^{-0.64}$ where self-sustained flame spread was no longer possible for the thicker fuels. The residence time increased with the diameter, and it was shown that for the fuel used (diameter of $2 - 8mm$), residence time could be modelled linearly. The width and the height of the flame changed

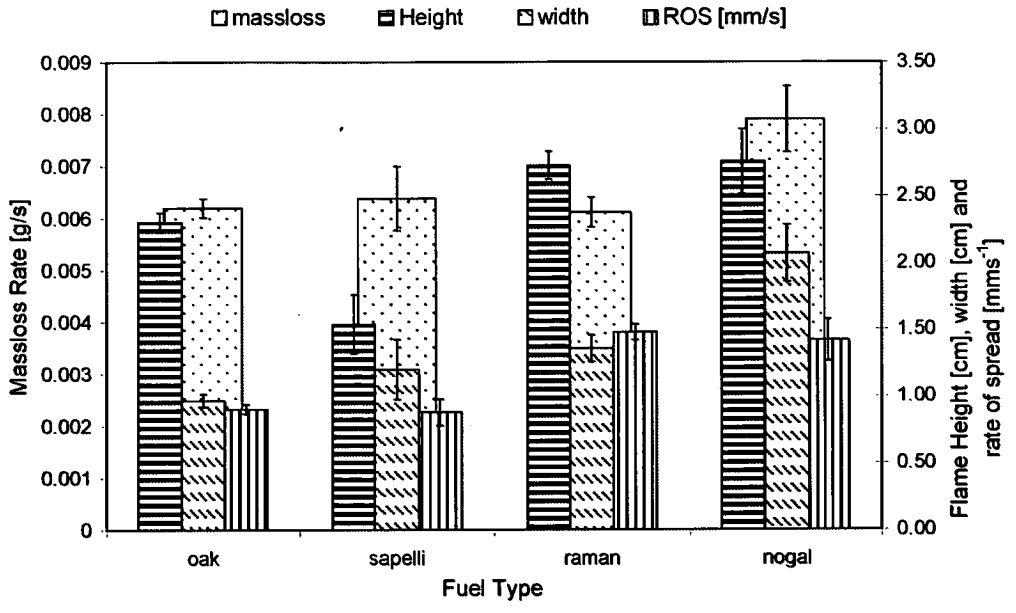

Figure 3.33: Flame height and mass loss rate for different type 4 mm diameter fuel. Error bars represent standard error in averaging samples.

parabolically with increase of the fuel thickness, whereas the mass loss per unit volume and the efficiency of the combustion decreased exponentially.

Increasing the fuel moisture content slowed the rate of spread, whilst the residence time remained unaffected. Thus flame width reduced at the same rate as the flame spread, as did the rate of mass loss and the flame height. The efficiency of combustion for the elements used was nearly at 100%.

Changing the orientation of the fuel affected the rate of spread and was well described following Weber & De Mestre's (1990) model of cyclic relation to the horizontal spread with -0.8 coefficient. Other authors ((Hirano et al. 1974)) noted that for thin fuel the downward rate of spread was nearly constant for angles $-90°$ to $-30°$, then increasing nearly three times for the horizontal fuel, and up to 50 fold increase from vertically downwards to vertically upwards spread. However for fuel of intermediate thickness (4 mm) used here, the downwards rate of spread was nearly constant for $-90°$ to $-45°$ range. A two fold increase in the rate of spread was observed for fuel orientations from $-45°$ to the horizontal, and all over only ten fold increase from $-75°$ to $+75°$ angle of incline.

Table 3.5: Some wood and flame properties measured for 4mm diameter cylinders of Tasmanian oak, sapelli, ramin and nogal. The results were given with two standard errors.

	calorific value $[J/K]$	emissivity	temperature $[K]$	density $[kg/m^3]$
Oak	$19,200 \pm 180$	0.0145 ± 0.0008	$1,220 \pm 40$	636 ± 20
Sapelli	$20,600 \pm 910$	0.0193 ± 0.0014	$1,050 \pm 36$	598 ± 28
Ramin	$20,100 \pm 190$	0.0187 ± 0.0010	$1,090 \pm 56$	510 ± 50
Nogal	$20,400 \pm 180$	0.0214 ± 0.0016	$1,100 \pm 46$	578 ± 15

Flame height and width could be modelled in similar fashion however it was inconclusive whether the efficiency, the rate of mass loss per unit length and residence time changed due to the fuel orientation.

Separating elements provides more buoyancy to the flame gasses, creating a higher flame, with maximum height obtained at the midpoint between the joined elements and separation where the flame is no longer merged. However increased flame height had no affect on the rate of flame spread indicating that for flames of this size the radiation has very little affect on the rate of spread. This could also be due to the fact that the elements were dry prior to the burn.

Chapter 4

EMISSIVITY OF SMALL FLAMES

4.1 INTRODUCTION

The thermal radiation of the luminous flames is an important factor in the physical modeling of fire spread and ignition. One of the basic parameters in the radiative heat transfer equations is emissivity of the flame. In an incomplete combustion of materials that contain hydrocarbons, solid carbon-bearing particles are formed in flames. These are called soot particles and in a flame they act as mini black-body or gray-body emitters. The presence of soot particles in flame is characterized by yellow luminous colour of the flame. An increase of soot in a flame is associated with an increase in the rate of radiation transfer from the flame to the surroundings.

The emissivity of a material is defined later in section 4.2.1, but it is essentially the ratio of energy radiated by the material to energy radiated by a black body at the same temperature.

A flame is a hot gas of indeterminate surface area, rather then a uniform emitting surface. It therefore does not have a fixed temperature and emissivity. What we have done in this chapter is to measure a mean effective emissivity based on a heat flux and temperature measurements.

A wide range of flame emissivity values appear in literature; however, very little has been reported on the emissivity of wood fires. In modelling heat transfer Anderson (1969) estimates that, for pine wood, flame emissivity would vary between 0.16 and 0.28 for flames of diameter between 6.4 *cm* and 50 *cm*, whereas Muraszew (1974) uses value of 0.23 as an average flame emissivity of flames thinner than a centimeter. Telisin (1974) on the other hand found that for flame thickness of 0.3 to 2.5 *m*, flame zone emissivity ranges from 0.11 to 0.3. His estimate of total emissivity is

$$\varepsilon = 1 - e^{-0.16(L+0.375)},$$

where factor 0.375 is due to glowing embers and $\varepsilon = 1 - e^{-0.16L}$ is emissivity due to the flame only. This equation estimates emissivity of flame, for the fuel bed of 0.3 to 2.5 meters to range between 0.047 and 0.33. Anderson's (1969) measurements show that fuel moisture content decreases emissivity values only for values higher than 16% and Telisin (1974) estimates that increase of fuel moisture content from 12 to 34% increases attenuation factor from 0.15 to 0.17.

It is considered that for small luminous flames the concentration and the size of the soot particles affect the value of emissivity. Theoretical models for the dependence of emissivity on the size and concentration of the soot particles are based on Mie's (1908) theory on particle attenuation and were developed by several authors (e.g. Siddall & McGrath (1963) , Felske & Tien (1973), Lowes & Newall (1971) and Kunitomo (1974)). The first part of this chapter defines emissivity and describes theoretical models used for its determination.

This study concentrates on fire ignition where the ignition source is thin cylindrical wood. It is then necessary to investigate emissivity of thin flames. In estimating emissivity most of the work reported in the literature investigates flames from gas and oil burners. Interest in this work is in emissivity values for wooden fuel, and how it varies with packing, fuel loading and flame thickness. The second part of the chapter describes the experimental method and the results obtained for the experiments performed. To investigate how fuels of different diameters affect emissivity, Tasmanian oak (*Eucalyptus* species) and nogal cylinders (*Juglandaceae* species) of less than 1 *cm* diameters were used. Here the pathlength of the radiation is not significantly different for the range of diameters used; however, differences in the emissivity were detected. To investigate the effect of pathlength on the resultant emissivity, sheets of pine

(*Pinus Radiata*) and balsa *(Ochroma pyramidale)* wood were burned. This resulted in flames that were less than 10 mm in flame depth. The emissivity of larger flames, up to 1 m, from pine needles (*Pinus Radiata*) was also measured. Another aspect of small flames that was investigated is related to the separation between elements in the fuel bed. A number of white birchwood cylinders (of the *Betulaceae* family) with varied separation between them were burned. In the previous chapter it was noticed that for horizontal elements with varied separation the flame height is parabolically related to separation. The flame height is minimum when there is no separation between the elements and at the critical separation when the flames are just merged. The maximum flame height is obtained at the mid-point of these two separations. In this chapter emissivity versus separation between the elements is measured.

4.2 THEORETICAL BACKGROUND

4.2.1 Spectral Radiance of Flame

Every object with temperature above absolute zero emits energy. The spectral radiance of a perfect emitter or black body emitted per unit area for a packet of wavelengths between λ and $\lambda + d\lambda$ is described by Plank's radiation law:

$$I_{\lambda,T} = \frac{2\pi c^2 h \lambda^{-5}}{e^{\left(\frac{hc}{\lambda kT}\right)} - 1}, \tag{4.1}$$

where c is the speed of light ($3 \times 10^8 ms^{-1}$), h is Planck's constant ($6.63 \times 10^{-34} Js$), k is Boltzmann's constant ($1.38 \times 10^{-23} JK^{-1}$) and T is the temperature of the object. The total radiance emitted by a black body of temperature T is then

$$I = \int I_{\lambda,T}\, d\lambda = \frac{2\pi^5 k^4}{15c^2h^3} T^4.$$

The constant $\frac{2\pi^5 k^4}{15c^2h^3}$ is represented as σ ($5.67 \times 10^{-8} Wm^{-2}K^4$), from the relation of total radiation emitted by a black body derived semi-empirically by Stefan and Boltzmann, so that

$$I = \sigma T^4.$$

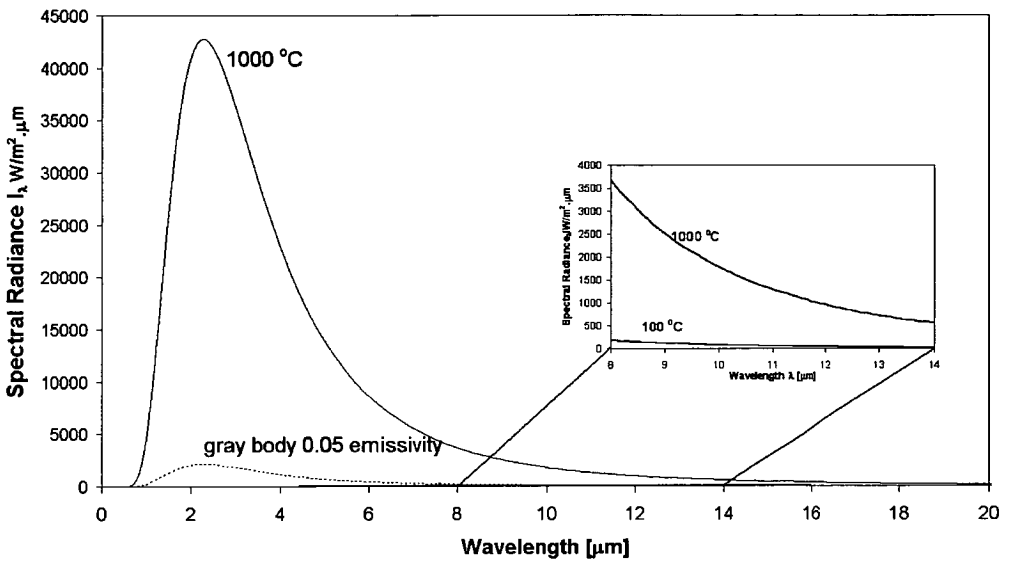

Figure 4.1: Black body radiance as a function of temperature and wavelength, for black body of 1000°C, and a gray body with the same temperature and emissivity of 0.05. Diagram on the right shows black body function for 100°C and 1000°C black body in the spectra detectable by *3M Scotchtrack Infrared Heat tracer IR-1600.*

Most objects are not perfect emitters and their spectral radiance is described by

$$I = \varepsilon_\lambda I_{\lambda,T},$$

where ε_λ is the monochromatic emissivity of the object. Emissivity is dependent on wavelength and is defined as

$$\varepsilon_\lambda = \frac{I}{I_{\lambda,T}}.$$

In practice, it is convenient to approximate the emissivity ε with a factor that is independent of the wavelength. Total radiation of an object can then be described by the Stefan-Boltzmann equation

$$I = \int_0^\infty \varepsilon_\lambda I_{\lambda,T}\, d\lambda = \varepsilon\sigma T^4,$$

and such object is called a gray body.

Figure 4.1 shows the spectral radiance of a black body at 1000°C temperature, and a gray body with the same temperature but emissivity 0.05.

In wood fires, carbon based particles of $10 - 100nm$size, called soot particles, are created (Drysdale 2002). Soot particles are heated in the flame and act as small black or gray body emitters. The spectrum of a cloud of soot particles is thus continuous. The presence of soot in a flame is characterized by a yellow luminous flame.

Due to the small size of soot particles in flames, the flame above wooden fuel is thus often described as a gray body. It was shown, however, that the flame spectrum above crib fires contains peaks imposed on the gray body radiation curve that correspond to emissions due to $H_2O$and CO_2(Hagglund & Persson 1976). Sato et al. (1969) showed that the radiation spectrum from the flame of a liquid fuel is continuous due to the high emissivity of soot particle with superimposed gas band spectrum. Felske & Tien (1973) provided a theoretical determination of flame emissivity considering both continuous spectrum and band spectrum of water vapour and carbon dioxide.

It was found that the monochromatic emissivity of soot particles is of the form

$$\varepsilon_\lambda = 1 - e^{-k_\lambda L}, \tag{4.2}$$

where L is pathlength and k_λ is a spectral absorption coefficient that is proportional to the 'soot volume fraction', the fraction of the flame volume occupied by soot particles.

Empirical derivations of k_λ have been published by many authors. Hottel & Broughon (1932), Rößler & Behrens (1950), Pepperhoff (1951) and Siddall & McGrath (1963) reported the relation $k_\lambda \propto \lambda^{-\alpha}$, in which the perimeter in the exponent is in the interval $0.65 \lesssim \alpha \lesssim 1.95$. The variations in the value of α are thought to be independent of the flame thickness but depend on the type of fuel from which the soot is formed (Rößler & Behrens 1950). Different values were obtained for the same fuel in the visible and infrared spectrum (Hottel 1954). Pepperhoff (1951) indicates that the difference in the diameter size of soot particles accounts for some variations in α, although Siddall & McGrath (1963) found no such correlation for same size distribution and particle size of several gas fuels.

Theoretical prediction of k_λ was undertaken by Hawksely (1952) who, based on Mie's (1908) theory on particle attenuation, showed that the spectral extinction

of radiation by an absorbing sphere is given by

$$k_\lambda = \frac{36\pi}{\lambda} f_v \frac{n^2\kappa}{\left[n^2\left(1-\kappa^2\right)+2\right]^2 + 4n^4\kappa^2} \tag{4.3}$$

where f_v is the volume fraction of the particles, and n and κ are particle optical constants dependent on the wavelength of the radiation, provided $\pi x/\lambda << 1$ where x is the particle diameter. Several authors have estimated theoretical value of emissivity based on this equation (e.g. Felske & Tien (1973), Siddall & McGrath (1963) and Lowes & Newall (1971)).

In this experiment, the spectral response range of the instrument used $(8 - 12\mu m)$ is outside the peak emissions of H_2O and CO_2. The radiance measured was thus considered to represent gray body radiation due to the soot particles. Nevertheless, gray body emission of the flame was approximated for modelling purposes in later chapters.

4.2.2 Theoretical Calculation of Soot Emissivity

Accurate theoretical estimates of soot emissivity depend on the adequate knowledge of the soot optical constants and soot volume fractions in the flames used. Those measurements were not possible in the scope of this work; however, theoretical calculation of emissivity was performed here for comparison purposes with the experimental results that were derived. This work is following calculations performed by other authors (e.g. Felske & Tien (1973), Siddall & McGrath (1963) and Lowes & Newall (1971)), although the emphasis of the present work is focused on thin flames. Hence calculations on pathlength smaller than 5 cm are performed, which have not been reported by the above authors.

The total emissivity of a flame is calculated from

$$\varepsilon = \frac{1}{\sigma T^4} \int_0^\infty I_{\lambda,T}\varepsilon_\lambda d\lambda, \tag{4.4}$$

where $I_{\lambda,T}$ is the radiative energy per area obtained from Plank's radiation law (Equation (4.1)) and ε_λ is the monochromatic emissivity. Felske & Tien (1973) calculated emissivity of a luminous flame considering soot and gas emissions,

in which the monochromatic emissivity was taken to be

$$\varepsilon_\lambda = 1 - e^{k_s L_s + k_w L_w + k_c L_c} \tag{4.5}$$

and kL terms are products of the spectral absorption coefficient and mass pathlength of soot, water vapours and carbon, respectively, and k_s is described by equation (4.3). The emissivity due to soot only is calculated using the monochromatic emissivity in the form

$$\varepsilon_\lambda = 1 - e^{k_s L_s}. \tag{4.6}$$

The interval in the equation (4.4) requires numerical evaluation, when the emissivity (4.6) is assumed; however, Felske & Tien (1973) state that approximating k_s with Hottel's (1954) observation of $\frac{c}{\lambda}$ in the infrared allows the emissivity due to soot to be calculated in the analytical form

$$\varepsilon_s = 1 - \frac{15}{\pi^4}\psi^{(3)}\left(1 + \frac{cLT}{C_2}\right). \tag{4.7}$$

In this equation (4.7), the symbol c is a constant proportional to soot concentration, L is the pathlength, T is the flame temperature and C_2 is the second Plank's constant $\left(\frac{hc}{k} = 0.014388 Km\right)$. The function $\psi^{(3)}$ is called the pentagamma function, and it is defined to be the third derivative of the logarithm of the gamma function Γ :

$$\psi^{(3)}(z) = \frac{d^3}{dz^3}\ln\left(\Gamma(z)\right), \tag{4.8}$$

in which the gamma function Γ is the extension of the factorial function

$$\Gamma(z) = \int_0^\infty t^{z-1}e^{-t}dt \tag{4.9}$$

defined in (Abramowitz & Stegun 1972), for example. This equation, however, requires experimental determination of the constant c.

Describing k_s by means of equation (4.3) requires optical constants n and κ to be known. Dispersion equations for n and κ are:

$$n^2 - n^2\kappa^2 = 1 + \frac{e^2}{m\epsilon_0}\sum_j \frac{n_j\left(\omega_{0j}^2 - \omega^2\right)}{\left(\omega_{0j}^2 - \omega^2\right)^2 + \omega^2 g_j^2} - \frac{e^2}{m\epsilon_0}\frac{n_c}{\omega^2 + g_c^2} \tag{4.10}$$

$$2n^2\kappa = \frac{e^2}{m\epsilon_0}\sum_j \frac{n_j\omega g_j}{\left(\omega_{0j}^2 - \omega^2\right)^2 + \omega^2 g_j^2} + \frac{e^2}{m\epsilon_0}\frac{n_c g_c}{\omega\left(g_c^2 + \omega^2\right)}, \tag{4.11}$$

where ω is the angular frequency of the incident radiation, e and m are the charge and mass of an electron, ϵ_0 is the electric inductive capacity in a vacuum, n_c is the number of conduction electrons per unit volume, g_c is the damping constant for conduction electrons and n_j, ω_{0j} and g_j are number of bound electrons per unit volume, natural frequency and damping constant of electrons in j^{th} state. This model (4.10) and (4.11) is taken from (Stull & Plass 1960).

From the experimental data on amorphous carbon found at room temperature Stull & Plass (1960) extrapolated the dispersion equation for the optical constant at flame temperature to be:

$$\begin{aligned} n^2 - n^2\kappa^2 &= 1 + \frac{6.448\times10^{32}}{4.062\times10^{35}-\omega^2} + \frac{3.224\times10^{32}}{9.549\times10^{33}-\omega^2} + \frac{3.224\times10^{32}}{5.217\times10^{33}-\omega^2} \\ &\quad + \frac{6.348\times10^{32}\left(1.966\times10^{32}-\omega^2\right)}{(1.956\times10^{32}-\omega^2)^2+1.369\times10^{33}\omega^2} - \frac{3.05\times10^{31}}{2.323\times10^{31}+\omega^2} \qquad (4.12) \\ 2n^2\kappa &= \frac{6.347\times10^{32}\times3.70\times10^{16}\omega}{(1.956\times10^{32}-\omega^2)^2+1.369\times10^{33}\omega^2} + \frac{3.05\times10^{31}\times4.82\times10^{15}}{(2.323\times10^{31}+\omega^2)\omega}, \qquad (4.13) \end{aligned}$$

where ω is again the angular frequency of the incident radiation. These constants are used here for the theoretical estimate of the soot particles' emissivity. It must be noted that there is a difference in optical properties between amorphous carbon and different soot particles, partly due to the differences in their crystal structure and mostly due to the variations in hydrogen to carbon ratio (Dalzell & Sarofim 1969).

Re-writing equations (4.12) and (4.13) as

$$n^2 - n^2\kappa^2 = f(\omega) \qquad (4.14)$$

$$2n^2\kappa = g(\omega), \qquad (4.15)$$

the spectral absorption coefficient k_s from equation (4.3) is calculated to be:

$$k_\lambda = \frac{36\pi}{\lambda} f_v \frac{g(\omega)}{2\left[f(\omega)+2\right]^2 + 2g(\omega)^2}. \qquad (4.16)$$

Based on these constants, the monochromatic emissivity of the flame is found using equation (4.6). Its dependence on wavelength for a temperature of $1300°K$ is displayed in Figure 4.2. The dependence of $I_\lambda\epsilon_\lambda$ on wavelength at the same temperature is shown in Figure 4.3. This curve is integrated according to the equation (4.4). Numerical integration was performed using the

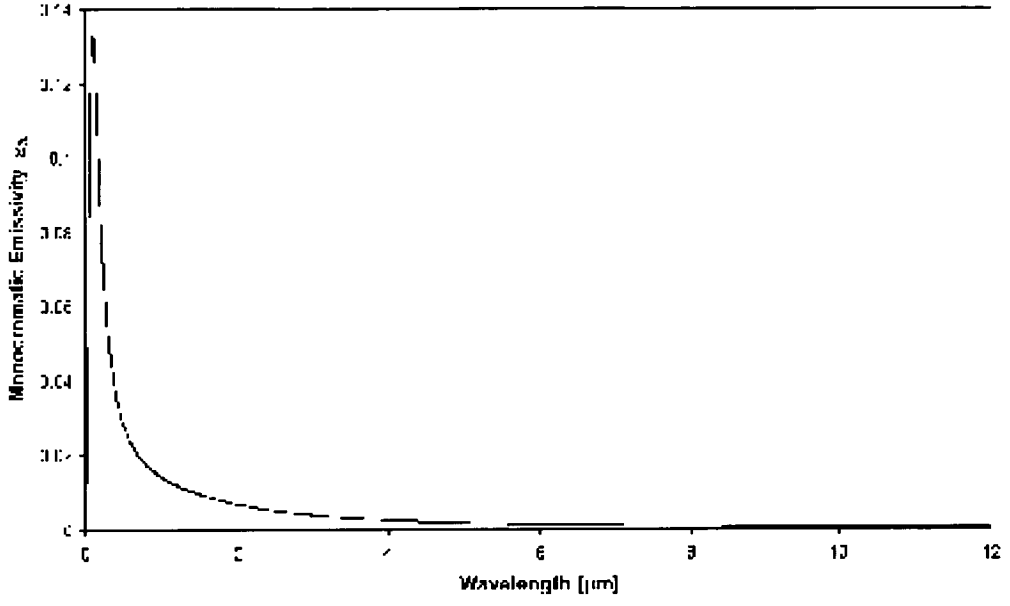

Figure 4.2: Monochromatic emissivity versus wavelength calculated for $5cm$ pathlength and soot volume fraction of 5×10^{-8} at temperature of 1300°K

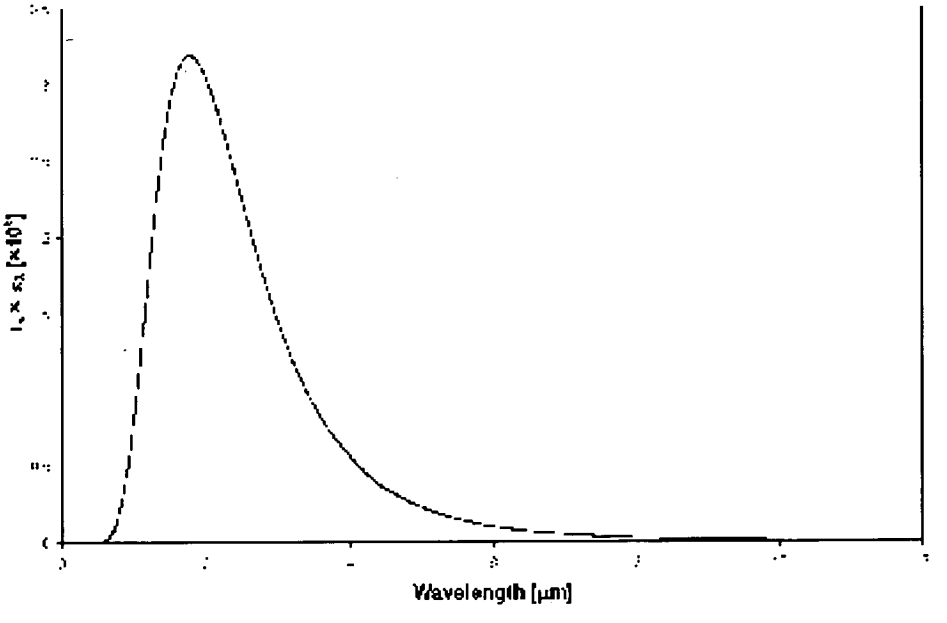

Figure 4.3: $I_\lambda \varepsilon_\lambda$ versus wavelength calculated for pathlength of 5 cm and soot volume fraction of 5×10^{-8} at temperature of 1300°K

trapezoidal rule. Considering that the temperature peak $I_\lambda \varepsilon_\lambda$ is between 1 and 10 μm, numerical integration was performed between 0.1 and 100 μm, with the integral partitioned in 10,000 sections.

The volume fraction of soot in the flame has been measured by many authors (e.g. Choi et al. (1994, 1995), Kennedy et al. (1996), Santoro et al. (1987), Dalzell & Sarofim (1969)). However, very few measurements were performed for wooden fuel, with the exception of Hueglin et al. (1997), Stith et al. (1981), De Vries & Breejen (1993). Stith et al. (1981) and De Vries & Breejen (1993) report soot number concentrations of 8.7×10^7 and $1.3 \times 10^6 cm^{-3}$ respectively for mean particle diameters of 0.12 and 0.53 μm. Hueglin et al. (1997) measured soot volume fractions of wood log fires to be 4.4×10^7 in start up, 7.8×10^6 in intermediate and 1.5×10^7 in burnout stage. They also found that the particles size is the highest at the start-up stage ($0.26 \mu m$), but reduces in intermediate and burnout stages (0.19 and 0.05 μm respectively). The soot concentration is found from $\frac{N \pi D^3}{6}$, and thus the soot volume fractions reported here are between 10^{-15} and 10^{-12}. However Muraszew (1974) estimates the soot volume fraction to be of the order of 10^{-5}. Dalzell & Sarofim (1969) measured the soot volume fraction to be of order of 10^{-8} while Santoro et al. (1987) and Choi et al. (1994) published values of 10^7. There is a great diversity in the numbers reported, as the type of fuel and efficiency of combustion would determine the size and concentration of soot in flame.

A range of emissivity values was calculated for soot volume fraction of 10^{-6}, 10^{-7} and 10^{-8}. These are plotted in Figure 4.4 for pathlength of up to 1 m. In Figure 4.5 emissivity was calculated for pathlength up to 10 cm for a range of soot volume fractions, where the emissivity values respond to the values obtained in the experiments outlines in the next section.

The dependence of the soot absorption coefficient on wavelength from theoretical predictions for soot volume fraction of 5×10^{-8}, and soot optical constants given by equations (4.12) and (4.13) is shown in Figure 4.6. Dotted lines represent relations $k_s = c\lambda^{-\alpha}$, which is an empirical estimate of spectral absorption coefficient reported by several authors (see Section 4.2.1). Figure 4.6 shows that for the wavelength range 0.1 to 4 μm, k_s can be estimated with $k_s \propto \lambda^{-1.1}$, but for the range of $4 - 100 \mu m$, a value $\alpha \approx 1.95$ is more appropriate. For both of the wavelength ranges proportionality constant c is different. However according to Figure 4.3 most of the radiance is detected for the range of 0.1 to

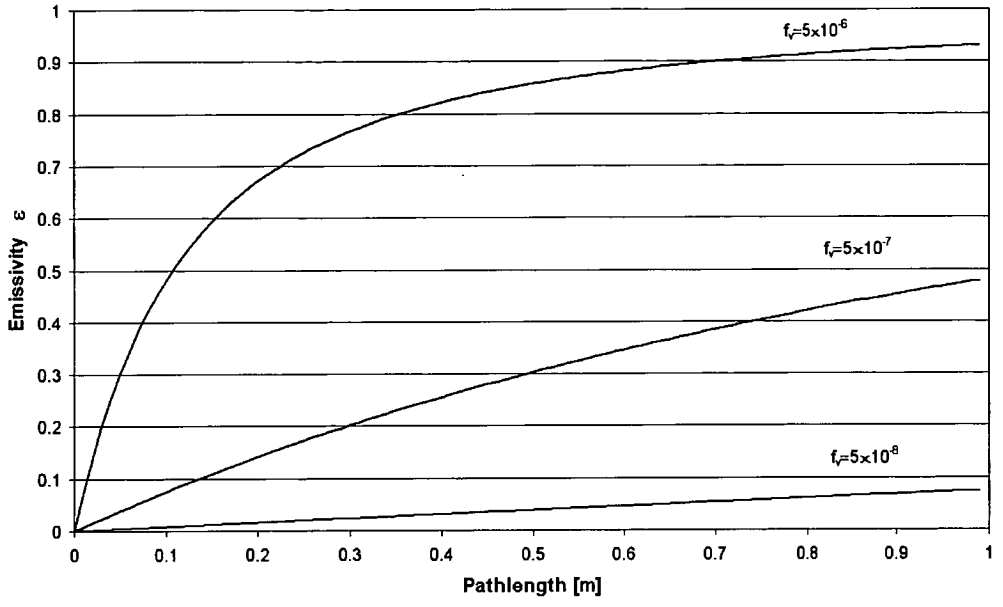

Figure 4.4: Emissivity versus path length for different soot volume fractions.

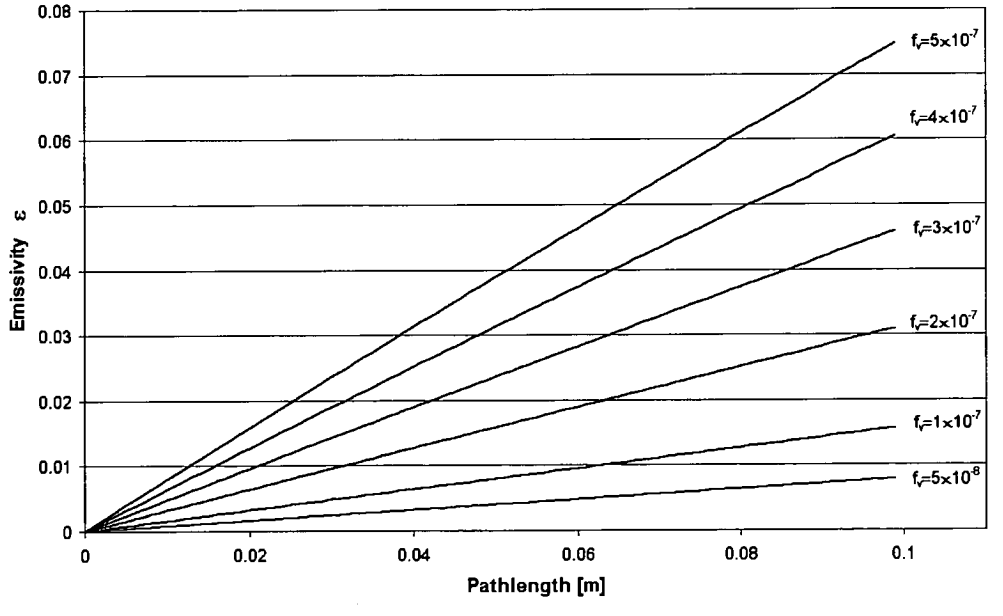

Figure 4.5: Emissivity versus pathlength for flames under 10 cm

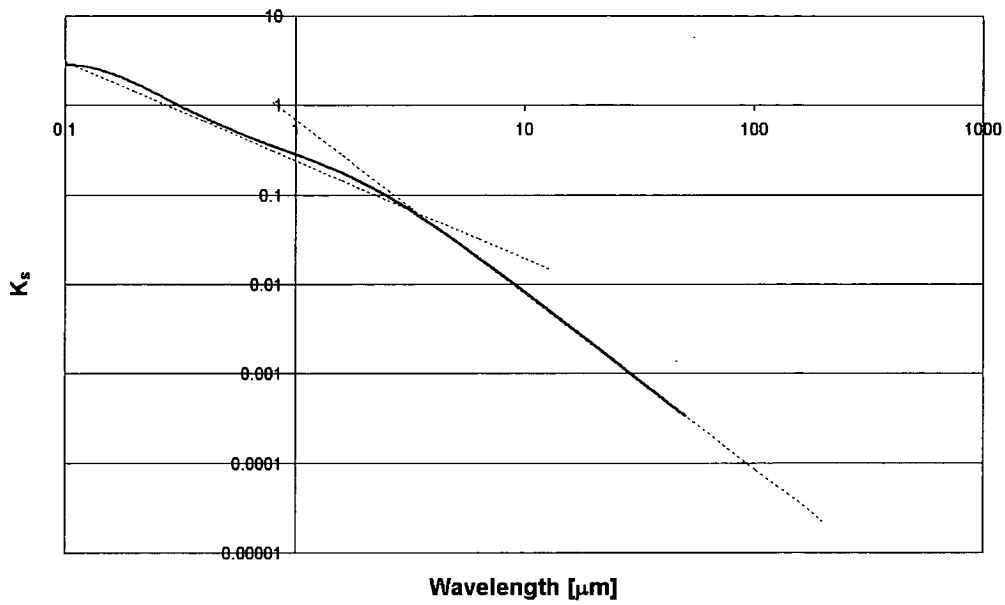

Figure 4.6: Soot spectral absorption coefficient versus wavelength for soot volume fraction of 5×10^{-8}. Dotted lines represent relations $k_s \propto \frac{1}{\lambda^\alpha}$. Line in the range 0.1 to 4 μm is fitted to $\alpha = 1.1$ and 4 to 100 μm to $\alpha = 1.95$.

4 μm, hence the analytical solution in equation (4.7) might be considered as an adequate approximation to the soot emissivity if constant c is known.

4.3 METHOD

In measuring emissivity many authors avoid measuring temperature. Schmidt (1909) suggested a method where flame radiance is measured against a cold and a hot background. Then using the radiance of the background and the readings of the flame in front the hot and cold background, the emissivity of the flame can be estimated without measuring flame temperature. Hottel & Broughon (1932) proposed measuring radiance through two colour filters and Kurlbaum (1902) adjusted the background radiation intensity so that the instrument reading of the background is independent of flame observations. Choi et al. (1994) used a 'three-wavelength technique' where, by measuring radiation intensity at two wavelengths and using theoretical model for intensity attenuation, temperature and soot volume fraction can be evaluated. Block

et al. (1998) suggest a theoretical model for determining flame temperature based on its luminosity in a time-resolved way and back-calculating emissivity. Brahmi et al. (1999) determine emissivity of flames in microgravity by comparing radiance in the infrared region to thermocouple readings. However to avoid intrusion of thermocouples into flames, temperature measurements were obtained from vertical array of thermocouples placed far downstream of the leading edge, treating the flame as a solid surface.

In the experiments performed here however, the temperature of the flame was measured using fine thermocouples and the emissivity is estimated from the radiance measurements (see section 4.3.4).

4.3.1 Fuel types

Several effects of fuel on emissivity were investigated in this set of experiments. Emissivity versus fuel diameter for flames thinner than 1 cm was modelled for Tasmanian oak and nogal. Diameters used were $4, 6, 8$ and 9.5 mm for Tasmanian oak and $2, 3, 4, 5, 6$, and 8 mm for nogal. Elements were approximately 8 cm in length, oven dried over night at temperature of $110°C$. Prior to use they were placed in a desiccator to achieve room temperature.

The difference in emissivity, all samples having the same size and geometry, was estimated for four types of wood: oak, nogal, sapelli and ramin. Dimensions were 4 mm in diameter, 8 cm in length and the fuel was oven dried.

The effect of sooth concentration and pathlength on emissivity was investigated using a number of birchwood cylinders. White birchwood oven dried toothpicks of 2 mm diameter were burned in a series of experiments in which the separation between the elements was varied.

The effect of the fuel bed thickness on resultant emissivity was studied using balsa, pine and pine needles from *Pinus radiata.*

An attempt was made to measure the effect of fuel moisture content on the emissivity. However it was not possible to distinguish whether the differences in the output were due to moisture or change in flame height of the element (Section 4.5.5).

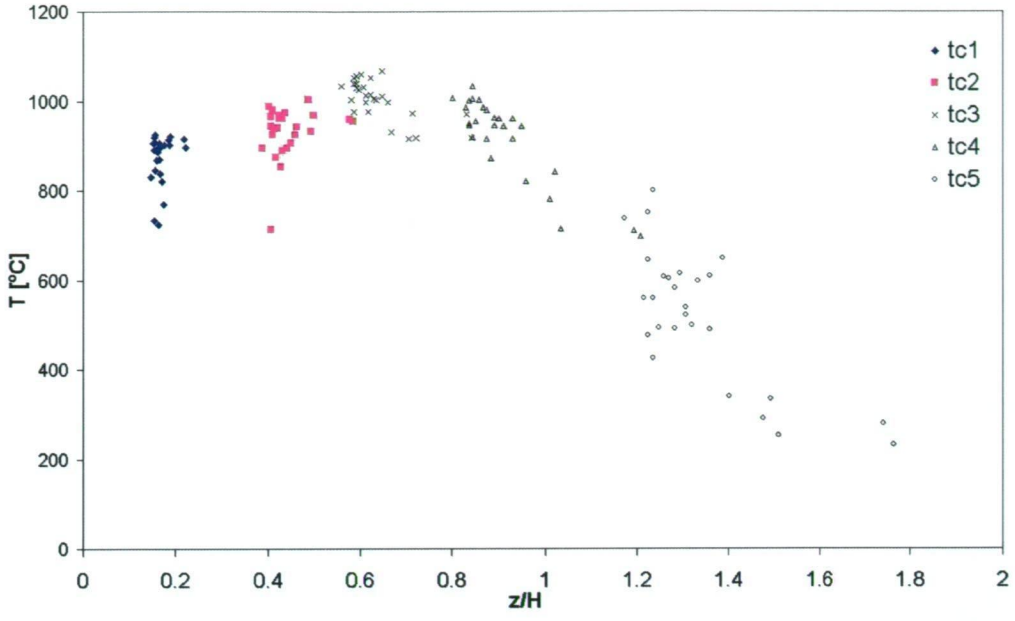

Figure 4.7: Flame temperature versus height above the element for 6 mm Tasmanian oak horizontal cylinder. Temperature is plotted against $\frac{z}{H}$, where z is the vertical height from the bottom of the element and H is the flame height.

The emissivity of larger flames was measured for pine needles (*Pinus radiata*), in which fuel beds from width of 1 cm up to 1 m were used.

4.3.2 Temperature profile over height

In order to calculate emissivity in a spectral band it is necessary to know the temperature of the object. The temperature of the flame was measured using a type K thermocouple of gauge 40 $A.G.W.$ (0.079 mm diameter) to minimize radiative effects.

Flame temperature profile above cylindrical elements of Tasmanian oak were measured for diameters $4, 6, 8$ and 10 mm. The profile of temperature versus height for a flame above 6 mm diameter oak cylinder is shown is Figure 4.7. These experiments have shown that the temperature is maximum in the middle of the flame, where the radiance was measured.

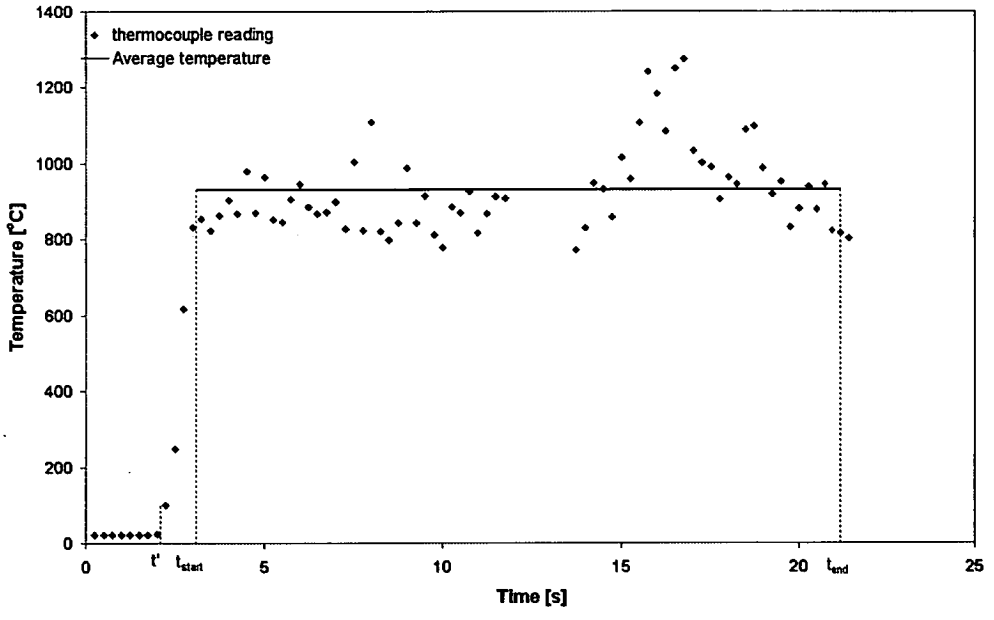

Figure 4.8: Flame temperature versus time at half height point for Tasmanian oak

4.3.3 Temperature

Emissivity was calculated based on the weighted mean flame temperature measured at the half height of the flame. Temperature was measured using type K thermocouple of $40AGW$ (0.079 mm diameter) at the half height of the flame. Output was recorded every $0.25s$.

A code written in IDL was employed to detect the beginning and the end of the temperature measurement time interval. An example of one of the measurements is shown in Figure 4.8. Time t' represents the time when the thermocouple was inserted in the flame, t_{start} represents the time when the thermocouple reached flame temperature and time t_{end} is the end of the burning. Although the use of variable t_{end} is not evident in the measurement shown in Figure 4.8, occasionally the data logger was switched off shortly after the thermocouple was removed from the flame. Variable t_{end} thus allowed for marking the correct end of temperature measurement time interval. The code fitted the data to a trapezoidal function where temperatures T_{start} and T_{flame}, and t', t_{start} and t_{end} are variables. For $t < t'$, output is fitted to $T = T_{start}$,

and for $t_{start} < t < t_{end}$, to $T = T_{flame}$.

Data recorded between the times t_{start} and t_{end} where then used to find the average temperature reading and its standard error. The squared inverse of the standard error (w_i) was used find the weights for different temperature measurement runs. Weights were normalized and the weighted average for N temperature runs was found using

$$\overline{T} = \sum_{i=1}^{N} w_i' T_i, \tag{4.17}$$

where w_i' are normalized weights

$$w_i' = \frac{w_i}{\sum_{i=1}^{N} w_i}. \tag{4.18}$$

Half-height temperature was measured this way for Tasmanian oak, nogal, sapelli and ramin, burning horizontal 4 mm diameter cylinders. For white birchwood fuel, 2 mm diameter toothpicks were used. To measure temperature of flame above pine and balsa, horizontal elements were burned with cross-sections of 3.5 mm × 3.5 mm and 3 mm × 3 mm respectively. A summary of the results obtained are given in Table 4.1.

Table 4.1: Summary of the average half height flame temperature measured

	$\overline{T}$ [°C]	σ_ε	N	95% CI
Tasmanian oak	955	24	20	[907,1003]
nogal	963	21	18	[921,1005]
ramin	911	21	21	[869, 953]
sapelli	875	20	21	[835, 915]
pine	1010	13	10	[984,1036]
balsa	976	7	13	[962, 990]
birchwood	922	24	30	[874, 970]
pine needles	892	25	10	[867, 949]

4.3.4 Radiance Measurements

Measurements of the flame radiance were performed using a *3M Scotchtrack Infrared Heat Tracer IR-1600* radiometer. This instrument has temperature range of $0 - 870°C$, field view of $(distance : diameter) = 30 : 1$, adjustable

emissivity factor and a laser guidance pointing in the direction of the measurement. The spectral response of the instrument is between 8 and 14 microns. Attenuation of the spectral energy due to atmospheric absorption of gases such as CO_2, O_2 and HO_2, is minimal in this spectral window. The output of the instrument is displayed in temperature units of the surface and is calculated based on the emissivity setting entered. During the experiment, the emissivity factor was set to 1.

The instrument was calibrated against a black body, and the results of calibration are presented in section 4.4. All of the consequent readings were adjusted to adjust by the calibration factor given in equation (4.23).

The output of the instrument is temperature in degrees Celsius. To convert this to radiance, Plank's radiation law (equation (4.1)) was integrated between the limits of the instrument,

$$I_{(8-14)\mu} = \int_{8\mu}^{14\mu} I_{\lambda,T} d\lambda = \int_{8\mu}^{14\mu} \frac{2\pi c^2 h \lambda^{-5}}{e^{\left(\frac{hc}{\lambda kT}\right)} - 1} d\lambda. \tag{4.19}$$

Integration was performed using trapezoidal rule with 1000 partitions.

4.3.5 Experimental Setup

The following set up was used for most of the experiments. The laser guide of the instrument was pointed to the middle of the flame and the readings were recorded on a data logger every $0.25s$. The instrument measured the readings on the wall behind the fire before and after the burn. Measurements were taken for ten burns in each configuration.

Field of view

Fuel was placed 15 cm away from the instrument, except for the experiments were the fuel bed was 50cm or wider when the instrument was held further back for safety reasons. However for the fires of that size, the field view of the instrument was not an issue.

The field of view of the instrument is 30 : 1, although the minimum field of view guaranteed by the manufacturer is 2 cm. To ensure the field of view was

Figure 4.9: Experimental set-up

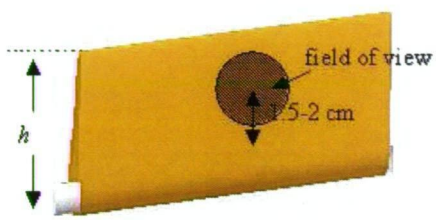

Figure 4.10: Field of view of the radiometer at distance of 15 cm is 20 mm. Center of the field of view was positioned so that no part of the fuel was in the field view while the field view is entrely filled with the flame.

less than 2 cm for the set up used, a 2.5 cm disc was placed 15 cm from the instrument. The flame above a burning 4 mm diameter stick of wood was extinguished, and the hot charred stick was moved in front of the disk. It was noted that the radiation detected from the wood was significant when it was in the middle of the disc, but no increase in the radiance was detected when it was at the edge of the disc.

Using the laser guiding of the radiometer, the center of the field view was approximately $1.5 - 2.0$ cm above the top of the fuel. This was done to ensure that the field of view of the instrument was entirely filled by the flame (Figure 4.10).

For the experiment in which the emissivity of fuel above a fuel bed of pine needles was measured, the radiometer was pointed to the middle of the flame, and the distance from the fuel bed increased with the increased fuel bed width. For example, when emissivity of a fuel bed of 1 cm was measured, radiometer was placed 15 cm away, although for fuel beds of widths: 25, 50, 75 and 100 cm, the radiometer was placed further away in order to protect the filter on the instrument. This should have no effect on the reading since the increase

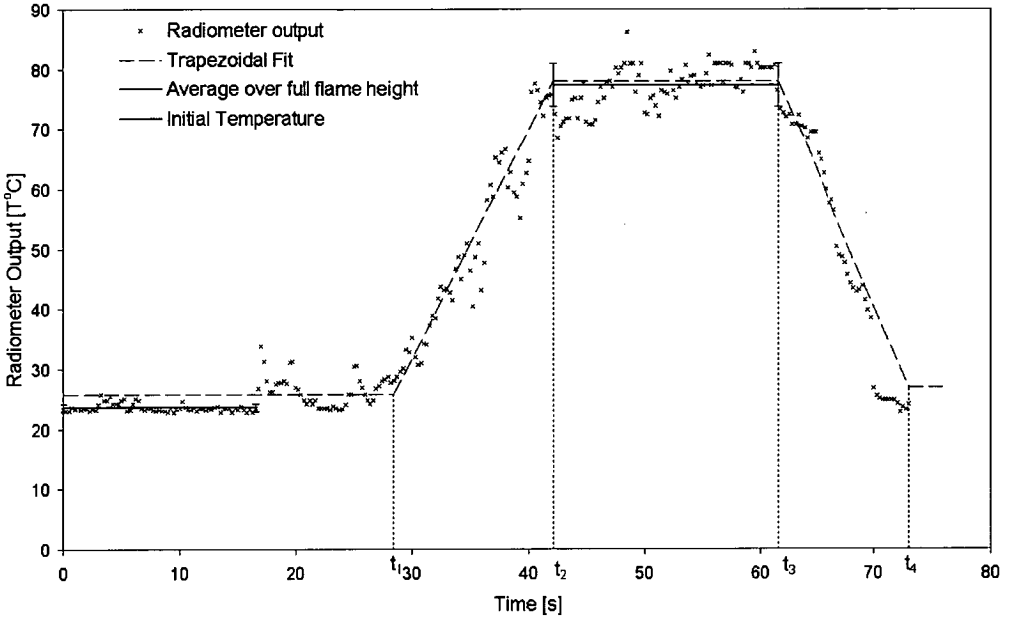

Figure 4.11: Output of radiometer measurements for flame above 4 mm diameter Tasmanian oak

in the flame height allowed for a larger field of view.

4.3.6 Emissivity readings

The radiometer was positioned in front of the flame and its output was logged every 0.25 seconds. Output of one burn is shown in Figure 4.11. Initial readings represent the wall behind the fuel, and the small increase in the output at 20 seconds is due to the ignition source. Readings between 40 and 70 seconds represent the flame radiance.

In order to extract the radiance due to the flame from the radiometer output, a program code was written to detect a trapezoid, where initial readings T_i, readings due to the flame T_e, and final readings T_f were parameters that describe the flat lines on the Figure 4.11, and four time parameters marking the vertices of the trapezoid are sought to fit to the original data. The trapezoidal fit obtained is compared to the radiometer output using χ^2 test, to test acceptability of the fit. The final outputs were T_i, T_i, T_f and T_1, T_2, T_3, T_4 (see Figure 4.11). The model output gave a series of predicted model temperatures

(T_e) which were than compared with measurements within a χ^2 framework. A χ^2 test calculated the χ^2 statistic:

$$\sum_{i=1}^{N} \frac{(\text{observed}_i\text{-expected}_i)^2}{\text{expected}_i},$$

and the probability of obtaining value of χ^2 or greater. For majority of the readings for laminar flames (experiments with Tasmanian oak, nogal, sapelli, ramin, white birchwood and experiments with smaller dimension of balsa and pine) probabilities greater than 0.9 were obtained. For turbulent flames (larger dimensions of pine and balsa, and experiments with pine needless) due to the variability of the flame readings, better fit was not achievable by adjusting the initial time variables. In such cases visual observation was employed to confirm accurate detection of the flame start and end.

There are two emissivity readings obtained this way. They are the horizontal line obtained from the trapezoidal fit T_e, and value obtained by averaging readings between the time parameters t_2 and t_3 (at 42.1 and 61.6 seconds in Figure 4.11). The average reading of the raw data was used for the emissivity calculation. Inverse squared of the standard error in the reading was used to find the weighting for the reading, according to the formula

$$w_i = \frac{1}{\sigma_i^2}.$$

Given a set of N observations, the weights were normalized using

$$w' = \frac{w_i}{\sum_{i=1}^{N} w_i}.$$

These weights were used in data analysis of the results.

For flames of emissivity less then 1, the flame transmissivity needs to be taken into account. Thus for each emissivity measurement, the radiance of the background was measured prior to a burn., The average value of the initial few seconds of readings were used as a measurement of the flame background. The background was measured after the flame extinguished to ensure that the background is not affected by the flame (Figure 4.11). This was also used to confirm that the heat of the flame did not affect the filter of the instrument.

4.3.7 Emissivity calculation

Consider now the radiation measured by the radiometer in the experiment (Figure 4.9). The temperature output is converted to radiance I as described in Section 4.3.4, and all radiances used here iwere between 8 and 14 microns.

When the flame is not between the radiometer and the wall, the measured radiation is that of the background, I_C. When a flame is in the field view of the radiometer, radiance detected is

$$I_{TOTAL} = I_F^* + I_{CF}, \tag{4.20}$$

where I_F^* is the flame radiation, and I_{CF} is the background radiation transmitted by the flame.

Approximating the flame to a gray body radiator, flame radiance can than be described using εI_F, where I_F is the radiance of a black body of the same temperature as the flame and ε is the flame emissivity.

Radiation from the wall 'seen' through the flame is τIc, where τ is flame transmissivity. It is reasonable to assume that the reflectivity of flames is zero. Thus it follows from Kirchhoff's law that $\tau = 1 - \varepsilon$.

Total radiance detected by the radiometer is then

$$I_{TOTAL} = \varepsilon I_F + (1 - \varepsilon) I_C, \tag{4.21}$$

and thus emissivity is calculated using

$$\varepsilon = \frac{I_{TOTAL} - I_C}{I_F - I_C}. \tag{4.22}$$

4.4 Calibration of the 3M Scotchtrack Infrared Heat Tracer IR-1600

To measure the emissivity of small flames, a 3M Scotchtrack Infrared Heat Tracer IR-1600 instrument was used. This instrument has temperature range of 0-870C, field view of distance : diameter = 30 : 1, adjustable emissivity factor and displays temperature of the surface. It also has laser tracking which allows more accurate positioning of the instrument for the required field of view. This instrument was used combined with a thermocouple, to estimate flame emissivity, as well as for measuring emissivity of the same size flames against different temperature background. Therefore it was necessary first to calibrate the radiometer.

In order to calibrate the instrument for temperatures ranging from 20° to 900°C a stainless steel black body was built, with the dimensions outlined in Diagram 4.12. The steel used was 6.3 mm thick, and 5 thermocouples were drilled into the sides to measure the uniformity of the temperature within the black body. Marked by × on the diagrams below, three thermocouples were placed along the long side of the black body and two to 120° to the left and right of the middle one. Thermocouples used are type K, gauge 20 $A.G.W.$ (0.81 mm diameter).

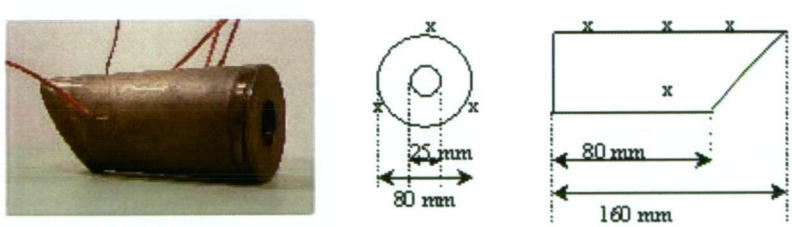

Figure 4.12: Dimensions of the black body used for calibration of the radiometer

To test whether then field of view was truly 30 : 1, 2.5 cm diameter stainless steel disc was heated. Using laser guidance to point the instrument to the center of the disc, the instrument was moved away and towards the disc. Although the rate of cooling of steel is rapid, it was evident that for distances less than 30 cm, radiation from the disc was filling the entire field of view.

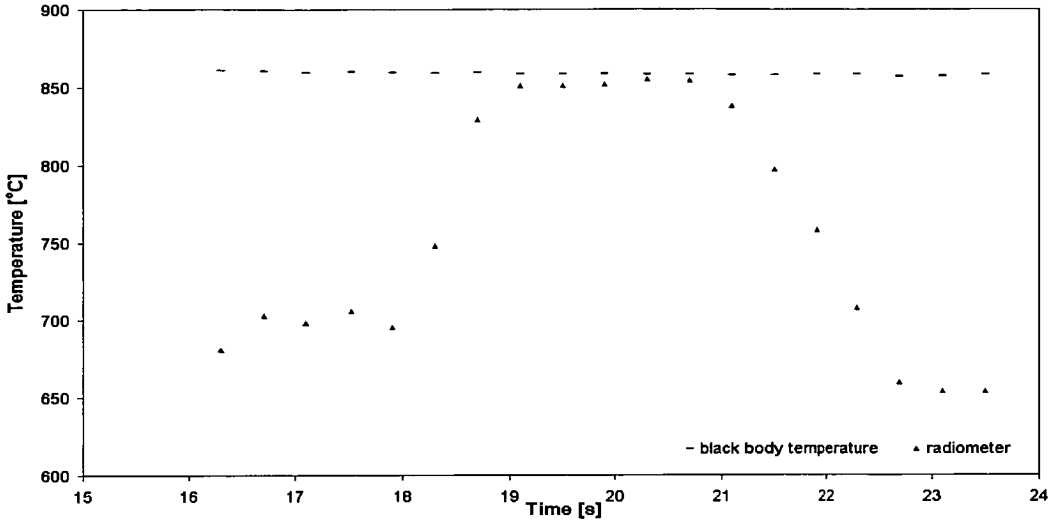

Figure 4.13: Output of one set of radiometer readings over black body cavity at 860C

The second test was performed using a cold disc and a charred hot piece of wood. When the wood was in front of the disc the reading of the instrument significantly increased; however, when just below or above the disc no change in the output was detected. Thus during the calibration, the instrument was positioned at 30 cm distance from the black body.

The oven was heated to temperatures up to 900°C, at 50°C intervals, leaving the oven on a fixed temperature for 30 minutes to ensure uniform temperature distribution through the thickness of the black body. The measurements were taken by sliding the laser pointer along the diameter of the black body. Emissivity on the instrument was set to 1. An output recorded from one of the readings is shown in the Figure 4.13. The maximum from a reading was taken to be the radiometer reading from the black body cavity, where no part of the metal from the front of the black body was in the field of view. The maximum temperature for which the results were recorded was 900°C. Any temperature higher than 900°C required the instrument to be further away from the black body in order to protect the filter, thus widening the field of view above the opening of the black body cavity.

The full set of readings is shown at Fig. 4.14. In the two diagrams it can be seen that the radiometer was constantly reading lower temperature than the

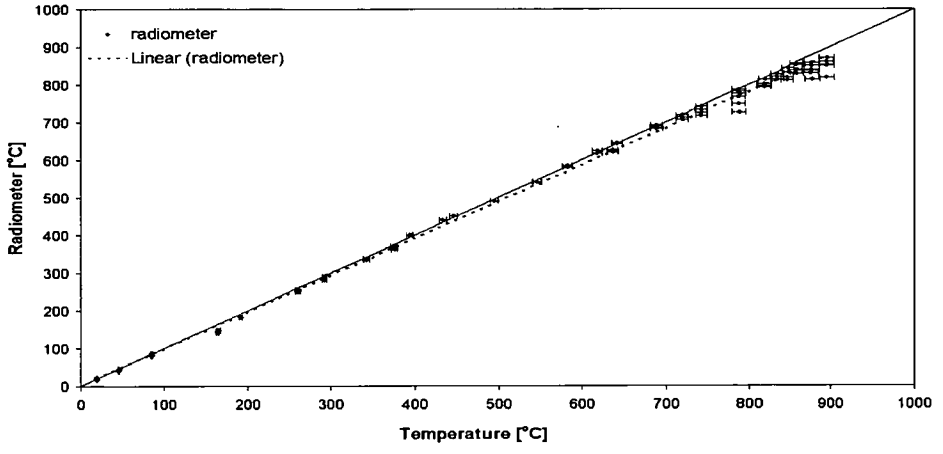

Figure 4.14: Temperature of the black body versus Temperature measured by the radiometer. The response of the radiometer was found to be very linear, and reading 2.24% below the actual temperature.

black body. The linear relation between these was found to be

$$T_{Radiometer} = 0.9776 \times T_{BlackBody} \tag{4.23}$$

and this serves to calibrate the instrument, as explained in section 4.3.4.

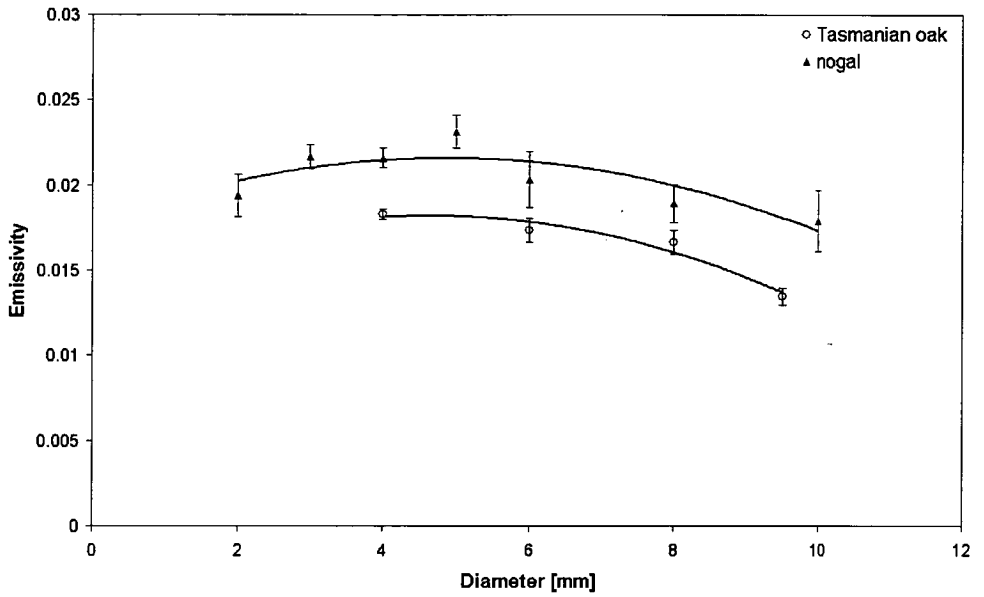

Figure 4.15: Emissivity versus diameter for oak and nogal. Total of 57 burns were performed for oak and 71 for nogal. Error bars represent one standard error.

4.5 RESULTS

4.5.1 Diameter

Emissivity versus diameter for flames thinner than 1 cm was modelled for Tasmanian oak and nogal. Diameters used were $4, 6, 8$ and 9.5 mm for Tasmanian oak and $2, 3, 4, 5, 6$, and 8 mm for nogal. Elements were approximately 8 cm in length, oven dried over night at temperature of $110°C$. Prior to use they were placed in a desiccator to achieve room temperature. Elements were oriented horizontally, held above ground in a metal stand, side-on to the radiometer. The pathlength of the instrument was thus a thin flame above the diameter.

Figure 4.15 shows the average emissivity values versus diameter for nogal and Tasmanian Oak. The parabolic shape of the fit indicates the dependence of emissivity on D^2 or the cross-section area of the fuel.

Analyzing the data using a general linear model, it was shown that there is

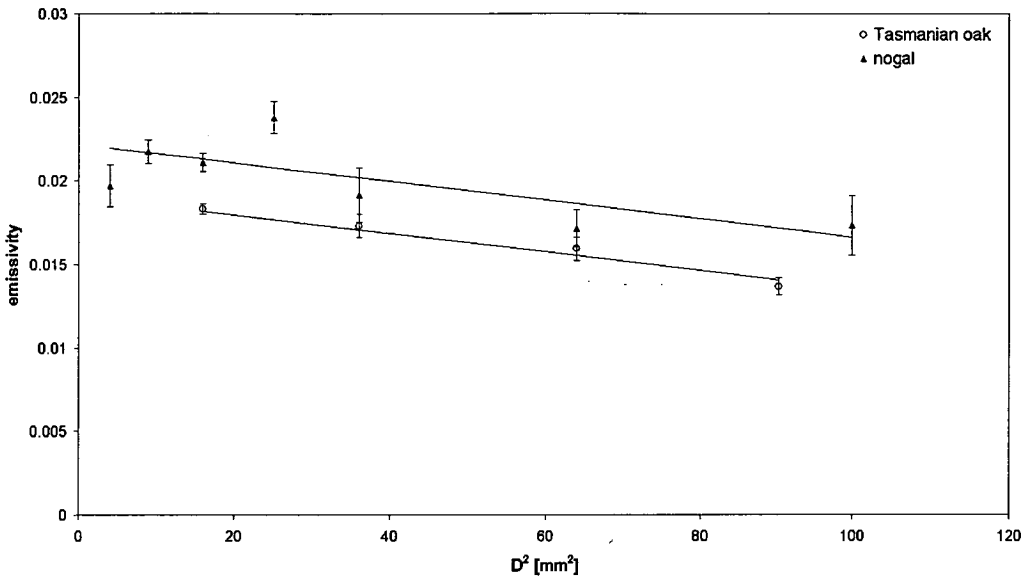

Figure 4.16: Emissivity versus D^2, weighted averages are used for emissivity, error bars represend standard error.

strong evidence that the linear model for emissivity differs in intercept for nogal and oak ($p < 0.001$), but there was no evidence that the slopes differ ($p = 0.348$). The best fit for the model was thus:

$$\varepsilon_{oak} = 0.0222 - 55.5D^2 \quad (4.24)$$

$$\varepsilon_{nogal} = 0.0191 - 55.5D^2. \quad (4.25)$$

These relations are shown in Figure 4.16 with weighted average emissivity values for each diameter. Weighted averages are calculated using

$$\bar{\varepsilon}_w = \sum_{i=1}^{N} w' \varepsilon_i$$

where w' are normalized weights described in Section 4.3.6. Standard errors shown in Figure 4.16 are not weighed.

It is interesting to note that the emissivity decreases with increasing diameter, but as was see in the previous chapter, so do the dimentions of the flame. The difference in the pathlength across this range of diameters is not significant.

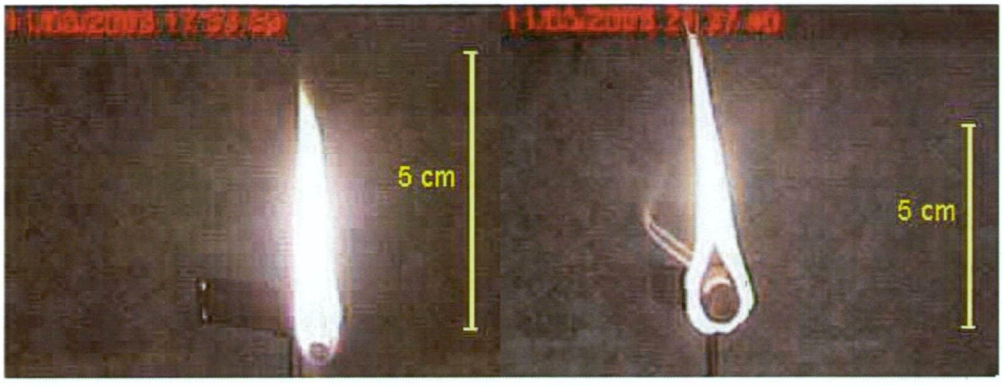

Figure 4.17: Image of flames above 4 mm and 9.5 mm elements of Tasmanian Oak

This can be seen from the images in Figure 4.17. The image to the left is 4 *mm* and to the right is 9.5 *mm* diameter Tasmanian oak. This would imply that the soot volume fraction decreases with increasing the diameter. To the knowledge of the author, no study has been reported in this area. The efficiency of combustion decreases with increasing the diameter. This would imply an increase in the soot, and a consequent increase in the efficiency, which was not seen in these experiments.

4.5.2 White Birchwood toothpicks:

This experiment was designed to measure effect of fuel width for the same fuel loading. Hence two, three, four and five toothpicks were ignited and the separation between them was varied from 0 up to 6 mm, since for these distances the flame was still merged.

Figure 4.18 shows an increase in emissivity for the wider fuel bed, while keeping the same fuel loading. However, since the flames are not merged after a separation of 6 mm (total fuel width of 24 mm for 4 toothpicks), not enough data is available for a quantitative description.

Note that varying the separation affected the flame height, the maximum flame height was reached for separation of 4 mm, but for 6 mm separation, the flame height reduces to the height of no separation, yet there is an increase in emissivity indicating that indeed the length of the path effects the emissivity,

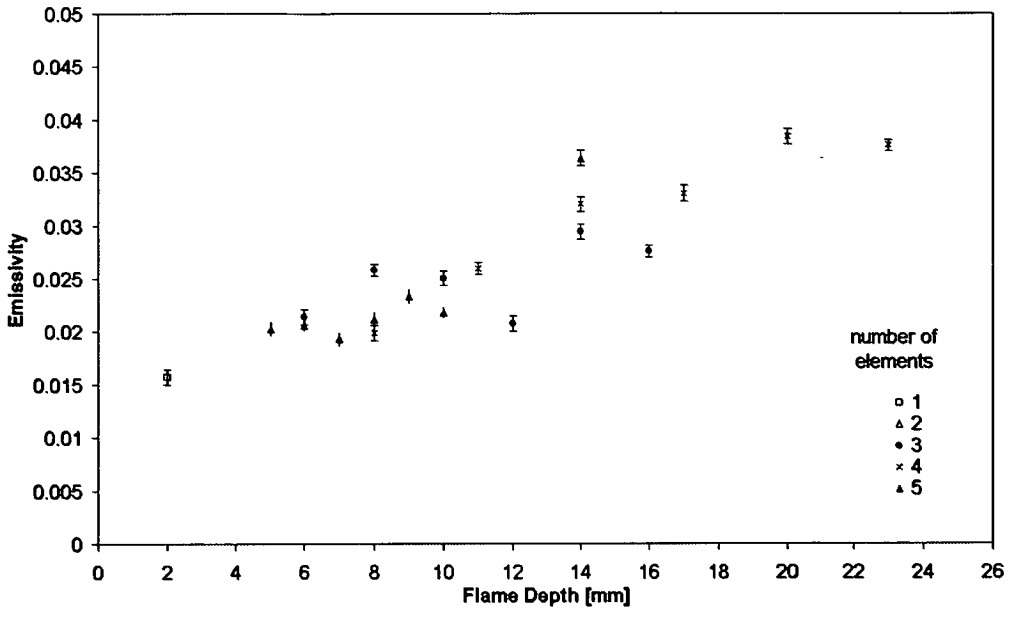

Figure 4.18: Emissivity of white birchwood toothpicks versus flame depth.

for the same fuel load.

4.5.3 Pine and balsa wood:

Experiments involving flame emissivity versus pathlength were performed on various dimensions of solid sheets of pine and balsa wood. Samples of balsa and pine used are given in Table 4.2. Element of width approximately 8 cm were used. The fuel was positioned horizontally and was held above ground with a metal stand. Elements larger than 50 cm for balsa and 20 cm for pine had holes punched through them to allow flow of oxygen, and hence a uniformly ignited element. Radiance was measured with varying depth of samples. A schematic diagram of the experimental arrangeent is given in Figure 4.19.

Using a general linear model it is evident that there is a linear dependence between emissivity and the depth of the fuel bed with a different intercept ($p < 0.001$). However there was no evidence that there is difference in the

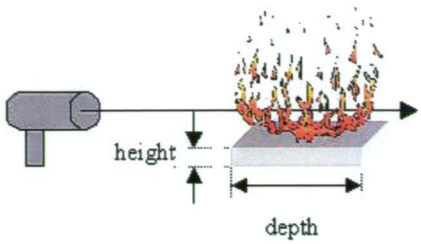

Figure 4.19: Experimental set-up

slope ($p = 0.192$). Thus we conculude that

$$\varepsilon_{balsa} = 0.00421 + 0.283D \quad (4.26)$$

$$\varepsilon_{pine} = 0.01164 + 0.283D \quad (4.27)$$

Comparing emissivity to the area of cross-section, a similar conclusion was reached. The rate of increase in emissivity versus cross-sectional area is the same for both pine and balsa ($p = 0.362$); however, there is a difference in the emissivity readings for the same cross-sectional area between the two wood types ($p < 0.001$). This gave the scaling laws

$$\varepsilon_{balsa} = 0.00496 + 81.5A \quad (4.28)$$

$$\varepsilon_{pine} = 0.01042 + 81.5A. \quad (4.29)$$

These results are shown in Figures 4.20 and 4.21. The difference in the emissivity for the same pathlength appears to be due to different soot volume fraction. The flame above pine wood was visually sootier than flame over balsa, although no direct measurement of soot volume fractions were performed for these wood types.

Emissivity values were compared to the proposed equation (4.6) for emissivity. The following attenuation coefficients were found:

$$\varepsilon_{balsa} = 1 - e^{-0.318D} \quad (4.30)$$

$$\varepsilon_{\pi ne} = 1 - e^{-0.544D} \quad (4.31)$$

with correlation coefficient R^2 of 0.802 for balsa and 0.436 for pine. Similar measurements by Telisin (1974) on oak leaves resulted in an attenuation coefficient of $-0.16\,m^{-1}$.

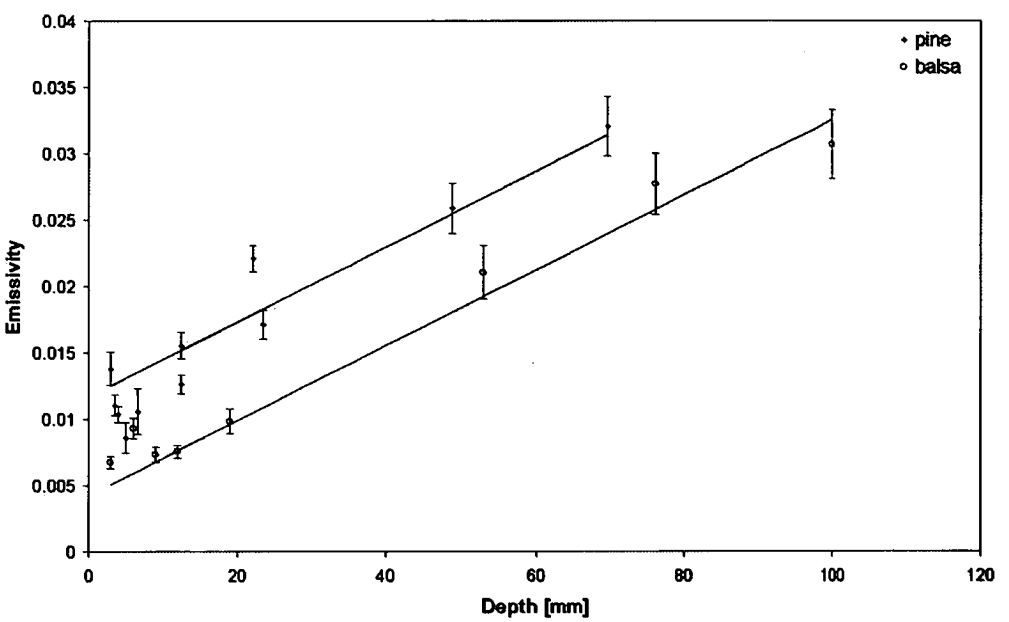

Figure 4.20: Emissivity versus depth of the fuel bed for pine and balsa. Total of 109 burns were performed for balsa and 202 for pine. Error bars represent one standard error. Note that the scatter readings for same depth may be due to the differences in the height of the element (see Table 4.2).

Table 4.2: Summary of the pine and balsa dimensions used. $\rho_{oak} \approx 500\frac{kg}{m^3}$, $\rho_{balsa} \sim 100kg/m^3$ (density of balsa varies significantly from stick to stick to anywhere between 80 and 200 kg/m^3)
*Holes punched through the block to allow flow of oxygen (diameter 3.5 mm, 1 hole/cm^2)

Pine	
depth [mm]	height [mm]
3.0	3.2
3.5	3.5
4.0	4.0
5.0	5.0
6.6	4.8
12.5	3.0
12.4	6.5
23.4	3.1
22.0*	5.0
31.5*	5.0
48.8*	4.5
69.7*	3.6

Balsa	
depth [mm]	height [mm]
3.0	3.0
6.2	6.2
9.4	3.5
12.3	3.5
29	3.5
53*	3.5
76.6*	3.5
100*	3.5

4.5.4 Wood type

Different properties of Tasmanian oak, nogal, sapelli and ramin were investigated in this theses so as to qualitatively compare differences in flame height and spread to wood properties such as their density, heat content or emissivity. Oven dried samples of 4 mm diameter and 8 cm length were cooled to room temperature using desiccator. They were placed in a stand and ignited along their length. Emissivity was measured using previously described method in section 4.3.6. Figure 4.22 shows results obtained for these types as well as results obtained for balsa and pine of similar dimensions. Note that the cross-section of pine is $4.0 \times 4.0\, mm^2$ and that the balsa result is a linear interpolation from lower ($3.0 \times 3.0\, mm^2$) and higher ($6.0 \times 6.0\, mm^2$) cross-section.

4.5.5 Fuel Moisture Content

Fuel moisture effects were studied on 4 mm diameter Tasmanian oak. Elements of approximately 8 cm lengths were used. Since it is impossible to estimate

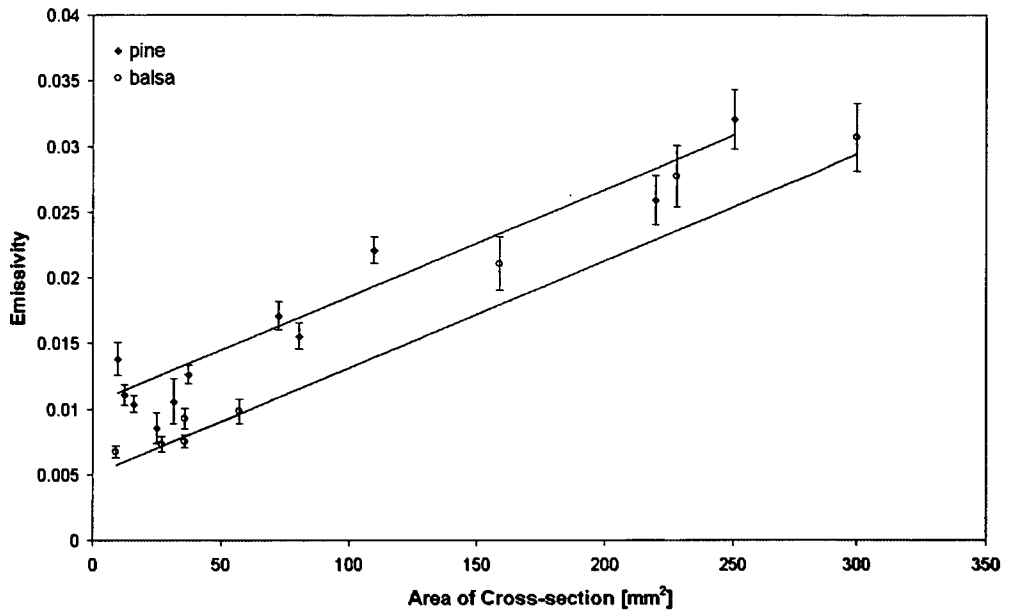

Figure 4.21: Emissivity of flame above pine wood and balsa wood versus cross-section area. Error bars represent one standard error.

fuel moisture content prior to burning an element, a number of elements were dried in an oven at $110°C$. At time intervals of between 15 and 30 minutes, number of elements would be taken out of the oven. Ten elements were used to measure the emissivity and the rest were weighted and returned to the oven to continue drying. Fuel moisture content was measured using gravimetric sampling methods where the initial weight is compared to the oven dried weight of the sample. Elements used for emissivity estimates were placed in zip-lock bags to ensure the fuel moisture content remains unchanged.

The fuel was ignited along the length and flame radiance was recorded every $0.25s$. Figure 4.23 shows the outputs of two measurements for oven dry sample and a sample at fuel moisture content of 9.1%. It is evident from this figure that there is a difference in time the maximum emissivity is reached. Figure 4.24 shows the difference in rates at which the maximum radiance is reached for different moisture levels. Maximum emissivity reached for all moisture content values used is given in Figure 4.25. Regression analysis of the maximum emissivity reached versus the initial fuel moisture content results in relation

$$\varepsilon = -0.000219 M_f + 0.0171, \tag{4.32}$$

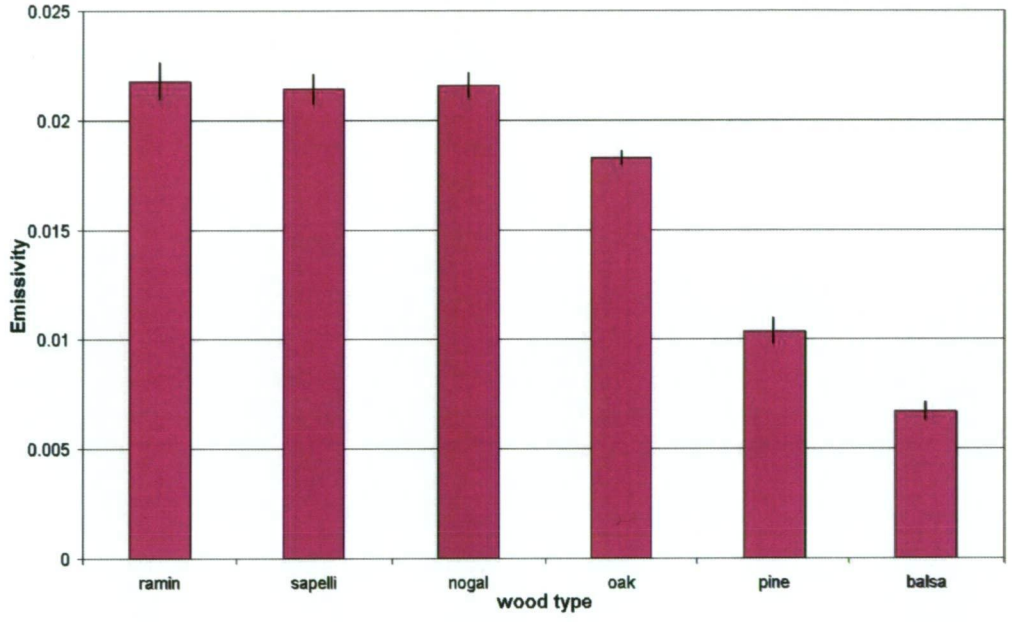

Figure 4.22: Emissivity versus wood type. Elements used for ramin, sapelli, oak and nogal observations have 4 mm diameter, whereas cross-section of pine elements is 4×4 mm^2. Balsa result is a linear interpolation to 4×4 mm^2 cross-section of the results obtained for elements of 3.0×3.0 mm^2 and 6.0×6.0 mm^2 cross-sections.

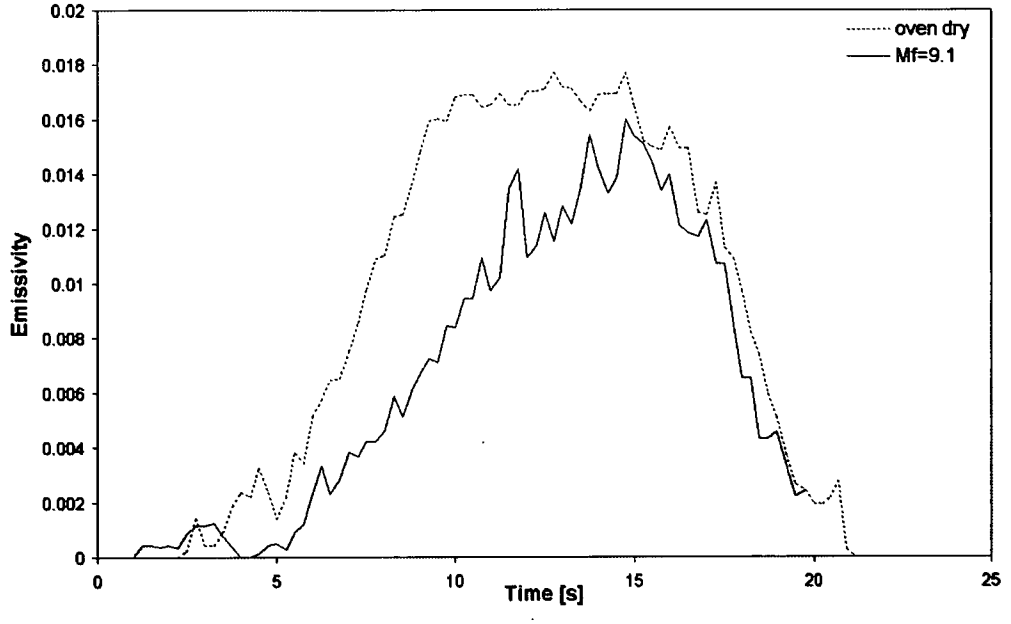

Figure 4.23: Emissivity recoding versus time for 4 mm Tasmanian oak. Two curves represent recordings for oven dry sample and sample with 9.1 fuel moisture content.

with R^2 of 0.05 and $p-$value for coefficient of 0.039 indicating there is not sufficient evidence that the coefficient is not zero. There hence seems to be little evidence that fuel moisture effects maximum emissivity readings (Pearson's correlation of -0.229). However it is impossible to estimate whether this reading occurs when all of the moisture has evaporated off the fuel.

The difference in the rate of increase when reaching maximum emissivity at different moisture content levels is evident. However, it is impossible to estimate whether this results from changes in flame height as the element dries or whether attenuation in radiance is caused by the water vapour particles in the flame.

4.5.6 Pine needles

In this experiment the emissivity of larger flames is investigated. The fuel used in this experiment consists of the pine needles from *Pinus radiata*. These were collected at a site near Seven Miles Beach in Tasmania. Care was taken to

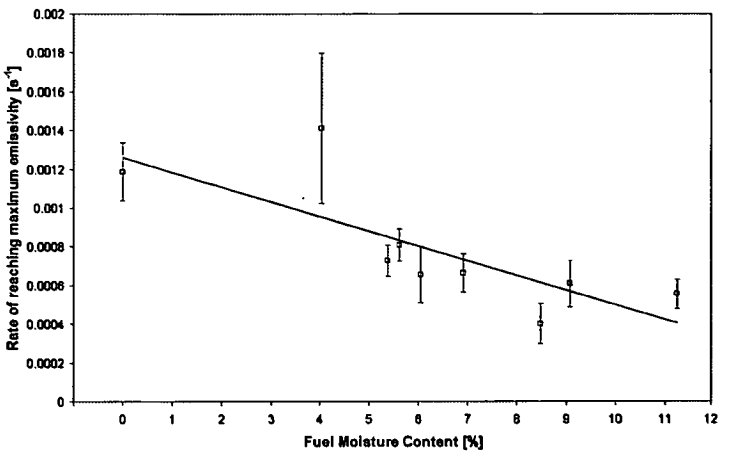

Figure 4.24: Rate of maximum emissivity reached versus fuel moisture content. Error bars represent one standard error.

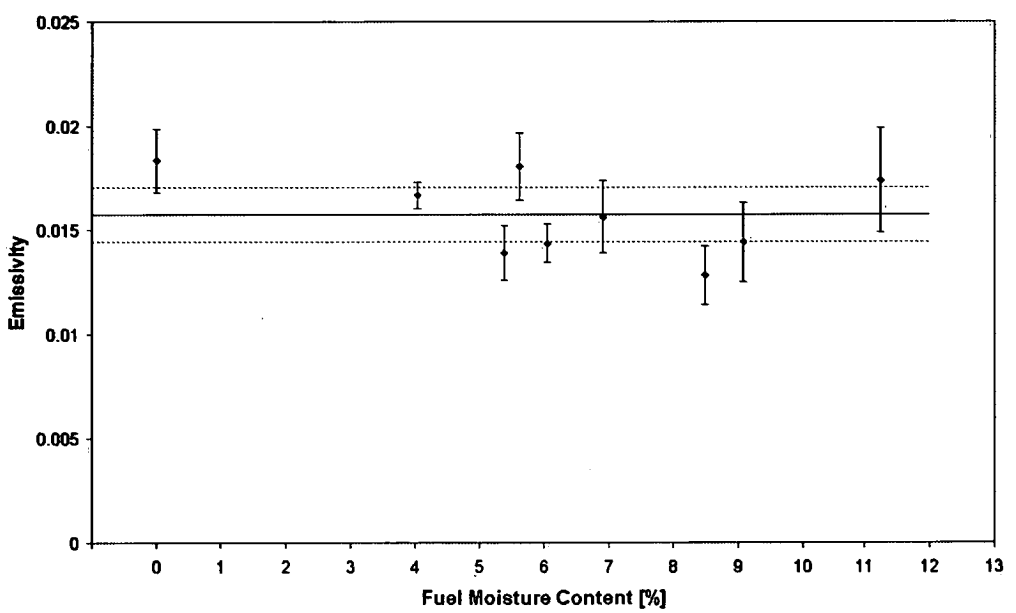

Figure 4.25: Average emissivity versus fuel moisture content. Error bars represent standard error.

collect only fallen needles and avoid any twigs, grass, sand or soil. Needles were taken to a laboratory where they were spread on plastic bags and left for four days to reach a uniform moisture level. Needles were occasionally turned over to promote uniform drying though the fuel. Smaller samples were burned in the laboratory; however, larger samples were taken to the field in plastic bags which were kept tied to ensure even fuel moisture content between the samples. Fuel used in experiments was at fuel moisture content of 13.7%.

Pine needles were burned in mesh wire frames which were raised from the ground to ensure free flow of oxygen and promote burning. This was needed to establish that the full width of the fuel bed was burning at the time of the measurement. It was still difficult to ensure that large widths of the fuel were fully burning, and hence the error bar for fuel width on these readings was set as sufficiently large. The fuel width, w is the width of the fuel burning at the time of the measurements. This is the dimension of the fuel bed that is in line with the pathlength of the instrument (Figure 4.5.6).

For each width measured, the pine needles were weighted to ensure equal fuel loading between repetitions. The fuel bed thickness was kept at approximately $2-3cm$. The fuel bed packing ratio is estimated to be 0.1 and bulk density at approximately 40 kg/m^3.

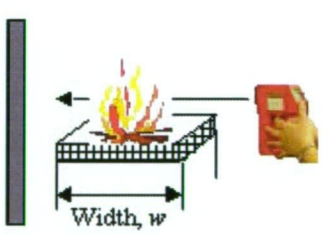

As the width of the fuel bed increased, there was a significant increase in the flame height fluctuations. This can be observed in the emissivity readings shown for a 75cm fuel bed (Figure 4.26). For fuel beds larger then 30cm, the fuel was ignited by piloted ignition at several positions. As the fuel bed is relatively thin, it was difficult to establish that for the width greater then 50cm, entire fuel bed was flaming at the times of the highest readings. This is why these readings were given higher uncertainty, to be accounted for in the model fitted.

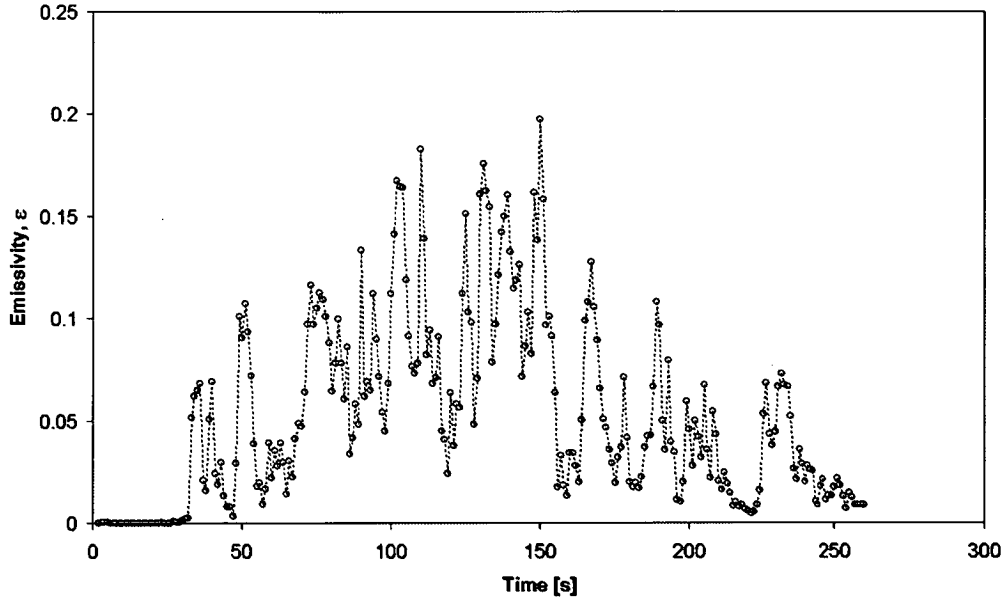

Figure 4.26: Emissivity readings for flame over bed of pine needles of 75 cm depth.

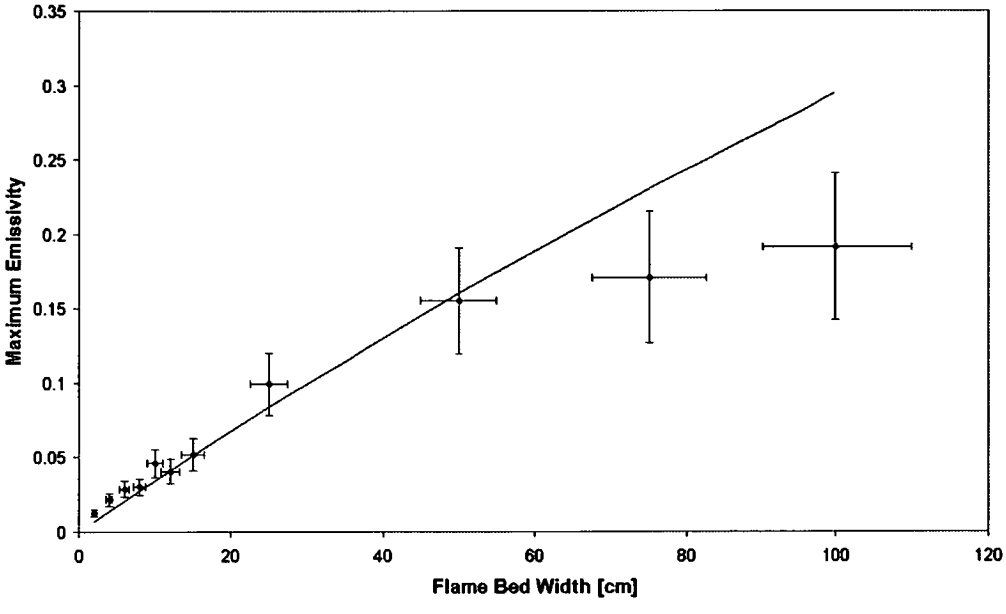

Figure 4.27: Emissivity of pine needles versus width of the fuel bed. Packing ratio is kept the same for all fuel widths thus fuel loading increases as the fuel bed width increases

Figure 4.27 shows weighted average values in emissivity measured versus width of the fuel bed. These were modelled to the exponential relationship:

$$\varepsilon = 1 - e^{-0.35w}, \tag{4.33}$$

where w is in SI units. Thr error values placed on the $x-$coordinate are at 10% of the width. This is because of the difficulty in igniting the full width of the fuel bed at large widths. Equation (4.33) yields an R^2 of 0.886 indicating a reasonable fit. This relation is in agreement with other values reported in literature.

4.5.7 All wood types

A summary of all wood types burned in these experiments is shown in Figure 4.28. This diagram is a log-linear graph of all of the emissivity values recorded versus the width of the fuel bed, with the fit for the pine needles given by equation (4.33). We can see that whilst the emissivity can be described by $1 - e^{-kw}$ relation, with the coefficient k in the range of -0.35 to -0.5 were appropriate for larger widths (beds of pine needles and balsa and pine), this underestimates the emissivity observed for smaller pathlengths.

The radiance observed for all small flames (up to 15cm depth) was less then 5% to that of a black body with the same temperature.

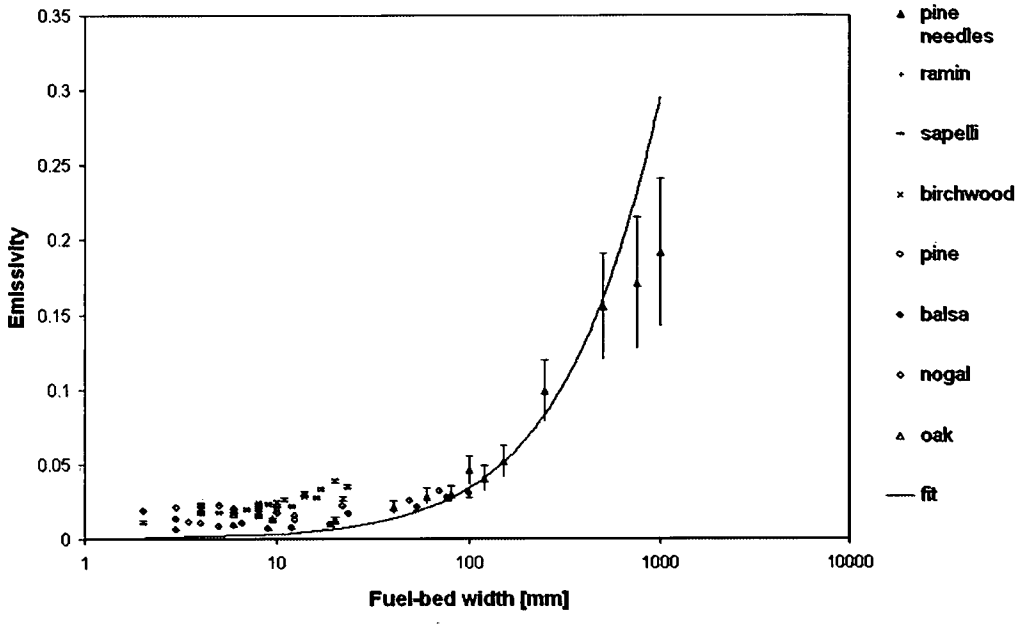

Figure 4.28: Emissivity values for all for fuel types versus width of the flaming fuel bed

Chapter 5

Flame Spread Along a Cylindrical Wooden Brand

In this chapter a model of the flame spread along a wooden cylindrical brand is presented. Development of the model described and its outcomes are compared with the experimental results described in previous chapters

Wood is an inhomogeneous and non-isotropic material, which physical structure and chemical composition vary with species and age of the tree. It is composed predominantly from cellulose, hemicellulose and lignin as well as wide range of extractives and mineral constituents (Chandler et al. 1991), the proportions of which components in wood varies between species.

The grain structure of wood affects some of its properties. The thermal conductivity of the wood is greater along the grain than transversly, as is also the gas permeability. The volatiles generated underneath the surface of the wood escape easier along the grain, which is evident from jets formed on the sides of burning brands.

Water molecules present in wood affect its thermal properties (Steinhagen 1977) and are dependent on temperature and relative humidity (Spearpoint 1999).

When exposed to external heating, temperature of wood gradually increases from surface inwards. When temperature of $100°C$ is reached, free moisture evaporates.

The variations in the characteristics of wood depend on the species and the age of a tree, the change in properties due to the grain direction of a brand and the complex nature of processes leading to the combustion make accurate physical interpretation of this phenomenon problematic.

Models of pyrolysis process existing in the literature can be divided into two categories: models using a critical measure of ignition and comprehensive models. The first group of models uses measures such as ignition temperature, mass loss rate, heat release rate or a similar measure to define fuel ignition. These models can be further divided in algebraic and analytical models where a closed form solution is obtained or integral models (Moghtaderi 2006). Comprehensive models take into consideration kinetic schemes of fuel decomposition (Babrauskas 2004).

In this chapter a comprehensive one dimensional model of pyrolysis of a cylindrical wooden brand is developed. The wood structure is simplified by assuming it to be composed of a homogeneous material consisting of one element. The physical properties of such an element are derived from experimental observations of the wood type shown in previous chapter. Heat is transferred through the element via conduction and lost through convective cooling with the energy source provided by the combustion reaction.

5.1 Energy Balance

Consider a cylindrical wooden brand of length L ignited at one end. In order to describe the heat transfer within the cylinder, consider a section of the element of width dx,as shown in Figure 5.1. This section is at temperature $T(x)$.

The net heat rate transfer to this element can be described by

$$q_{net} = q_{conductive} + q_{radiative} + q_{chemical} - q_{cooling}, \tag{5.1}$$

where $q_{conductive}$ is conductive heat diffusion along the element, $q_{chemical}$ is the energy gained from the pyrolysis reaction and $q_{cooling}$ is the heat lost to the surrounding.

Making an assumption that the temperature increases uniformly across the entire section of width dx, the net heat transferred will result in the temperature

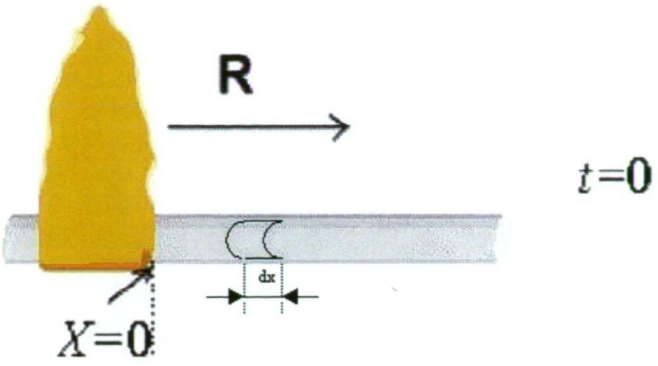

Figure 5.1: Flame spread along a horizontal element

rise

$$r^2\pi dx\rho c^* \frac{dT}{dt} = q_{net} \tag{5.2}$$

where $r^2\pi dx$ is the volume, ρ is the density of the material, T is the temperature of the element at time t. The specific heat c^* is an "average specific heat" of fuel and which accounts for the latent heat of moisture as described by Catchpole & Catchpole (n.d.).

Average Specific Heat

When moist wood is exposed to heat, the surface temperature reaches $100°C$ and moisture from the wood begins to evaporate. At this stage most of the energy is used to evaporate free water. As the drying process continues the evaporation front moves into the solid, where moisture is still present in liquid form. Behind the evaporation front water vapor is transferred through convection and diffusion, and the diffusion of bound water across the cell walls occurs as well (Moghtaderi 2006). At higher temperatures, mixing of volatiles and water vapor further affects process of pyrolysis. Despite its importance on the pyrolysis process, effect of the fuel moisture content in wood pyrolysis is often more simplified than other pyrolysis processes (Moghtaderi 2006). To account for fuel moisture desorbtion in some models an energy sink at $100°C$ is used to account for the energy balance, others add an additional chemical reaction. More detailed treatment in using local moisture vapour equilibrium and tracking movement of vapour and liquid water was given by (Moghtaderi et al. 1998). In many models though, heat required to evaporate moisture was

included into the heat of ignition (Albini & Reinhardt (1995),Simms & Law (1967)). Fuel moisture content was treated similarly in this model too.

Consider the heat absorbed by an element to raise the temperature of the moist fuel up to $100°C$. At this point, the moisture within the wood evaporates, and the remaining dry fuel may ignite. The heat energy per unit mass required for the fuel ignition is given by (Dunlap 1912):

$$q_{ig} = (c_p + M_f c_w)(373 - T_0) + LM_f + c_p(T_{ig} - 373), \tag{5.3}$$

where q_{ig} is amount of heat per unit mass of fuel required for the fuel ignition, c_p is specific heat of dry fuel, M_f is the fuel moisture content (a fraction of weight of water to the weight of the oven-dried wood (*Wood Handbook - Wood as an Engineering Material* 1999)), c_w is specific heat of water, L is the latent heat of water and T_0 and T_{ig} are the initial and the ignition temperatures. Since moisture is absorbed by the fuel cell walls, more energy is required to dry the fuel than to evaporate the equivalent amount of free water. Some of the moisture evaporates into the unburned zone and re-condenses where temperatures are below $100°C$ (Janssens 2004). This is beyond the scope of this model where the heat required to evaporate fuel moisture was modelled using 'average specific heat'.

Average specific heat c^* is defined such that

$$q_{ig} = c^*(T_{ig} - T_0) \tag{5.4}$$

describes the heat per unit mass required for the the ignition. Equations (5.3) and (5.4) are graphed in Figure 5.2. This is following Rothermel (1972) based on Dunlap's (1912) method.

The average specific heat is calculated from equations (5.3) and (5.4):

$$c^* = c_p + \frac{(c_w(373 - T_0) + L)}{(T_{ig} - T_0)} M_f. \tag{5.5}$$

Using the values defined in Table 5.1, for Tasmanian oak it is

$$c^* = 2500 + 8543 M_f\ , \tag{5.6}$$

which is in the range of $2500 - 3350\ Jkg^{-1}K^{-1}$ for dry fuel and fuel of up to 10% of moisture content. Note that M_f is a mass fraction of moisture to the dry fuel mass.

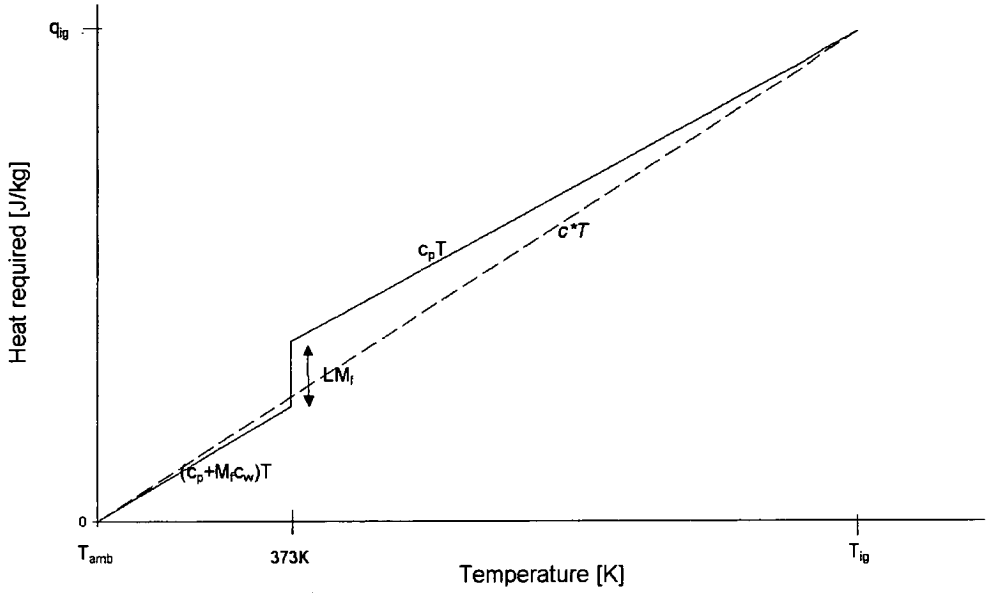

Figure 5.2: Heat required to raise the temperature of the fuel with 5% moisture content to 100^0C. The solid line represents Equation (5.3) while the dashed line represents Equation (5.4).

Table 5.1: Table of constants for average specific heat calculations

c_p	2.50	$kJkg^{-1}K^{-1}$	Strezov et al. (2003)
c_w	4.19	$kJkg^{-1}K^{-1}$	*CRC Handbook of Chemistry and Physics, 80th Edition* (1999)
L	2257	$kJkg^{-1}$	*CRC Handbook of Chemistry and Physics, 80th Edition* (1999)
T_{ig}	600	K	Albini & Reinhardt (1995)
T_0	300	K	measured

5.1.1 Conduction

The rate of heat transfer via conduction at position x is given by Fourier's law

$$q''_x = -K_{cond}\frac{\partial T}{\partial x}, \tag{5.7}$$

where q''_x is the heat flux in the $x-$direction per unit of cross-sectional area and K_{cond} is the heat conduction coefficient.

The heat conduction rate at the other end of the segment of the length dx can be expressed as a Taylor series expansion, neglecting the higher terms, as

$$q''_{x+dx} = q''_x + \frac{\partial q''_x}{\partial x}dx \tag{5.8}$$

The heat stored in section dx due the the conductive transfer is then

$$q_{conductive} = r^2\pi \left(q''_{x+dx} - q''_x\right) = -K_{cond}\frac{\partial^2 T}{\partial x^2} r^2 \pi dx \tag{5.9}$$

The thermal conductivity of wood or its heat conduction coefficient K_{cond} is varied depending on the grain direction. In the brands used in experimental observation described in Chapter 3 the grain was in the direction of the length of the cylinder. The heat transfer thus was in the direction of the grain.

For Tasmanian oak thermal conductivity range of 0.166 to $0.187 Js^{-1}m^{-1}K^{-1}$is reported in temperature range of $318 - 331K$ (Madhusudana 2006). Heat conductivity of hard woods ranges from 0.10 to $0.20 Js^{-1}m^{-1}K^{-1}$ (Incropera & DeWitt 1981).

5.1.2 Radiation

Radiative transfer is energy emitted by all objects with temperature above absolute zero. If an object is a perfect radiator it emits black body radiation, where the rate of energy radiated is described by Plank's law as σT^4, where σ is the Stefan-Boltzman constant ($5.67 \times 10^{-8} Wm^{-2}K^{-1}$) and T is the temperature of the object. A flame attached to a burning object emits "gray body" radiation, where the rate of energy release is described by Plank's law with emissivity factor ε_f. Radiative heat flux between two elements of temperatures T_1 and T_2 is described by

$$q''_{rad} = F_{1,2}\varepsilon_1\varepsilon_2\sigma\left(T_1^4 - T_2^4\right),$$

where $F_{1,2}$ is view factor between the two surfaces, and $\varepsilon_1$and ε_2 are surface emissivities.

The transfer of heat by process of radiation between the flame and the element is given by:

$$\dot{q}_{rad} = (2rdx)\, F(h,d,l)\, \varepsilon_a \varepsilon_{fl} \sigma \left(T_{fl}^4 - T^4\right),$$

where $2rl$ is the area of an element "seen" by the flame, T_{fl} is the flame temperature, T is the temperature of the element, σ is the Stefan-Boltzman constant, ε_{fl} is the flame emissivity, ε_a is the particle absorptivity and $F(h,d,l)$ is the view factor between the flame and the cylinder it depends on the height

and width of the flame, as well as the separation between the element and the flame.

A closed form expressions of view factor for a differential element and tilted cylindrical object is given by Guelzim et al. (1993)..

Flame is a hot gas rather than a uniform emitting surface, so it's emissivity readings fluctuate. The mean effective emissivity of flames of this size was found in Chapter ?? to be of the order of 0.02.

With the low emissivity measurements and the low values of view factor for the flame heights used here, the radiation contribution to the flame spread was found to be negligible and was therefore omitted from the model.

5.1.3 Convection

The loss of heat to the surroundings occurs when the temperature T increases above the ambient temperature $T_{amb.}$ This transfer of energy is described by Newton's law of cooling

$$q''_{cooling} = h_{cooling} \left(T\left(x\right) - T_{amb} \right) \tag{5.10}$$

where $q''_{cooling}$ is the heat flux per unit of the surface area and $h_{cooling}$ is the convection heat transfer coefficient dependent on the geometry, atmospheric conditions, thermodynamical and transport property of the element and the surroundings. For the segment dx the heat rate due to convective cooling is then

$$q_{cooling} = 2r\pi dx h_{cooling} \left(T\left(x\right) - T_{amb} \right) \tag{5.11}$$

Convection Heat Transfer Coefficient

The convection heat transfer coefficient $h_{cooling}$ for Newtonian cooling in a horizontal cylindrical element can found as follows (Incropera & DeWitt 1981)

$$h_{cooling} = \frac{Nu * k_{air}}{2 * r}, \tag{5.12}$$

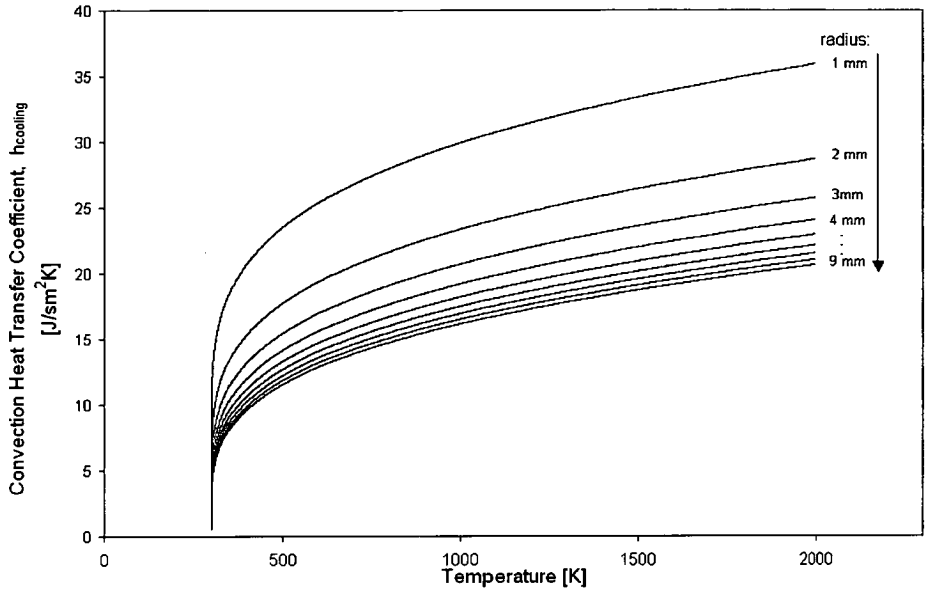

Figure 5.3: Range of convection heat transfer coefficient $h_{cooling}$ values for free convection in horizontal cylinder.

where Nu, k_{air} and r are Nusselt number, heat conduction of air and radius of the element respectively. The Nusselt number, for this configuration, is

$$Nu = \left\{ 0.60 + \frac{0.387 * Ra^{1/6}}{[1 + (0.559/Pr)^{9/16}]^{(8/27)}} \right\}^2, \tag{5.13}$$

in which we also have the parameters

$$Pr = \nu_{air}/\alpha, \tag{5.14}$$

$$Ra = \frac{g\beta(T - T_{amb})(2r)^3}{\nu_{air}\alpha}, \tag{5.15}$$

which are the Prandtl and Rayleigh numbers respectively (Incropera & DeWitt 1981). The constants ν_{air}, α and β are viscosity, thermal diffusivity and expansion coefficient of the surrounding air respectively and g is the acceleration due to gravity (9.81 ms^{-2}). The surrounding air temperature is taken to be $300K$. At this temperature viscosity of air ν_{air} is 112.2 x 10^{-6} m^2s^{-1}, the thermal diffusivity is 22.5 x 10^{-6} m^2s^{-1} and the expansion coefficient is $1/300K^{-1}$ (Incropera & DeWitt 1981).

The range of values that the convection heat transfer coefficient $h_{cooling}$ has for the configuration in this model is calculated from equations (5.12) to (5.15). Values obtained for the temperature range of $300K$ to $2000K$ and for radius up to 9 mm are shown in Figure 5.3.

5.1.4 Heat of the Chemical Reaction

Wood is a complex inhomogeneous material. Tasmanian oak is composed of 49.8% carbon, 44% oxygen, 5.79% hydrogen 0.16% nitrogen and 0.08% sulfur (Strezov et al. 2003). In this model, however, a simplifying assumption was made in which the element was assumed to contain only one combustive component, say carbon, for which properties were derived from experimental results.

The pyrolysis reaction of carbon

$$C + O_2 \rightarrow CO_2$$

can be described by the first rate reaction equation

$$\frac{d[C]}{dt} = -k[C][O_2], \tag{5.16}$$

where [] denotes molar concentration of the elements. The reaction rate k is temperature dependent and is typically described by Arrhenius kinetics:

$$k(T) = Ae^{-\frac{E}{RT}}, \tag{5.17}$$

where E is the activation energy, A is the Arrhenius pre-exponential factor, R is the universal gas constant (8.314472 $JK^{-1}mol^{-1}$) and T is the temperature in Kelvins. The form of this equation however assumes that small amounts of energy are released even at very low temperatures. This, of course, does not happen in practice, and is known as the "cold boundary" problem in models of this sort (Weber et al. (1997),Gubernov et al. (2005), Zeldovich et al. (1985), Mandel et al. (2008)). To overcome this difficulty in a simple way, we introduce an artificial "cut-off" condition (Zeldovich et al. 1985) at the ambient temperature T_{amb}, below which no reaction takes place.

Arrhenius' law (Equation 5.17) is thus replaced with the rate law

$$k(T) = \begin{cases} Ae^{-\frac{E}{RT}} & \text{for } T \geqslant T_{amb} \\ 0 & \text{for } T < T_{amb} \end{cases} . \tag{5.18}$$

Finally, it is necessary to model the chemical energy associated with the pyrolysis reaction, since this drives the spread of the flame. This heat rate generated in the segment dx of the cylinder can be described by

$$\begin{aligned} q_{chemical} &= H_c \frac{d[C]}{dt} \left(r^2 \pi dx\right) \\ &= H_c k(T) [C] [O_2] r^2 \pi dx, \end{aligned} \tag{5.19}$$

where H_c is the energy released by the combustion of one mole of carbon ($393,500\ Jmol^{-1}$ (*CRC Handbook of Chemistry and Physics, 80th Edition* 1999)) and $k(T)$ is the reaction rate described by equation (5.18). Molar concentration of carbon $[C]$ in the element section is found from equation (5.16), whereas the molar concentration of oxygen $[O_2]$ is assumed to be constant throughout the reaction, as oxygen is readily available in this configuration.

Oxygen concentration

The molar concentration of oxygen in the vicinity of the element is considered to be constant at the level available in the air. The air density at room temperature is taken to be $1.168\ kgm^{-3}$, and the average molecular weight of air is $0.0289\ kgmol^{-1}$. Therefore $1\ m^3$ of air contains $40.415\ mol$ of air. The concentration of oxygen in air is approximately 20.95% by volume. The molar concentration of oxygen in air is thus

$$[O] = 8.4669\ mol\ m^{-3}. \tag{5.20}$$

Initial Carbon concentration

One of the simplifications of this model is that it represents the chemical structure of wood in terms of a single element, carbon. In order to estimate what would be the initial concentration of carbon in one brand of wood, consider

the heat released by combustion of the material used. The results of the bomb calorimetry measurements on different wood types are shown in the Appendix A.

The energy released by combustion of Tasmanian oak is found to be $19,291\ Jg^{-1}$ (Appendix A). Therefore, if combustion of 1 g of Tasmanian oak releases $19,291\ J$ and combustion of 1 mol of carbon releases $393,500J$ of energy, then with our assumption that all of the combustible compounds are carbon, there are 0.049 mol of carbon per gram of Tasmanian oak.

The dry density of Tasmanian oak used was measured to be approximately 650 kgm^{-3}; therefore considering the initial molar concentration of carbon in the oak sample to be

$$[C]_0 = 31,865 mol/m^3 \tag{5.21}$$

would generate the appropriate amount of heat during combustion.

Ignition Temperature

Ignition temperature is the "minimum temperature a substance must attain in order to ignite under specific conditions" (NFP 2001). Ignition temperatures for a piloted ignition are difficult to measure. A variety of temperatures are reported in the literature varying between $593°K$ and $657°K$. Most commonly an ignition temperature of around $600°K$ is reported ($603°K$ Simms & Law (1967) , $593°K$ Anderson (1969), Kanury (1972), Baines (1990) and Rothermel (1972), $600°K$ Albini & Reinhardt (1995)). However higher values have been reported as well ($623°K$ Drysdale (2002), $643 - 650°K$ Williams (1976) Williams (1976, 1982), $598 - 648°K$ Atreya (1998)). An ignition temperature of $600°K$ was used for this model.

Arrhenius Law Constants

A wide range of Arrhenius constants for wood are cited in literature 5.2. These are usually based on the pyrolysis of the main components of wood, in particular cellulose. Activation energy E for wood pyrolysis fall in range of 60 to $180kJ/mol$. Pre-exponentail constants however seemed to be of order form

10^{-9} to 10^{12}. Arrhenius constants used in this model were estimated from the experimental results shown in Chapter 3 as described in the following section.

Table 5.2: Table of Arrhenius parameters for wood

$E(kJmol^{-1})$	$A(s^{-1})$	Authors/remarks
67.34	890	Willner & Brunner (2005)
125	1.5×10^{-9}	Vovelle et al. (1981)
126	7×10^{7}	Roberts (1970)
104.6	7.1×10^{8}	Roberts & Clough (1963) (< 300)
94.6	4.41×10^{6}	P.L. Blackshear & Murty (1965) ($r/a = 0.86$)
124.7	$6 \times 10^{7} - 7.5 \times 10^{8}$	Tinney (1965) (upper limits)
87.7	3.48×10^{15}	P.L. Blackshear & Murty (1965) ($r/a = 1.0$)
62.8	1.5×10^{3}	Roberts & Clough (1963) (> 300)
$152.3 - 178.6$	$6 \times 10^{7} - 7.5 \times 10^{8}$	Tinney (1965) (lower limits)
48	2×10^{2}	Svenson et al. (2004) above 360°C
160	1.3×10^{11}	Svenson et al. (2004) below 360°C

Arrhenius Constants Approximation Experimental results on the flame spread over cylindrical fuel are presented in Chapter 3. The results obtained for the thermal residence of the wood can be used to estimate values of Arrhenius pre-exponential for this configuration.

In order to approximate the rate constants for the Tasmanian oak wood, consider equation (5.16). If the rate k at which the reaction occurred has the constant value k_0, the rate of carbon depletion would be described as

$$[C] = [C]_0 \, e^{-k_0[O_2]t}. \tag{5.22}$$

Experimental evidence described in Chapter 3 on combustion of Tasmanian oak brand when flame is spread across a horizontally placed element showed that the efficiency of combustion is

$$\eta_{oak}(D) = 1.123e^{-55.5D} \tag{5.23}$$

The residence time t_r, or the time needed for a flame to pass a point, can be modelled as

$$t_{r\,oak}(D) = 4056D - 4.59 \tag{5.24}$$

Then the amount of fuel remaining after residence time is if initial concentration of fuel is

$$[C](t_r) = 1 - \eta_{oak}[C]_0, \tag{5.25}$$

From equation (5.22) it follows that k_0 is calculated from

$$k_0(D) = \frac{\ln(1 - \eta_{oak}(D))}{[O_2] t_r(D)} \tag{5.26}$$

For a brand of Tasmanian oak of a $4mm$ diameter, the residence time is calculated to be 11.6 seconds (equation 5.24) and the efficiency of combustion is 0.90 (5.23). Initial oxygen concentration is $8.4669\frac{mol}{m^3}$ (5.20). Therefore from equation (??), for a $4mm$ diameter element of Tasmanian oak k_0 is calculated to be

$$k_0 = 0.0236 m^3 mol^{-1} s^{-1}. \tag{5.27}$$

.Using the activation energy of $50000 Jmol^{-1}$, and assuming that the bulk of combustion occurs at flame temperature $1223K$, the Arrhenius pre-exponential factor for a $4mm$ diameter Tasmanian oak is calculated from equation (5.17) to be

$$A = 3.19\ m^3 mols^{-1} \tag{5.28}$$

5.2 Balanced Equation

From equations (5.1), (5.9), (5.19) and (5.11) we have:

$$\frac{\partial T}{\partial t} = -\frac{K_{cond}}{\rho c^*}\frac{\partial^2 T}{\partial x^2} + \frac{H_c[C][O_2]}{\rho c^*}k(T) - \frac{2}{r\rho c^*}h_{cooling}(T)(T - T_{amb}), \tag{5.29}$$

and with

$$\frac{d[C]}{dt} = -k(T)[C][O_2], \tag{5.30}$$

and boundary conditions:

(i) initially, all but the tip of the element is at the ambient temperature: $T(x) = T_{amb}, X \neq 0$

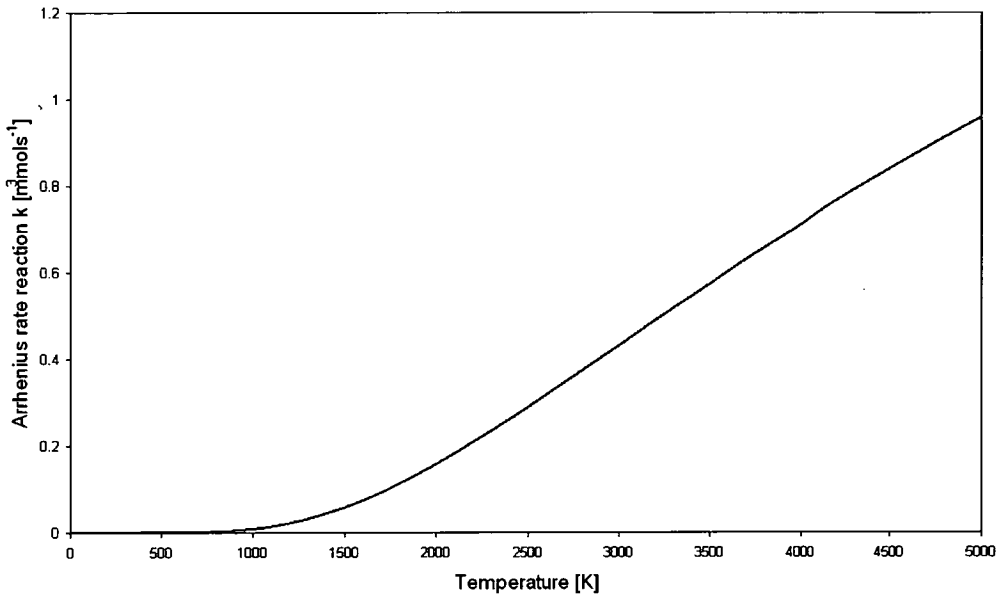

Figure 5.4: Arrhenius rate coefficient versus temperature with pre-exponential coefficient 0.06425 $m^3 mols^{-1}$ and activation energy 10000 $Jmol^{-1}$

(ii) The tip of the element is at the flame temperature: $T(0) = T_{fl}$

(iii) Initial carbon concentration across the element is $31,865\ mol/m^3$ (5.21).

5.2.1 Numerical Solution

Equation (5.29) was solved numerically by means of a forward-time, centred-space explicit finite difference method. The approximate equation for temperature is

$$\frac{T_j^{k+1} - T j^k}{\Delta t} = \frac{-K_{cond}}{\rho c^*}\left(\frac{T_{j+1}^k - 2T_j^k + T_{j-1}^k}{\Delta x^2}\right) + \frac{H_c\left[O_2\right]}{\rho c^*} k\left(T_j^k\right) C_j^k - \frac{2}{r\rho c^*} h_{cooling}\left(T_j^k\right)\left(T_j^k - T_{amb}\right) \quad (5.31)$$

$$\frac{C_j^{k+1} - C_j^k}{\Delta t} = -k\left(T_j^k\right) C_j^k\left[O_2\right], \quad (5.32)$$

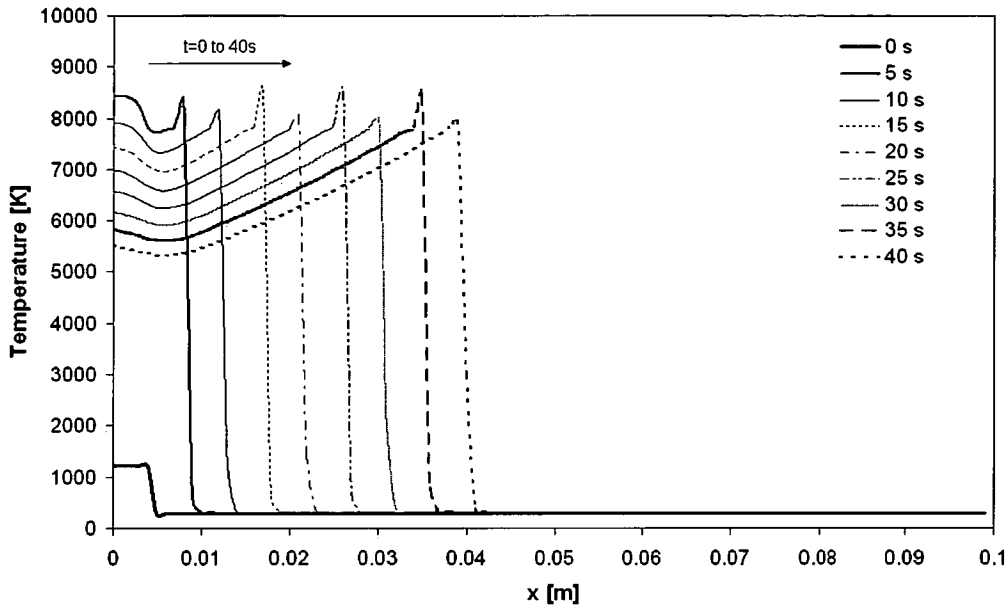

Figure 5.5: Temperature profile change on 10cm cylindrical element over 40s interval

where carbon concentration $[C]$ and temperature T have been approximated by point values C_j^k and T_j^k respectively, at positions x_j and times t_k.

Here, care must be taken to observe the numerical stability criterion

$$\left|\frac{-K_{cond}}{\rho c^*}\right| \frac{\Delta t}{\Delta x^2} \leq \frac{1}{2}.$$

This well known restriction on the time step Δt may be found in Ames (1977) for example.

5.2.2 Results

With initial conditions described above, the change in temperature profile over $40s$ interval obtained for 4mm diameter dry cylinder of Tasmanian oak is shown in Figure 5.5, and the concentration of fuel available in Figure 5.6. The rate of spread shown in Figure 5.7, is obtained by noting the time when an element reaches temperature of ignition. According to these initial conditions set, the rate of flame spread predicted was

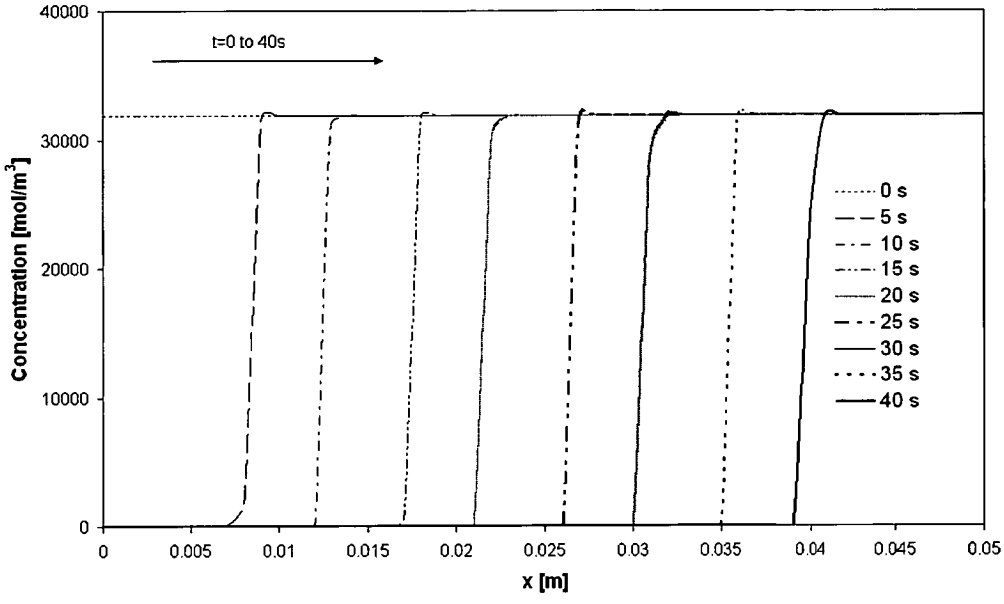

Figure 5.6: Profile of fuel available over 40 s interval

$$R = 9.08 \times 10^{-4} m/s \tag{5.33}$$

with $R^2 = 1.00$, whereas the experimental result obtained for 4mm diameter Tasmanian oak

$$R = 8.58 \times 10^{-4} + 0.34 \times 10^{-4} m/s \tag{5.34}$$

While this is a very close result, it is worth noting that all the fuel available was consumed in $0.5s$, much before residence time.

5.3 Effect of Diameter

In Chapter 3 experiments were performed for flame spread across cylindrical horizontal elements with different diameters for wood types of Tasmanian *Eucalyptus* species with generic name Tasmanian oak and South American walnut from *Juglandaceae* family with generic name nogal. Using the empirically derived relations for residence time and efficiency of combustion, we derive the Arrhenius pre-exponential coefficient for different diameters to evaluate the effect on rate of spread in the numerical model.

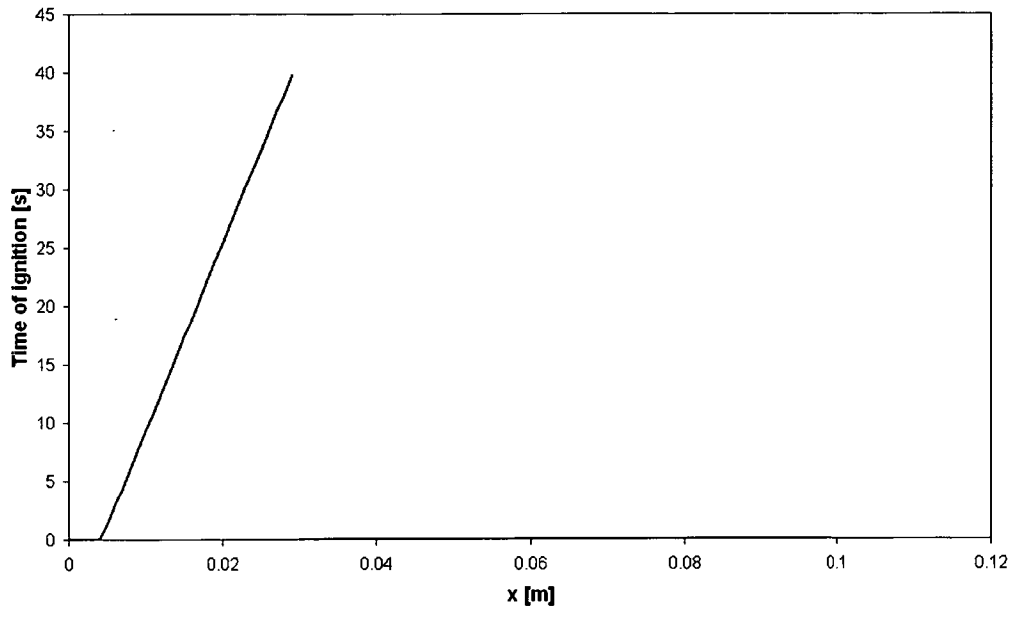

Figure 5.7: Time element at position x first reached temperature of 600K.

5.3.1 Tasmanian oak

Following the same method of calculating Arrhenius pre-exponential rate constant from the fuel available, based on the experimental results on residence time and fuel available and linear approximation of the Arrhenius constant, we have calculated the pre-exponential constant for all the diameters used in the experiments. From equations (5.22), (5.23) and (5.24), we have that

$$k_0(D) = -\frac{\ln\left(1 - 1.123e^{-55.5D}\right)}{[O_2] \times (4056D - 4.59)} \tag{5.35}$$

Again, using activation energy of $50000 Jmol^{-1}$and assuming that the bulk of combustion occurs at flame temperature $1223K$, the Arrhenius pre-exponential factor from equation (5.17) is

$$A = k_0(D)\, e^{\frac{E}{RT_{fl}}} = -\frac{\ln\left(1 - 1.123e^{-55.5D}\right)}{[O_2] \times (4056D - 4.59)} e^{\frac{E}{RT_{fl}}}$$

Using pre-exponential constants as shown in Table 5.3, new rate of spread was measured for the numerical model. The results obtained are plotted in Figure

Table 5.3: Table of Arrhenius pre-exponential coefficents for different diameter

$D[mm]$	t_r	η	k_0	A
4	11.6	0.90	0.0233	3.19
5	15.7	0.85	0.0143	1.96
6	19.7	0.80	0.0098	1.33
7	23.8	0.76	0.0071	0.97
8	27.8	0.72	0.0054	0.74

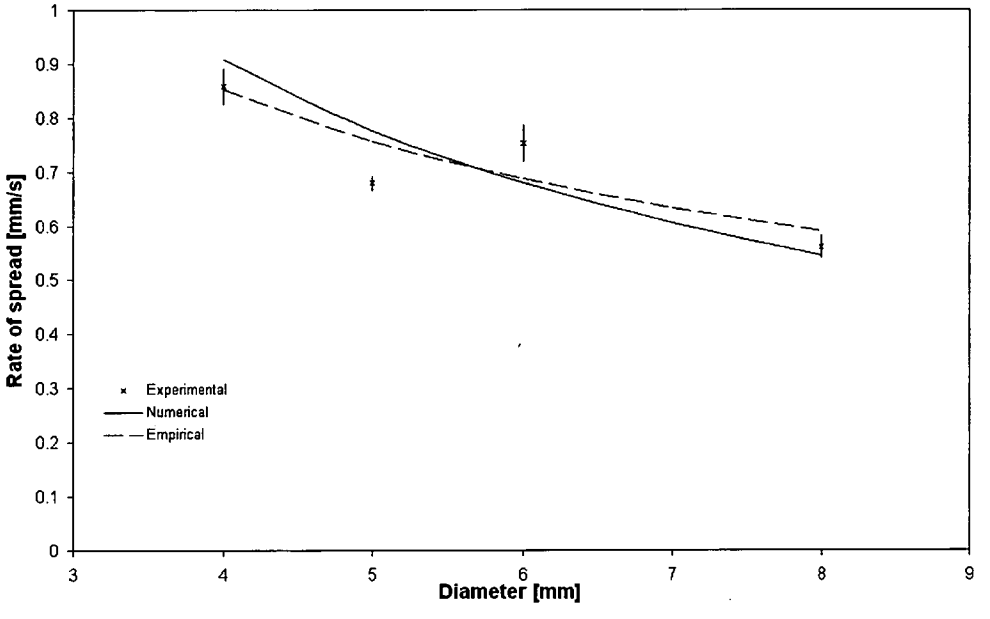

Figure 5.8: Rate of spread for Tasmanian oak, experimental, empirical and numerical data

5.8 against values obtained experimentally, as well as empirical fit given by equation (3.17). We can see that the numerical model manages to adequately predict the rate of spread for Tasmanian oak the diameters of with in this range,with the Arrhenius pre-exponential coefficient defined based on empirical data on resonance time and efficiency of combustion.

5.3.2 Nogal

Initial fuel concentration

Similar to the method used for oak, we now calculate initial 'carbon' concentration for nogal, based on their calorific values.

The energy released by combustion of nogal is found to be $20,478\ Jg^{-1}$ (Appendix A). Therefore, if combustion of 1 g of nogal releases $20,478\ J$ and combustion of 1 mol of carbon releases $393,500J$ of energy, then with our assumption that all of the combustible compounds are carbon, there are 0.052 mol of carbon per gram of nogal.

The dry density of nogal used was measured to be approximately 578 kgm^{-3}; therefore considering the initial molar concentration of carbon in the nogal element to be

$$[C]_0 = 35,283 mol/m^3 \tag{5.36}$$

would generate the appropriate amount of heat during combustion.

Arrhenius pre-exponential constant

Again, we estimate rate constant our assumed constant reaction rate, k_0, from the empirical fits of residence time and efficiency of combustion derived in Chapter 3. Similarly to equation (5.35) we now have

$$k_0(D) = -\frac{\ln\left(1 - 1.123e^{-55.5D}\right)}{[O_2] \times (5723D - 3.94)}, \tag{5.37}$$

from equations (3.29), (3.35) and (5.26).

Again, using activation energy of $50000 Jmol^{-1}$and assuming that the bulk of combustion occurs at flame temperature $1223K$, the Arrhenius pre-exponential factor from equation (5.17) is

$$A = -\frac{\ln\left(1 - 1.123e^{-55.5D}\right)}{[O_2] \times (5723D - 3.94)} e^{\frac{E}{RT_{fl}}} \tag{5.38}$$

which for diameters used in experiments ($2mm$ to $8mm$) is shown in Table 5.4.

Table 5.4: Table of Arrhenius pre-exponential coefficents for different diameter

$D[mm]$	$t_r[s]$	η	k_0	A
2	7.1	0.96	0.0528	7.23
3	12.0	0.93	0.0261	3.58
4	17.6	0.88	0.0143	1.96
5	26.9	0.89	0.0096	1.31
6	33.4	0.86	0.0069	0.95
8	36.0	0.70	0.0040	0.55

Other parameters

The density of nogal wood used in the experiments was measured to be $578kg/m^3$.

The coefficient for conductivity and specific heat used were the same as used for oak, due to the inability to obtain exact values for nogal wood. Specific heat is generally affected by moisture content and temperature, but is hardly varied with wood species (Steinhagen 1977).

Results

Using the parameters described above a numerical simulation was run for $10cm$ long horizontal nogal cylinder. The temperature and fuel concentration profiles simulated across a 10cm long and 2mm diameter element over period of 40 seconds is shown in Figures 5.10 and 5.9.

The rate of spread was again measured by recording the time when each section of the element reached ignition temperature. These times of 'ignition' along the length of the element are shown in Figure 5.11 for different diameters. The rate of spread of flame against time recorded for each diameter is plotted in figure 5.12, as well as the experimental results from Chapter 3 and the empirical fit for the rate of spread (equation 3.16) is shown in the Figure 5.12. We see that the numerical simulation consistently underestimates the observed values. This may be able to be improved upon by using coefficients for conductivity and specific heat capacity obtained for this particular wood. However, using the method of adjusting the pre-exponential coefficient to the experimental results of residence time and efficiency, appears to have provided numerical simulation that underestimates the observed rate of spread by only 11% on

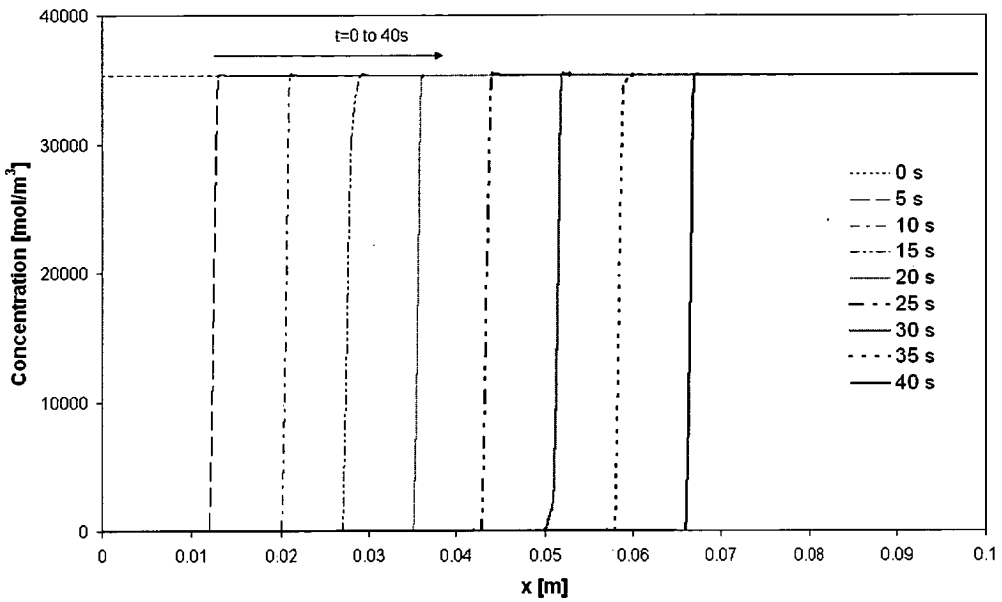

Figure 5.9: Profile of fuel concentration across a 10cm long nogal cylinder of 2mm diamter over 40s time interval.

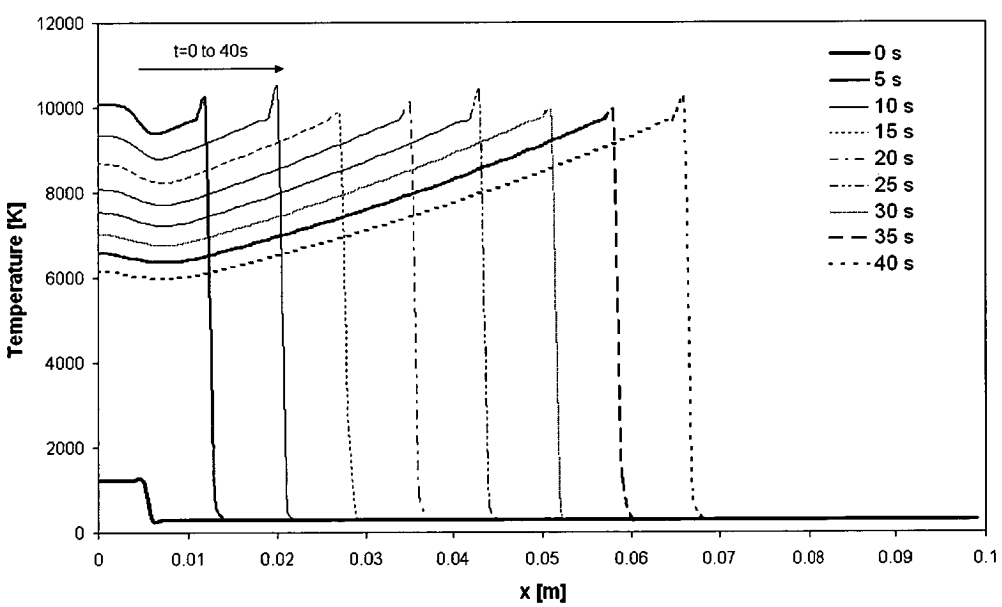

Figure 5.10: Temperature profiles for 2mm diameter cylinder of nogal wood over 40s interval

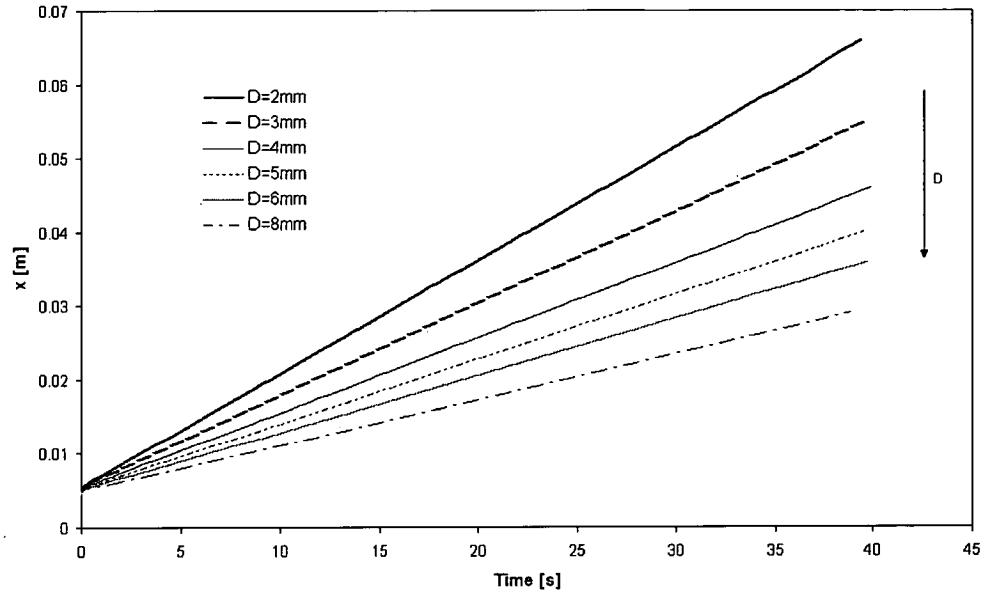

Figure 5.11: Times that a section of element (x) first reached the ignition temperature, for different diameters of nogal wood.

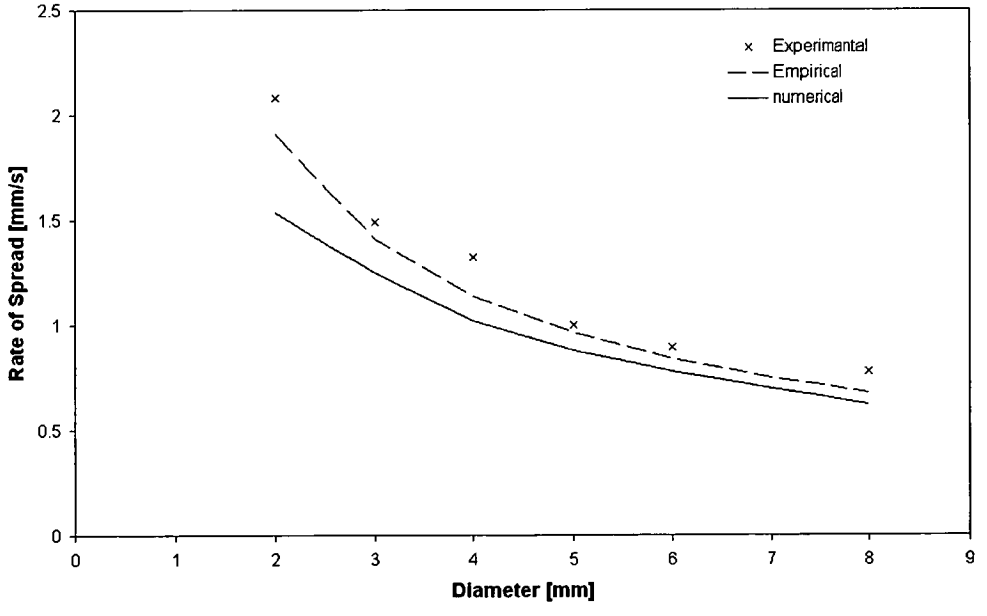

Figure 5.12: Average values of the rate of spread for different diameter of nogal wood, empirical fit and numerical solution. Error bars represent standard error.

average.

5.4 Effects of Fuel Moisture

Moisture content in fuel in this model is simplified through the usage of 'average specific heat' coefficient (equation 5.5). In the previous section, the model was simulating flame spread across dry elements. In this section, we are investigating whether this simplification can adequately describe the slowing of the flame progress observed in Chapter 3 as the moisture in the fuel increases. The fuel used in experiments was 2 mm diameter birch wood and the parameters used in model are described below.

5.4.1 Initial fuel concentration

We now calculate the initial 'carbon' concentration for birch wood elements, based on their calorific values. The energy released by combustion of birch wood is found to be $19,713\ Jg^{-1}$ (Appendix A). Again, as 1 mol of carbon releases $393,500J$ of energy, then with our assumption that all of the combustible compounds are carbon, there are 0.052 mol of carbon per gram of birch wood used.

The dry density of the elements used was measured as 642 kgm^{-3}; therefore we consider that the initial molar concentration of carbon in the birch element of

$$[C]_0 = 32,162 mol/m^3 \tag{5.39}$$

would generate the appropriate amount of heat during combustion.

5.4.2 Parameters

Density of $642 kg/m^3$ was measured for this wood type.

Suleiman et al. (1999) measured thermal conductivity for birch of $0.291 - 0.323 W/mK$ in parallel and $0.177 - 0.214 W/mK$ perpendicular to the grain

direction. As the direction of grain could not be ascertain in the elements used, a value of $0.25W/mK$ was for thermal conductivity of birch in this model.

The specific heat of birch used was $2500J/kgK$ as was for the previous elements.

5.4.3 Arrhenius pre-exponential constant

In the experiments performed for this fuel after the flame passed the remaining fuel glowed until the remaining ash broke off the element. Therefore it was not possible to estimate the correct efficiency of combustion, though it was apparent that it was quite high. However taking the efficiency to be 100% makes it impossible to estimate the coefficient k_0 from Equation (5.22). As we are interested in the effect of altering average specific heat coefficient c^* the pre-exponential coefficient in Arrhenius rate reaction was chosen to such that the simulated rate of flame spread for dry element matched the simulated one. This was observed to be the case for the pre-exponential coefficient 8.25 m^3mols^{-1}.This is the coefficient that would have been calculated had the efficiency of combustion been at 96%, with activation energy of $50000Jmol^{-1}$and assuming that the bulk of combustion occurs at flame temperature $1223K$, and with residence time of $6.3s$ (Equation 3.52). That is

$$A = -\frac{\ln(1-0.96)}{[O_2]\times 6.3} e^{\frac{E}{RT_{fl}}} = 8.25\ m^3mols^{-1}, \tag{5.40}$$

which was the pre-exponential coefficient used for all the simulations shown, as the efficiency and residence time was taken to be unaffected with the moisture content change.

5.4.4 Dry Element

With the parameters described above the flame spread simulated for a dry element is shown in the following graphs. The temperature profile is shown in Figure 5.13 and the fuel concentration is plotted in Figure 5.14.

The rate of spread is again detected as the time when the section of the element first reached the temperature of ignition. These are shown in Figure 5.15.

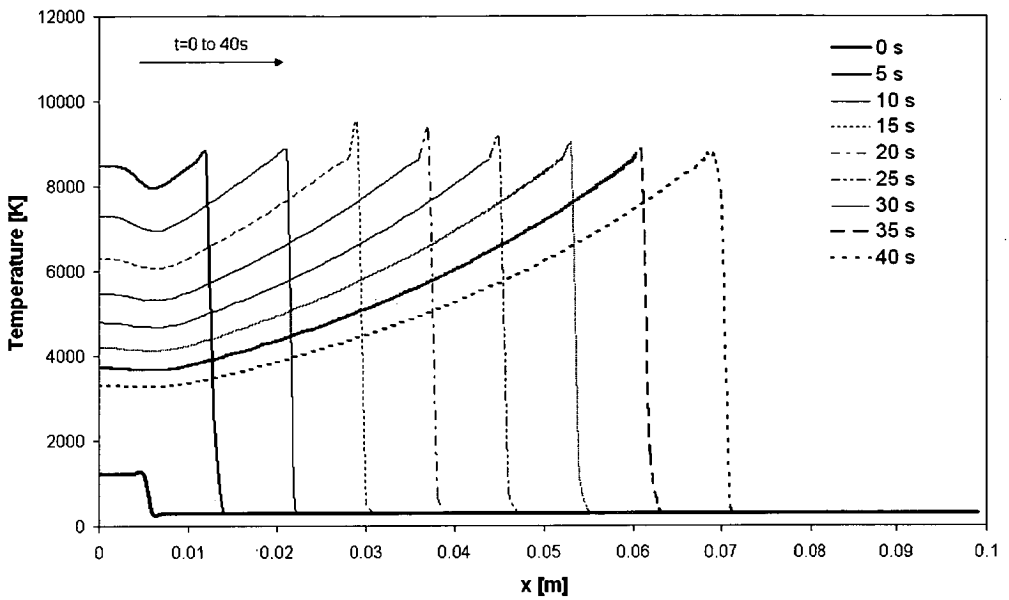

Figure 5.13: Temperature profiles across 10cm long dry birch wood cylinder of 2 mm diameter over 40s time interval.

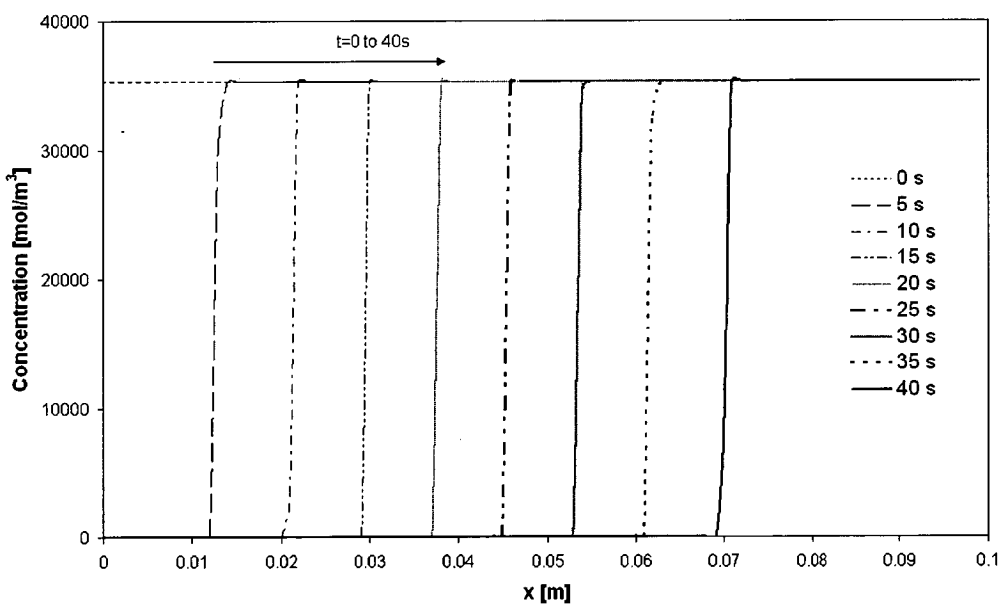

Figure 5.14: Fuel concentration profiles over 40 seconds interval for flame progression across a dry birchwood cylinder of 10 cm length and 2 mm diameter.

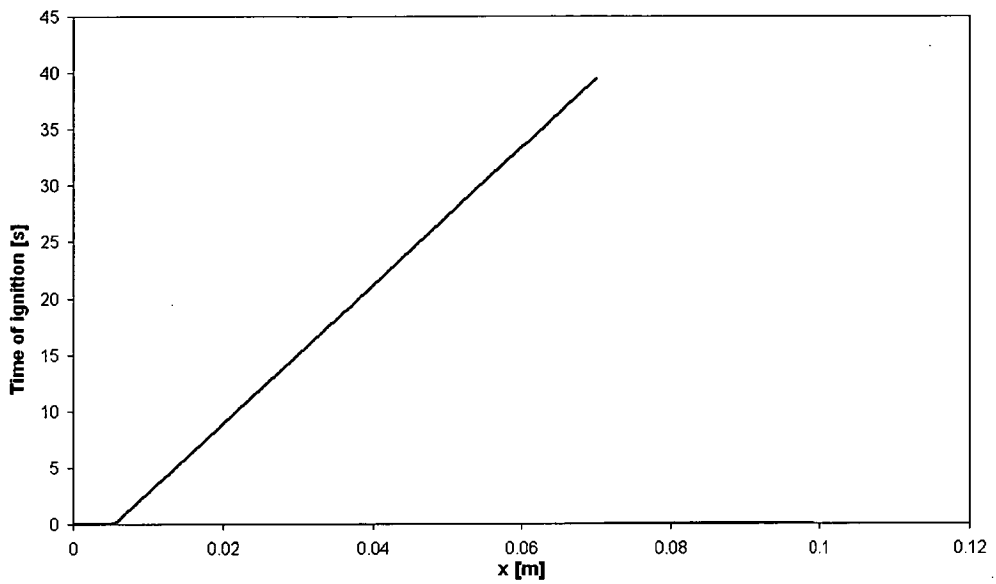

Figure 5.15: Ignition time across the length of a dry birch wood cylinder of 2 mm diameter over 40s time interval.

5.4.5 Varying Fuel Moisture Content

Varying fuel moisture content in this model affects only average specific heat. Figure 5.16 shows that the rate of spread simulated for fuel moisture content up to 10% has slowed down with increased moisture content. The rate of flame spread simulated for different moisture content is compared to the experimentally obtained values as well as those predicted by the empirical fit given in Chapter 3 by equation (3.37). We see that the model manages to adequately represent the observed change in the rate of spread with this simple assumption.

5.5 Conclusion

In this chapter a one dimensional numerical model is proposed for the flame spread across horizontal element. The heat is spread through conduction, lost through Newton cooling and generated through heat reaction. The fuel is described through one element, the properties of which are derived from the

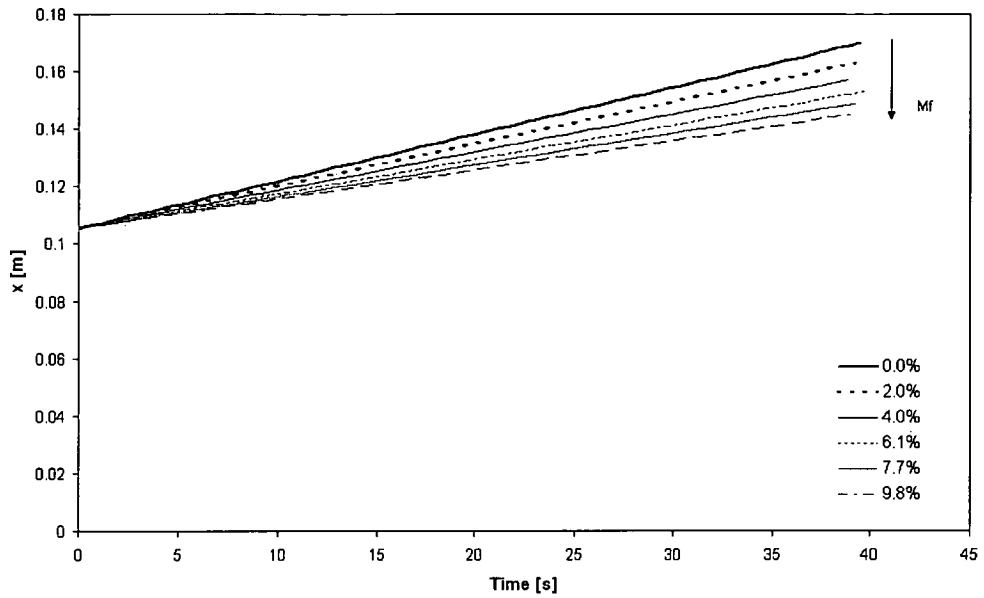

Figure 5.16: Change in the flame ignition across an element versus fuel moisture content

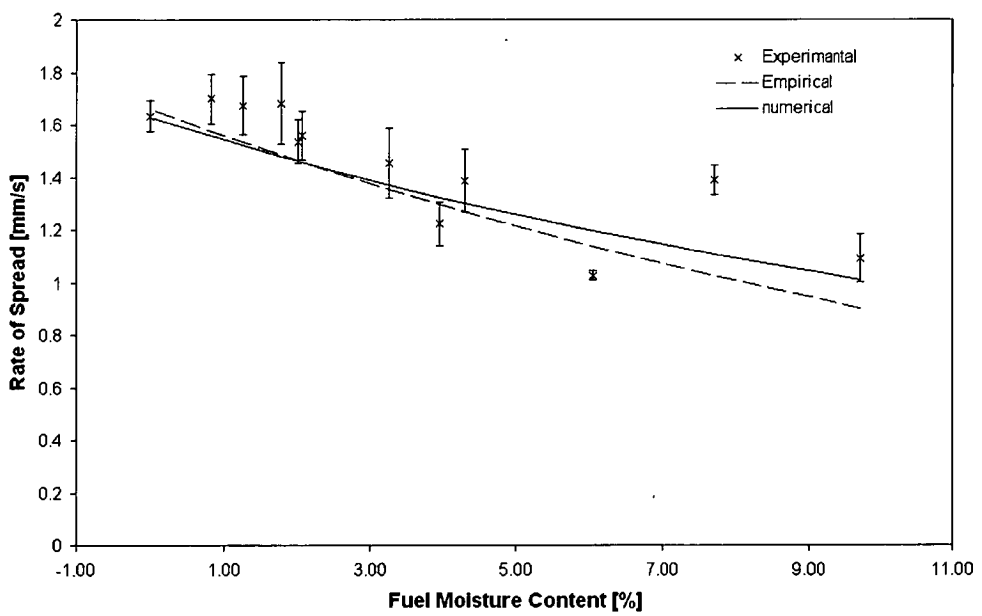

Figure 5.17: Rate of spread for 2mm birch wood cylinders versus fuel moisture content for experimental values, empirical fit and numerical simulation. Error bars on experimental values represent standard error of the mean.

experimental data observed. The rate of reaction is described using Arrhenius rate reaction where the Arrhenius pre-exponential is varied depending on the efficiency of combustion and residence time experimentally observed. The fuel moisture content was treated through use of average specific heat coefficient.

The numerical model has managed to adequately reflect the change in rate of flame spread with the change of diameter for Tasmanian oak, whilst under predicting by 11% rate of spread of nogal wood.

The use of average specific heat coefficient has managed to simulate the rate of flame spread observed in the experiments for 2 mm birch wood cylinders.

Chapter 6

Conclusion

This thesis investigated the properties of flame and the propagation of fire on cylindrical fuel beds composed of several types of wood. The majority of experiments were conducted on Tasmanian Oak, although several other fuel types were considered as well with the empirical and physical models of flame propagation were presented.

The rate of mass loss of a fully ignited horizontal wooden brand was found to be adequately represented by Gaussian bell curve, with parameters dependent on the diameter of fuel. the rate of its mass loss. The flame height was modelled similarly, with the relation between the two developed. The change in the flame shape during the period of burning, the time over which burning occurred and the burn efficiency were also modelled empirically. Correlations relating these quantities to the geometry of the fuel bed and the rate of the fuel mass loss were performed.

A further set of experiments was then performed on flame propagation along the cylindrical brand, for several wood types. The speed of the flame front, the flame height and width, the rate of fuel consumption and the efficiency were all measured, and their behaviour was correlated to the angle of the fuel bed to the horizontal, and to the diameter of the fuel cylinder and the initial moisture content. Some additional experiments were also performed on parallel horizontal cylindrical fuel brands, and the separation between them was found to have a significant effect on flame height. The rate of flame spread as expected, reduced with the increase in diameter, fuel moisture content and

inclination of the angle. The efficiency of combustion and the time of flaming were used for the parameters in the numerical model. The separation between elements allowed more buoyancy to the flame with flame height only affected in this configuration, indicating that for such small dry fuel, radiation from the flame has a negligent effect on the rate of flame progress.

Measuring mean effective emissivity of small flames further confirmed this with very low values detected (order of 0.02). The mean effective emissivity increased with the pathlength with the relation described by $1 - e^{-k\lambda}$, were coefficient k was dependent on the fuel configuration.

A mathematical model is presented for describing flame propagation along a horizontal fuel cylinder. Using the heat transfer equations and the one-step kinetic scheme for fuel decomposition, this results in a system of two non-linear coupled partial differential equations involving temperature and carbon concentration in the available fuel, as functions of time and the distance along the fuel bed. Some of the experimentally derived rules were used in the model, and some model parameters have been determined from the experimental observations. A detailed comparison with the experimental observations was undertaken. The model is capable of predicting the observed behaviour. This model is a simplified description of a complex behaviour, with the obvious limitation on depending on experimental observations for the parameters. It would be interesting to investigate whether a convective heating term dependant on the angle of fuel inclination would be adequate to represent the observed flame behaviour for this configuration.

It would also be interesting to investigate how these results might scale to a larger fire or to non-uniform fuel. In larger fires, radiation effects would be more dominant and therefore necessary to include in the model. Fuel bed packing ratio and availability of oxygen would also be factors that would need to be considered. The extent to which these may be incorporated in this model may be of interest in the future research.

Appendix A

Heat of Combustion

Experiments to determine the heat of combustion for different wood types were conducted using a Gallenkamp Automatic Adiabatic Bomb Calorimeter, $CBA - 301 - 010$. This instrument consists of a bomb, calorimetric vessel, water jacket and the ignition mechanism.

The bomb contains a fuel crucible, an electrode and a firing wire. A strand of cotton is tied to the firing wire with the other end immersed in the fuel crucible filled with finely ground fuel. The fuel crucible is hung in the bomb which is filled with 1 ml of distilled water. The bomb is then sealed and filled with oxygen gas to 30 bar pressure.

The bomb is placed in a calorific vessel filled with distilled water. Extreme care is taken to ensure the weight of the vessel and the water does not vary by more than 0.5 g between the tests. There is a water jacket around the calorimetric vessel that provides an enclosure for the calorimetric system. Throughout a test, the temperature of the water jacket is maintained at the level of the calorimetric vessel's temperature, using a heating and cooling system. The heat transfer between the vessel and the surroundings is thus minimized.

When the instrument is assembled, it is allowed time to stabilise so that the temperatures of the bomb, calorimetric vessel and the water jacket can reach equilibrium. An electric pulse ignites the cotton strand, which then ignites the fuel. When the fuel is ignited, the heat of the bomb is transferred to the water in the calorimetric vessel. The change between the maximum temperature

reached and the initial temperature of the water is used to calculate the calorific value of the fuel.

The instrument is calibrated against benzoic acid, $C_7H_6O_2$, which has calorific value of $26,442\ Jg^{-1}$ (*CRC Handbook of Chemistry and Physics, 80th Edition* 1999, p 5-89). The temperature difference measured from combustion of $1g$ of benzoic acid provides the effective heat capacity of the apparatus. The average effective heat capacity of the apparatus $Q_{apparatus}$ was measured to be $10,533J/C$ with standard error of $\pm 15J/C$.

All the fuel used in this experiment was oven dried over night and chipped into fine fuel. The apparatus was calibrated prior to each series of tests to ensure that the results are not affected by the instrument setup. The variations between the effective heat capacity of the apparatus measurements were found to be less than 1%. After a fuel sample had been prepared and inserted into the apparatus, the temperature of the vessel was recorded every 30 s. Initially, the equilibrium between the apparatus and the fuel bomb needed to be reached. This was considered to be the case after four readings of unchanged temperature T_0 were reported. At that time, the fuel was ignited, and temperature rise began. The temperature change in the vessel was recorded until it plateaued; that is, when four readings of unchanged temperature, T_f, were reached. A set of data recorded during one measurement is shown in Figure A.1.

The mass m of fuel used was about $1g$ for most of the runs. The only exception to this was the case of the balsa samples. The density of balsa wood is very low and the volume occupied by even a finely cut mass $1g$ of balsa was too large for the fuel crucible. A mass of about $0.5g$ was therefore used for combustion of balsa runs. At the end of the combustion the bomb and the fuel crucible were inspected to ensure that complete combustion occurred and the only remnants were ashes. Runs in which a small piece of wood was not burned, due to fuel falling out of the crucible during or prior to ignition, were disregarded.

The temperature rise that the combustion of the fuel caused in the vessel $\Delta T = T_f - T_0$, the effective heat capacity of the apparatus $Q_{apparatus}$ and the mass of the fuel used m, were used to calculate the heat of combustion,

$$H_c = \frac{\Delta T \times Q_{apparatus}}{m}. \tag{A.1}$$

The heat of combustion was measured for the following wood types: Tasmanian

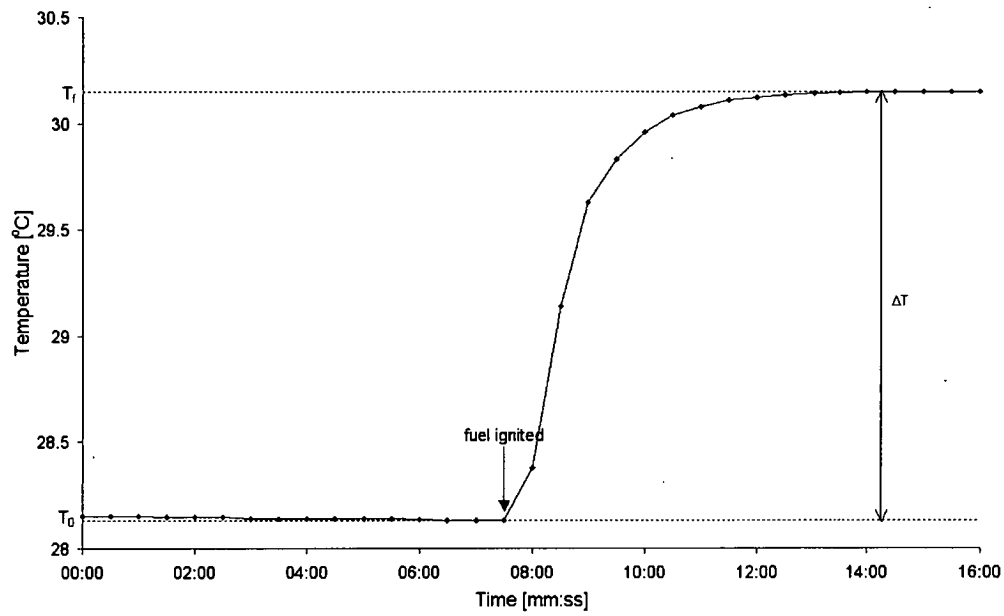

Figure A.1: Heat of combustion measurement for $1.009g$ of oven dried pine needles.

	Birchwood	Pine	Pine Needles	Balsa	Nogal	Ramin	Sapelli	Oak
$H_c[J/g]$	19,713	19,897	21,001	20,440	20,478	20,388	20,307	19,291
σ_{h_c}	115	489	409	570	305	717	1,407	308
$s.e.$	36	155	129	180	96	227	445	97

Table A.1: Heat of combustion

oak, pine, pine needles, nogal, ramin, sapelli, balsa and birchwood. For each of the wood types used, ten repetitions were performed. The results obtained are reported in Table A and Figure A.2. The largest variation in results was recorded for sapelli, which may be related to the large sap content observed during the combustion of sapelli cylinders. Significant difference between the samples measured was tested using ANOVA and is recorded in Table A.

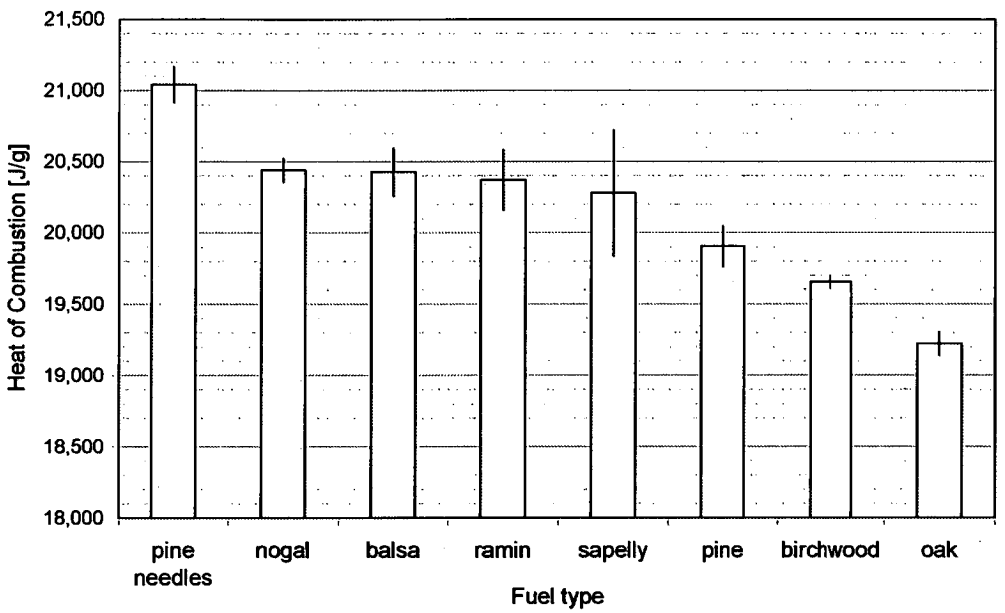

Figure A.2: Heat of combustion for different fuels

	Bw	P	Pn	Bs	N	R	S
P	×						
Pn	✓	✓					
Bs	×	×	×				
N	×	×	×	×			
R	×	×	×	×	×		
S	×	×	×	×	×	×	
O	×	×	✓	✓	✓	✓	✓
$Bw-$ birchwood, $P-$ pine, $Pn-$ pine needles, $Bs-$ balsa, $N-$ nogal, $R-$ ramin, $S-$sapelli, $O-$oak							
×− no significant difference, ✓− significant difference measured							

Table A.2: Heat of combustion

Appendix B

Flame Height And Mass Loss Rate Fit Statistics

Table B.1 lists parameters obtained and their deviation from the Gaussian fit to the mass loss rate data [g] measured, $\dot{m} = \dot{m}_{\max} e^{-\frac{(t'-t^*)^2}{2\sigma_m^2}}$. Note that $t = 0$ represents the time when 50% mass loss was achieved; hence, t^* is the correction to the time t, of the experimental measurement time. There were therefore 3 parameters fitted, $\dot{m}_{\max}, \sigma_m$ and t^* but t^* was irrelevant to the model, and hence is not given here. The model is fitted using the CURVEFIT function in the IDL programming language, based on a code from Bevington (Bevington 1969) p237-239. The error in data points was considered to be no more than 10% of the maximum value measured, and all data points were given equal weight. The parameters obtained, standard error in the parameters estimated, R^2 correlation between the observed and predicted data, and reduced χ^2 values are given in this table.

Table B.1: Parameters for Gaussian rate of massloss function

run	D	$\dot{m}_{\max}$	*st.dev* in $\dot{m}_{\max}$	σ_m	*st.dev* in σ_m	R^2	χ^2
0-cdoa	4	0.0470	0.0026	6.52	0.40	0.954	0.557

1-cdoA	4	0.0425	0.0018	8.10	0.41	0.953	0.649
2-cdoA	4	0.0419	0.0017	7.13	0.32	0.969	0.646
3-cdoA	4	0.0440	0.0020	6.42	0.32	0.967	0.594
4-cdoA	4	0.0413	0.0014	7.65	0.30	0.978	0.599
5-cdoA	4	0.0388	0.0015	9.68	0.43	0.915	1.079
6-cdoA	4	0.0385	0.0017	6.73	0.32	0.975	0.419
7-cdoA	4	0.0382	0.0015	7.02	0.31	0.984	0.280
8-cdoA	4	0.0411	0.0013	8.99	0.33	0.982	0.361
9-cdoA	4	0.0357	0.0012	10.3	0.41	0.972	0.403
10-cdoA	4	0.0394	0.0015	7.66	0.34	0.945	0.918
0-cdoB	4	0.0302	0.0011	7.06	0.29	0.982	0.331
1-cdoB	4	0.0335	0.0013	6.53	0.30	0.983	0.528
2-cdoB	4	0.0326	0.0014	6.52	0.33	0.970	0.704
3-cdoB	4	0.0344	0.0014	5.91	0.26	0.975	0.619
4-cdoB	4	0.0330	0.0015	5.52	0.27	0.969	0.681
5-cdoB	4	0.0365	0.0014	7.15	0.30	0.980	0.517
6-cdoB	4	0.0396	0.0019	5.25	0.28	0.980	0.523
7-cdoB	4	0.0334	0.0014	6.26	0.30	0.978	0.622
8-cdoB	4	0.0327	0.0014	6.33	0.30	0.969	0.630
9-cdoB	4	0.0356	0.0020	4.12	0.26	0.942	1.246
10-cdoB	4	0.0326	0.0013	7.20	0.32	0.967	0.917
11-cdoB	4	0.0378	0.0018	5.25	0.28	0.979	0.418
11-cdoA	5	0.0408	0.0015	9.35	0.38	0.979	0.371
13-cdoA	5	0.0357	0.0012	10.1	0.38	0.980	0.423
14-cdoA	5	0.0355	0.0013	7.58	0.32	0.977	0.479
15-cdoA	5	0.0439	0.0019	7.64	0.38	0.968	0.532
16-cdoA	5	0.0406	0.0013	9.69	0.35	0.972	0.649
17-cdoA	5	0.0348	0.0012	10.1	0.39	0.967	0.651
18-cdoA	5	0.0387	0.0014	10.2	0.40	0.965	0.694
19-cdoA	5	0.0444	0.0016	11.2	0.50	0.973	0.531
20-cdoA	5	0.0387	0.0018	8.53	0.45	0.953	0.602
21-cdoA	5	0.0377	0.0011	10.3	0.34	0.986	0.326
22-cdoA	5	0.0395	0.0019	6.86	0.38	0.960	0.662
12-cdoB	5	0.0234	0.0008	9.87	0.36	0.973	0.690
13-cdoB	5	0.0331	0.0011	9.05	0.34	0.972	0.605
14-cdoB	5	0.0332	0.0011	10.7	0.40	0.966	0.708
15-cdoB	5	0.0313	0.0010	10.2	0.39	0.960	1.045

16-cdoB	5	0.0280	0.0010	11.2	0.55	0.923	1.718
17-cdoB	5	0.0365	0.0012	8.85	0.34	0.980	0.501
18-cdoB	5	0.0340	0.0011	10.9	0.40	0.967	0.677
19-cdoB	5	0.0237	0.0007	10.8	0.42	0.975	0.642
20-cdoB	5	0.0337	0.0011	9.93	0.40	0.976	0.558
21-cdoB	5	0.0328	0.0011	9.82	0.44	0.977	0.606
22-cdoB	5	0.0328	0.0011	9.89	0.38	0.971	0.657
23-cdoA	6	0.0432	0.0013	10.3	0.36	0.983	0.432
24-cdoA	6	0.0360	0.0011	13.5	0.45	0.976	0.397
25-cdoA	6	0.0394	0.0011	11.7	0.38	0.985	0.365
26-cdoA	6	0.0423	0.0012	14.2	0.46	0.975	0.405
27-cdoA	6	0.0394	0.0016	9.93	0.45	0.957	0.716
28-cdoA	6	0.0338	0.0010	12.9	0.44	0.979	0.394
29-cdoA	6	0.0449	0.0014	11.0	0.38	0.972	0.734
30-cdoA	6	0.0390	0.0011	12.2	0.37	0.977	0.656
31-cdoA	6	0.0351	0.0011	10.9	0.38	0.967	0.789
32-cdoA	6	0.0358	0.0011	11.0	0.38	0.975	0.631
33-cdoA	6	0.0444	0.0013	11.4	0.37	0.979	0.613
34-cdoA	6	0.0443	0.0013	12.2	0.75	0.988	0.356
35-cdoA	6	0.0422	0.0013	11.2	0.40	0.943	1.317
36-cdoA	6	0.0334	0.0010	13.1	0.44	0.974	0.450
23-cdoB	6	0.0450	0.0014	10.5	0.36	0.987	0.355
24-cdoB	6	0.0400	0.0013	11.1	0.40	0.963	0.823
25-cdoB	6	0.0429	0.0014	11.3	0.43	0.969	0.615
26-cdoB	6	0.0377	0.0013	11.7	0.50	0.976	0.454
27-cdoB	6	0.0442	0.0013	12.7	0.47	0.979	0.455
28-cdoB	6	0.0412	0.0013	11.3	0.39	0.967	0.836
29-cdoB	6	0.0373	0.0013	10.6	0.47	0.936	1.335
30-cdoB	6	0.0384	0.0014	10.4	0.47	0.963	0.743
31-cdoB	6	0.0453	0.0015	9.86	0.38	0.989	0.255
32-cdoB	6	0.0391	0.0012	10.6	0.38	0.974	0.590
37-cdoA	8	0.0476	0.0011	20.8	0.56	0.971	0.652
38-cdoA	8	0.0529	0.0012	20.2	0.52	0.968	0.859
39-cdoA	8	0.0443	0.0010	18.1	0.49	0.969	0.824
40-cdoA	8	0.0461	0.0011	18.4	0.48	0.974	0.695
41-cdoA	8	0.0598	0.0015	19.7	0.56	0.978	0.457
42-cdoA	8	0.0465	0.0010	20.7	0.51	0.972	0.762

43-cdoA	8	0.0416	0.0009	20.1	0.52	0.967	0.834
44-cdoA	8	0.0425	0.0011	19.7	0.57	0.947	1.192
45-cdoA	8	0.0451	0.0012	23.0	0.86	0.916	1.330
46-cdoA	8	0.0449	0.0010	20.2	0.49	0.974	0.727
47-cdoA	8	0.0435	0.0012	19.6	0.64	0.957	0.714
33-cdoB	8	0.0438	0.0010	25.3	1.02	0.957	0.923
35-cdoB	8	0.0387	0.0008	24.7	0.64	0.970	0.590
36-cdoB	8	0.0407	0.0010	20.5	0.60	0.963	0.712
37-cdoB	8	0.0480	0.0011	19.7	0.52	0.965	0.876
38-cdoB	8	0.0369	0.0008	22.7	0.59	0.948	1.224
48-cdoA	9.5	0.0510	0.0010	24.0	0.56	0.969	0.834
49-cdoA	9.5	0.0495	0.0012	23.4	0.76	0.941	1.055
50-cdoA	9.5	0.0485	0.0013	21.8	0.65	0.956	0.737
51-cdoA	9.5	0.0434	0.0009	24.1	0.57	0.966	0.846
52-cdoA	9.5	0.0414	0.0008	27.0	0.74	0.942	1.078
53-cdoA	9.5	0.0513	0.0012	26.7	0.72	0.948	0.911
54-cdoA	9.5	0.0555	0.0016	21.2	0.67	0.951	0.807
55-cdoA	9.5	0.0385	0.0009	24.3	0.80	0.937	1.036
56-cdoA	9.5	0.0493	0.0010	25.5	0.60	0.956	1.071
57-cdoA	9.5	0.0588	0.0013	25.3	0.67	0.958	0.792
58-cdoA	9.5	0.0469	0.0012	24.3	0.76	0.920	1.266
59-cdoA	9.5	0.0580	0.0014	22.1	0.60	0.963	0.806
34-cdoB	9.5	0.0398	0.0008	25.7	0.61	0.962	0.867
39-cdoB	9.5	0.0447	0.0010	25.0	1.20	0.944	1.187
40-cdoB	9.5	0.0497	0.0009	25.1	0.56	0.971	0.831
41-cdoB	9.5	0.0431	0.0009	24.9	0.60	0.954	1.047
42-cdoB	9.5	0.0462	0.0009	25.2	0.57	0.967	0.860
43-cdoB	9.5	0.0450	0.0011	25.6	0.77	0.938	0.960

Table B.2 lists parameters and their deviation from the Gaussian fit to the average flame height data [cm] measured, $H = H_{\max} e^{-\frac{(t'-t^*)^2}{2\sigma_f^2}}$. Note that $t = 0$ represents the time when 50% mass loss was achieved; hence, t^* represents the peak time difference between mass loss rate and flame height. The model is fitted for three parameters: $\dot{m}_{\max}, \sigma_m$ and t^*, using the CURVEFIT

function in the IDL programming language based on code from Bevington (Bevington 1969) p237-239. The standard deviation in data points was considered to be no more than 10% value of the maximum point, and all data points were given equal weight. The parameters obtained, standard deviation in the parameters estimated, R^2 correlation between the observed and predicted data, and reduced χ^2 value are given in this table.

Table B.2: Parameters for Gaussian average flame height function

run	D	$H_{\max}$	*st.dev* in $H_{\max}$	σ_f	*st.dev* in σ_f	t^*	*st.dev* in t^*	R^2	χ^2
1-cdoA	4	3.28	0.14	6.63	0.42	-1.24	0.51	0.963	0.503
2-cdoA	4	3.18	0.13	9.72	1.10	-1.09	0.67	0.959	0.197
3-cdoA	4	2.90	0.13	8.19	1.51	-1.65	0.90	0.966	0.125
4-cdoA	4	3.04	0.11	11.5	1.47	-0.47	0.87	0.943	0.248
5-cdoA	4	2.80	0.10	9.92	0.59	-3.31	0.61	0.979	0.218
6-cdoA	4	3.09	0.12	6.82	0.47	-2.08	0.47	0.976	0.320
7-cdoA	4	3.05	0.12	7.72	0.63	-3.53	0.58	0.989	0.149
8-cdoA	4	2.80	0.10	10.4	0.73	-2.66	0.61	0.970	0.278
9-cdoA	4	2.94	0.09	13.1	1.24	-4.54	1.01	0.983	0.133
10-cdoA	4	2.88	0.12	8.77	0.70	-2.53	0.56	0.979	0.145
0-cdoB	4	3.45	0.15	7.08	0.51	-3.51	0.51	0.979	0.333
1-cdoB	4	3.20	0.13	7.49	0.54	-2.83	0.51	0.956	0.710
2-cdoB	4	3.51	0.16	6.45	0.42	-2.74	0.46	0.970	0.570
3-cdoB	4	2.88	0.12	6.71	0.53	-3.94	0.57	0.990	0.267
4-cdoB	4	2.75	0.13	6.61	1.06	-3.95	0.86	0.971	0.285
5-cdoB	4	2.90	0.13	7.32	0.89	-5.45	0.80	0.983	0.180
6-cdoB	4	2.59	0.14	5.32	0.83	-2.69	0.50	0.977	0.093
7-cdoB	4	2.93	0.12	7.65	0.81	-3.41	0.70	0.979	0.225
10-cdoB	4	2.93	0.14	6.78	0.82	-3.66	0.57	0.988	0.066
11-cdoB	4	2.46	0.21	10.1	3.21	-6.58	3.86	0.753	2.778
11-cdoA	5	8.14	0.37	9.65	1.30	-2.11	0.77	0.905	0.330
13-cdoA	5	2.94	0.10	10.4	0.65	-2.69	0.59	0.943	0.496
14-cdoA	5	3.06	0.13	10.8	1.57	-1.69	0.82	0.972	0.084
15-cdoA	5	2.60	0.11	8.74	0.82	-3.73	0.77	0.980	0.278
16-cdoA	5	2.60	0.12	12.5	1.99	0.35	1.20	0.854	0.920

17-cdoA	5	3.33	0.12	13.1	1.51	-2.81	0.83	0.932	0.181
18-cdoA	5	2.79	0.12	12.9	1.93	-1.90	0.99	0.872	0.279
19-cdoA	5	2.82	0.10	14.9	1.25	-3.98	1.01	0.970	0.266
20-cdoA	5	3.00	0.15	7.68	0.57	1.18	0.60	0.896	0.837
21-cdoA	5	3.45	0.11	14.4	1.46	-3.10	0.81	0.966	0.093
22-cdoA	5	2.77	0.12	7.95	0.67	-1.71	0.56	0.894	0.850
12-cdoB	5	3.01	0.10	11.4	0.76	-4.12	0.69	0.952	0.578
13-cdoB	5	3.62	0.13	8.55	0.48	-3.68	0.51	0.978	0.360
15-cdoB	5	3.14	0.11	11.5	0.76	-3.72	0.75	0.962	0.555
16-cdoB	5	2.87	0.09	11.8	0.86	-6.07	0.91	0.978	0.310
17-cdoB	5	3.33	0.12	8.89	0.46	-4.13	0.50	0.986	0.234
18-cdoB	5	2.97	0.10	14.4	1.23	-5.26	1.37	0.964	0.528
19-cdoB	5	2.89	0.14	15.1	2.46	-10.3	3.14	0.985	0.190
20-cdoB	5	3.30	0.12	10.2	0.68	-3.48	0.66	0.947	0.653
21-cdoB	5	3.31	0.11	10.2	0.60	-6.06	0.64	0.982	0.301
22-cdoB	5	3.18	0.12	10.8	0.68	-3.38	0.64	0.931	0.744
23-cdoA	6	3.04	0.10	10.2	0.53	-3.82	0.56	0.967	0.508
24-cdoA	6	2.86	0.08	15.3	0.93	-6.13	0.91	0.984	0.191
25-cdoA	6	3.35	0.11	12.9	0.79	-5.25	0.70	0.967	0.346
26-cdoA	6	3.15	0.09	16.8	1.07	-4.77	0.86	0.987	0.086
27-cdoA	6	2.93	0.12	9.98	0.76	-5.50	0.66	0.818	2.424
28-cdoA	6	3.22	0.11	12.8	0.58	-3.79	0.63	0.968	0.428
29-cdoA	6	2.86	0.11	14.9	1.76	-1.65	0.90	0.947	0.136
30-cdoA	6	3.18	0.11	14.1	0.89	-5.83	0.80	0.984	0.159
31-cdoA	6	2.82	0.09	13.0	0.71	-4.97	0.67	0.953	0.559
32-cdoA	6	3.25	0.00	12.3	0.01	-2.94	0.37	0.976	0.200
33-cdoA	6	3.09	0.10	11.6	0.80	-2.25	0.67	0.959	0.409
34-cdoA	6	3.28	0.12	11.4	0.92	-6.56	0.93	0.900	0.530
35-cdoA	6	3.22	0.10	15.4	1.88	-3.54	1.15	0.884	0.356
36-cdoA	6	2.30	0.07	16.3	0.98	-7.16	0.95	0.991	0.136
23-cdoB	6	3.69	0.13	9.11	0.47	-5.81	0.55	0.982	0.397
24-cdoB	6	3.10	0.09	14.3	1.17	-7.94	1.07	0.962	0.436
25-cdoB	6	3.25	0.11	13.9	1.21	-4.79	0.79	0.863	0.578
26-cdoB	6	3.41	0.11	12.9	0.70	-4.93	0.72	0.952	0.591
27-cdoB	6	2.74	0.07	19.3	1.88	-8.65	1.66	0.947	0.474
28-cdoB	6	3.43	0.14	12.9	1.00	-4.70	0.88	0.978	0.290
29-cdoB	6	3.33	0.12	10.5	0.82	-5.14	0.76	0.977	0.216

30-cdoB	6	3.19	0.10	14.8	1.43	-6.17	1.15	0.949	0.373
31-cdoB	6	3.25	0.11	19.1	3.37	-3.63	1.57	0.874	0.230
32-cdoB	6	3.45	0.11	11.8	0.80	-5.30	0.73	0.986	0.150
37-cdoA	8	3.56	0.08	28.7	1.57	-9.46	1.22	0.925	0.495
38-cdoA	8	3.14	0.07	27.5	1.67	-11.4	1.40	0.957	0.385
39-cdoA	8	2.63	0.06	26.9	2.17	-12.3	1.99	0.968	0.265
40-cdoA	8	2.78	0.07	21.0	1.19	-8.58	1.09	0.949	0.552
41-cdoA	8	3.27	0.11	24.2	1.35	-8.88	1.01	0.929	0.659
42-cdoA	8	3.02	0.07	27.6	1.87	-10.8	1.32	0.950	0.282
43-cdoA	8	3.48	0.14	25.6	2.35	-8.74	1.77	0.958	0.449
44-cdoA	8	2.82	0.07	29.9	2.92	-10.5	1.56	0.872	0.405
45-cdoA	8	3.29	0.10	26.2	1.85	-9.64	1.84	0.979	0.310
46-cdoA	8	3.54	0.09	22.6	1.18	-8.70	1.10	0.970	0.419
47-cdoA	8	2.40	0.08	26.6	3.02	-12.8	3.49	0.976	0.227
33-cdoB	8	3.37	0.08	31.3	2.73	-11.1	1.63	0.917	0.181
34-cdoB	8	4.06	0.08	30.0	1.15	-13.9	1.12	0.964	0.546
35-cdoB	8	3.05	0.06	31.6	1.91	-11.2	1.64	0.963	0.317
36-cdoB	8	3.42	0.07	25.0	1.18	-8.36	1.02	0.919	0.873
37-cdoB	8	3.19	0.07	25.2	1.43	-9.73	1.22	0.916	0.762
48-cdoA	9.5	3.50	0.13	29.1	1.97	-12.4	1.40	0.953	0.392
49-cdoA	9.5	3.41	0.12	28.8	3.15	-10.1	2.90	0.963	0.525
50-cdoA	9.5	4.04	0.16	27.9	2.02	-3.48	1.55	0.941	0.714
51-cdoA	9.5	3.58	0.07	32.7	1.59	-10.3	1.25	0.947	0.353
52-cdoA	9.5	3.53	0.07	29.6	1.19	-7.79	1.14	0.973	0.278
53-cdoA	9.5	3.35	0.11	28.3	2.42	-16.4	2.37	0.983	0.306
54-cdoA	9.5	3.72	0.09	26.1	1.29	-5.96	1.15	0.872	1.116
55-cdoA	9.5	3.21	0.06	33.3	1.91	-14.6	1.71	0.969	0.284
56-cdoA	9.5	3.35	0.07	33.1	1.85	-14.0	1.73	0.920	0.770
57-cdoA	9.5	3.46	0.07	34.9	1.77	-13.8	1.50	0.976	0.198
59-cdoA	9.5	3.49	0.09	24.2	1.11	-7.07	1.06	0.949	0.535
38-cdoB	9.5	3.27	0.07	25.9	1.26	-11.6	1.21	0.969	0.379
39-cdoB	9.5	3.63	0.09	27.9	2.79	-7.52	1.73	0.911	0.186
40-cdoB	9.5	3.51	0.07	35.5	1.91	-12.5	1.59	0.949	0.471
41-cdoB	9.5	3.77	0.09	27.9	1.10	-6.86	1.07	0.969	0.302
42-cdoB	9.5	3.55	0.04	38.6	1.01	-14.7	1.09	0.935	0.472

References

Abramowitz, M. & Stegun, I. (1972), *Handbook of Mathematical Functions*, Dover Publications, Inc., New York.

Albini, F. & Reinhardt, E. (1995), 'Modelling ignition and burning rate of large woody natural fuels', *Int. Journal of Wildland Fire* **5**(2), 81–91.

Ames, W. F. (1977), *Numerical Methods for Partial Differential Equations*, Thomas Nelson & Sons.

Anderson, H. (1969), Heat transfer and fire spread, Technical Report Research Paper INT-69, USDA Forest Service.

Atreya, A. (1983), Pyrolysis, Ignition and Fire Spread on Horizontal Surfaces of Wood, PhD thesis, Harvard University, USA.

Atreya, A. (1998), 'Ignition of fires', *Philosophical Transactions: Mathematical, Physical & Engineering Sciences (The Royal Society)* **356**, 2787–2813.

Babrauskas, V. (2004), *Ignition Handbook*, Fire Science Publishers.

Baines, P. (1990), 'Physical mechanisms for the propagation of surface fires', *Mathematical and computer modelling* **13**, 83–94.

Bamford, C., Crank, J. & Malan, D. (1945), 'The combustion of wood: Part', *Proceedings of the Cambridge Philosiphical Society* **42**, 162–182.

Bevington, P. (1969), *Data Reduction and Error Analysis for the Physical Sciences*, McGraw-Hill Book Company.

Blake, T. & McDonald, M. (1993), 'An examination of flame length data from vertical turbulant diffusion flames', *Combustion and Flame* **94**, 426–432.

Blasi, C. D. (1993), 'Analysis of convection and secondary reacion effects within porous solid fuels undergoing pyrolysis', *Combustion Science and Technology* **90**, 315–340.

Blasi, C. D. (1994), 'Numerical simulation of cellulose pyrolysis', *Biomass and Bioenergy* **7**, 87–98.

Block, B., Hentschel, W. & Ertmer, W. (1998), 'Pyrometric determination of temperature in rich flames and wavelength dependence of their emissivity', *Combustion and Flame* **114**, 359–369.

Brahmi, L., Vietoris, T., Torero, J. & Joulain, P. (1999), 'Estimation of boundary layer diffusion flame temperatures by means of an infrared camera under microgravity conditions', *Measurement Science and Technology* **10**, 859–865.

Catchpole, E. & Catchpole, W. (n.d.), Final report 1999.

Chandler, C., Chaney, P., Thomas, P., Trabaud, L. & Williams, D. (1991), *Fire in Forestry, Volume I, Forest Fire and Behavior*, Krieger Publishing Company, Malabar, Florida.

Choi, M., Hamins, A., Mulholland, G. & Kashiwagi, T. (1994), 'Simultaneous optical measurement of soot volume fraction and temperature in premixed flames', *Combustion and Flame* **99**, 174–186.

Choi, M., Mulholland, G., Hamins, A. & Kashiwagi, T. (1995), 'Comparisons of the soot volume fraction using gravimetric and light extinction techniques', *Combustion and Flame* **102**, 161–169.

CRC Handbook of Chemistry and Physics, 80th Edition (1999), CRC Press LLC.

Dalzell, W. & Sarofim, A. (1969), 'Optical constants of soot and their application to heat-flux calculation', *Journal of Heat Transfer* **91**, 100–104.

De Vries, J. & Breejen, E. D. (1993), Characterization of the visibility of wildfire smoke clouds, *in* A. Kohnle & W. Miller, eds, 'Atmospheric Propagation and Remote Sensing II', Vol. 1968, Proc. SPIE, pp. 716–723.

Delichatsios, M. (2000), 'Flame heat fluxes and correlations of upward flame spread along vertical cylinders in various oxigen environments', *Proceedings of the Combustion Institute* **28**, 2899–2904.

Drysdale, D. (2002), *An Introduction to Fire Dynamics, Second Edition*, John Wiley & Sons.

Dunlap, F. (1912), The specific heat of wood, Technical Report Bulletin 110, USDA Forest Service.

Felske, J. & Tien, C. (1973), 'Calculation of the emissivity of luminous flames', *Combustion Science and Technology* **7**, 25–31.

Fernandez-Pello, A. & Williams, F. (1974), 'Laminar flame spread over PMMA surfaces', *15th Symposium (International) on Combustion* pp. 217–231.

Fonda, R. W. (2001), 'Burning characteristics of needles from eight pine species', *Forset Science* **47**(3), 390–396.

Fons, W., Clements, H. & George, P. (1963), 'Scale effects on propagation rate of laboratory crib fires', *Nineth Symposium (International) on Combustion* pp. 860–866.

Forbes, L. & Gray, B. (1998), 'Burning down the house: The time to ignition of an irradiated solid', *Proceedings of the Royal Society of London A* **454**, 2667–2688.

Gubernov, V., Sidhu, H. & Mercer, G. (2005), 'The effect of ambient temperature on the propagation of nonadiabetic combustion waves', *Journal of Mathematical Chemistry* **37**(2), 149–162.

Guelzim, A., Souil, J. & Vanelon, J. (1993), 'Suitable configuration factors for radiation calculation concerning tilted flames', *Journal of Heat Transfer* **115**, 489–492.

Hagglund, B. & Persson, L. (1976), 'An experimental study of radiation from wood flames', *FoU-Brand* **1**, 2–6.

Hastaoglu, M. & Berruti, F. (1989), 'A gas-solid reaction model for flash wood pyrolysis', *Fuel* **44**, 1408–1413.

Hawksely, P. G. W. (1952), 'The physics of particle size measurement: Part II. optical methods and light scattering', *The Brithish Coal Utilisation Research Association Bulletin XVI* **4 & 5**, 117–147 & 181–209.

Heskestad, G. (1983), 'Luminous heights of turbulent diffusion flames', *Fire Safety Journal* **5**, 103–108.

Heskestad, G. (1991), 'A reduced-scale mass fire experiment', *Combustion and Flame* **83**, 293–301.

Heskestad, G. (1999), 'Turbulant jet diffusion flames: Consolidation of flame height data', *Combustion and Flame* **118**, 51–60.

Higuera, F. (2002), 'Flame spread along horizontal solid fuel cylinders', *Proceedings of the Combustion Institute* **29**, 211–217.

Hirano, T., Noreikis, S. E. & Waterman, T. (1974), 'Postulations of flame spread mechanisms', *Combustion and Flame* **22**, 353–363.

Hottel, H. (1954), *In W.H. McAdams, Heat Transmission*, McGaw-Hill Book Company Inc. New York, chapter 6, pp. 55–125.

Hottel, H. & Broughon, F. (1932), 'Determination of true temperature and total radiation from luminous gas flames', *Industrial and Enginering Chemistry, Analytical Edition* **4**(2), 166–175.

Hueglin, C., Geagauf, C., Kunzel, S. & Burtscher, H. (1997), 'Characterization of wood combustion partcles: Morphology, mobility and photoelectric activity', *Environmantal Science and Technology* **31**, 3439–3447.

Incropera, F. & DeWitt, D. (1981), *Fundamentals of Heat Transfer*, John Wiley & Sons.

ISO (2000), *Fire Safety - Vocabulary*, International Organization for Standardisation, Geneva. ISO 13943.

Ito, A., Kudo, Y. & Oyama, H. (2005), 'Propagation and extinction mechanisms of opposed-flow flame spread over PMMA for different sample orientations', *Combustion and Flame* **142**(4), 428–437.

Janssens, M. (2004), 'Modeling of the thermal degradation of structural wood members exposed to fire', *Fire and Materials* **28**, 199–207.

Kanury, A. (1972), 'Ignition of cellulosic solids - a review', *Fire Research: Abstracts & Reviews* **14**, 24–52.

Kennedy, I., Yam, C., Rapp, D. & Santoro, R. (1996), 'Modeling and measurement of soot and species in a laminar diffusion flame', *Combustion and Flame* **107**, 368–382.

Kodson, F., Williams, F. & Buman, C. (1969), 'Combustion of vertical cellulosic cylinders in air', *Twelfth Symposium (International) on Combustion* pp. 253–264.

Kunitomo, T. (1974), Lumious flame emission under pressure up to 20 atm, *in* N. Afgan & J. Beers, eds, 'Heat Transfer in Flames', Scripta Book Company, Washington DC, chapter 18, pp. 271–280.

Kurlbaum, F. (1902), 'über eine einfache methode, die temperatur leuchtender flammen zu bestimmen', *Physik. Z.* **3**, 187–188.

Kurosaki, Y., Ito, A. & Chiba, M. (1971), 'Downward flame spread along two vertical, parallel sheets of thin combustible solid', *Seventeenth Symposium (International) on Combustion* pp. 1211–1220.

Lawson, D. & Simms, D. (1952), 'The ingnition of wood by radiation', *British Journal of Applied Physics* **3**, 288–292.

Lowes, T. & Newall, A. (1971), 'The emissivities of flame soot dispertions', *Combustion and Flame* **16**, 191–194.

Lyons, P. & Weber, R. (1991), Single-strand tests of wildfire potential, *in* '11th Conference Fire and Forest Meteorology', Society of American Foresters, pp. 204–211.

Lyons, P. & Weber, R. (1993), 'Geometrical effects on flame spread rate for wildland fine fuels', *Combustion Science and Technology* **89**, 153–165.

Madhusudana, C. (2006), 'Low thermal conductivity measurements with a GHP apparatus', *International Heat Transfer Conference* **13**.

Magee, R. & McAlevy, R. (1971), 'The mechanism of fire spread', *Journal of Fire and Flammability* **2**, 271–297.

Mandel, J., Bennethum, L., Beezley, J., Coen, J., Douglas, C., Kim, M. & Vodacek, A. (2008), 'A wildland fire model with data assimilation', *MATHEMATICS AND COMPUTERS IN SIMULATION* **79**(3), 584–606.

Mie, G. (1908), 'Beiträge zur optik trüber medien, speziell kolloidaler metallösungen', *Annalen Der Physik* **25**, 377–445.

Min (2000), *MINITAB*. Release 13.

Moghtaderi, B. (2006), 'The state-of-the-art in pyrolysis modelling of lignocellulosic solid fuels', *Fire and Materials* **30**, 1–34.

Moghtaderi, B., Dlugogorski, B., Kennedy, E. & Fletcher, D. (1998), 'Effects of the structural properties of solid fuel on their re-ignition characteristics', *Fire and Materials* **22**, 155–165.

Moghtaderi, B., Novozhilov, V., Fletcher, D. & Kent, J. (1997), 'An integral model for the transient pyrolysis of solid materials', *Fire and Materials* **21**, 7–16.

Muraszew, A. (1974), Firebrand phenomena, Technical Report ATR-74 (8165-01)-1, Engineering Space Operations, The Aerospace Corporation.

NFP (2001), *Guide for Fire and Explosion Investigations.* NFPA 921.

NFPA (2001), *Guide for Fire and Explosion Investigations.* NFPA 921.

Panagiotou, T. & Delichatsios, M. (1989), 'A numerical solution for the surface temperature rise history of a material including surface re-radiation losses', *Factory Mutual Research Corp. (FMRC J.I. 0Q0J1.BU)* .

Pepperhoff, W. (1951), 'über die dispersion des optichen absorptionsvermögens von flammenrußben', *Optik* **8**, 354–366.

Pizzo, Y., Consalvi, J., Querre, P., Coutin, M., Audouin, L., J.L., B. P. & Torero (2008), 'Experimental observations on the steady-state burning rate of a vertically oriented PMMA slab', *Combustion and flame* **152**(3), 451–460.

P.L. Blackshear, J. & Murty, K. (1965), 'Heat and mass transfer to, from, and within cellulosic solids burning in air', *Tenth Symposium (International) on Combustion* pp. 911–923.

Putnam, A. & Speich, C. (1963), 'A model study of the interaction of multiple turbulant diffusion flames', *Nineth Symposium (International) on Combustion* pp. 867–877.

Roberts, A. (1970), 'Problems associated with the theoretical analysis of the burning wood', *Thirteenth Symposium (International) on Combustion* pp. 893–903.

Roberts, A. & Clough, G. (1963), *Nineth Symposium (International) on Combustion* p. 158.

Rohsenow, W., Hartnett, J. & Ganić, E. (1985), *Handbook of Heat Transfer Fundamentals*, McGraw-Hill Book Company, New York.

Rößler, F. & Behrens, H. (1950), 'Bestimmung des absorptionskoeffizienten von rußteilchen verschiedener flammen', *Optik* **6**, 145–151.

Rothermel, R. (1972), A mathematical model for predicting fire spread in wildland fuels, Technical Report INT-115, USDA Forest Service, Intermountain Research Station, Utah, USA.

Santoro, R., Yeh, T., Horvath, J. & Semerjian, H. (1987), *Combustion Science and Technology* **53**, 89–115.

Sato, T., Kunitomo, T., Yoshii, S. & Hashimoto, T. (1969), 'On the monogromatic distribution of the radiation from the luminous flame', *Bulletin of JSME* **12**(53), 1135–1143.

Schmidt, H. (1909), 'Prüfung der strahlungsgesetze der bunsenflamme', *Ann. Physik* **29**, 971–1029.

Sibulkin, M. & Lee, C. K. (1974), 'Flame propagation measurements and energy feedback analysis for burning cylinders', *Combustion Science and Technology* **9**, 137–147.

Siddall, R. & McGrath, I. (1963), 'The emissivity of luminous flames', *Nineth Symposium (International) on Combustion* pp. 102–110.

Simms, D. (1962), 'Demage to cellulosic materials by thermal radiation', *Combustion and Flame* **6**(4), 303–318.

Simms, D. & Law, M. (1967), 'The ignition of wet and dry wood by radiation', *Combustion and Flame* **11**, 377–388.

Sparrow, E. & Cess, R. (1978), *Radiation Heat Transfer*, Hemisphere Publishing Corporation, McGraw-Hill Book Company.

Spearpoint, M. J. (1999), Predicting the ignition and burning rate of wood in the cone calorimeter using an integral model, Technical Report NIST GCR 99-775, National Institute of Standards and Technology, United States Department of Commerce.

Spearpoint, M. & Quintiere, J. (2000), 'Predicting the burning of wood using an integral model', *Combustion and Flame* **123**(3), 308–325.

Steinhagen, H. (1977), Thermal conductive properties of wood, green or dry, from -40 tp +100 degrees celsius; a literature review, Technical Report FPL-9, USDA Forest Service.

Steward, F. & Tennankore, K. (1981), 'The measurement of the burning rate for an individual dowel in a uniform fuel matrix', *Eighteenth Symposium (International) on Combustion* pp. 641–646.

Stith, J., Radke, L. & Hobbs, P. (1981), 'Particle emissions and the production of ozone and nitrogen oxides from the burning of forest slash', *Atmospheric Environment* **15**, 73–82.

Strezov, V., Moghtaderi, B. & Lucas, J. (2003), 'Thermal study of decomposition of selected biomass samples', *Journal of Thermal Analysis and Calorimetry* **72**, 1041–1048.

Stull, V. & Plass, G. (1960), 'Emissivity of dispersed carbon particles', *The Optical Sociaty of America* **50**(2), 121–129.

Suleiman, B., Larfeldt, J., Leckner, B. & Gustavsson, M. (1999), 'Thermal conductivity and diffusivity of wood', *Wood Science and Technology* **33**(6), 465–473.

Suzuki, M., Doboshi, R. & Hirano, T. (1994), 'Behaviour of fire spreading downward over thick paper', *25th Symposium (International) on Combustion* pp. 1439–1446.

Svenson, J., Pettersson, J. & Davidsson, K. (2004), 'Fast pyrolysis of the main components of birch wood', *Combustion Science and Technology* **176**, 977–990.

Telisin, H. (1974), Flame radiation as a mechanism of fire spread in forests, *in* N. Afgan & J. Beer, eds, 'Heat Transfer in Flames', Scripta Book Company, Washington DC, pp. 441–449.

Thomas, P. (1963), 'The size of flames from natural fires', *Ninth Symposium (International) on Combustion* pp. 844–859.

Thomas, P. (1974), Effects of fuel geometry in fires, Technical Report CP29/74, Building Research Establishment.

Thomas, P., Baldwin, R. & Heselden, A. (1965), 'Buoyant diffusion flames: Some measurement of air entrainment, heat transfer, and flame merging', *Tenth Symposium (International) on Combustion* pp. 983–996.

Thomas, P., Webster, C. & Raftery, M. (1961), 'Some experiments on buoyant diffusion flames', *Combustion and Flame* **5**, 359–367.

Tinney, E. (1965), 'The combustion of wooden dowels in heated air', *Tenth Symposium (International) on Combustion* pp. 925–930.

Tsai, K. & Drysdale, D. (2002), 'Flame height correlation and upward flame spread', *Fire and Materials* **26**, 279–287.

Vovelle, C., Akrich, R. & Delbourgo, R. (1981), 'Temperature evolution prior to ignition of cellulosic materials', *First Specialist Meeting (International) of the Combustion Institute* **II**, 586–91.

Weber, R. (1990), 'The moist strand and the burning bed', *Canadian journal of forest research* **20**, 845–848.

Weber, R. & De Mestre, N. (1990), 'Flame spread measurements on single ponderosa pine needles: Effects of sample orientation and concurrent external flow', *Combustion Science and Technology* **70**, 17–32.

Weber, R., Mercer, G., Sidhu, H. & Gray, B. (1997), 'Combustion waves for gases (le=1) and solids (le$\rightarrow\infty$)', *Proceedings of the Royal Society of London Series A* **453**, 1105 – –1118.

Williams, F. (1976), 'Mechanisms of fire spread', *Sixteenth Symposium on Combustion* pp. 1281–1294.

Williams, F. (1982), 'Urban and wildfire phenomenology', *Progress in Energy and Combsustion Science* **8**, 317–354.

Willner, T. & Brunner, G. (2005), 'Pyrolysis kinetics of wood and wood components', *Chemical Engineering and Technology* **28**(10), 1212–1225.

Wood Handbook - Wood as an Engineering Material (1999), Technical Report FPL-GTR-113, USDA Forest Service.

Zeldovich, Y., Barenblatt, G., Librovich, V. & Makhviladze, G. (1985), *The Mathematical Theory of Combustion and Explosions*, Consultants Bureau, New York.

Zukoski, E. (1986), Fluid dynamic aspects of room fires, *in* 'Proceedings of the 1st International Symposium on Fire Safety Science', Hemisphere Publishing Corporation, pp. 1–30.